

2015

Hierarchical Porous Structures with Aligned Carbon Nanotubes as Efficient Adsorbents and Metal-Catalyst Supports

Hema Vijwani
Wright State University

Follow this and additional works at: https://corescholar.libraries.wright.edu/etd_all



Part of the [Engineering Commons](#)

Repository Citation

Vijwani, Hema, "Hierarchical Porous Structures with Aligned Carbon Nanotubes as Efficient Adsorbents and Metal-Catalyst Supports" (2015). *Browse all Theses and Dissertations*. 1309.
https://corescholar.libraries.wright.edu/etd_all/1309

This Dissertation is brought to you for free and open access by the Theses and Dissertations at CORE Scholar. It has been accepted for inclusion in Browse all Theses and Dissertations by an authorized administrator of CORE Scholar. For more information, please contact library-corescholar@wright.edu.

Hierarchical Porous Structures with Aligned Carbon Nanotubes as Efficient Adsorbents and Metal-Catalyst Supports

A dissertation submitted in partial fulfillment
of the requirements for the degree of
Doctor of Philosophy

By

Hema Vijwani

M.S., Wright State University, 2011

2015

Wright State University

WRIGHT STATE UNIVERSITY
THE GRADUATE SCHOOL

May 21, 2015

I HEREBY RECOMMEND THAT THE DISSERTATION PREPARED UNDER MY SUPERVISION BY Hema Vijwani ENTITLED Hierarchical Porous Structures with Aligned Carbon Nanotubes as Efficient Adsorbents and Metal-Catalyst Supports BE ACCEPTED IN PARTIAL FULFILLMENT OF THE REQUIREMENTS FOR THE DEGREE OF Doctor of Philosophy.

Sharmila M. Mukhopadhyay, Ph.D.
Dissertation Director

Ramana V. Grandhi, Ph.D.
Director, Ph.D. in Engineering Program

Robert E. W. Fyffe, Ph.D.
Vice President for Research and Dean of the
Graduate School

Committee on Final Examination

Sharmila M. Mukhopadhyay, Ph.D.

Mallikarjuna N. Nadagouda, Ph.D.

Amir A. Farajian, Ph.D.

Hong Huang, Ph.D.

Mark N. Goltz, Ph.D.

ABSTRACT

Vijwani, Hema. Ph.D., Department of Mechanical and Materials Science Engineering, Engineering Ph.D. Program, Wright State University, 2015. Title: Hierarchical Porous Structures with Aligned Carbon Nanotubes as Efficient Adsorbents and Metal-Catalyst Supports.

The overall goal of this study is two-fold: synthesis of multiscale nanostructures by growing aligned carbon nanotubes on porous foam substrates and investigation of their applicability as adsorbents and catalyst supports for environmental remediation applications. High purity, vertically-aligned arrays of carbon nanotubes (CNT) are grown on open-cell interconnected porous carbon foams by pre-activating them with an oxide buffer layer followed by chemical vapor deposition (CVD). This type of hierarchical morphology provides the capability of increasing surface area by several orders of magnitude, while tuning its morphology for targeted applications. Analytical models are also proposed in this study for specific surface area calculations, those agree well with the experimental measurements. These hierarchical carbon materials are seen to be powerful adsorbents of aqueous pollutants such as methylene blue dye. Their monolayer adsorption capacities correlate very well with the total CNT surface area determined from analytical models and with BET measurements, indicating full utilization of the nanotube surfaces.

The hierarchical structures can also serve as base supports for attachment of metal nanoparticle catalysts. The catalysts investigated in this study are metallic palladium (Pd), oxidized palladium (PdO), and silver-palladium (Ag-Pd) nanoparticles combination. These are suitable for a variety of industrial applications such as hydrocarbon conversion, hydrogen storage, fuel cell electrodes and pollutant degradation. The current architecture

allows synthesis of highly active catalyst structures utilizing very small quantities of precious metal that make the catalyst component significantly lighter and more compact than conventional systems. Detailed characterization of structure and surface chemical states of these nano-catalysts have been performed and their catalytic activities are tested by measuring the degradation kinetics of organic contaminants via bench-scale experiments. Catalytic degradation of atrazine, an emerging problematic contaminant, was quantified using high-performance liquid chromatography. Among Pd, PdO, and Ag-Pd nanoparticles, PdO in the presence of hydrogen was seen to provide the most rapid reaction rate. These nanocatalysts also enable rapid degradation of chlorinated hydrocarbons such as trichloroethylene and trichloroethane quantified using head-space gas chromatography, with PdO providing the fastest kinetic route.

Durability tests indicated that the nano-particles and nanotubes are robust, and remain attached to the base support after long periods of rapid rotation in water. These results imply that such materials can provide compact and powerful surface active materials in future applications such as adsorbents, catalysts, porous electrodes, and energy storage devices.

TABLE OF CONTENTS

1.	Chapter 1: Introduction and Background.....	1
1.1	Importance of Surface Area	1
1.2	Porous Materials.....	2
1.3	Hierarchical (Multi-Scale) Materials	3
1.3.1	Nature Inspired Hierarchical Materials.....	3
1.3.2	Emerging Hierarchical Materials	3
1.4	Current Trends in Water Treatment Applications.....	4
1.4.1	Water Contamination and Purification Issues.....	4
1.4.2	Nanomaterials used in Water Purification	5
1.5	Research Objectives	7
1.6	Dissertation Outline.....	7
2	Chapter 2: Materials and Methods.....	10
2.1	Chemicals	10
2.2	Porous Materials used in this Study.....	10
2.2.1	Micro-Cellular Carbon Foam (Ce-Foam).....	10
2.2.2	Reticulated Vitreous Carbon Foam (RVC-Foam)	11
2.3	Experimental Methods	13
2.3.1	Fabrication of Carbon Nanotubes on Porous Structures.....	13
2.3.2	Synthesis of Supported Palladium Nano-Particles	17
2.4	Characterization Techniques	18
2.4.1	Scanning Electron Microscopy (SEM).....	18
2.4.2	Energy Dispersive X-Ray Spectroscopy (EDS)	19
2.4.3	X-Ray Photoelectron Spectroscopy (XPS).....	19

2.4.4	X-Ray Diffraction (XRD).....	20
2.4.5	UV-Vis Spectrophotometry (UV-Vis).....	20
2.4.6	Brunauer-Emmett-Teller Surface Area Analysis (BET).....	20
2.4.7	Gas Chromatography – Mass Spectrometry (GC-MS).....	20
2.4.8	Liquid Chromatography – Mass Spectrometry (LC-MS).....	21
3	Chapter 3: Fabrication of Vertically Aligned Carbon Nanotubes through the Porous Materials	22
3.1	Introduction	22
3.1.1	Chemical Vapor Deposition.....	25
3.2	Experimental	26
3.2.1	Materials	26
3.2.2	Support Details.....	26
3.2.3	Synthesis of Vertically Aligned CNT on 3D Porous Structures.....	26
3.2.4	Controlling CNT Fabrication Process Parameters	28
3.3	Results and Discussion.....	30
3.3.1	Nanotubes Arrays on Porous Carbon Structures	30
3.3.2	Structural and Chemical Characterization	36
3.4	Factors Influencing CNT Growth Quality	37
3.4.1	Run-to-Run Variation – System Factors.....	37
3.4.2	Study of Key Process Parameters	40
3.5	Conclusion.....	45
4	Chapter 4: Analysis of Specific Surface Area of CNT-Foam Structures	46
4.1	Introduction	46
4.2	Experimental	47
4.2.1	Support Details.....	47

4.2.2	Varying Amount of CNT Coating	49
4.2.3	Estimating the Surface Area of CNT Arrays	49
4.2.4	BET Characterization Method	50
4.3	Results and Discussion.....	50
4.3.1	Controlling CNT Carpet Length/Height	50
4.3.2	Estimating the Surface Area of CNT Arrays	53
4.3.3	BET Measurements.....	60
4.4	Conclusion.....	65
5	Chapter 5: Adsorption of Methylene Blue Dye Compound	66
5.1	Introduction	66
5.2	Experimental	69
5.2.1	Materials and Chemicals.....	69
5.2.2	Supports Used	69
5.2.3	Batch Studies – Adsorption, Desorption, and Repeatability Studies.....	70
5.2.4	Data Treatment – Rate Kinetics and Adsorption Isotherms	71
5.3	Results and Discussion.....	75
5.3.1	Adsorption of Methylene Blue.....	75
5.3.2	Kinetics Analysis	79
5.3.3	Adsorption Isotherms.....	80
5.3.4	Desorption of MB and Regeneration of the Adsorbent	86
5.3.5	Repeatability Test	86
5.4	Conclusion.....	90
6	Chapter 6: Palladium and Palladium-Oxide Nanoparticles on Hierarchical Carbon Nanostructures	91
6.1	Introduction	91

6.2	Experimental	92
6.2.1	Materials	92
6.2.2	Support Preparation	93
6.2.3	Synthesis of Supported Palladium Nano-Particles	93
6.2.4	Synthesis of Supported Palladium-Oxide Nanoparticles	93
6.2.5	Materials Characterization	93
6.3	Results and Discussion.....	94
6.3.1	Crystal Structure Characterization – XRD	94
6.3.2	Microstructure Characterization – Pd on Various Porous Structures	96
6.3.3	Microstructure of Pd-O Nanoparticles.....	97
6.3.4	Chemical State of Pd and Pd-O Nanoparticles	97
6.4	Conclusion.....	112
7	Chapter 7: Bimetallic Nanoparticles: Palladium – Silver Bimetallic Nanoparticles on Hierarchical Carbon Nanostructures.....	113
7.1	Introduction	113
7.2	Experimental	114
7.2.1	Materials	114
7.2.2	Synthesis of Silver-Palladium Bimetallic Nanoparticles	114
7.3	Results and Discussion.....	118
7.4	Conclusion.....	125
8	Chapter 8: Catalytic Dechlorination of Trichloroethylene and Trichloroethane using Palladium Based Catalysts.....	126
8.1	Introduction	126
8.2	Experimental	129
8.2.1	Chemicals.....	129
8.2.2	Stock Solution and Standards	129

8.2.3	Batch Experiments	130
8.3	Results and Discussion.....	131
8.3.1	Trichloroethylene (TCE) Experiments	131
8.3.2	Trichloroethane (TCA) Experiments	144
8.3.3	Dechlorination Mechanisms with the Pd/H ₂ System	154
8.4	Conclusion.....	155
9	Chapter 9: Catalytic Degradation of Emerging Contaminants – Atrazine using Palladium Based Catalysts.....	156
9.1	Introduction	156
9.2	Experimental	163
9.2.1	Materials and Chemicals.....	163
9.2.2	Substrates used.....	163
9.2.3	Batch Degradation Studies.....	163
9.2.4	Standard Concentration Analysis.....	165
9.2.5	Chemical Analysis – HPLC	165
9.3	Results and Discussion.....	166
9.3.1	Atrazine Degradation	166
9.3.2	Catalyst Chemical Analysis	170
9.3.3	Daughter Products Formation.....	175
9.3.4	Atrazine Degradation Mechanism with Pd/H ₂ System	175
9.4	Conclusion.....	176
10	Summary.....	178
11	Future Work	180
12	Bibliography	182
	Appendix A: Methylene Blue Removal - using supported Pd-NPs.....	199

Appendix B : Chlorinated Hydrocarbons Quantification	200
Appendix C: Abbreviations and Chemical Compounds.....	203

LIST OF FIGURES

Figure 2.1 Scanning Electron Microscopy (SEM) low magnification images showing microstructure of (a) Cellular foam - L1a, (b) Reticulated vitreous carbon RVC - 80 ppi and (c) RVC - 45 ppi foam	12
Figure 2.2 Three-zone chemical vapor deposition (CVD) system used for fabrication of carbon nanotubes (a-b) furnace images, and (c) schematics showing CVD furnace zones.	16
Figure 3.1 Optical images of (a) Cellular foam: Ce-Foam, (b-c) Reticulated Vitreous Foam: RVC-Foam. SEM micrographs of (d) Ce-Foam, and (e) RVC-Foam.....	32
Figure 3.2 (a) Optical image of the CNT grown on RVC disc showing black film like layer of nanotubes. SEM micrographs showing the CNT grown on (b) RVC-foam, and (c) Ce-foam. (d) Bare RVC-foam, and CNT-foam interface of CNT grown (e) on RVC-foam, and (f) on Ce-foam.....	32
Figure 3.3 SEM micrographs showing (a) low magnification of the interface of vertically aligned CNT arrays on RVC Foam, (b-d) degree of alignment or entanglement through the height of the CNT arrays, (e-f) shows STEM images of the interface and CNT arrays.	33
Figure 3.4 X-ray diffraction pattern for (a) Cellular (Ce-Foam), (b) RVC-Foam, (c) CNT grafted Ce-Foam, and (d) CNT grafted RVC-Foam, range $20^\circ < 2\theta < 90^\circ$	34
Figure 3.5 XPS spectra - (a) survey scan, and fine scans of (b) carbon, C <i>1s</i> , and (c) Oxygen, O <i>1s</i> for pristine Ce-foam (pink), pristine RVC-foam (black), CNT grown on Ce-foam (red) and CNT on RVC-foam (blue).....	35
Figure 3.6 Schematic representation of CVD Furnace, (a) 3-zone system, and (b) 2-zone system	39
Figure 3.7 SEM micrographs showing (a-b) CNT-arrays blocking the pores of the foam, and (c) Fe-NPs as impurities on already grown CNT.....	39
Figure 3.8 Cross-sectional analysis of silica coating thickness through porous foam using Energy Dispersive Spectroscopy (EDS) obtained for sample coated with silica on both sides of disc foam <i>i.e.</i> Front 20 and Back 20 minutes	44
Figure 3.9 SEM micrographs showing CNT growth throughout the porous foam structures at (a) Front -exterior, (b) Center – interior, and (c) Back – posterior side of the foam	44

Figure 4.1 SEM images showing typical height of the CNT arrays obtained on the RVC foam sample (exterior side) with CVD run-times of (a) 10, (b) 20, (c,) 30, (d) 40, and (e) 60 minutes. Low magnification SEM images showing pores filled by CNT arrays for (f) 30 and (g) 60 minutes coating.....	48
Figure 4.2 Cross-sectional SEM micrographs of RVC-CNT 30 at cross-section thickness (a) 0 mm - front, (b) 1 mm, (c) 2 mm, (d) 3 mm, (e) 4 mm, and (f) 5 mm - back.....	51
Figure 4.3 Plot obtained for the (a) length of CNT carpet with respect to the cross-sectional thickness (starting from the front side, $x = 0$ mm), and (b) a typical polynomial fit plot.....	51
Figure 4.4 SEM/STEM micrographs of (a) a typical RVC-CNT hybrid interface for linear density analysis, (b -d) typical STEM images used for inner and outer diameter measurements, and size distribution graph of (e) inner diameter of CNT, and (f) outer diameter of CNT.	59
Figure 4.5 (a) Full BET isotherm and (b) linear analysis plot for RVC-CNT 60.....	63
Figure 4.6 (a) Full BET isotherm and (b) linear analysis plot for Isolated CNT.....	64
Figure 5.1 (a) UV-Vis absorbance spectrum of MB solution, $\lambda_{max} \sim 665$ nm, (b) Plot showing influence of different porous structures on adsorption of methylene blue obtained with bare and CNT coated: cellular (Ce-foam) and reticulated (RVC) foams, at initial concentration – 2 mg/L.....	77
Figure 5.2 Adsorption efficiency of methylene blue (initial concentration 2 mg/L) using RVC-CNT hybrids CNT obtained by (a) varying CVD growth time - 10, 20, 30, and 40 minutes, (silica coating time fixed at 10 mins), (b) Silica coating time -10 and 15 mins (CVD run time fixed at 30 mins).....	77
Figure 5.3 Graph showing correlation between MB removal capacity and specific surface area of RVC-CNT hybrid samples (Bare RVC foam and RVC-CNT 10, 20, 30, 40, Table 5.1). Initial concentration of MB was ~ 2 mg/L for all tests.	78
Figure 5.4 Kinetic rate plots of MB adsorbed on to RVC-CNT hybrid structure (CNT 40) showing (a) Pseudo-first order rate model and (b) Pseudo-second order rate model.....	83
Figure 5.5 Plots showing adsorption isotherms for the adsorption of MB on to the RVC-CNT hybrid structures, CNT-40, (a) Langmuir isotherm, and (b) Freundlich isotherm ..	84
Figure 5.6. Images of the vials representing adsorption and desorption of MB using RVC-CNT foam, (a) MB in water, (b) colorless solution indicating MB adsorbed on hybrid	

sample, (c) 2-Propanol solution, (d) MB-adsorbed sample placed in 2-Propanol – blue ring indicates release of MB from sample, and (e) MB desorbed completely in 2-propanol solution and RVC-CNT sample is retained. 88

Figure 5.7 Methylene blue removal plots obtained by re-using RVC-CNT hybrid structures (a) adsorption for up to 6 cycles and samples stored in 2-propanol overnight (at cycles 3-4), (b) adsorption-desorption analysis for up to 10 cycles where the samples were stored in water and in air overnight (at cycles 8-9), and (c) adsorption-desorption cycles..... 89

Figure 6.1 X-ray diffraction pattern for CNT grafted Ce-Foam and Pd-CNT grafted Ce-Foam, range $20^\circ < 2\theta < 90^\circ$ 95

Figure 6.2 SEM micrographs showing Pd-NPs fabricated on (a) Ce-foam and (b) RVC foam 95

Figure 6.3 Typical SEM images of one-coating cycle of Pd-NPs fabricated on CNT-coated foams (a-d) top view of CNT arrays, (e-f) side view of the CNT arrays 98

Figure 6.4 SEM micrographs showing Pd-NPs fabricated on CNT-grafted cellular foam by one-coating cycle (a), and two-coating cycle (b), processes 99

Figure 6.5 SEM micrographs showing Pd-NPs fabricated on CNT-grafted RVC-foam by one-coating cycle (a), two-coating cycle (b), and three-coating cycle (c), processes 99

Figure 6.6 SEM micrographs of (a-b) Pd, (c-d) Pd-O₂₅₀, and (e-h) Pd-O₃₀₀ synthesized on RVC-CNT hybrid structures 101

Figure 6.7 Survey scan (general scan) of as-prepared palladium nanoparticles sample 102

Figure 6.8 Survey scans (general scan) of oxidized palladium nanoparticles samples, (a) Pd-O₂₅₀ and (b) Pd-O₃₀₀ treated at 250 °C and 300 °C, respectively..... 103

Figure 6.9 XPS C 1s peak fine-scan obtained from (a) Pd, (b) Pd-O₂₅₀ and (c) Pd-O₃₀₀ samples..... 104

Figure 6.10 XPS fine-scan spectra of Pd 3d peak obtained from palladium nanoparticles (Pd-NPs)..... 108

Figure 6.11 XPS Pd 3d fine-scan of samples oxidized at (a) 250 °C (Pd-O₂₅₀), and (b) 300 °C (Pd-O₃₀₀) 109

Figure 6.12 XPS fine-scan spectra of O 1s and Pd 3p peaks obtained from (a) Pd NPs, (b) Pd-O₂₅₀, and (C) Pd-O₃₀₀ samples..... 110

Figure 7.1 SEM micrograph of Pd-NPs attached on CNT-RVC foam samples.....	116
Figure 7.2 SEM micrographs of Ag coated Pd-NPs attached on CNT-RVC foam samples (Ag-Pd NPs).....	117
Figure 7.3 XPS survey scan (general scan) of Ag-Pd bimetallic nanoparticles on RVC-CNT foam samples	119
Figure 7.4 XPS C <i>1s</i> fine-scan obtained from Ag-Pd bimetallic nanoparticles on RVC-CNT foam samples	119
Figure 7.5 XPS fine scan spectra of (a) Ag <i>3d</i> and (b) Pd <i>3d</i> obtained from Ag-Pd bimetallic nanoparticles	120
Figure 7.6 XPS fine scan spectra of (a) Ag <i>3p</i> , and (b) O <i>1s</i> – Pd <i>3p</i> obtained from Ag-Pd bimetallic nanoparticles	121
Figure 8.1 Calibration curves of TCE compound in 60 mL reactors with mass varying from 0.028 μ moles to 1.389 μ moles (a) without H ₂ purging, and (b) with H ₂ purging in the reactors obtained by plotting peak areas with known TCE standards	134
Figure 8.2 Dechlorination profile of TCE using various carbon and Pd-based catalysts (a) without Hydrogen gas purging, and (b) with Hydrogen gas purging (5% H ₂ balance N ₂) for 20 minutes. Total initial mass of TCE in bottle, [TCE] ₀ = 0.278 μ moles.....	135
Figure 8.3 Dechlorination profile of TCE using various carbon and Pd-based catalysts with hydrogen gas purging (5% H ₂ balance N ₂) for 20 minutes. Total initial mass of TCE in bottle, [TCE] ₀ = 1.389 μ moles.....	136
Figure 8.4 Trichloroethylene removal plots obtained by re-using Pd-CNT and PdO-CNT hybrid structures as catalysts showing repeatability of TCE removal capacity after three cycles.....	136
Figure 8.5 Pseudo-first order rate plots for the dechlorination of TCE by Pd-based catalysts on RVC foams with H ₂ showing total initial mass (a) [TCE] ₀ – 0.278 μ moles, and (b) [TCE] ₀ – 1.389 μ moles.....	137
Figure 8.6 XPS Pd <i>3d</i> fine-scan spectra of PdO-CNT on RVC foam (a) before and (b) after TCE dechlorination.....	141
Figure 8.7 XPS C <i>1s</i> fine-scan spectra of PdO-CNT-Foam before and after TCE dechlorination	141

Figure 8.8. Formation of daughter products of TCE ($[TCE]_0 = 1.389 \mu\text{moles}$ or $C_0 = 5 \mu\text{g/mL}$) during dechlorination with (a) Pd-CNT Foam, and (b) PdO-CNT Foam samples in the presence of H_2 .	142
Figure 8.9 Calibration curves of TCA compound in 60 mL reactors for mass varying from $0.025 \mu\text{moles}$ to $1.237 \mu\text{moles}$ with H_2 purging in the reactors obtained by plotting peak areas with known TCA standard	147
Figure 8.10. Dechlorination kinetics profile of TCA ($[TCA]_0 = 0.247 \mu\text{moles}$ or $C_0 = \sim 1 \mu\text{g/mL}$) showing the effect of H_2 gas obtained for the control and Pd-CNT foam samples without and with H_2 purging.	147
Figure 8.11 Dechlorination kinetics profile of TCA ($[TCA]_0 = 0.247 \mu\text{moles}$ or $C_0 = \sim 1 \mu\text{g/mL}$) obtained with different samples in the presence of H_2	148
Figure 8.12 Dechlorination kinetics profile of TCA ($[TCA]_0 = 1.237 \mu\text{moles}$ or $C_0 = \sim 5 \mu\text{g/mL}$) obtained using Pd-CNT, and PdO-CNT foam samples in the presence H_2 .	148
Figure 8.13 Pseudo-first order rate plots for the dechlorination of TCA by Pd-based catalysts with H_2 showing for total initial mass (a) $[TCA]_0 = 0.247 \mu\text{moles}$, and (b) $[TCA]_0 = 1.237 \mu\text{moles}$.	149
Figure 8.14 Formation of daughter products of TCA during dechlorination with (a) Pd-CNT Foam, and (b) PdO-CNT Foam samples in the presence of H_2 .	152
Figure 9.2 Calibration curve of atrazine concentrations varying from $0.01 \mu\text{g/mL}$ to $1 \mu\text{g/mL}$ obtained by plotting peak area ratios (Atrazine to d_5 -atrazine peak area ratio) with known standard atrazine concentration.	168
Figure 9.1 A typical (a) full scan TIC chromatograph and (b) LC-MS/MS chromatogram acquired in multiple reaction monitoring mode for Atrazine (216.2) and d_5 -Atrazine (221.1) ion channels.	168
Figure 9.3 Degradation kinetics of atrazine (initial concentration of $1 \mu\text{g/mL}$) obtained for the control, CNT foam, and Pd-CNT foam reactor samples with and without H_2 gas purging. Dotted lines are reactions without H_2 purging.	169
Figure 9.4 Degradation kinetics of atrazine (initial concentration of $1 \mu\text{g/mL}$) obtained for the Pd-CNT, PdO-CNT, and bimetallic Ag-Pd CNT foam samples with H_2 gas purging (5% H_2 balance N_2) for 30 minutes.	169
Figure 9.5 XPS Pd $3d$ fine-scan spectra of before and after atrazine degradation using (a) Pd-CNT and (b) PdO-CNT on RVC foam.	171

Figure 9.6. Atrazine degradation and daughter products formation curves with (a) Pd-CNT Foam, (b) PdO-CNT Foam, and (c) Ag-Pd CNT Foam samples in the presence of hydrogen gas. 172

Figure 9.7 Proposed mechanism for hydrogenated products of atrazine - catalytic degradation with palladium based catalysts in the presence of hydrogen 173

Figure 9.8 Proposed mechanism for hydroxylated products of atrazine - catalytic degradation with palladium (oxide) catalysts in the presence of hydrogen [148], [150] 174

Figure A1 Methylene blue removal plot obtained with (a) Ce-Foam, (b)Pd/Ce-Foam, (c) CNT Ce-Foam, and (d) Pd/CNT Ce-Foam hybrid structures. 199

LIST OF TABLES

Table 2.1 Standard material properties of cellular (Ce) carbon foam and reticulated vitreous carbon (RVC) Foam.....	12
Table 3.1 Variations of key process parameters for optimizing CNT growth through porous structure using CVD techniques	29
Table 4.1 Showing the sample ID of various RVC-CNT hybrids used in this study	48
Table 4.2 Estimated values of average length of CNT arrays and average growth rate of CNT through foam for various RVC-CNT hybrids.....	52
Table 4.3 Estimated values of CNT morphology obtained using SEM analysis. Specific surface area of reticulated foams – RVC of 80 ppi obtained from literature.....	52
Table 4.4 The mass of RVC-CNT hybrids before and after CNT growth, percent weight loss of foams due to heat in CVD environment, absolute weight gain (% increase) in weight after CNT growth, and areal density of CNT obtained from various CVD run times, $t_{\text{CVD}} = 10, 20, 30, 40, \text{ and } 60$	58
Table 4.5 Total estimated available surface area created by grafting varying amount of CNT on RVC-foam supports	58
Table 4.6 BET surface areas and Langmuir surface areas measured using N_2 adsorption BET technique	62
Table 5.1 Estimated specific surface area of RVC-CNT hybrids and removal efficiency at initial concentration 2 mg/L methylene blue	78
Table 5.2. Adsorption kinetic parameters obtained using Pseudo-First order and Pseudo-Second order rate kinetics for adsorption of MB on CNT-40	85
Table 5.3. Isotherm parameters obtained using Langmuir and Freundlich isotherm for the adsorption of MB on CNT-40.....	85
Table 5.4 Adsorption capacities of MB on various adsorbents as reported in the literature for comparison	85
Table 6.1 Elemental composition obtained from EDS analysis of Pd-NPs fabricated on the Cellular foam and RVC foams with one, two, or three coating cycles.....	100
Table 6.2 Elemental chemical composition and characteristic core spectra positions of elements from Pd, Pd-O ₂₅₀ , and Pd-O ₃₀₀ samples using XPS analysis.....	111

Table 6.3 Elemental chemical composition obtained using EDS analysis for Pd, Pd-O ₂₅₀ , and Pd-O ₃₀₀ samples	111
Table 7.1 Elemental chemical composition and characteristic core spectra positions of elements from Pd and Ag-Pd bimetallic samples using XPS analysis	124
Table 7.2 Elemental chemical composition obtained using EDS analysis for Pd and Ag-Pd bimetallic on RVC-CNT foam samples.....	124
Table 8.1 Pseudo-first order rate constants for dechlorination of TCE using Pd based catalysts in the presence of H ₂	138
Table 8.2 Daughter products of TCE by dechlorination with Pd and PdO as catalysts .	143
Table 8.3 Pseudo-first order rate constants for dechlorination of TCA using Pd-based catalysts in the presence of H ₂	150
Table 8.4 Daughter products of TCA by dechlorination with Pd and PdO as catalysts .	153
Table 9.1 Chemical structure, chemical name, molecular formula, molecular weight of atrazine and related hydrogenated atrazine products	159
Table 9.2 Chemical structure, chemical name, molecular formula, molecular weight of atrazine and related hydroxylated atrazine products [148]	161
Table B.1 Chlorinated hydrocarbons compounds (CHCs) - stock solution calculations	201
Table B.2 Chlorinated hydrocarbon compounds (CHCs) standard calculations	201
Table B.3 Pseudo-first order equation and rate constant calculations for chlorinated hydrocarbons (CHCs) in reactors.....	202

ACKNOWLEDGEMENTS

This work would not have been possible without the support, guidance, efforts, and friendship of many people.

First and foremost, I would like to thank my advisor, Professor Sharmila Mukhopadhyay for her guidance and support throughout this study. She has been a true inspiration to me and her mentoring has helped me become a better researcher.

I would also like to thank Dr. Mallikarjuna Nadagouda for providing me with invaluable advice and with all the support in coordinating my experiments at USEPA. Furthermore, I would like to thank all my committee members for their insightful inputs on my dissertation and positive feedback during all the conversations.

This PhD would not have been possible without the unrelenting support and the backing of my family. I sincerely thank my parents Mr. Prahalad Mal Vijwani and Mrs. Padma Vijwani for their love, encouragement, and understanding. Thank you both for providing the strength to accomplish my goals. Special thanks go to my sisters Roma Vijwani and Mona Vijwani as well as my brothers Raja Vijwani and Anil Vijwani for their love, support, and belief in me. I would also like to mention those that are no longer with us: My grand parents, Narumal Vijwani and Gangabai Vijwani, and my uncle Gopal Vijwani, whose memories live strong with me.

I would also like to thank my colleagues Ian Barney, Anil Karumuri, Betty Quinton, Wenhui Wang, and Lvmeng He for their time to discuss and exchange ideas related to research and other things in life. I would like to thank Wayne Brashear for the technical guidance with experiments at EPA.

This acknowledgement would be incomplete without thanking my friends for being the social support throughout my time at Wright State. Many thanks go to Kunal Sengupta, who has always provided me with the motivation and has helped me through this journey. I would like to thank my long time friend Kirtikant Paulla for the support and help during my PhD. I would also like to thank my friends Adam Maleszewski and Jared McCoppin for letting me bounce my ideas through them and for making my stay at Wright State enjoyable.

DEDICATION

This dissertation is dedicated to my family
For their endless love, support, and encouragement

Specially dedicated to my brother Anil Vijwani

1. Chapter 1: Introduction and Background

1.1 Importance of Surface Area

The characteristic behavior of solid materials is determined not only by their chemical nature but also by their physical properties such as surface morphology, specific surface area, density, and porosity. The surface of a solid material is the region by which it interacts with the surroundings, which may consist of gas, liquid and other solid materials. Mechanisms controlled by the surface interactions include chemical reactions, atomic diffusion, energy transport, absorption, adsorption, desorption, and separation. The rates of such interactions are influenced by the interfacial contact between two interacting phases, which is determined by the amount of material on the surface. The surface morphology and specific surface areas of a solid material are therefore critical to the effectiveness of any system involved and can significantly influence its performance characteristics. The performance of applications can be enhanced by the use of materials having high surface area.

Specific surface area (SSA) is the measure of surface area per unit volume or mass of a material. The SSA of a material can be increased either by granulating a large solid into smaller fragments (e.g. coarse/fine powders) or by synthesizing materials at very small dimensions that have high-aspect ratios (surface-to-volume ratios), for example nano-tubes. Besides reducing the size of the material, the true surface area of materials can also be enhanced by altering their geometric shape. The irregular shapes of many solids account for the increase in the surface area, which is useful for various functionalities. Similarly, the surface area of a material can be increased by inducing porosity to the solid. The pores or voids within a porous material account for an increase in the specific surface area as the exposed pores

provide additional surfaces and the voids (empty space) account for reduction in the weight of the material. Porous materials are a step towards obtaining high SSA materials [1], [2]. Materials in the form of powders, particles, porous materials or nano-materials have received significant interest for various applications requiring high surface area such as catalysis, adsorption/absorption, filtration, and thermal applications.

1.2 Porous Materials

Materials containing pores, spaces, or voids within are known as porous materials. Many different classifications of the porous materials have been proposed depending on the pore-geometry (size, porosity), pore-structure (closed pore or open pore structures), pore-arrangement (random or ordered pore arrangements), and material composition (metal, oxide, or carbon) [3], [4]. The physical attributes such as surface area of a porous material are often characterized by its pore size and porosity. Porous materials that have small pores and high pore-densities exhibit very high SSA and vice versa [4].

Open-pore structured (open-cell or interconnected) porous materials, owing to their high accessible surface area, are widely known for their outstanding heat/mass capture and transfer properties. They possess a wide range of applications and are adapted as catalysts supports, water filters, heat exchangers, absorbers and many more [1]. However, the increase in surface area of the porous material is restricted by the porosity that compromises the structural integrity. Therefore, there has been an ever-rising demand to increase the surface area as much as possible. This can be achieved by using nature-inspired multi-scale hybrid structures that address the limitations of porous materials.

1.3 Hierarchical (Multi-Scale) Materials

A hierarchical material consists of assemblies of structures or components having multi-scale dimensions. The hierarchical nature of such structures is known for its remarkably unique characteristics, which plays an important role in the enhancement of available surface area. The concept of multi-level architectures is derived from our very own nature, which has been widely accepted for the functionality of many living entities.

1.3.1 Nature Inspired Hierarchical Materials

Hierarchy in materials naturally exists in many aspects of the environment such as in biological living systems. Some examples include wood, leaves, roots, bone, tendon, and glass sponges [5], [6]. The multi-level architecture of these materials exhibit components on more than one length scale in hierarchical pattern so as to accommodate nature's underlying challenges. Natural hierarchical materials are the perfect known hierarchical materials that have ambient growth conditions and possess self-organization mechanisms at all levels in the hierarchy. Such characteristics have been the root of inspiration for imitating nature's own trait to make synthetic hierarchical structures [7]. It is significantly challenging to replicate nature's intellect and develop microscopic hierarchical structures suitable for practical applications.

1.3.2 Emerging Hierarchical Materials

Hierarchy in synthetic materials has been studied and developed in various forms including, (1) hierarchical porous structures that have multi-level porous systems (macro/meso/micro- pores) within the material [8], (2) nano-structures on fibrous materials, and (3) nano-structures on flat supports. Some examples of the

emerging hierarchical structures include carbon nanotubes (CNT) grafted on free standing fibers or weaved fibers and nanoparticles supported on free standing CNT or fibers [9]–[11].

Another kind of approach to hierarchy, can be obtained by incorporation of fibrous nanostructures (nanotubes) on porous materials (foams). CNT have been reportedly grown on simple geometries like flat surfaces and fibers [12], but research on complex geometries like interconnected porous structures is relatively new and has been mostly restricted to oxide or metallic foams due to their growth requirements and conditions [13] [14]. The hierarchical structure used in this study is a hybrid material obtained by direct growth of carbon nanotubes onto microcellular carbon porous foam having interconnected open-pore structure [15]. This hybrid structure is robust in nature and holds the capability of tuning the surface area, which can be increased by several orders of magnitude without adding any significant weight to the material. Such a phenomenal hierarchical rigid support can be adapted for a wide range of applications ranging from novel catalyst supports to water filters [16]–[18].

1.4 Current Trends in Water Treatment Applications

Materials having high specific surface area are desirable for the effectiveness of a system as the interfacial surface area is the limiting factor that plays an important role in many emerging technologies. One of the important applications is in water treatment technology and that has been studied in this research.

1.4.1 Water Contamination and Purification Issues

The contamination of water bodies (aquifers, groundwater, lakes, rivers, and oceans) is a significant and ever-growing problem worldwide. The levels of water pollution have become progressively complex to a point that the problem appears

intractable. The pollution of water by a multitude of contaminants has harmful impact on the ecosystem resulting in an unprecedented crisis and affecting all the living entities. A wide variety of contaminants are from industrial chemical wastes that are discharged into the environment without proper treatment, these contaminants include inorganic and organic compounds such as heavy metals (e.g. lead, chromium), chemical toxins (e.g. halogenated hydrocarbons, dyes, aromatic compounds), petroleum products, and microorganisms (e.g. bacteria, fungi). Chemical compounds such as halogenated hydrocarbons, aromatic compounds are of great concern worldwide because they exhibit toxicity to the receptors [19]. Two major reasons for their existence are due to their (1) widespread use in industrial applications, and (2) high resistance to biological degradation. Other major concern is due to the newly emerging contaminants known as contaminants of emerging concern (CECs) such as fertilizers, herbicides, pesticides, pharmaceuticals, plasticizers, detergents, and antimicrobial agents. The demand for clean water is rapidly increasing and there has been emphasis on developing efficient methods for purification of water and wastewater. The removal of pollutant from water can be carried out by capturing the pollutants onto materials (adsorbing) and/or degrading (e.g. using catalyst metal nanoparticles) by reducing/breaking the toxic compound into less or non-toxic smaller compounds. For such surface specific applications, materials having high specific surface area are desirable.

1.4.2 Nanomaterials used in Water Purification

Carbon-based materials with a high specific surface area such as activated carbon, carbon fibers, and nanostructures of carbon are well-suited for water treatment applications. Recently, nanostructures of carbon including graphene, carbon nanotubes, and bucky-balls have been considered as materials for removal of

pollutants from water. Among them, CNT have proven to be a promising material for the removal of many environmental pollutants due to their high aspect ratio, fibrous mesoporous structure, and large specific surface area. For similar reasons, CNT have also been considered as an attractive support for anchoring metal nanoparticles [20]. However, these structures are mostly in the isolated or free-standing form, which for water treatment applications can pose a significant challenge [21]. As the nanomaterial can get dispersed into the surrounding medium during use and their recovery from the treated water can be difficult, which may result in material loss as well as poses health and environmental hazards [21], [22].

The hierarchical carbon structures used in this study address the above issue by introducing carbon nano-structures that are attached to porous supports so as to facilitate easy loading and unloading of the material in the liquid environments [17], [18]. Micro-porous carbon supports with strongly attached high surface area carbon nanotubes can surpass the other types of currently available porous materials in robustness, ease of handling, and structural integrity.

1.5 Research Objectives

The main objectives of this research are:

1. To investigate efficient approaches to fabrication and optimization of novel hierarchical porous structures having tailorable surface areas for targeted catalytic activities.
2. To investigate the key growth parameters that influences the CNT morphology and permeation through porous foam structures (into the deeper pores).
3. To develop analytical models for predicting specific surface area (SSA) using structural properties such as nanotube density, CNT morphology, length distribution through different levels of porosity, and total surface area of the CNT.
4. To investigate the surface adsorption activity and kinetics of these materials for selected reactions related to removal of contaminants from water.
5. To synthesis and characterize mono/bi - metallic nanoparticles (Pd, Ag/Pd) as well as oxidized palladium nanoparticles (PdO) on these structures and demonstrate their suitability for environmental remediation and catalytic applications.
6. Investigate the catalytic activity of the Pd and Ag-Pd based hierarchical structures for treating select chlorinated and emerging contaminants in water.

1.6 Dissertation Outline

This dissertation is structured as nine broad chapters followed by summary and future works sections. Chapter 1 provides the background for high surface area and hierarchical architecture materials and also provides motivation to the current research. The goals and objectives of this research are outlined in this chapter.

Chapter 2 describes the chemical and materials used in this study. It includes the description of various porous materials used in this study. The details of

fabrication and characterization methods used in this research are given in this chapter.

Chapter 3 focuses on fabrication of hierarchical structures obtained by growing aligned carbon nanotubes (CNT) on porous structures using chemical vapor deposition. Key process parameters for growth and permeation of CNT through the porous structures are identified.

Chapter 4 describes the approaches to tune the surface area of porous structures by varying the morphology of CNT arrays. This chapter includes proposed analytical models and experimental approaches of predicting specific surface area (SSA) of CNT-foam hybrid structures. Three different approaches have been used: calculation from microstructural features, weight gain data as well as direct BET analysis. Their predictions are seen to be in reasonable agreement, indicating that the entire surface would be available for future applications.

Chapter 5 focuses on the adsorption application of the hierarchical structures for removal of a model contaminant: methylene blue from water. Detailed kinetics and isotherm analysis to determine maximum adsorption capacity of the CNT is shown here.

Chapter 6 focuses on fabrication and characterization of palladium (Pd) and palladium oxide (PdO) nanoparticles on these hierarchical structures. Detailed surface chemical analysis of the Pd and PdO is shown in this chapter.

Chapter 7 focuses on fabrication and characterization of silver and palladium (Ag-Pd) bimetallic nanoparticles on these hierarchical structures. Surface chemical analysis of Ag-Pd nanoparticles is shown in this chapter.

Chapter 8 demonstrates the suitability of the Pd-based catalysts (Pd and PdO) on hierarchical structures for environmental remediation applications. This includes investigation of the activity of these catalysts for treating chlorinated contaminants such as trichloroethylene and trichloroethane. The dechlorination mechanisms using palladium-hydrogen systems and surface chemical states of the spent catalysts are discussed in this chapter.

Chapter 9 focuses on the investigation of the catalytic activity of the three Pd-based catalysts (Pd, PdO and Pd-Ag) structures for treating select emerging contaminants: atrazine in water. The dechlorination mechanisms and surface chemical analysis after reactions are shown.

Chapter 10 summarizes the dissertation in the whole and Chapter 11 provides insight to useful potential applications and future research work requirements.

2 Chapter 2: Materials and Methods

2.1 Chemicals

All the reagents used in this study were of analytical grade and used without further purification. These include Hexamethyl-di-siloxane (99.5%, HMDSO, $(\text{CH}_3)_6\text{Si}_2\text{O}$, Sigma-Aldrich chemicals), Ferrocene (99%, $\text{C}_{10}\text{H}_{10}\text{Fe}$, Alfa-Aesar Ltd), Xylene ($\text{C}_6\text{H}_4\text{C}_2\text{H}_6$, PTI Process Chemicals), Tetraamine Palladium (II) Nitrate solution (99.9% TAPN, $\text{Pd}(\text{NO}_3)_2 \cdot 4\text{NH}_3$, 0.375M, 5% Pd, Alfa- Aesar Ltd), and methanol. Other materials were de-ionized water (DI water) and laboratory grade gases that include oxygen, argon, and hydrogen. The microcellular carbon foam used in this study was obtained from Koppers© Inc., and the reticulated vitreous carbon foams were obtained from Ultramet© Inc.

2.2 Porous Materials used in this Study

In this study, two types of carbon foams were employed as base supports for creating hierarchical structures: (1) Cellular carbon (Ce) foam, and (2) Reticulated vitreous carbon (RVC) foam. The RVC foams have various pore densities ranging from 10 to 500 pores per inch (ppi). In this study, we used 80 ppi and 45 ppi. Figure 2.1 shows the SEM images for microstructure of (a) cellular foam, (b) RVC-80 ppi, and (c) RVC-45 ppi. Standard material properties for these foams are provided in the Table 2.1, those were obtained from respective providers.

2.2.1 Micro-Cellular Carbon Foam (Ce-Foam)

Micro-cellular carbon foams that were used in this study are open cell porous structures with interconnected seamless pores that are ordered three dimensionally. The foams are rigid, lightweight, permeable, thermally conductive, and have high

porosities ranging from 68% to 94% [15]. Carbon foam structures are known for high specific strength, chemical stability, lower coefficient of thermal expansion, good thermal and electrical properties, and have potential aerospace and thermal applications.

The microcellular carbon foam samples were obtained as large blocks from Koppers© Inc. The cellular foam used in this study is ‘L1a’ grade foam that has approximately 80% porosity. The specific surface area of this foam was estimated to be approximately $6.2 \times 10^3 \text{ m}^2 \text{ m}^{-3}$ [15]. Figure 2.1a shows the low magnification SEM image of cellular carbon foam used in this study.

2.2.2 Reticulated Vitreous Carbon Foam (RVC-Foam)

Reticulated vitreous carbon (RVC) foams are highly porous, open cell, low density carbon foam structures that have unique physical, thermal, and electric properties. The porosities of RVC foams can range from 90% to 97% with varying pore densities ranging from 10 ppi to as high as 500 ppi. The specific surface area increases with decreasing pore sizes and increasing pore densities.

RVC foams used in this study were obtained from Ultramet Inc., having 97% open porosity and 80 ppi. Preliminary experiments were also carried out using RVC foam having 97% porosity and 45 ppi. Considering the open porosity and their three-dimensional cellular structure they have very low pressure drops. The skeletal structure of RVC is brittle compared to cellular carbon foams. RVC foam structures have a wide range of applications including filters, high temperature insulation, electrodes, energy storage devices, biological scaffolding, and catalysis [23].

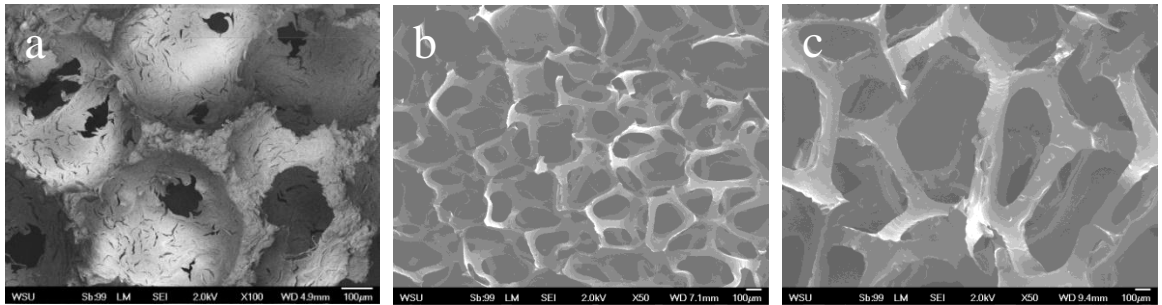


Figure 2.1 Scanning Electron Microscopy (SEM) low magnification images showing microstructure of (a) Cellular foam - L1a, (b) Reticulated vitreous carbon RVC - 80 ppi and (c) RVC - 45 ppi foam

Table 2.1 Standard material properties of cellular (Ce) carbon foam and reticulated vitreous carbon (RVC) Foam

Standard Properties	Cellular (Ce) Carbon Foam	RVC Foam (45, 80 ppi)
Average Pore Volume, Porosity (%)	78	97
Average Pore Size (μm)	500	~ 500, 300
Bulk density (g/cm^3)	0.38	0.045
Compressive Strength at 20 °C (Mpa)	1.7	0.763
Electrical conductivity (S/cm)	24.51	1.33
Thermal conductivity at 200C (W/m.k)	55	0.085

2.3 Experimental Methods

This section presents the experimental procedures developed in this research. Details of the fabrication of carbon nanotubes on advanced porous structures to obtain hierarchical structures and the details of the synthesis of palladium nanoparticles on such advanced hierarchical porous structures are discussed in this section.

2.3.1 Fabrication of Carbon Nanotubes on Porous Structures

In this study, vertically aligned carbon nanotubes were fabricated on porous foam structures using a two-step coating process adapted from earlier research [15] that includes plasma enhanced deposition of a nano-layer of silica on the porous structures followed by carbon nanotubes coating using thermal chemical vapor deposition (CVD) technique. Carbon nanotubes (CNT) were grown on cellular carbon foam and reticulated vitreous carbon foam structures. This section describes the standard optimized process developed in this study for fabrication of CNT on various porous structures using a three-zone CVD furnace. CNT on porous samples were grown using the standard process of CVD described in this section (unless specified otherwise).

Support Details:

Circular disc shaped foam structures of diameter fitting the CVD tube diameter ($\text{\O} \sim 70$ mm) were used for this study. The thickness of the sample varied for different porous structure depending on their open pore structure. The thickness of cellular foams was uniformly maintained at 2.5 ± 0.1 mm, whereas the thickness for RVC foams having substantial open porosity was selected to be 5.0 ± 0.1 mm.

As mentioned above, the fabrication process has two steps described as follows:

Plasma-Enhanced Silicon Oxide (SiO_x) Coating:

In the first step for synthesizing CNT on foams, the foam supports were pre-coated with a nano-layer of silica (SiO_x) by a gas-phase plasma technique. The oxide coating of silicon was carried out using a plasma assisted microwave reactor (V15GL manufactured by PlasmaTech Inc.). The silica deposition technique used in this study was studied and designed by [15], [24]. A slightly modified silica process suitable for this study has been developed here.

The foam supports were placed on a wire mesh holder while securely sealing the ends of the holder with a saran wrap ensuring that all the gases in the microwave chamber pass through the porous foam. The silica was deposited using gas phase precursors in the microwave (MW) plasma reactor in several cycles, where each cycle is a different and a multiple sub-step process. The gas-precursors used were hexamethyl di-siloxane (HMDSO) and oxygen gas. The sub-steps in silica coating process can be defined as following:

1. Etching: Plasma etching in the presence of O₂ for 180 s at high MW power.
2. Coating: Plasma coating using a mixture of HMDSO and O₂ for 300 s at high MW power. This step determines the time of silica deposition.
3. Stabilizing: running plasma O₂ for 60 s at low power for stabilization purposes.

One coating cycle of silica deposition includes the above-mentioned steps carried out in the following order; 1. etching, 2. coating (300 s), 3. stabilizing, 2. coating (300 s), and 3. stabilizing steps. Therefore, one coating cycle is termed as 10 minutes of silica coating. In this study, both sides of the disc shape supports were coated with silica. One surface of the porous disc support was coated with one cycle of silica referred as front (surface facing the CVD flow direction) surface. And, the

other side surface of the disc (back side) foam was coated by flipping the support in the microwave chamber with two successive coating cycles of silica *i.e.* for 20 mins.

Chemical Vapor Deposition – Fabrication of Aligned Carbon Nanotubes:

Carbon nanotubes were fabricated using chemical vapor deposition (CVD) technique adapted from earlier research [15]. In this study, the floating catalyst CVD technique was carried out in a three-zone furnace (MTI Corporation LTD.) consisting of a quartz tube ($\text{Ø } 80\text{OD} \times \text{Ø } 72\text{ID} \times 1400\text{L mm}^3$) with stainless-steel end caps that has openings for inlet for gas flows as well as for catalyst and carbon precursors, and outlet for exhaust. The catalyst and precursor mixture was injected using a syringe and a pump (MTI©). Figure 2.2 shows the image of the three-zone furnace used in this study.

The three zones of this furnace were referred as left, center, and right zones as shown in Figure 2.2. The left and the center zones are called growth zones, and the right zone is known as the pre-heat/catalyst zone. The circular disc support (D: ~70mm) was kept at 90° angle in the quartz tube, *i.e.* perpendicular to the gas flow direction with the aid of the graphite ring. It was placed in the center zone close to the left zone. Once samples were positioned in the reactor, the furnace was heated in the flow of Argon (Ar). The growth zones were maintained at 700°C . To start the growth process, a measured amount of ferrocene (0.1 g) dissolved in xylene (10 mL) solution was injected at 12.5 ml/hr using a syringe-pump, into pre-heat zone that was maintained at 380°C . The reactions were allowed to take place at 700°C for a specific length of time in an Ar/H₂ environment to facilitate the growth of CNT. The flow rate of Ar/H₂ was 1200/240 cc/min.

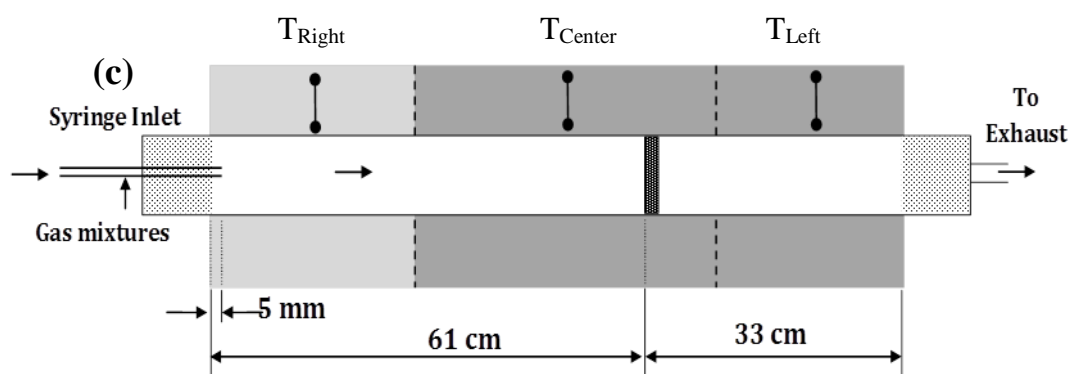
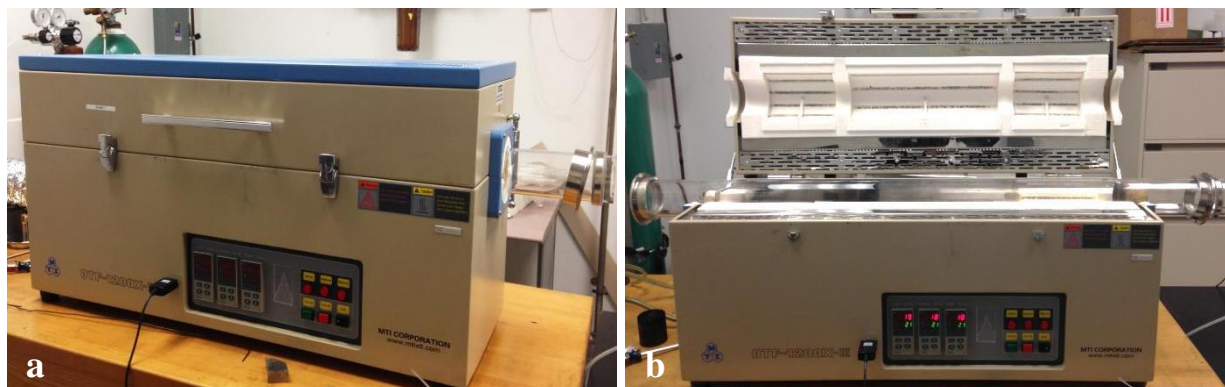


Figure 2.2 Three-zone chemical vapor deposition (CVD) system used for fabrication of carbon nanotubes (a-b) furnace images, and (c) schematics showing CVD furnace zones.

A reaction time of 30 minutes (unless specified otherwise) was carried out to grow CNT on the carbon supports used in this study. The furnace was allowed to cool down to room temperature in a reduced flow of Ar. The CVD process described here is the standard optimized process for growing CNT on the different porous supports and the optimized process was used in this study (unless specified otherwise).

2.3.2 Synthesis of Supported Palladium Nano-Particles

In this study, palladium nanoparticles on the CNT coated cellular (Ce) and reticulated vitreous carbon (RVC) foam supports were fabricated by the liquid-phase synthesis technique combined with thermal reduction process. The process used in this study was developed earlier [16], [18].

Support Preparations

The size of C-foam support used was $\text{\O} 8 \text{ mm} \times 2.5 \text{ mm}$, weighing $\sim 100 \text{ mg}$ whereas the RVC-foam support used was $\text{\O} 8 \text{ mm} \times 5 \text{ mm}$, weighing $\sim 25 \text{ mg}$ each. All the supports were rinsed with methanol and water prior to palladium deposition.

Precursor Equilibrium-Adsorption – Stage I

Tetraamine palladium (II) nitrate (TAPN) of known concentration (62.5 mM TAPN) was used as the metal precursor solution. The rinsed carbon supports were immersed in an aqueous precursor solution of TAPN for specified length of time *i.e.* 30 minutes for Ce-foams and 120 minutes for RVC-foams. The solid supports were recovered from the TAPN solution and the excess (non-interacting) solution on the sample was washed-off by briefly dipping the support in methanol.

Thermal Treatment and Reduction – Stage II

The thermal reduction is carried out in a quartz tube (length 1400 mm, inner diameter 70 mm) closed with stainless steel end-caps in a heating furnace. The

precursor coated samples were placed on a ceramic boat that was placed in the tube at the center of the heating furnace. The ends of the quartz tube were closed with stainless steel end caps that have openings for inlet and exhaust gas flows.

The thermal treatment consists of three individual steps known as drying, calcining, and reducing. In the drying step, the precursor infiltrated samples were dried at 100 °C for 12 hrs. Calcination, often referred to as heat treatment or pyrolysis step, was carried out at 400 °C for 2 hrs. The furnace was heated at a ramp rate of 10 °C/min. Calcination step was done in oxygen rich atmosphere (air) for foam samples, and oxygen deficient inert atmosphere (Ar) for CNT attached hierarchical samples. In this step the amines and nitrates groups of TAPN decompose thermally forming Pd oxide. The samples were subsequently reduced at 450 °C (ramp rate - 10 °C/min) for 2 hrs using hydrogen as the reducing gas and Ar as the carrier gas (reduction step). The furnace was allowed to cool down to room temperature in the reduced flow of H₂ and Ar.

For additional metal loading, the immersing, drying and calcining steps can be repeated multiple times (multiple coating cycles of Pd) prior to the reduction step until desired amount of Pd is obtained. In this study, one, two, and/or three coating cycles of Pd were used suitable to the hierarchical porous structure.

2.4 Characterization Techniques

In this study the following characterization techniques were used.

2.4.1 Scanning Electron Microscopy (SEM)

Surface morphology of the Carbon nanotube hierarchical architectures and metal nanoparticles were observed using JEOL 7401F Field Emission Scanning Electron Microscope (FE-SEM). The SEM analysis on the samples was carried out

using secondary mode and a mixture of secondary and backscattered modes. Quantitative analysis was carried out on SEM images using Scandium© SEM imaging software provided by JEOL 7401F for FESEM.

2.4.2 Energy Dispersive X-Ray Spectroscopy (EDS)

Energy dispersive X-ray spectroscopy (EDS) using Ametek Inc. EDAX system, which is coupled with JEOL FE-SEM, was performed for elemental data analysis. It is capable of providing qualitative elemental analysis of elements present in a sample for up to a surface depth of several microns. In addition to identifying the elements present in a sample, it also quantifies their chemical ratio. The intensity of the characteristic x-rays allows the elemental composition of the sample to be measured.

2.4.3 X-Ray Photoelectron Spectroscopy (XPS)

X-ray photoelectron spectroscopy (XPS) was performed using Kratos (Axis Ultra) system with mono-chromatized Al K α (1486.6 eV) source in ultra-high vacuum environment (UHV $\sim 10^{-9}$ Torr). The X-ray source with a 10mA emission current at a power of 120W was used. Spectra were taken in the analyzer mode of pass energy 20eV. The survey scans (BE: 1000 - 0 eV) were taken in the retarding sweep modes and similarly high resolution fine scans of respective elements were also collected. A charge neutralizer was used to neutralize the charge in the sample. Any static charge built on the samples was corrected by assigning a value of 284.4 eV to C 1s spectrum, which is a known binding energy value of carbon in graphite [25]. The XPS spectra processing and peak quantification was done using CasaXPS© software provided for Windows© PC. The peak positions determined the elemental characteristics whereas

the peak intensities were converted using predefined relative sensitivity factors (RSF) for atomic percentages of respective elements given by CasaXPS© Library.

2.4.4 X-Ray Diffraction (XRD)

X-ray diffraction (XRD) patterns were obtained by X-ray minidiffractometer, MD-10, using a monochromotized Cu K α radiation ($\lambda = 1.5418 \text{ \AA}$) at 25 kV and 0.4 mA. XRD data was collected in the range of $20^\circ < 2\Theta < 90^\circ$ diffraction angle. The interplanar distance, dL was calculated from first order Bragg's reflection.

2.4.5 UV-Vis Spectrophotometry (UV-Vis)

The absorbance peaks of methylene blue dye solution were obtained by UV-vis spectrophotometry technique, using a Cary 50 UV-Visible Spectrophotometer. The spectrophotometer was set to absorbance range (Y-axis) of -0.5 to 1.0. The spectral range (X-axis) was set to 200-800 nm with a scan rate of $\sim 4,100 \text{ nm/min}$. A baseline correction was performed using high-quality DI water. $\sim 1.5 \text{ mL}$ solution was transferred to a disposable polystyrene cuvette of width 1 cm for analyzing the absorbance peaks.

2.4.6 Brunauer-Emmett-Teller Surface Area Analysis (BET)

Brunauer-Emmett-Teller (BET) was done on Micromeritics TriStar II 3000 using N₂ gas adsorption isothermal analysis by stabilizing at liquid nitrogen temperatures. Surface area is calculated from the volume of gas adsorbed onto the sample surface as a function of relative partial pressure.

2.4.7 Gas Chromatography – Mass Spectrometry (GC-MS)

Headspace sample analysis was done on an HP 6890 gas chromatographic system, equipped with a HP 5973 mass selective detector (MSD). The column used

in GC is DB-5MS of dimensions as length 30 m, diameter 0.25 mm and the film thickness of 0.25 μm . 100 μL of gaseous sample was manually injected at the injection port using front injector that was maintained at temperature 150 $^{\circ}\text{C}$. A splitless mode of injection was used. High purity 'He' gas was used as a carrier gas with a flow rate of 1 mL/min. MSD transfer line was maintained at auxiliary temperature of 250 $^{\circ}\text{C}$. The oven method used is described as follows.

S.No	Rate, $^{\circ}\text{C}/\text{min}$	Final Temp, $^{\circ}\text{C}$	Hold time, mins	Final Time, mins
1	Initial	35	3	3
2	10	40	0	3.5
3	30	105	0	5.67

The peak area values of analytes from gas chromatography were transformed into their respective amount at equilibrium using laboratory calibration curves.

2.4.8 Liquid Chromatography – Mass Spectrometry (LC-MS)

High Performance Liquid Chromatography (HPLC) was carried out on Waters Micromass Quattro Micro equipped with a mass spectrometer for liquid chromatography (LC-MS). The HPLC column is a Restek Biphenyl Column - Pinnacle DB Biphenyl Column of dimensions 100 x 2.1 mm² (1.9 μm). The HPLC solvents were; (A) 90% Water 10% Methanol with 2 mM Acetic acid (NH_4OAc) and (B) 100% Methanol 2 mM Acetic acid (NH_4OAc). Injection sample size is 20 μL and at flow rate of 0.3 mL/min. Each HPLC run was programmed for analysis of 24 minutes as shown in the method below:

Time	Solvent A, %	Solvent B, %
0	50	50
2	50	50
18	0	100
22	0	100
24	50	50

3 Chapter 3: Fabrication of Vertically Aligned Carbon Nanotubes through the Porous Materials

3.1 Introduction

Engineered materials with hierarchical nano-scale architecture offer large available surface area as well as good interfacial contact and they present great potential to explore functionalities in wide-spread applications including catalysis, separation, bio-filters, energy storage, and sensors [9]–[11], [26], [27]. The possibility of varying physical or chemical properties of the components at different levels allows fine tuning the performance of the hybrid material [27][28]. A considerable amount of research is focused on developing hierarchical materials consisting of graphitic nanostructures such as *carbon nanotubes* for surface related interactions [29]–[31].

Carbon nanotubes (CNT) are nanoscale structures that have unique physico-chemical, mechanical, optical, and electrical properties, which make them fascinating materials for wide range of applications including sensors, filters, energy storage, and catalyst supports [32][33]. The CNT are often integrated with larger solids to create macroscopic structures for practical applications. Few of the most common attempts that make use of CNT in hierarchical structures to improve their functionality include (i) CNT incorporated in polymers as composites [34], [35], (ii) yarns or buckypapers consisting of CNT and fibers [26], (iii) CNT or CNT-graphene sponge structures [31], [36] or and (iv) direct growth of CNT on fibers or flat substrates [10]. Another possible approach to improve the existing hierarchical architecture would be to introduce an open porous structure as the base substrate for direct growth of CNT. Compared to many flat substrates, the three-dimensional solid open porous structure

offers large surface areas critical for various applications. Most studies for growing CNT on such porous structures have been limited to metal or oxide foams [13], [14]. Wenmakers *et.al.* has reported hairy foam structures demonstrating synthesis of carbon nanofibers on nickel coated carbon foam structures [37]. Moreover, in a published study [15] that reports the direct growth of CNT on carbon foams using a chemical vapor deposition (CVD) technique. Where, an oxide layer (silica in this case) is coated to aid the growth of CNT on carbon. CVD is the most commonly reported technique for growing CNT as it is the most scalable and versatile method as well as widely suitable for the direct growth of CNT on a substrate [38]–[40]. Numerous studies have been reported in the literature for the influence of process parameters on the growth of CNT [39]. It is well known that an oxide layer is required to synthesize CNT on non-oxide substrates like graphitic carbon [15], [24]. In this study, such a method has been adapted from previous studies to grow high purity CNT of controlled morphology on advanced porous carbon structures. The porous structures studied here are micro-cellular carbon foams, which have 80% porosity and reticulated vitreous carbon foams that have 97% porosity.

CNT in various forms including single walled nanotubes (SWNT), multiwalled CNT (MWCNT), and vertically aligned multiwalled CNT (VACNT) have received significant interest for many applications [32], [39], [41], [42]. Recently, vertically aligned CNT forests due to their vertical architectures have been considered as most distinguished form of CNT in the development of new material structures for applications involving interactions at surfaces and interfaces [42]–[44]. Vertical aligned CNT can be very long as high as few cms in length [43]. The growth of vertically-aligned CNT on flat substrates like silicon (with oxide layer) or flakes of

quartz has been studied extensively [44][45], whereas the growth of vertically-aligned CNT on porous structure have received minimal attention (if not none).

In this study, we report vertically-aligned CNT grown on carbon porous structures using a floating catalyst chemical vapor deposition (CVD) technique. High purity aligned CNT that grow vertical to foam surfaces in the form of CNT arrays were synthesized in a three-zone thermal CVD system. This work is built up on earlier developed process, where multi-walled CNT were grown on silica coated cellular foams [15]. Growing carbon nanotubes on the complex geometries like interconnected porous structures is significantly challenging as CNT permeation through the porous materials requires controlled process parameters. Detailed characterization on the influence of parameters for CNT growth on carbon foams has been reported in the earlier publications [15], however, there hasn't been enough focus on study of the influence of such parameters for the permeation of CNT through porous structure.

Various key parameters that influence the growth and permeation of CNT through the porous structures were investigated in this study. The parameters studied are CVD run time, gas composition and flow rates, catalyst and source flow rates, furnace temperatures (pre-catalyst and CNT-growth zone), silica coating thickness, substrate geometry, and unidentified run-run variations. Statistical studies reported by Oliver *et.al.*, shows the variations due to system factors and provide recommendations for consistent growth of CNT [46]. We also report, the influence of such parameters on growth rate, morphology, height and density of CNT arrays.

3.1.1 Chemical Vapor Deposition

Carbon nanotubes can be synthesized using different techniques that include electric arc discharge, flame synthesis, high pressure carbon monoxide, laser ablation, spray pyrolysis, and chemical vapor deposition techniques. Among these techniques chemical vapor deposition is known to be the most versatile process for growing CNT as it provides the ability to control the nanotube growth rates, growth time, nanotubes diameter and length [38][47]–[51] . It provides the capability of growing individual (free-standing) nanotubes as well as CNT on a support material. A standard CVD technique requires a carbon precursor (source for carbon) and metal nanoparticles (to catalyze the reactions) in reducing environment, at high temperature, and inert atmospheric conditions [39]. The metal catalyst can be pre-coated on the support surface *i.e.* in an immobilized form known as coated catalyst or the metal precursor can be injected into the furnace where it evaporates and is carried with the aid of gas flow onto the sample, known as a floating catalyst method [40].

This work focuses on growing CNT on porous structures using a floating catalyst thermal chemical vapor deposition technique. The technique is reproduced from a two-zone home-built system with a 30mm mullite tube to a large scale three-zone system with an 80 mm quartz tube. Although, CNT growth with CVD technique has been perfected by numerous researches ever-since it was established, it may vary significantly for a system (or a support). Replicating the technique from one CVD system to another as well as on different surface geometries needs careful re-evaluation. Therefore, in this study the synthesis of CNT using pre-developed CVD process was recalibrated and optimized suitable to various porous structures using a new deposition furnace with a three-zone automated system having a large quartz tube (Ø 80 mm, L 1400mm) for large scale synthesis.

3.2 Experimental

3.2.1 Materials

All the reagents used in this study were of analytical grade and used without further purification including Hexamethyl-di-siloxane (99.5%, HMDSO, $(\text{CH}_3)_6\text{Si}_2\text{O}$, Sigma-Aldrich chemicals), Ferrocene (99%, $\text{C}_{10}\text{H}_{10}\text{Fe}$, Alfa-Aesar Ltd), and Xylene ($\text{C}_6\text{H}_4\text{C}_2\text{H}_6$, PTI Process Chemicals). Other materials are de-ionized water (DI water) and laboratory grade gases that include argon and hydrogen. The microcellular carbon foam used in this study is L1a grade and was obtained from Koppers Inc. The reticulated vitreous carbon foam is 80 pores per inch (ppi) that was obtained from Ultramet Inc.

3.2.2 Support Details

Carbon foams structures were cut into the shape of circular discs of diameter (\O) ~ 70 mm or ~ 3 inches (to fit the CVD tube diameter). Depending on their open pore structure, the thickness was uniformly maintained at 2.5 ± 0.1 mm for cellular foams and at 5.0 ± 0.5 mm for RVC foams. The uniform thickness was obtained by cutting the foam blocks and subsequently sanding them using a sand paper. CNT were grown on these foams by coating with silica followed by thermal CVD process as described in Section 2.3.1.

3.2.3 Synthesis of Vertically Aligned CNT on 3D Porous Structures

Vertically aligned carbon nanotubes were fabricated on porous foam structures using a two-step process involving, plasma enhanced chemical vapor deposition of a nano-layer of silica on the porous structures followed by carbon nanotubes coating using thermal chemical vapor deposition technique. The process described here is to optimize the CVD process for growing CNT through various

advanced porous structures using a 3-zone CVD furnace. Carbon nanotubes were essentially grown on disc shaped micro-cellular carbon foam and reticulated vitreous carbon foam structures. The process described here is to obtain CNT growth through various interconnected open cell porous structures.

Silica was deposited on porous structures in the microwave plasma reactor (V15GL Plasma, PlasmaTech Inc.), using gas phase mixture of HMDSO and oxygen in cyclic steps at 300W microwave power. As a result of this process, thin layer of SiO₂ was deposited on the open surfaces of the foam. Both sides of the disc shaped foams were coated with silica for a specific length of time. Detailed characterization on the influence of silica functional groups (buffer layer) on the mechanism of catalyst (Fe) activity for CNT growth has been reported in earlier publications [52]. The influence of thickness of such functional layers obtained with coating silica for different times as shown in Table 3.1, on porous foams is studied for CNT morphology and permeation through porous structure.

Vertically aligned CNT were grown on the silica coated porous structures in the quartz tube of a three-zone CVD furnace system. The circular disc sample was kept in the growth zone of the quartz tube, at 90° angle i.e. perpendicular to the direction of gas flow. The mixture of ferrocene–xylene solution at 0.1g in 10 mL was used as a catalyst–carbon source, which was injected in the pre-heated zone. The reactions were allowed to take place in the growth zone for a specific length of time in an Ar/H₂ environment to facilitate the growth of CNT as shown in Table 3.1. The furnace was allowed to cool down to room temperature in a reduced flow of Ar.

3.2.4 Controlling CNT Fabrication Process Parameters

The influence of following key parameters on CNT growth through the porous structure was studied as shown in Table 3.1:

1. Furnace temperature - CNT growth zone
2. Furnace temperature - Precursor injection zone,
3. Gas composition and flow rates, [Ar, H₂]
4. Catalyst and source precursor (Fe/Xy) flow rates,
5. Silica coating time (for thickness) [front, back], and
6. CVD run time or CNT growth time

These parameters are inter-dependent and play a significant role for growth and permeation of CNT on porous structures. The parameters were studied and optimized based on the results of CNT growth patterns throughout the foam thickness as observed in SEM imaging. The results are thus qualitative and presented here representing the samples as reasonably as possible.

Table 3.1 Variations of key process parameters for optimizing CNT growth through porous structure using CVD techniques

S.No	CVD Parameters	Variations	Units
1.	CNT growth zone Temperature	700, 750	°C
2.	Precursor injection zone Temperature	380, 400	°C
3.	Ferrocene and Xylene flow rates (Fe/Xy: 0.1g/10mL)	9.25, 12.5, 25	mL/hr
4.	Gas flow ratios, [Ar:H ₂] 1=120 cc/min	20:2, 10:1, 10:1.5, 10:2,	cc/min
5.	Silica coating time, [front, back]	[10, 20], [20, 20], [30, 30]	minutes

3.3 Results and Discussion

Figure 3.1(a-c) shows the optical images of typical foam structures that were used as base porous substrates for growing CNT arrays using CVD technique. Figure 3.1(d-e) shows the SEM micrographs of pristine cellular carbon (Figure 3.1d) and pristine reticulated vitreous carbon foam (Figure 3.1e) structures.

3.3.1 Nanotubes Arrays on Porous Carbon Structures

CNT were grafted on porous carbon substrates using thermal CVD technique, where silica was initially coated using plasma CVD technique. Figure 3.2a shows the optical image of the CNT grown on the porous foams showing black film like coating layer after CNT growth. We found that dense and relatively uniform black nanotube film like layer was grown on full 3-inch diameter circular disc surfaces of foam inclusive in the pores as shown in Figure 3.2a. Typical low magnification microstructure of CNT grown on silica coated porous structures are shown for CNT-RVC foam (Figure 3.2b) and CNT-cellular foam (Figure 3.2c). The SEM micrographs as shown in Figure 3.2, reveals that our CVD process produced CNT films consisting of aligned multi-walled carbon nanotubes that grow vertical to the surface of the pores and the ligaments on the foam (Figure 3.2d-f). The CNT films were observed to be in the form of tall carpets representing highly dense CNT forests. The low magnification images show vertically well-aligned CNT on the porous substrate but the high magnification images (Figure 3.3) show some entanglement of the CNT arrays referred to as having certain degree of entanglement. In the CNT arrays, the CNT show increase in the degree of entanglement as moving towards the top, and a complete entanglement was observed near the termination end as shown in Figure 3.3.

In a floating catalyst thermal CVD method, the CNT are grown on a substrate from vapor-phase pyrolysis of catalyst and carbon source solution mixture, under Ar/H₂ environment. It is well known that while growing CNT using CVD technique, an oxide layer of silica on substrates such as carbon foam enhances the growth of the carbon nanotubes [15], [24]. For similar reasons, CNT films were also formed on the walls of the quartz (crystalline SiO₂) reactor in the growth zone of the CVD. In the growth conditions that lead to high yield, densely packed CNTs with tight spacing were formed resulting in vertical alignment of the individual CNT. It was also observed that higher density of CNT leads to more aligned CNT arrays. It is considered that when CNT begin to grow on the substrate at high areal density, the van der-Waals forces among the adjacent CNT will influence their vertical alignment while growing. This is due to the crowding effect as suggested and reported in literature [44], [53], [54].

Two different kinds of furnaces were used in this study that have different reactor tube lengths, CVD furnace with two-zone system and three-zone system. It was observed that the vertically aligned CNT with large carpet heights up to ~100 μm in 60 minutes were grown using three-zone furnace that has long reactor tube, whereas in the two-zone system with a short-reactor tube spaghetti-type CNT of up to few microns [15] were grown on the substrate. This is due to the long gas-residence time and prolonged path for the catalyst and source gases in the 3-zone furnace reactor tube that in fact shows a constructive effect on the CNT growth [55].

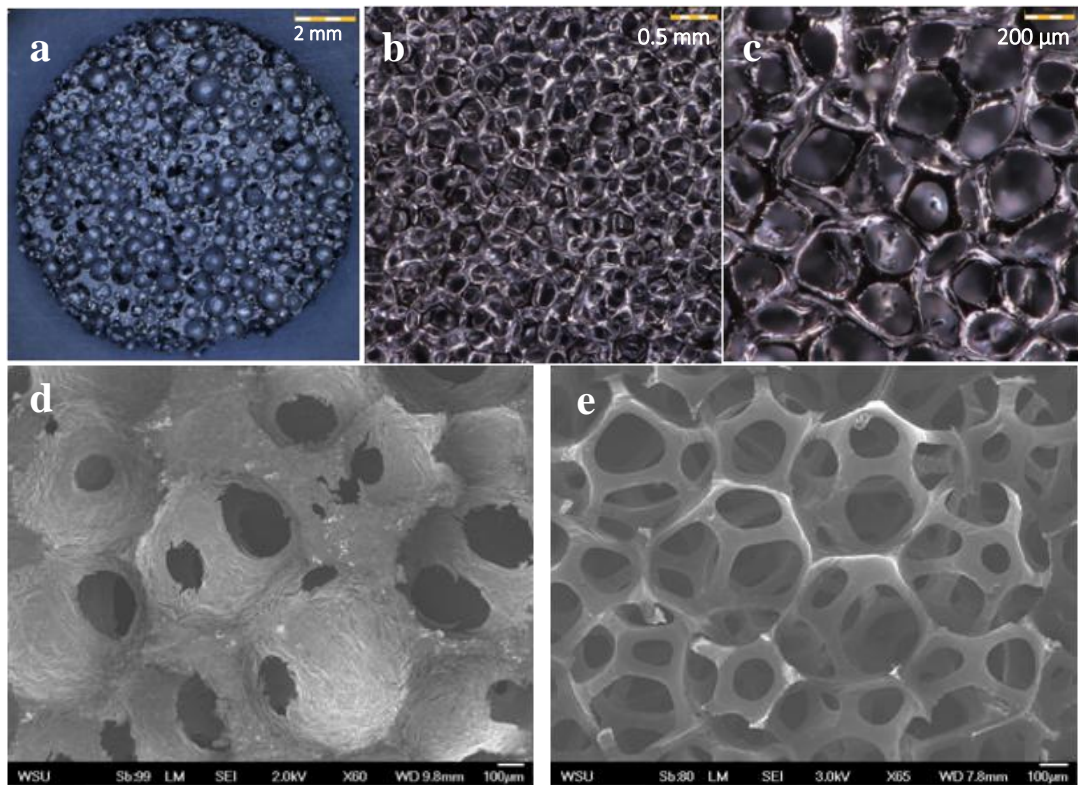


Figure 3.1 Optical images of (a) Cellular foam: Ce-Foam, (b-c) Reticulated Vitreous Foam: RVC-Foam. SEM micrographs of (d) Ce-Foam, and (e) RVC-Foam

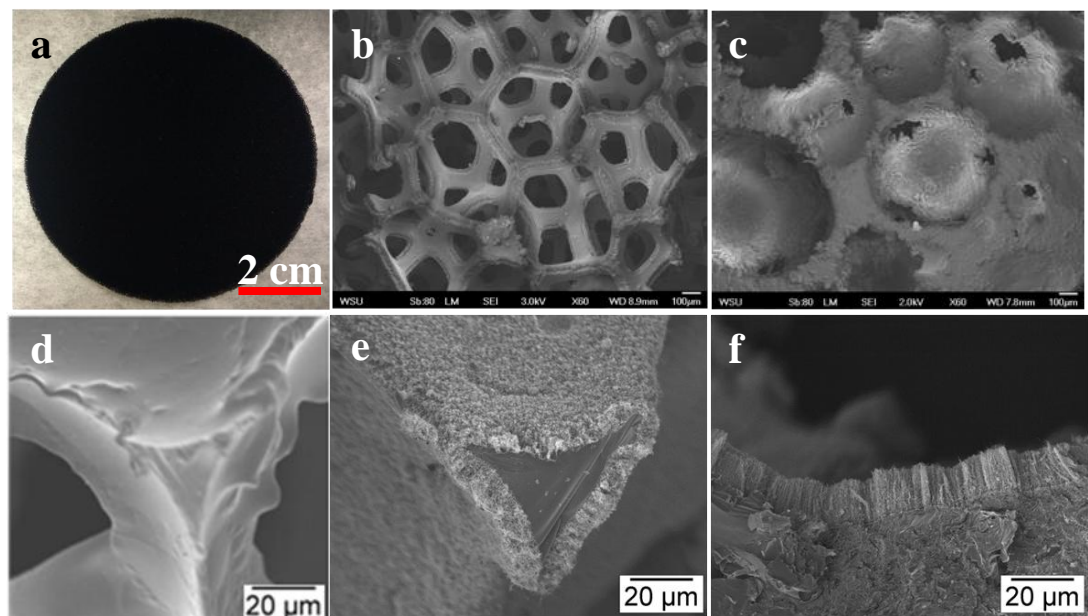


Figure 3.2 (a) Optical image of the CNT grown on RVC disc showing black film like layer of nanotubes. SEM micrographs showing the CNT grown on (b) RVC-foam, and (c) Ce-foam. (d) Bare RVC-foam, and CNT-foam interface of CNT grown (e) on RVC-foam, and (f) on Ce-foam.

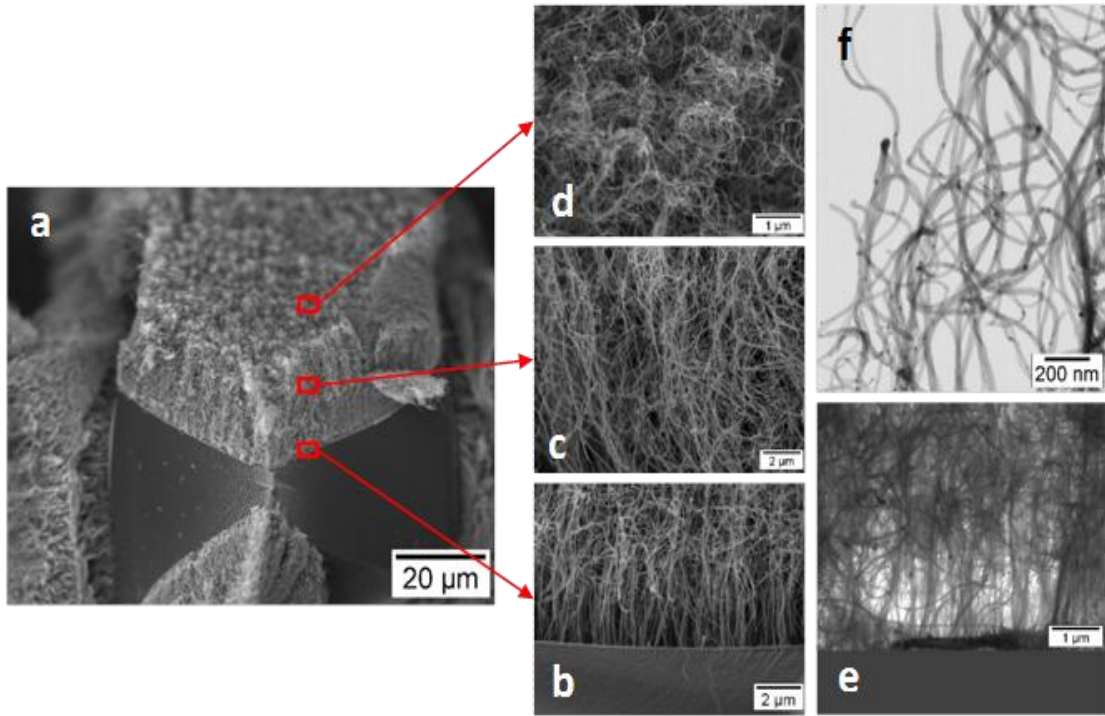


Figure 3.3 SEM micrographs showing (a) low magnification of the interface of vertically aligned CNT arrays on RVC Foam, (b-d) degree of alignment or entanglement through the height of the CNT arrays, (e-f) shows STEM images of the interface and CNT arrays.

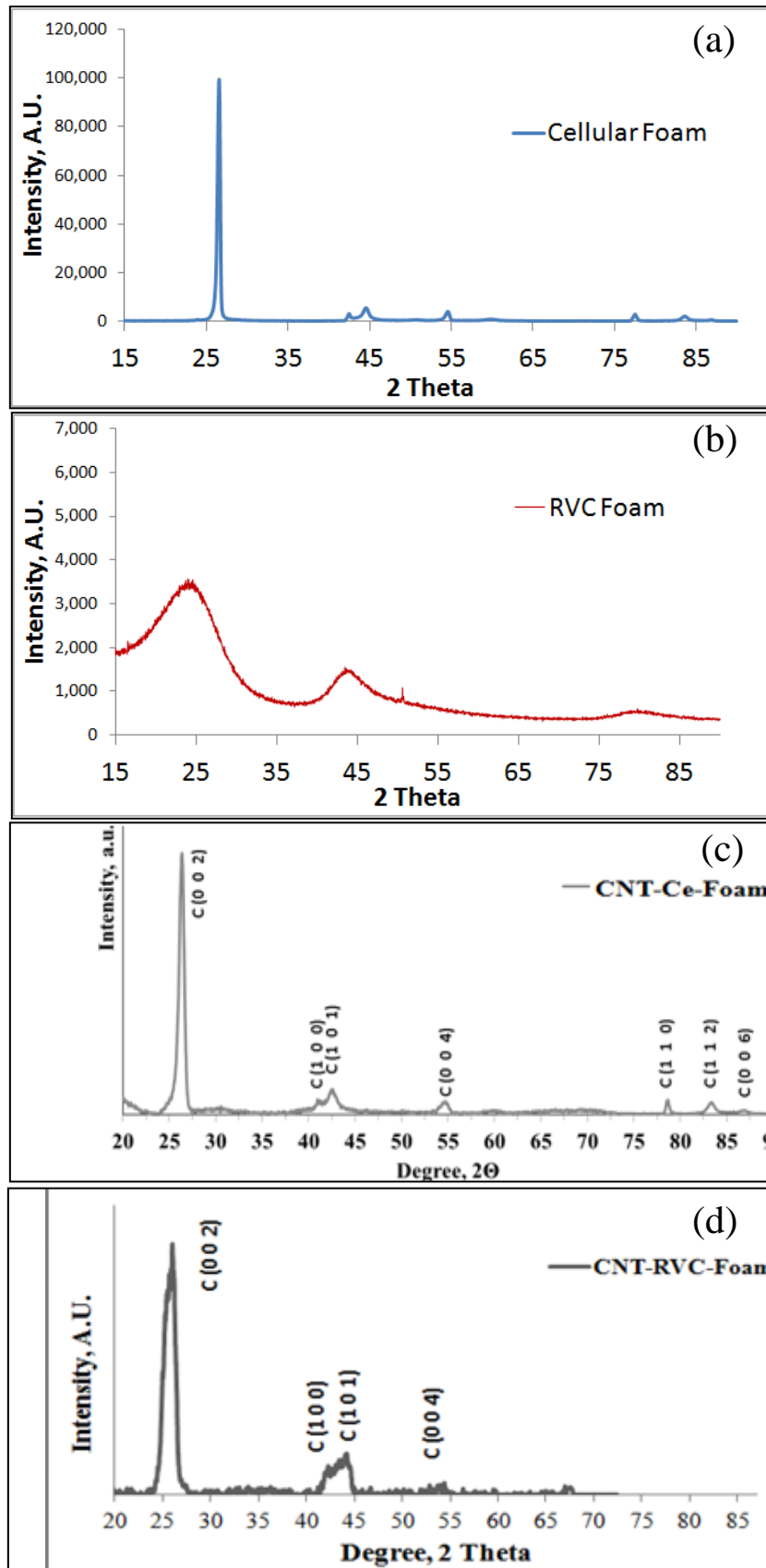


Figure 3.4 X-ray diffraction pattern for (a) Cellular (Ce-Foam), (b) RVC-Foam, (c) CNT grafted Ce-Foam, and (d) CNT grafted RVC-Foam, range $20^\circ < 2\theta < 90^\circ$

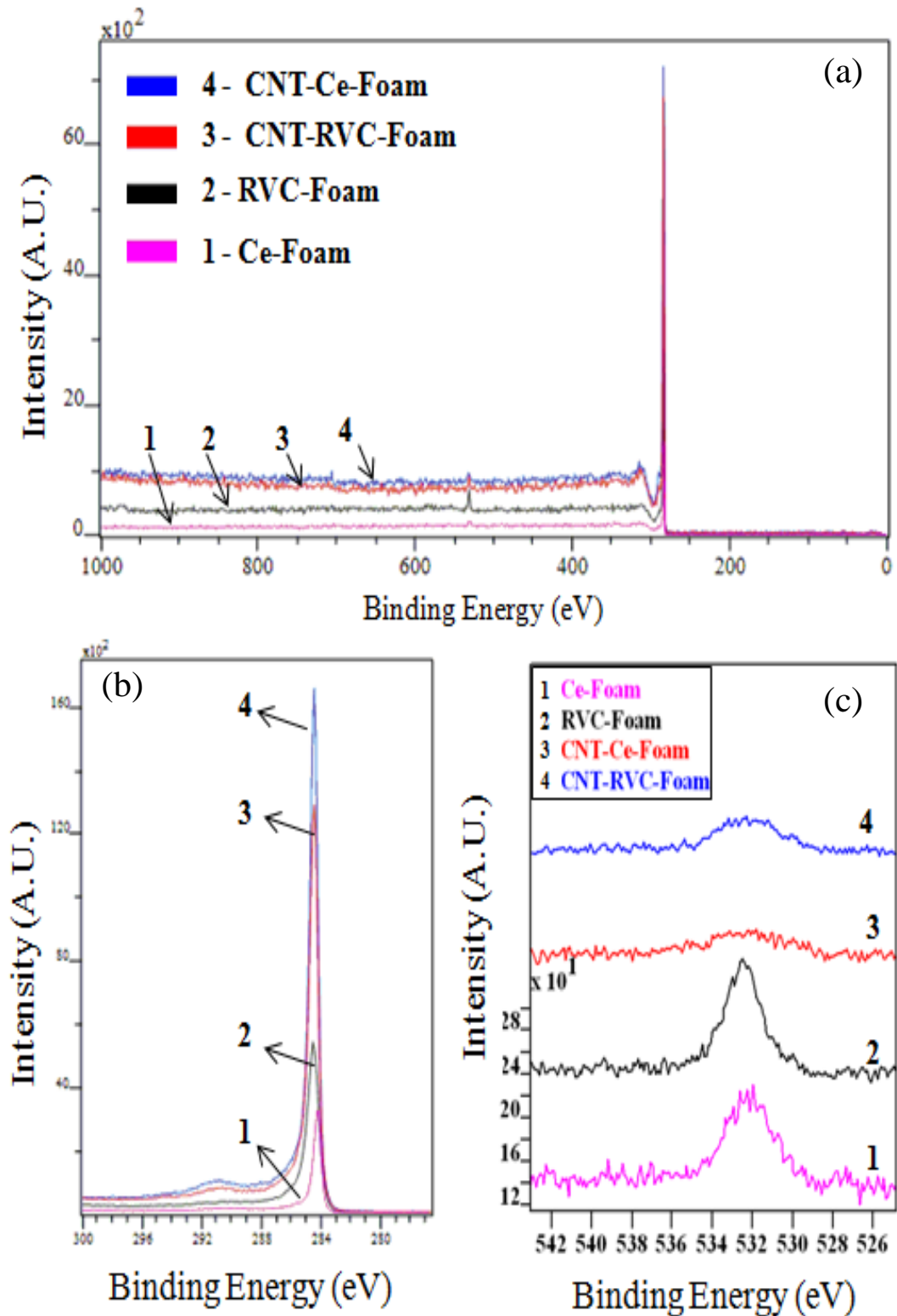


Figure 3.5 XPS spectra - (a) survey scan, and fine scans of (b) carbon, C $1s$, and (c) Oxygen, O $1s$ for pristine Ce-foam (pink), pristine RVC-foam (black), CNT grown on Ce-foam (red) and CNT on RVC-foam (blue)

3.3.2 Structural and Chemical Characterization

Figure 3.4 shows the XRD patterns obtained from pristine Ce-foam and pristine RVC-foams sample as well as CNT grown of these foam sample. The XRD pattern of Ce- foam exhibits peaks at 2θ values of 26° , 42° , 44° , 55° , 78° , 83° , and 87° , which corresponds to the graphitic structure of carbon. The strong peak at 26° corresponds to the (0 0 2) plane, a characteristic peak of hexagonal structure of graphite and CNT. The RVC-foam has no clear diffraction peaks (Figure 3.4b) that indicates the amorphous structure of the solid. Figure 3.4c and Figure 3.4d shows the XRD on CNT coated on Ce-foam and RVC-foam, respectively. The XRD pattern of CNT on these foams exhibit peaks at similar 2θ values as Ce-foam. These have the prominent peak at 26° corresponding to (0 0 2) plane of graphite, which is clear in the CNT structure.

Figure 3.5 shows the XPS data showing the survey scan (a), and fine scans of C 1s and O 1s peaks (Figure 3.5b-c) for pristine Ce-foam and RVC-foam, as well as CNT grown on Ce-foam and RVC-foam. The elements on the surface of the foams are carbon and oxygen. Carbon is the main constituent of these porous foam solids and oxygen signal comes from the surface contaminant adsorbed from air. This is normal for foam processed (commercial) in ambient atmosphere. Both pristine Ce-foam and pristine RVC-foam have similar chemical nature showing C 1s characteristic peak at 284.5 eV and O 1s peak at ~ 532 eV (Figure 3.5). The composition of surface from XPS analysis show decreased oxygen content after CNT growth, which is also expected because high purity nanotubes are covering the surface of foams.

3.4 Factors Influencing CNT Growth Quality

CNT growth using the vapor-phase pyrolysis CVD technique has been perfected on flat substrates but growing CNT on a porous substrate is significantly challenging. It must be noted that in a porous solid, CNT growth rates ($\mu\text{m}/\text{min}$) are higher at the outer surfaces, and lower in the deeper inner pores. In this study, we focus on permeation of CNT through the complex geometries like interconnected porous structures. Various parameters were investigated related to CVD system and growth process. These were evaluated based on the results of CNT growth patterns throughout the foam's cross-sectional thickness as observed with SEM imaging.

3.4.1 Run-to-Run Variation – System Factors

Consistent growth of nanotubes between the runs in a given reactor is critical. Any CVD system needs initial optimization for process parameters and layout for a given substrate (on which nanotubes are grown). The basic system factors that can vary from run-to run, include position of the sample in the furnace, placement of the syringe needle-end, and ambient conditions. These can limit the consistency of CNT growth using CVD method, which can significantly affect the quality (height, diameter, density, and impurities) of CNT.

Figure 3.6 shows the schematic of CVD system used in this study. The sample was placed in the center zone at 61 cm and the syringe needle was kept at 5 mm from the right end (Figure 3.6). It was observed that varying the sample position by ± 2 cm or the position of needle-end by ± 1 cm resulted in significant variation in the CNT growth and deposition of impurities. Samples when positioned close to upstream were observed to have more Fe-NPs as impurities and those farther in the tube were observed to have shorter CNT carpets. Similarly, positioning the needle-end further

into the furnace led to Fe-NPs as impurities on already grown CNT. Therefore, an optimum position for both sample and needle in the quartz tube was determined as shown in Figure 3.5. To obtain consistent results with precise control of CNT growth and quality, steps were followed meticulously to avoid run-to-run variations.

For maximum permeation of CNT through the porous structure, the gasses should pass through the foam rather than flow around it. The porous foams of circular disc shape were placed perpendicular to the flow fitting the round quartz tube. A graphite sheet was wrapped around the porous foam to maintain good sealing with the tube walls and to ensure the flow of gases through the porous structure.

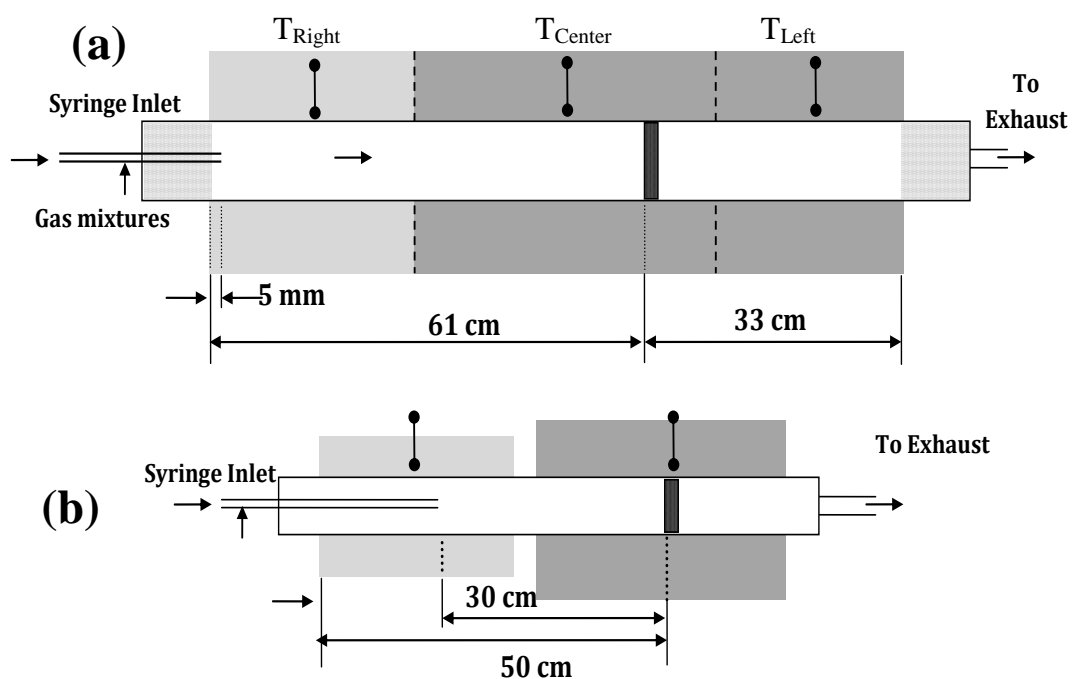


Figure 3.6 Schematic representation of CVD Furnace, (a) 3-zone system, and (b) 2-zone system

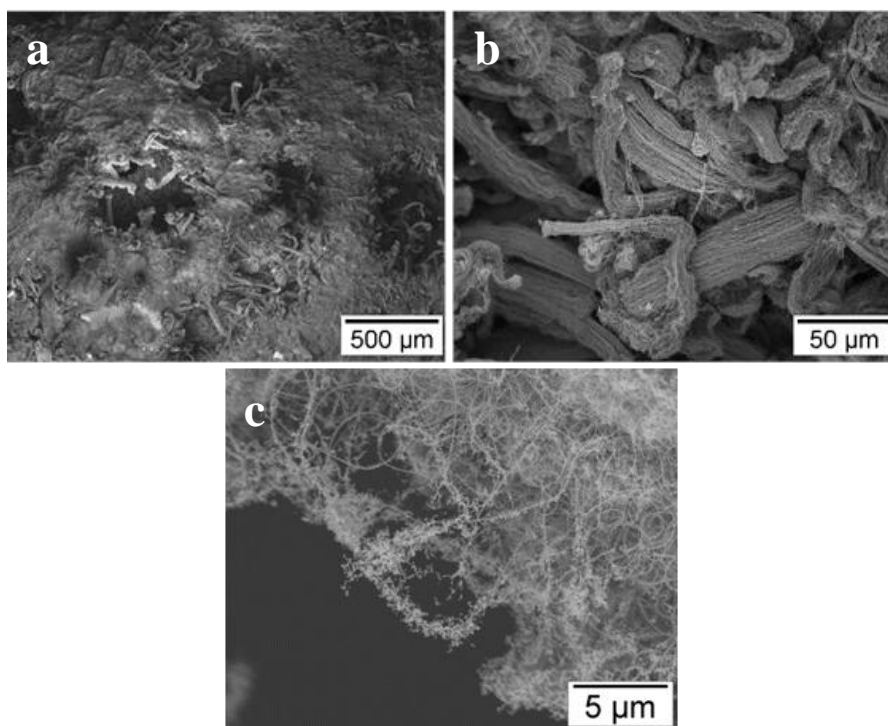


Figure 3.7 SEM micrographs showing (a-b) CNT-arrays blocking the pores of the foam, and (c) Fe-NPs as impurities on already grown CNT

3.4.2 Study of Key Process Parameters

In this study, once the system setup was optimized the influence of key parameters on CNT growth and CNT permeation in porous structure was investigated through systematic set of CVD experiments as shown in Table 3.1.

1. *CVD Run Time:*

CVD run time is the time for which the reactions to form CNT are carried out in the furnace. Therefore, increase in CVD run time is expected to produce high CNT growth (until the catalyst deactivation). However, it was found that for a porous structure a minimum injection time of 30 minutes is required to obtain significant growth of CNT towards the other side of porous structure. Consequently other parameters affecting the growth of CNT were studied for CVD run time of 30 minutes.

2. *Furnace Temperature:*

The temperature in the precursor injection zone and growth zone were studied as shown in Table 3.1. By increasing the temperatures in the injection or the growth zone, the yield of CNT increases as the reaction kinetics is governed by temperature. But at high injection temperature (400 °C) CNT were accompanied with more Fe as impurities as shown in Figure 3.7. High injection zone temperatures are known to deposit iron-nanoparticles on the already grown CNT [15]. It was observed that by increasing the furnace temperature, the yield of CNT increases mostly on the exteriors of the porous foams but permeation of CNT into the interiors was ineffective.

3. *Gas Flow Rates and Composition:*

The growth and permeation of CNT in the porous structure can be attained by changing the gas flow patterns in the tube. The CVD gas composition implies two

components that include evaporated mixture of catalyst-carbon source (ferrocene/xylene - Fe/Xy) gas and mixture of Ar/H₂ gas. With an increase in the Fe/Xy flow rate (as shown in Table 3.1) the CNT growth rate increases, which points out that rate is directly related to the feed stock of the CNT. However, the Fe content increase in the reactor flow affects the morphology of CNT as the CNT diameter grows bigger and also more Fe-NPs impurities gets deposited on already grown CNT.

We studied different combinations of Ar and H₂ flow rates as shown in Table 3.1. Changing the total Ar/H₂ gas flow rate directly affects the CNT growth rates. It was observed that when the total Ar/H₂ flow is reduced, the overall CNT growth (yield) is observed to decrease. However, thereon increasing the H₂ concentration in the gas flow from 0.1 vol% to 0.2 vol% (with respect to Ar) improves the CNT yield as well as the CNT permeation through porous structure. It is observed that with high H₂ concentration, the gas flow rates need to be slow enough for proper CNT growth and permeation. Increasing the H₂ concentrations also influences the morphology of CNT, as significantly lower diameters CNT with high purity were obtained. The presence of hydrogen usually prevents formation of amorphous carbon and the deactivation of the catalyst thereby enhancing the CNT growth [56].

4. Oxide Buffer Layer Thickness:

An oxide buffer layer is essential to grow CNT on a substrate like silicon or carbon, which acts as an effective barrier between the metal catalyst and the substrate. In the absence of such an oxide layer the catalyst will react with the substrate and form metal silicide or carbide, which leads to deactivation of catalyst that inhibits CNT growth [15]. In this study, a detailed analysis is carried out to understand the effect of thickness of silica buffer layer on porous structure (obtained by varying the

silica coating time) for the growth and permeation of CNT. Silica was coated on both sides of the circular foam discs as shown in Table 3.1.

CNT arrays were observed to grow on both exterior (upstream – front, nearest to inlet gas flow) and posterior (downstream - back, farther from inlet gas flow) sides of the porous foam which indicates that gas diffusion of carbon source and catalyst through the foam in the CVD furnace was not the limiting factor. The geometry of the substrate plays an important role in the permeation of CNT through the interior pores. Among the porous structures having porosities 80% (Ce-Foam) and 97% (RVC-Foam), it was observed that more open porous structure has higher CNT growth through the interior pores due to high mass transfer capability. This is also true for vapor deposition of silica on the porous structure in a microwave plasma reactor. However, maximum silica coating is obtained on the outer surfaces as the gas phase diffusion of silica into the porous structures appears to be the limiting factor in a plasma reactor. The cross-sectional EDS elemental analysis as shown in Figure 3.8 reveals that the exterior sides of porous foam gets maximum silica coating whereas the interior open pores show scarce silica content.

From the SEM analysis it is understood that the CNT growth is highest for the front part of the porous substrate *i.e.*, nearest to the inlet of gases into the furnace. The thick silica coating on the exteriors leads to this high growth rate of CNT on the exterior pores of foam structure, which hinders the permeation of CNT growth through the interior (center). In order to reduce the clogging of exterior pores by CNT and achieve uniform growth throughout the foam, the simplest approach was to decrease the silica thickness. A gradient of silica thickness on front to back was obtained by coating for 10 and 20 mins on front and back side of porous disc substrate, respectively. It produces desirable amount of uniform CNT coating on both

front and back sides as well as throughout the pores of the foam (Figure 3.9). This can be attributed to the reduced CNT growth rate on the front side of the foam that may allow the flow of mass inside the pores.

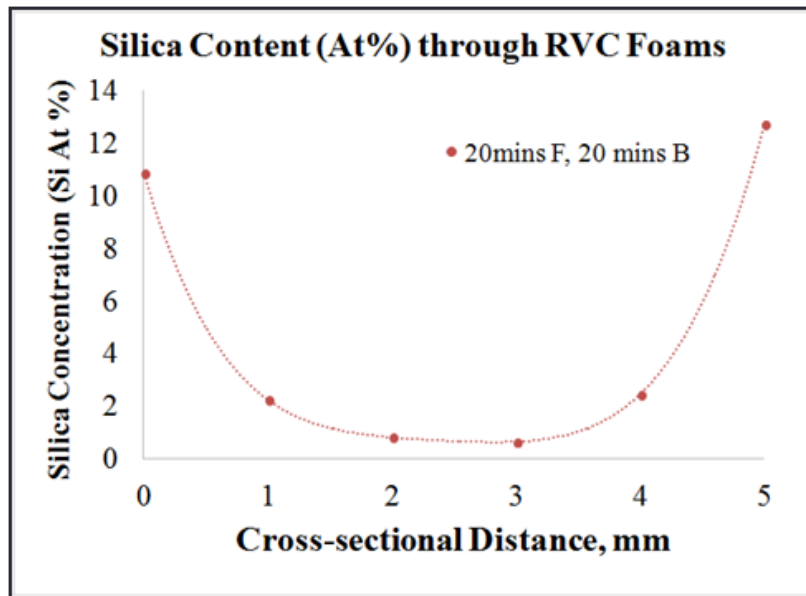


Figure 3.8 Cross-sectional analysis of silica coating thickness through porous foam using Energy Dispersive Spectroscopy (EDS) obtained for sample coated with silica on both sides of disc foam *i.e.* Front 20 and Back 20 minutes

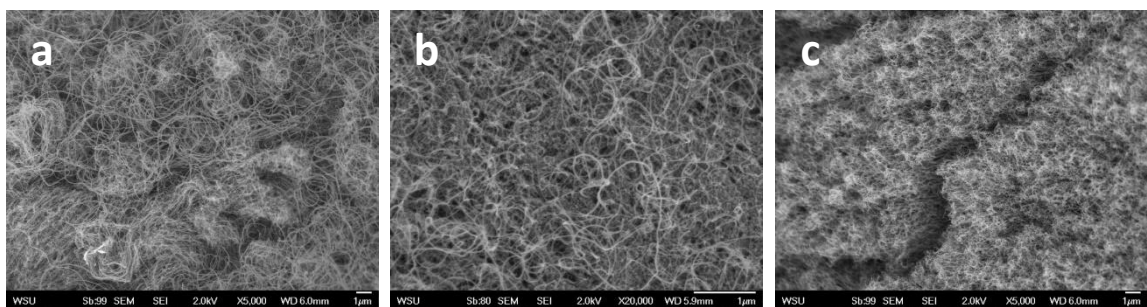


Figure 3.9 SEM micrographs showing CNT growth throughout the porous foam structures at (a) Front - exterior, (b) Center – interior, and (c) Back – posterior side of the foam

3.5 Conclusion

In this study, hierarchical carbon nanostructures have been successfully synthesized as demonstrated by multi-walled carbon nanotubes grafted through the micro-cellular carbon foams using thermal chemical vapor deposition technique. High purity, vertically aligned carbon nanotubes were grown on surfaces of open cell porous structures. In-depth investigations of process parameters that actually control the through-thickness CNT distribution on the walls of the interconnected pores were studied. Key parameters have been identified for controlling the growth of CNT through the porous structure. The buffer layer thickness and gas flow composition are identified as two important parameters for growth and permeation of CNT through the porous structure. It was seen that creating a thickness gradient of the silica buffer layer (thicker buffer layer towards the back end of the porous substrate) enhances CNT permeation deeper into the pores.

4 Chapter 4: Analysis of Specific Surface Area of CNT-Foam Structures

4.1 Introduction

Fabricating carbon nanotubes (CNT) on the porous structure can create additional increase of specific surface area (SSA) by several orders of magnitude without any decrease in strength or significant increase in weight. The hierarchical carbon nanostructures (CNT on porous structures) demonstrated here are potentially useful in many applications that depend upon surface area. Hence, tuning the available surface area without affecting the bulk volume of the support by varying the length of CNT can be advantageous. The versatility of the CVD technique offers additional control of the nanotube growth. The specific surface area can be increased by tuning the morphology of the CNT, such as diameter, length, and areal density using process parameters [47], [48], [57]. In this study, controlled length of CNT arrays were grown on the foam supports by varying key process parameters of the CVD technique in order to tune the SSA of the hybrid material.

Controlled length of CNT arrays were obtained on such porous structures by varying process parameters like CVD run time or silica coating time. In this study, the thickness of CNT layer or the length of CNT carpet was controlled by varying either the silica coating time ($t_{\text{silica}} = 10$ and 15 mins) or the CVD run time ($t_{\text{CVD}} = 10, 20, 30, 40,$ and 60 mins) and keeping the rest of the parameters constant. Detailed morphological analysis was carried out on each final structure in Field Emission Scanning Electron Microscopic (FE-SEM), to estimate CNT diameters, densities, and lengths of CNT arrays at different depths of porous foam. Owing to the high surface areas of CNT, these hierarchical structures offer very high SSA. The SSA of

microscopic samples is typically measured by the gas adsorption (typically N₂) using the Brunauer-Emmett-Teller (BET) isotherm method. In this study, we have developed some analytical models to estimate CNT surface areas using microstructural analysis method and weight-gain method, as well as verified these using BET analysis measurements (N₂ gas) and Langmuir adsorption studies using aqueous compound (discussed in Chapter 5) [58].

In this research, we report microscopic as well as macroscopic measurements and establish the theoretical models for SSA of CNT-foam hybrids based on the geometrical characteristics of CNT (diameter, length, number of walls, areal density) and the geometrical characteristics of porous structures (RVC in this case). By adjusting the synthesis parameters of CNT, one can vary the SSA of the hierarchical material and this model can provide useful information for determining its SSA. Additionally, knowledge of the available SSA would be desirable to understand the mechanism of various systems.

4.2 Experimental

4.2.1 Support Details

Circular disc shaped RVC foam supports of diameter (\emptyset) ~70 mm and thickness 5.0 ± 0.1 mm were used here to grow CNT. The uniform thickness was obtained by carefully cutting the foam blocks using a band saw machine and subsequently sanding using a fine grid sand paper. The foams were then coated with specified silica coating time and CVD run times to obtain different lengths of CNT.

Table 4.1 Showing the sample ID of various RVC-CNT hybrids used in this study

S.No	Silica coating (mins)		CNT coating (mins)	Sample ID
	Front	Back		
1	10	20	10	RVC-CNT 10
2	10	20	20	RVC-CNT 20
3	10	20	30	RVC-CNT 30
4	10	20	40	RVC-CNT 40
5	10	20	60	RVC-CNT 60
6	15	20	30	RVC-CNT 30 Si 35

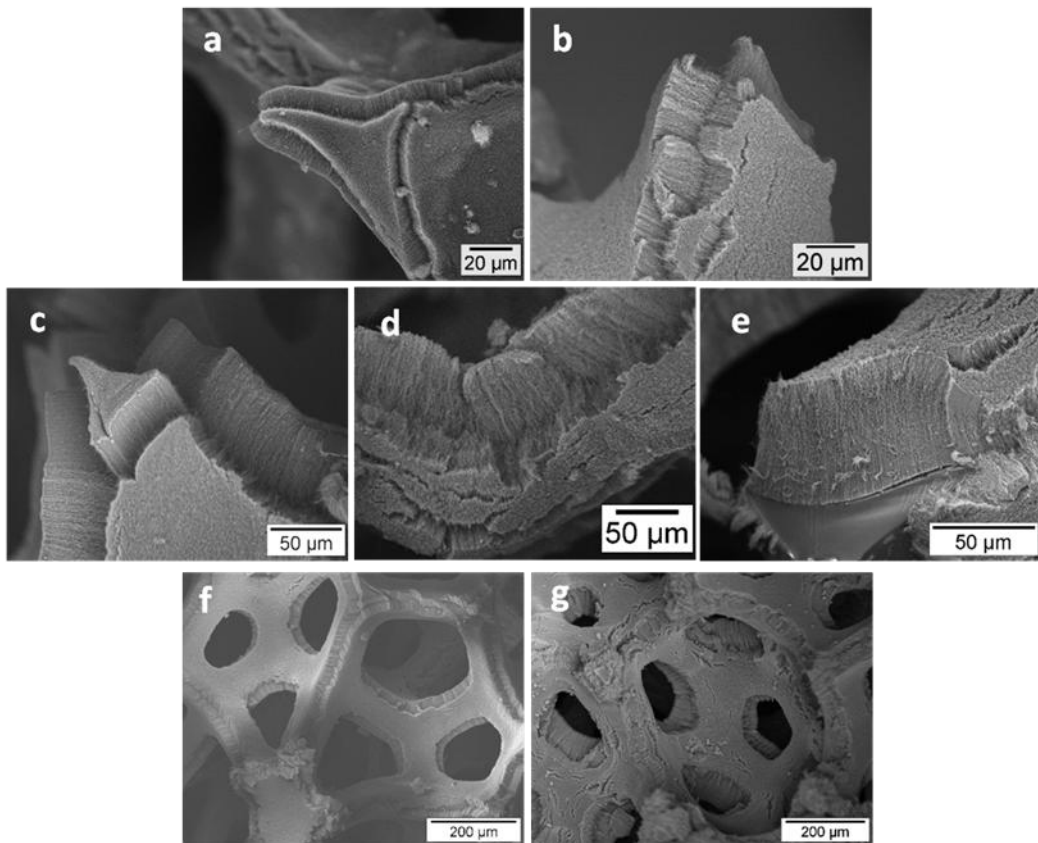


Figure 4.1 SEM images showing typical height of the CNT arrays obtained on the RVC foam sample (exterior side) with CVD run-times of (a) 10, (b) 20, (c,) 30, (d) 40, and (e) 60 minutes. Low magnification SEM images showing pores filled by CNT arrays for (f) 30 and (g) 60 minutes coating

4.2.2 Varying Amount of CNT Coating

The amount of CNT was varied by changing the following process parameters and keeping the rest of the variables constant as described in section 2.3.1.

1. Silica coating time on the front side; $t_{\text{silica}} = 10$ and 15 minutes - (constant CVD run time of 30 minutes)
2. CVD run time; $t_{\text{CVD}} = 10, 20, 30, 40,$ and 60 minutes - (constant silica coating time of 10 minutes)

The details along with the sample ID of the samples used here are tabulated in Table 4.1. To obtain the estimated surface area of CNT, a mathematical model was determined using the SEM images by measuring the length of the carpets at various spots throughout the foam and by determining the linear density of CNT.

4.2.3 Estimating the Surface Area of CNT Arrays

The surface area of CNT arrays on porous RVC samples can be estimated using different methods such as (1) Microstructural SEM analysis of CNT, (2) Weight gain method, and (3) Surface adsorption method. Surface area analysis was carried out for CNT arrays grown on RVC foam by varying CVD run time (10 to 60 mins).

The microstructural analysis method uses scanning or scanning transmission electron microscopy images (SEM/STEM) to estimate surface areas of CNT by analyzing lengths, diameters and area densities of the CNT arrays. This method is less quantitative but can provide reasonable estimates for the surface areas. The second method is weight gain method, where the surface area can be determined using area density obtained from weight gain due to CNT growth divided by weight of individual nanotube of length L . The third method is surface adsorption technique which is a semi-quantitative method. In this method an adsorbate is used which can be

a gas molecule or a compound in a liquid. This has been studied using (1) BET analysis measurements using N₂ gas adsorbate and (b) Langmuir measurements using an aqueous pollutant as adsorbate on the CNT surface where the available area can be related to monolayer adsorption of methylene blue compound and the Langmuir studies are discussed in Chapter 5 [58].

4.2.4 BET Characterization Method

SSA was measured using Brunauer-Emmett-Teller (BET) method with a Micromeritics TriStar 3000 (V6.05) for N₂ adsorption-desorption isothermal analysis at 77.3 K with a 5 s equilibration interval. The full isotherm was recorded from relative pressures of 0.05 – 0.99. Measurements were taken with duplicate samples and the average values are reported here.

4.3 Results and Discussion

4.3.1 Controlling CNT Carpet Length/Height

As discussed earlier, the height of CNT arrays grown on the porous foam support trend linearly with variations in silica thickness and CVD run time, and can be directly controlled by modifying these process parameters. The silica coating time, t_{silica} of 10 and 15 mins was studied here. Within these ranges longer silica coating time creates thicker silica buffer layer, which leads to longer CNT lengths. The CVD run time was investigated for t_{CVD} of 10, 20, 30, 40, and 60 minutes. It was observed that longer CVD time directly results in longer CNT carpet lengths. Figure 4.1 shows the height of the CNT arrays on foam surface obtained for different CVD run times. The increase in the height of CNT arrays grown on the porous structures allows packing more CNT that offers tuning the surface area within the same volume.

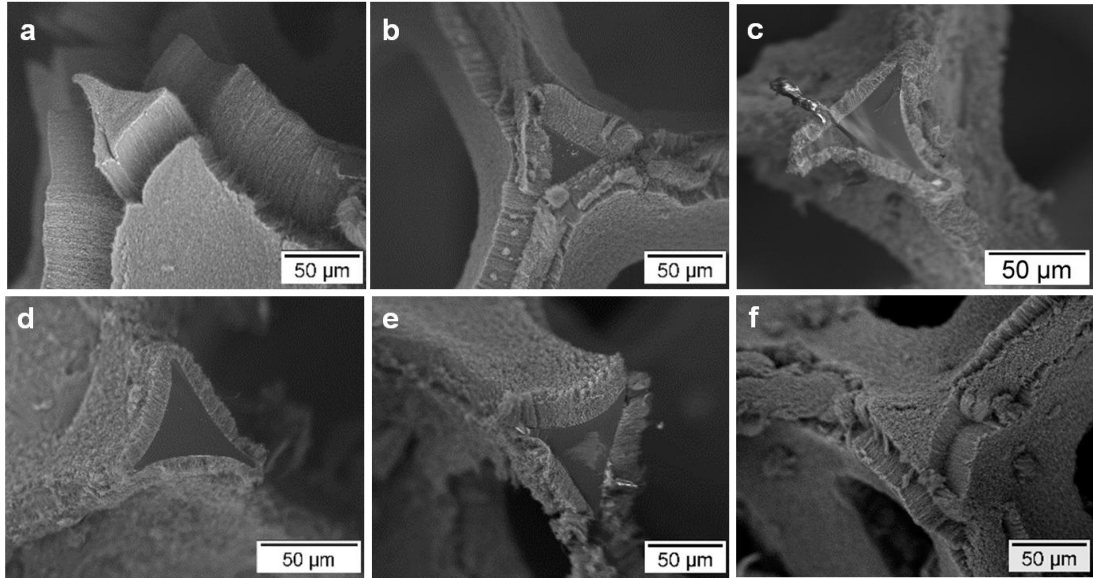


Figure 4.2 Cross-sectional SEM micrographs of RVC-CNT 30 at cross-section thickness (a) 0 mm - front, (b) 1 mm, (c) 2 mm, (d) 3 mm, (e) 4 mm, and (f) 5 mm - back

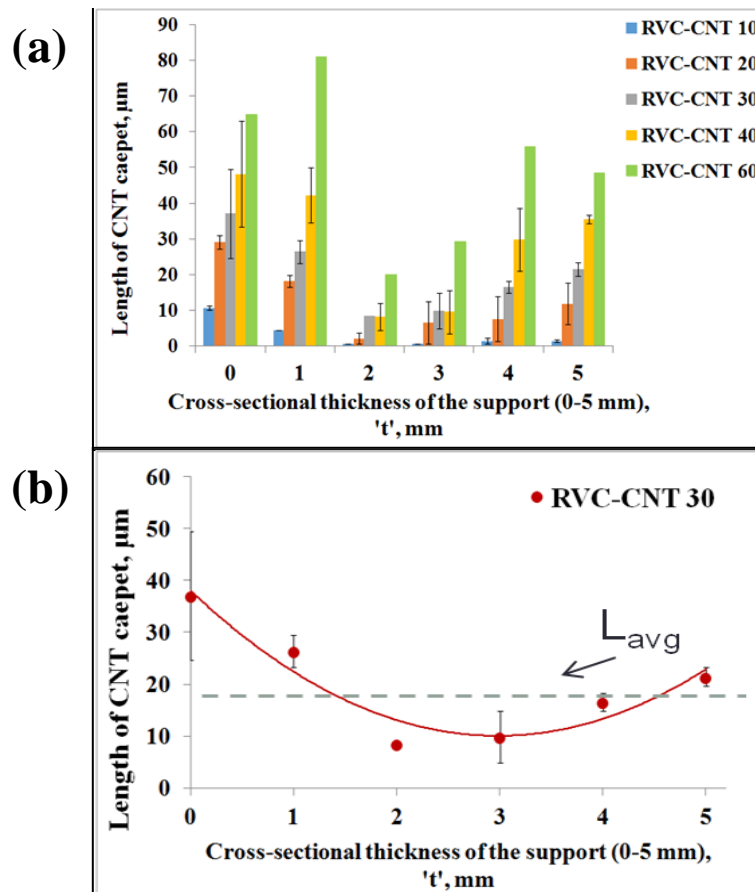


Figure 4.3 Plot obtained for the (a) length of CNT carpet with respect to the cross-sectional thickness (starting from the front side, $x = 0$ mm), and (b) a typical polynomial fit plot

Table 4.2 Estimated values of average length of CNT arrays and average growth rate of CNT through foam for various RVC-CNT hybrids

Sample ID	CVD Run time, minutes	Avg Length of CNT arrays, L_{avg} (μm)	Avg CNT growth rate through foam, $\mu\text{m}/\text{min}$
RVC-CNT 10	10	3	0.2
RVC-CNT 20	20	10	0.5
RVC-CNT 30	30	17	0.6
RVC-CNT 40	40	25	0.6
RVC-CNT 60	60	46	0.8

Table 4.3 Estimated values of CNT morphology obtained using SEM analysis. Specific surface area of reticulated foams – RVC of 80 ppi obtained from literature

Estimated CNT Morphology Values and SSA of RVC 80 ppi		
Avg. Outer Diameter, D_o	18	nm
Avg. Inner Diameter, D_i	8	nm
Avg. Number of walls, n	15	#
Density of MWCNT, ρ_{MW}	1.86	g/cm^3
Area Density of CNT on RVC, N_A	$1.5 * 10^{10}$	$\#/\text{cm}^2$
SSA of RVC foam, A_0 [23]	45	cm^2/cm^3
Density of RVC foam, ρ_{RVC}	0.045	g/cm^3
SSA of RVC foam, A_0	0.1	m^2/g

4.3.2 Estimating the Surface Area of CNT Arrays

The surface area of CNT arrays on porous RVC samples can be estimated using different methods such as (1) Microstructural SEM analysis of CNT, (2) Weight gain method, and (3) Surface adsorption method. Surface area analysis was carried out for CNT arrays grown on RVC foam by varying CVD run time (10 to 60 mins).

1. *Microstructural SEM Analysis:*

It must be noted that in a porous solid, CNT growth rates are higher at the outer surfaces, and lower in the deeper inner pores. In order to estimate the average length (height) of CNT arrays, detailed cross sectional image analysis was carried out for each of the final structure. This was done by slicing the sample into thin regions and performing detailed microstructural analysis of each slice using SEM. Figure 4.2 shows SEM micrographs indicating CNT carpet length at different spots through the thickness of porous RVC structure, *i.e.* cross-section from 0 to 5 mm. The length of CNT arrays at different depths (cross-section - CS) in 5 mm thick porous RVC foam are plotted against the CS depth of porous foam (where 0 mm is the exterior side of foam near to the inlet of gas flow - front), as shown in the graph of Figure 4.3. CNT carpet lengths are averaged over multiple samples and the error bars indicate the standard deviation. The CNT length profiles were observed to follow certain asymmetrical growth patterns through the foam: very high CNT growth on the front side, decrease in CNT growth towards the center followed by increase in the growth towards the back. From the graph in Figure 4.3a, it can be deduced that the CNT growth rate on front side is ~ 1 to $1.5 \mu\text{m}/\text{min}$, at center is ~ 0 to $0.5 \mu\text{m}/\text{min}$, and on back side is ~ 0.2 to $1 \mu\text{m}/\text{min}$. The average length of CNT arrays on RVC foams is observed to increase with CVD run time having an average CNT growth rate of $\sim 0.7 \mu\text{m}/\text{min}$. Polynomial trend lines, $L_c(x)$ were fit for each of the sample as shown in

Figure 4.3b. The average length of the CNT arrays was obtained by integrating $L_c(x)$ through the sample thickness ' t ', using Equation 4.1 and the L_{avg} values are tabulated in Table 4.2.

$$L_{avg} = \frac{1}{t} \int_0^t L_c(x) dx \quad \text{---- (4.1)}$$

The area densities of the CNT (number of CNT per unit area) can be estimated by counting the CNT in the CNT arrays using SEM images at the CNT-foam interface as shown in Figure 4.4(a). The depth of focus of SEM microscopy was taken into consideration and the average number of CNT per unit area was counted. The estimated area density of CNT on RVC samples with our setup was observed to be, $N_A = 150 \mu\text{m}^{-2}$ or $1.5 \times 10^{10} \text{cm}^{-2}$.

Figure 4.4(b-d) shows the typical SEM/STEM images and Figure 4.4(e-f) shows the distribution graphs for the outer and inner diameter of MWCNT. The estimated mean outer diameter (D_o) and mean inner diameter (D_i) of CNT were 18 nm and 8 nm, respectively and the CNT morphology estimates are tabulated in Table 4.3.

It is worth mentioning some of the assumptions that were made in this study: (1) CNT are assumed to have complete alignment with no degree of entanglement *i.e.* length of a CNT is equal to the average length of CNT carpet, $L_{CNT} = L_{avg}$; (2) it is also assumed that a CNT at the base grows till the tip of the carpet, (3) the area density of CNT arrays is the average and it is assumed to be the same throughout the foam structure.

Assuming that the CNT have closed ends, where $D \ll L_{CNT}$, the available surface area of an individual CNT is given by Equation 4.2. The CNT morphology data can be combined with specific surface area of support (A_o) to estimate the

available CNT surface area within each volume of the hierarchical structure given by total specific surface area (SSA) in the Equation 4.3.

$$SA_{CNT} = \pi D * L_{CNT} \quad \text{---- (4.2)}$$

$$SSA_{RVC-CNT} = \pi D * L_{CNT} * N_A * A_o \quad \text{---- (4.3)}$$

$SSA_{RVC-CNT}$ is the total available surface area of CNT per unit volume (m^2/m^3) or per gram (m^2/g) of the porous foam support. Where, $L_C(x)$ is the polynomial fit obtained from CNT carpet length profile; t is the cross-sectional thickness of the sample, $t = 5000 \mu m$ (5 mm); A_o is the specific surface area of the base support, $A_o=0.1 m^2/g$; D_o is the average diameter of the CNT, $D_o = 18 \text{ nm}$, and N_A is the areal density of CNT, (estimated $N_A = 1.5 \times 10^{10} \text{ cm}^{-2}$). The estimated SSA obtained using microstructural analysis for all the samples is tabulated in Table 4.4.

2. Weight Gain Method:

The weight gain for each of the RVC-CNT hybrids was monitored by weighing the foams before and after CNT deposition. For RVC-CNT hybrids samples, an increase in weight of up to 25% was seen for a 10 to 60 mins CNT growth as tabulated in Table 4.4. The mass of RVC foam when heated in Ar/H₂ CVD environment without carbon source was observed to decrease by 2 to 4% of initial weight of the RVC foam as shown in Table 4.4. Therefore, the absolute weight gain obtained by CNT for a 60 minutes CVD run time is up to 28.7% (compared to initial weight of foam).

The weight of individual CNT is obtained from the mass density equation of MWCNT that includes the outer diameter and inner diameter or number of nanotube walls. The outer and inner diameters were obtained using SEM/STEM images (Figure 4.4). In MWCNT, the inter-wall distance, d_i is approximately 0.34 nm as reported by

et al [59]. Therefore, the average number of nanotube walls (n) in MWCNT can be given by Equation 4.4 [60]. The mass density of MWCNT (ρ_{MW}) is obtained using Equation 4.5 and graphs as reported by Ch. Laurent et.al. [60].

$$n = \frac{D_o - D_i}{2 * d_i} + 1 \quad \text{---- (4.4)}$$

$$\rho_{MW} = \frac{4000}{1315} \left[\frac{n}{D_o} - \frac{d_i * n(n-1)}{D_o^2} \right] \quad \text{---- (4.5)}$$

Where, D_i and D_o are inner and outer diameters of MWCNT, respectively, ' d_i ' is inter-wall spacing, n is number of walls in MWCNT, and ρ_{MW} is the mass density of MWCNT. Some of these values are tabulated in Table 4.3.

The SSA (m^2/g) of an individual CNT is the surface area to mass ratio of the CNT that is determined by Equation 4.6. The total SSA of RVC-CNT ($SSA_{RVC-CNT}$) can be determined using Equation 4.7, *i.e.*, given by the SSA of individual CNT times the fraction of weight of CNT (M_{CNT}) and total weight of the RVC-CNT foam ($M_{RVC-CNT}$). The data obtained from this analysis for all the CNT samples are tabulated in Table 4.5.

$$SSA_{CNT} = \frac{SA_{CNT}}{m_{CNT}} = \frac{SA_{CNT}}{V_{CNT} * \rho_{MW}} = \frac{4}{D_o * \rho_{MW}} \quad \text{---- (4.6)}$$

$$SSA_{RVC-CNT} = SSA_{CNT} * \frac{M_{CNT}}{M_{RVC-CNT}} = \frac{4}{D_o * \rho_{MW}} * \frac{M_{CNT}}{M_{RVC-CNT}} \quad \text{---- (4.7)}$$

Where, $M_{RVC-CNT}$ is total mass of RVC-CNT sample after CNT growth, M_{CNT} mass of CNT (mass difference after CNT growth) grown on RVC sample, and SA_{CNT} , V_{CNT} , and m_{CNT} is the surface area, volume, and mass of an individual CNT respectively.

Attachment of CNT enhances the SSA on the RVC sample by two to three orders of magnitude. The multiplication factor increase in SSA, f, as tabulated in

Table 4.5 with varying amount of CNT on RVC foams indicates the surface area tuning ability of the hybrid structures.

Table 4.4 The mass of RVC-CNT hybrids before and after CNT growth, percent weight loss of foams due to heat in CVD environment, absolute weight gain (% increase) in weight after CNT growth, and areal density of CNT obtained from various CVD run times, $t_{\text{CVD}} = 10, 20, 30, 40,$ and 60.

Sample ID	Average Mass of sample before CNT growth, M_{RVC} (g)	Average total mass of RVC-CNT M_{T} (g)	weight gain after CNT, (% increase) A	Wt loss of Foam alone due to heat (% reduced) B	Absolute weight gain after CNT, (% increase) A+B	Avg # of CNT per area, N_{CNT} , $\#/\text{cm}^2 \times 10^{10}$
RVC-CNT 10	0.8382	0.834	-0.5	2.0	1.5	0.9
RVC-CNT 20	0.8951	0.9139	2.1	2.1	4.2	0.9
RVC-CNT 30	0.8486	0.9013	6.2	2.7	8.9	1.0
RVC-CNT 40	0.9032	1.0052	11.3	3.0	14.3	1.1
RVC-CNT 60	0.8909	1.1143	25.1	3.6	28.7	1.2

Table 4.5 Total estimated available surface area created by grafting varying amount of CNT on RVC-foam supports

Sample ID	Avg Length of CNT Carpet	Method 1 Microstructural SEM	Factor Increase in SSA with CNT	Method 2 Weight Gain	Factor Increase in SSA with CNT
	Lavg, μm	SSA, m^2/g	f_{SEM}	SSA, m^2/g	$f_{\text{weight-gain}}$
RVC Foam	NA	0.1	1	0.1	1
RVC CNT 10	2	2	20	2	17
RVC CNT 20	10	9	88	5	49
RVC CNT 30	17	15	147	10	100
RVC CNT 40	25	21	210	15	153
RVC CNT 60	46	39	394	27	274
Isolated CNT [23]	--			119	1190*

*Compared with RVC foam

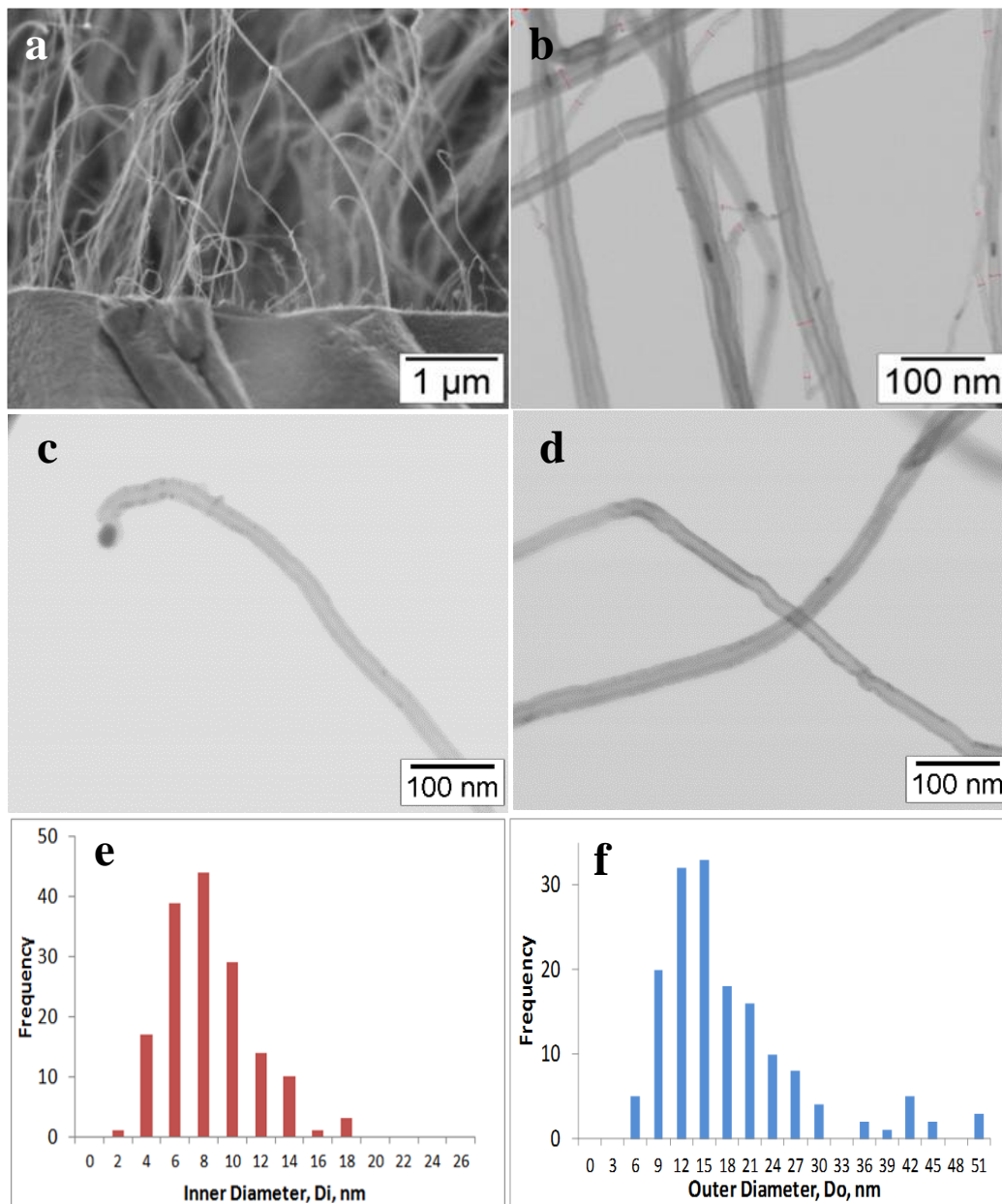


Figure 4.4 SEM/STEM micrographs of (a) a typical RVC-CNT hybrid interface for linear density analysis, (b -d) typical STEM images used for inner and outer diameter measurements, and size distribution graph of (e) inner diameter of CNT, and (f) outer diameter of CNT.

4.3.3 BET Measurements

Nitrogen BET was used to measure the SSA of RVC foam, RVC-CNT foam hierarchical structures, and isolated CNT. The measured BET SSA is averaged over duplicate samples and the mean values along with the standard error are tabulated in Table 4.6. The SSA of pristine RVC foam of 80 ppi is reported in earlier publications and is estimated to be $0.1 \text{ m}^2/\text{g}$ [23]. The average SSA of RVC foams measured using BET is $0.25 \pm 0.21 \text{ m}^2/\text{g}$, that shows very large standard error as the SSA of RVC foams ($\sim 0.1 \text{ m}^2/\text{g}$) is at the lower end of the detection limit of BET adsorption method with N_2 gas.

The BET areas of various RVC-CNT hybrids, RVC foams, and isolated CNT were measured and the mean values are shown in Table 4.6. Figure 4.5 and Figure 4.6 shows the full isotherm and the linear analysis of two samples: RVC-CNT 60 and Isolated CNT. The full isotherm for the samples shows steady adsorption and desorption with pressure variations. The analysis plots show high correlation coefficients, and the slope and intercept were used to determine the BET surface areas.

From Table 4.6, the SSA of RVC-CNT samples increase with increasing CVD run time, as the increase in CVD run time increases the height of CNT arrays and therefore this increases the SSA. The SSA is observed to increase proportionally from $2 \text{ m}^2/\text{g}$ to $24 \text{ m}^2/\text{g}$ for 10 minutes to 60 of minutes CNT growth on RVC foam. By grafting CNT on RVC foams the SSA increases by 2- 3 orders of magnitude within the same volume of RVC foam. The measured BET SSA of isolated CNT is $75 \text{ m}^2/\text{g}$, which is approximately 3 times higher than the SSA of RVC-CNT 60. It must be pointed out that the measured SSA value is lesser than the theoretical SSA values that

are between 110 – 130 m²/g for isolated CNT having 15 - 20 nm diameters and 15 walls nanotubes [61]. The isolated CNT typically tends to agglomerate by forming bundles and may also contain catalyst nanoparticles that adds mass to material and therefore reflects low SSA. Therefore, we may be underestimating the SSA value of isolated CNT.

The SSA values of the hybrid porous structures are tabulated in Table 4.6. From this table it is observed that the SSA values of such hybrid structures can further be increased by growing more CNT within the same volume, which can be achieved by adjusting the CVD parameters such as increasing the CVD run time (as long as it continues to grow CNT). The RVC foams are highly porous with 97% porosity and pore sizes of ~300 μm and the theoretical SSA of RVC-CNT hybrid when the pore volume is filled with the CNT carpets of same morphology (CNT diameter, length, and density) is estimated to be 182 m²/g. But filling the space with 100 % CNT is challenging through direct growth of CNT on RVC using CVD techniques due to mass transfer limitations into the porous structures. However, if the average length of CNT carpet grown on RVC foams is 150 μm, the SSA of RVC-CNT is estimated to be 127 m²/g (using Equation 4.3). This is within the range of the theoretical SSA of isolated CNT of above mentioned morphology, as the theoretical SSA values of isolated CNT having 15 - 20 nm diameters are between 110 – 130 m²/g given using mathematical model by Piegney *et.al.* [61]. The possibility of attaching CNT on a porous substrate distinguishably increases the surface area as well as it allows full utilization of the CNT surface as it avoids CNT agglomeration and therefore we can achieve higher SSA value.

Table 4.6 BET surface areas and Langmuir surface areas measured using N₂ adsorption BET technique

S. No	Samples	BET area SSA, m²/g	Langmuir area SSA, m²/g
1	RVC Foam	0.28 ± 0.2	0.44 ± 0.4
2	RVC CNT 10	2.2	3.6
3	RVC CNT 20	3.9 ± 1	6.6 ± 1.8
4	RVC CNT 30	8.6 ± 2.1	14.6 ± 3.9
5	RVC CNT 40	12.6 ± 0.5	21 ± 0.8
6	RVC CNT 60	24.7	42.2
7	Isolated CNT	75.1	127.7

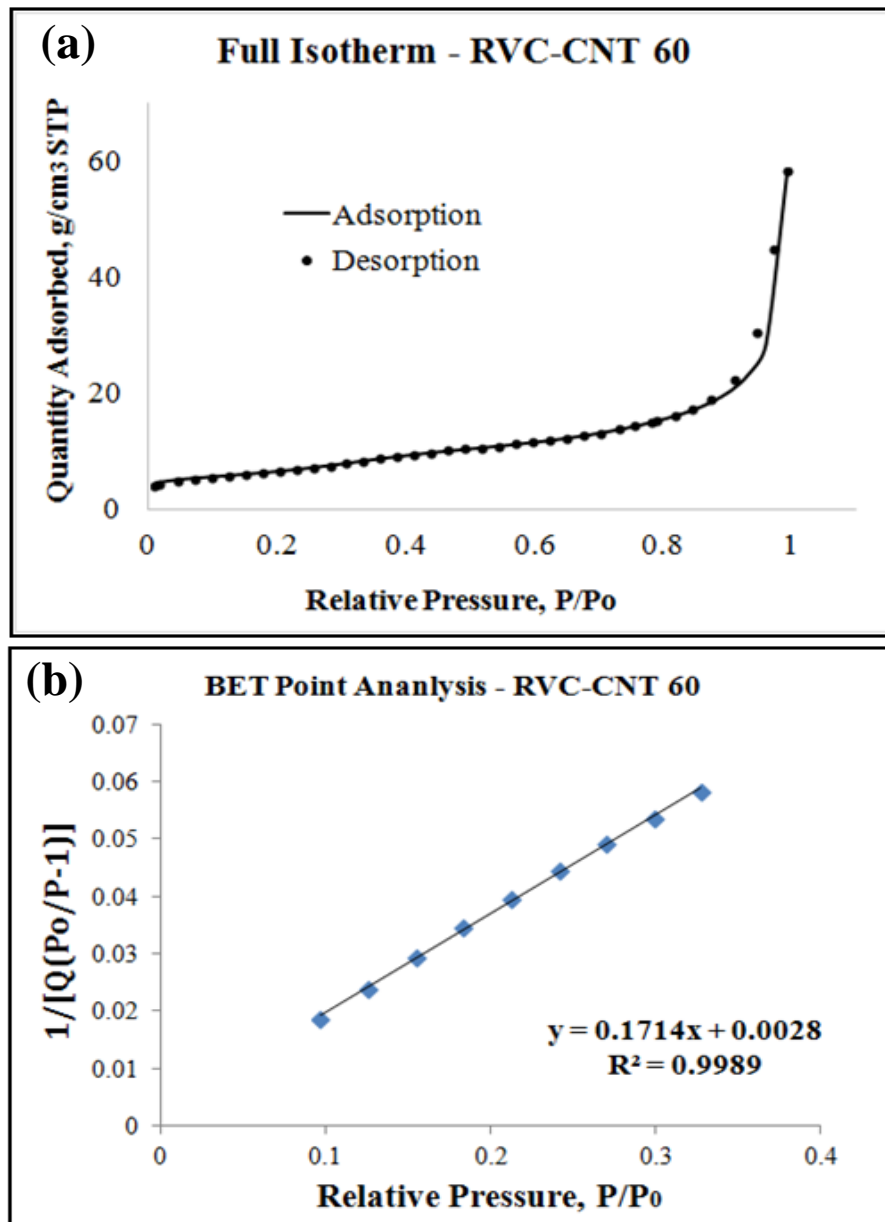


Figure 4.5 (a) Full BET isotherm and (b) linear analysis plot for RVC-CNT 60

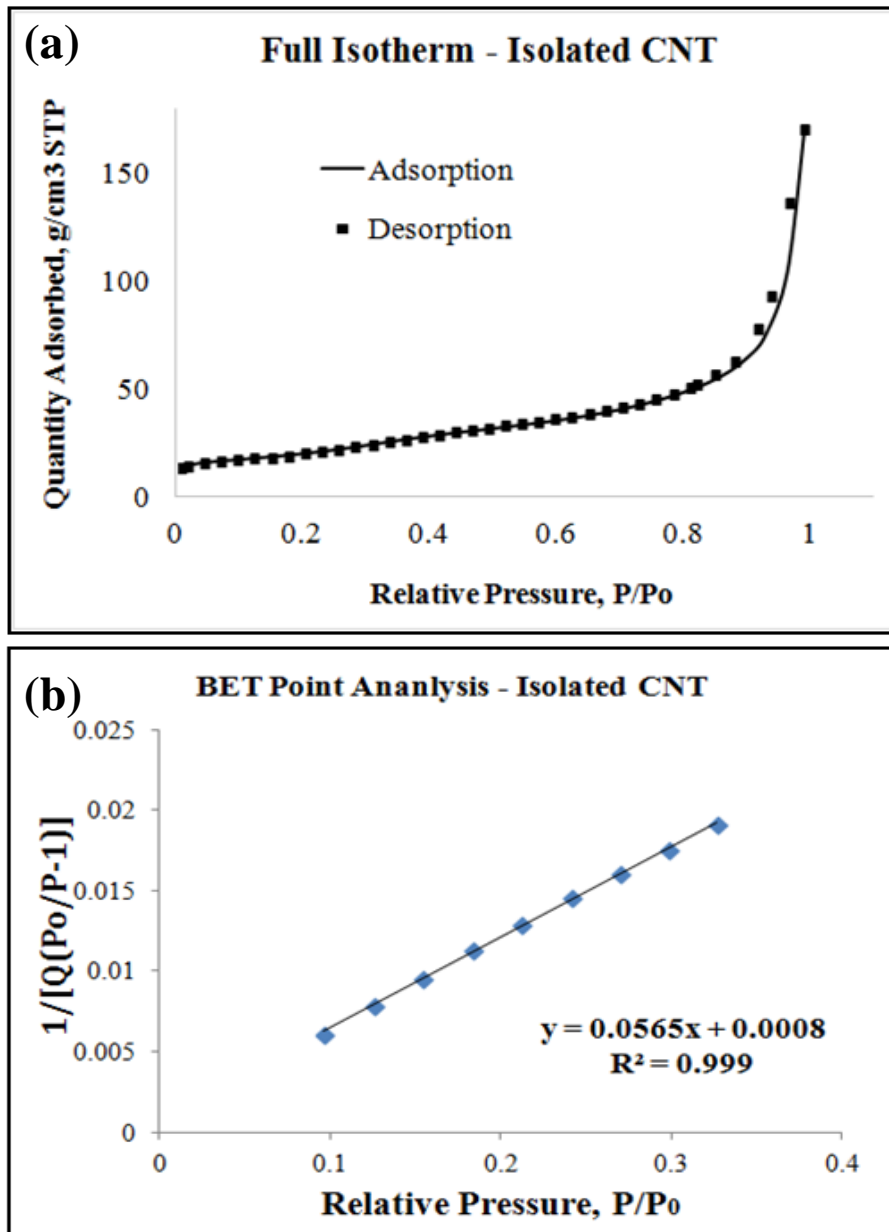


Figure 4.6 (a) Full BET isotherm and (b) linear analysis plot for Isolated CNT

4.4 Conclusion

The available surface area of CNT per unit volume of the RVC was tuned by varying the packing density and/or the height of CNT arrays using the CVD parameters. Two main process parameters were used to control the distribution of CNT arrays – (1) silica coating thickness, and (2) CVD run time. The longer CVD run times results in increased length of CNT carpet and the silica coating on RVC foam improves the CNT growth throughout the supports. Various growth patterns were observed for RVC-CNT hybrids used in this study. Detailed microstructural analysis reveals that the CNT growth through the porous structure follows polynomial trends, having longer CNT arrays on the exterior and less CNT growth towards the interior. The specific surface area of these hierarchical structures was estimated using analytical models and microstructural data, which shows that nanotubes grafting increases the available surface area by few orders of magnitude. This correlates well with the BET measurements. Tuning the surfaces of pores with aligned carbon nanotubes is an important factor for the effective performance of many applications.

This hybrid structure is robust in nature and holds the capability of tuning the surface area, which can be increased by several orders of magnitude without adding any significant weight to the material. Such a phenomenal hierarchical rigid support can be utilized for wide range of applications ranging from novel catalysts supports, electrodes, to water filters. The potential of such hetero-structures to improve the functionalities of existing materials is very promising.

5 Chapter 5: Adsorption of Methylene Blue Dye Compound

5.1 Introduction

The contamination of water bodies is an ever-growing problem worldwide, and water pollution issues are impacting all aspects of life [62]–[64]. In addition to population growth, water contamination is increased by widespread industrialization that can produce unprecedented amount of contaminants [65]. These include byproducts containing heavy metals, chemical toxins, petroleum derivatives, dyes, and other emerging contaminants [66], [67]. Dyes are common contaminants from textile, plastics and paper industries. They are complex aromatic synthetic compounds that have potential carcinogenic and mutagenic effects [63], [64], [67], [68], and are difficult to treat due to their chemical stability and resistance to natural biological degradation. Several techniques have been developed for dye degradation including chemical precipitation, filtration [69], adsorption [70]–[72], photo-catalysis [73], [74], electrochemical [75], ion-exchange [76] and oxidation/catalytic degradation [77], [78]. Among these techniques, adsorption is the most attractive due to its simplicity, high efficiency, ease of operation, and its ability to remove multiple components simultaneously. Moreover, adsorption techniques can be coupled with other mechanisms such as photo-degradation or catalysis, whereby the adsorbed and immobilized toxic compounds and their derivatives can be subsequently treated [79]. This has led to the study of a wide range of natural and synthetic materials as potential adsorbents [19], [80]. It is recognized that the desirable material characteristics of an adsorbent are chemical stability, structural durability, and high specific surface area. Hence, there has been growing emphasis on developing innovative adsorbent solids that can maximize the above characteristics.

Carbon-based materials such as activated carbon, carbon fibers, aerogels, and nanostructures of carbon are well-suited as adsorbents [81]–[83]. Nanostructures of carbon such as graphene, carbon nanotubes (CNT), and bucky-balls, have recently gained significant interest [21], [82]–[86]. Among them, CNT have shown special promise due to their high aspect ratio, fibrous meso-porous structure, and large specific surface area [86]. These have been reportedly used in isolated powder form and have shown high adsorption performance, but successful recovery of nanostructures poses a significant challenge and calls for additional separation steps [70], [87]. This is a serious limitation of stand-alone CNT and all isolated nanomaterials in general, since their dispersion in water can relate to uneconomical material loss and pose toxicity risks to the aquatic environment [88], [89]. Moreover, the cost-effectiveness will be significantly reduced if the material cannot be recovered and reused easily. Possible approaches proposed to address this limitation include centrifugation and attachment of magnetic iron nanoparticles that can be separated from liquid media using a magnet [90]–[93]. Both options add cost and complexity to the adsorption process.

More recent investigations have focused on designing aggregated materials containing nanostructures of carbon [36], [94]–[100]. Vecitis *et. al.* has reported a thin sheet of multiwalled carbon nanotubes - MWCNT (50 μm) as filter material held with PTFE membrane, encased in filter casing [98]. Zhao *et. al.* have developed a graphene sponge [36] and Ai *et. al.* have reported a graphene-carbon nanotube hybrid structure as adsorbent material [99]. These structures are improvements over isolated nanotubes, but still consist of loosely aggregated nanostructures that are not sustainable in flowing water because they lack the structural integrity of a covalently bonded continuous solid.

In this study, we demonstrate a new class of hybrid solid consisting of tall vertical carbon nanotube arrays chemically bonded to larger carbon supports through a reactive buffer layer of silicon dioxide. The CNT arrays are structurally robust, and provide the flexibility of tunable surface area, which can be several orders of magnitude higher than that of conventional high-porosity solids as shown in previous chapter. The hybrid structures can be used as effective reusable adsorbents since the nanotubes do not detach in liquid media, and therefore no additional recovery step is needed. Moreover, these structures, if successful as adsorbents, can be functionalized with suitable nanocatalysts in the future for degradation of the adsorbed species. These types of hierarchical materials are already proven to effectively host metal nanoparticles [16], which were successful in repeatable use for degradation of carbon tetrachloride [17] and biological contaminants in water [101].

This study focuses on bench-scale investigation of the CNT-Foam hybrid structures for removal of a model organic contaminant: methylene blue dye (MB). Methylene blue is a well-known cationic dye that has wide range of applications in textile, printing, biology, and chemistry. MB has some harmful effects to the environment but it is less toxic than most aromatic dyes and hence it is suitable as a good model pollutant.

Methylene blue adsorption experiments were studied using UV-VIS spectroscopy to monitor dye concentration in water. Rate kinetics and isotherm analysis for adsorption of MB on CNT arrays on foam structures have been performed, and results are compared with those from other advanced materials reported in the literature. The results of this study suggest that CNT arrays on foams compare well with other reported materials, while providing the additional benefit of structural durability and repeated use.

5.2 Experimental

5.2.1 Materials and Chemicals

The chemical reagents used in this study were of analytical grade and consumed without further purification. These include Methylene Blue ($C_{16}H_{18}N_3SCl$, MW: 319.85 g/mol, λ_{max} : 665 nm, Sigma-Aldrich chemicals), 2-propanol (99.9%, HPLC Grade, Fisher Scientific) and De-ionized (DI) water. Methylene blue stock solution was prepared by adding known amount of methylene blue in DI water. Further dilution was obtained on demand using DI water to obtain required concentration. Standard solutions were made with concentrations ranging from 0.25 mg/L to 10 mg/L of MB in DI water.

5.2.2 Supports Used

The porous foam structures that were used in this study are: cellular (Ce)-Foam and reticulated vitreous carbon (RVC)-Foam. The SSA of Ce-foams is ~ 0.017 m^2/g [15] and that of RVC-foams is ~ 0.1 m^2/g [23]. CNT were grown on these foam structures under identical growth conditions, involving 10 minutes of silica coating time followed by 30 minutes of CVD run time (unless specified otherwise). For these samples, estimated SSA of CNT coated Ce-foams (Ce-CNT foam) is ~ 1 m^2/g and that of CNT coated RVC-foams (RVC-CNT foam) is ~ 13 m^2/g [15], [102].

For this study, controlled length of CNT arrays was grown on foams as described in chapter 4 section 4.2.2. Parameters varied were (i) silica coating time ($t_{silica} = 10$ and 15 mins), and (ii) CVD run time ($t_{CVD} = 10, 20, 30,$ and 40 minutes). For this study, statistical estimates of specific surface areas were calculated using micro-structural analysis method as described in chapter 4 and are shown in Table 5.1.

5.2.3 Batch Studies – Adsorption, Desorption, and Repeatability Studies

Adsorption Studies:

The batch adsorption experiments were carried out at room temperature in 250 mL round bottomed flask containing 100 mL of aqueous MB dye solution of initial concentration 2 mg/L (unless specified otherwise) at 21 °C. Since earlier studies have reported that MB adsorption capacity may change with pH in the acidic range (pH < 6) [99], [100], the pH of MB solution was maintained at ~ 6.8 for all the experiments. This value was seen to be unaltered at the end of the experiment.

The hybrid supports were initially rinsed with 2-propanol and DI water thoroughly. The supports, typically weighing ~120 mg (unless specified otherwise) were introduced into the flask containing MB solution, and the adsorption time period was started. The flasks were stirred on a rotary shaker (New Brunswick Scientific Co. Inc.), operated at room temperature and 150 rpm for 120 minutes. Approximately 1.5 mL aliquot samples of MB solution were withdrawn using micro-pipets from the flask at pre-determined time intervals. The absorbance was analyzed by the spectrophotometry technique using Cary 50 UV-Vis Spectrophotometer to determine the residue concentration of dye in the solution. The maximum absorbance of MB was observed at wavelength ~665 nm, λ_{max} . It must be pointed out that several earlier studies have discussed a filtration step prior to UV-Vis analysis, but this was not required for these samples. The CNT arrays remained firmly attached to the larger foam supports and were not released in the solution. A detailed study on structural integrity has been reported earlier [17], where the CNT remained attached to the substrates even after several days of rotation in water. In another study [103], [104], it was shown that when the CNT-foam structure is subjected to ultrasonic bath using high power intensity until it fails, the failure occurs by delamination within the

supporting foam, and not by nanotube detachment. In fact, the nanotube carpet remained attached to the outer layer of peeled-off foam substrate, indicating that the CNT to substrate bond is stronger than the graphitic layers within the substrate. Each adsorption experiment was duplicated multiple times and the data reported here shows the mean values with standard error.

Desorption Studies and Repeatability/Reusability of Hybrid Structures:

After the adsorption of MB on the CNT-foam hybrid structure, the supports from the flask were immersed in a vial containing 15 mL 2-propanol alcohol for desorption analysis. The samples were held in the vial without stirring for few minutes followed by manual agitation. After desorption of MB the supports were finally rinsed with water and air-dried. Reusability of these hybrid structures for MB removal was performed under similar adsorption-desorption experimental conditions. The influence of storage media on repeatability was investigated by comparing their performances after storing them overnight in propanol, water, and air.

5.2.4 Data Treatment – Rate Kinetics and Adsorption Isotherms

For each adsorption experiment, the plots of MB removal were plotted using the normalized maximum absorbance, ‘Aⁿ’ at wavelength ‘λ_{max}’ of 665nm, with the elapsed time ‘t’ (minutes). Standard curve was obtained from the absorbance values of standard concentrations ranging from 0.25 mg/L to 10 mg/L, which was applied to convert the maximum absorbance value to respective concentration of MB in the solution (mg/L). The amount of MB adsorbed per unit mass of the adsorbent (mg/g) at time t was calculated from the following mass-balance equation;

$$q_t = \frac{(C_0 - C_t)V}{m} \quad \dots\dots (5.1)$$

Where, q_t is the amount of dye adsorbed on CNT (mg/g) at any time t , C_0 is the initial concentration and C_t is the concentration of MB in the liquid at any time t (mg/L), V is the volume of MB solution (L), and m is the mass of the nanotubes (CNT) within the sample (g).

Rate Constants:

The study of kinetics of adsorption plays an important role for determining the performance of the adsorbent and for designing the system for treatment applications. In order to study the kinetics and estimate the Langmuir monolayer adsorption capacity of the material, the adsorption study was repeated at different initial MB concentrations ranging from 1 mg/L to 16 mg/L using the RVC-CNT 40 samples. The MB removal rate constants were calculated using pseudo-first order and pseudo-second order kinetics and the data were fit with suitable kinetics rate model. To analyze the adsorption rate of MB on CNT, the linear form of the Pseudo-first order and Pseudo-second order rate equations were employed [105]–[107].

First order implies that the rate, governed by driving force, is directly proportional to the availability of surface sites on the adsorbent, hence the pseudo first order equation for adsorption is expressed as:

$$\frac{dq_t}{dt} = k_1(q_e - q_t) \quad \dots\dots (5.2)$$

Where, q_e and q_t are the amount of MB dye adsorbed per unit weight of CNT (mg/g) at equilibrium and at time t , respectively, k_1 is the pseudo-first order rate constant (min^{-1}).

Integrating the above equation with the boundary conditions, $q_t = 0$ at $t = 0$ and $q_t = q_t$ at $t = t$, and solving for the linear form, yields the following equation:

$$\log(q_e - q_t) = \log q_e - \frac{k_1}{2.303} t \quad \dots\dots (5.3)$$

Similarly, the second order rate equation for adsorption indicates that the kinetic rate is directly proportional to the square of available surface sites, hence the rate equation is given as

$$\frac{dq_t}{dt} = k_2(q_e - q_t)^2 \quad \dots\dots (5.4)$$

Integrating the equation 5.4 with appropriate boundary conditions of $q_t = 0$ at $t = 0$ and $q_t = q_t$ at $t = t$, gives:

$$\frac{1}{(q_e - q_t)} - \frac{1}{q_e} = k_2 t \quad \dots\dots (5.5)$$

Equation 5.5 can be rearranged to obtain the general form of integrated second-order reaction equation as given in Eq. 5.6

$$q_t = \frac{k_2 q_e^2 t}{1 + k_2 q_e t} = \frac{h t}{1 + k_2 q_e t} \quad \dots\dots (5.6)$$

Where, k_2 is the pseudo-second order rate constant ($\text{g mg}^{-1} \text{min}^{-1}$) and h is the initial adsorption rate ($\text{mg g}^{-1} \text{min}^{-1}$). Rearranging the above equation to obtain linear form of pseudo-second order:

$$\frac{t}{q_t} = \frac{1}{h} + \frac{1}{q_e} t \quad \dots\dots (5.7)$$

$$h = k_2 q_e^2 \quad \dots\dots (5.8)$$

Adsorption Isotherms:

The adsorption property of a new material is worth investigating through adsorption isotherms. It depicts the amount of adsorbate (MB in this case) that can be adsorbed on the adsorbent (selected hierarchical foam structure, RVC-CNT 40) as a function of concentration at constant temperature (room temperature in this case). The quantity adsorbed is normalized by the mass of the adsorbent to allow comparison

with other materials. In this study, the two widely studied isotherm models, Langmuir [108] and Freundlich [109], have been used.

The Langmuir model is a theoretical model primarily based on the following assumptions: (i) all adsorption sites are equivalent, (ii) adsorbed molecules do not interact, and (iii) at the maximum adsorption limit (represented by q_m), a complete monolayer is formed. The equilibrium adsorption capacity (q_e) is related to the concentration of adsorbate in the liquid at equilibrium (C_e). The linear form of this adsorption isotherm model can be represented by Equation 5.9 as follows:

$$\frac{C_e}{q_e} = \frac{1}{bq_m} + \frac{C_e}{q_m} \quad \dots\dots(5.9)$$

Where, b represents equilibrium constant (L/mg) that is associated with the energy of adsorption, q_m is the maximum adsorption capacity limit (mg/g) that correlates to a complete monolayer coverage [108].

Freundlich isotherm is a model that fits the adsorbed quantity (q_e) proportional to a fractional power ($1/n$) of the concentration in solution (C_e) at equilibrium. Therefore, it can be expressed as:

$$\log q_e = \log K_f + \frac{1}{n} \log C_e \quad \dots\dots(5.10)$$

Where, K_f is Freundlich constant related to the adsorption capacity of adsorbent; and the value of n must be in the range of 1 to 10 for noticeable adsorption [109].

5.3 Results and Discussion

5.3.1 Adsorption of Methylene Blue

5.3.1.1 *Influence of the base support geometry:*

The following CNT-foam materials have been investigated as adsorbents to study the effect of support geometry: (a) cellular carbon foam (Ce-foam), (b) reticulated vitreous carbon (RVC-foam), (c) CNT coated Ce-foam (Ce-CNT foam), and (d) CNT coated RVC-foam (RVC-CNT foam). For this study, the mass of Ce-foams introduced in each flask was ~ 400 mg and that of RVC foams was ~ 85 mg. Since the samples have vastly different specific surface areas, volumes, and CNT distributions, the mass of material introduced was varied to obtain comparable surface areas for the two samples. Figure 5.1a shows the absorption spectrum of methylene blue having λ_{max} at ~ 665 nm obtained using UV-Vis spectrophotometer. Figure 5.1b shows the plot of MB adsorbed on the aforementioned materials (a-d) as adsorbents obtained using the absorbance maximum at 665 nm, where the graph is normalized per gram of hybrid sample (mg/g).

It can be seen that the bare Ce-foam and the bare RVC-foam samples showed small but noticeable MB removal that saturates within the first 10 minutes (Figure 5.1b). When coated with CNT, the RVC foam shows significantly stronger dye reduction, with almost complete adsorption within 120 minutes of the reaction time. This is expected due to the increased surface area created by CNT forests. More interestingly, the CNT coated RVC-foam samples showed increased adsorption compared to CNT coated Ce-foams. This can be attributed to the denser and longer CNT growth on RVC-foams. The starting foams have higher SSA to begin with, and the more open porosity of RVC foams allows higher level of control and significantly

better growth of nanotube arrays on the surface. As indicated in the earlier section, the estimated SSA of CNT coated RVC foam materials is over 10 times that of CNT-coated Ce-foams. Due to this obvious advantage, RVC foam has been selected as the preferred support for future, more detailed quantitative studies of reaction kinetic rates.

5.3.1.2 Influence of nanotube carpet length:

Adsorption studies were carried out on various CNT carpet lengths on the base RVC-foam supports by modifying the CNT growth process. This was obtained either by changing the CVD run time ($t_{\text{cvd}} = 0, 10, 20, 30, \text{ or } 40$ minutes) or by varying the silica coating time ($t_{\text{silica}} = 10$ or 15 minutes), while keeping rest of the standard parameters constant.

Figure 5.2a shows the plot of MB removal using RVC-CNT hybrid supports with varying amount of CNT that was obtained by changing CVD run times. As the run time increases, the CNT carpet length increases offering more available surface area and therefore the MB adsorption increases systematically.

Another approach of increasing CNT growth without changing the CVD run time was to increase the pre-coating, or oxide buffer layer thickness on RVC foam prior to CNT attachment. It is expected that, within the range studied, thicker silica buffer layer results in faster nanotube growth. Figure 5.2b shows the plot of MB removal using RVC-CNT hybrid obtained by 10 and 15 minutes of silica coating time followed by a fixed (30 minutes) CVD run time. It is evident from the plot that silica coating by itself (no CNT growth) does not influence MB adsorption. However, higher silica coating thickness leading to increased CNT growth in the same CVD run time results in samples that adsorb higher amounts of MB in identical conditions.

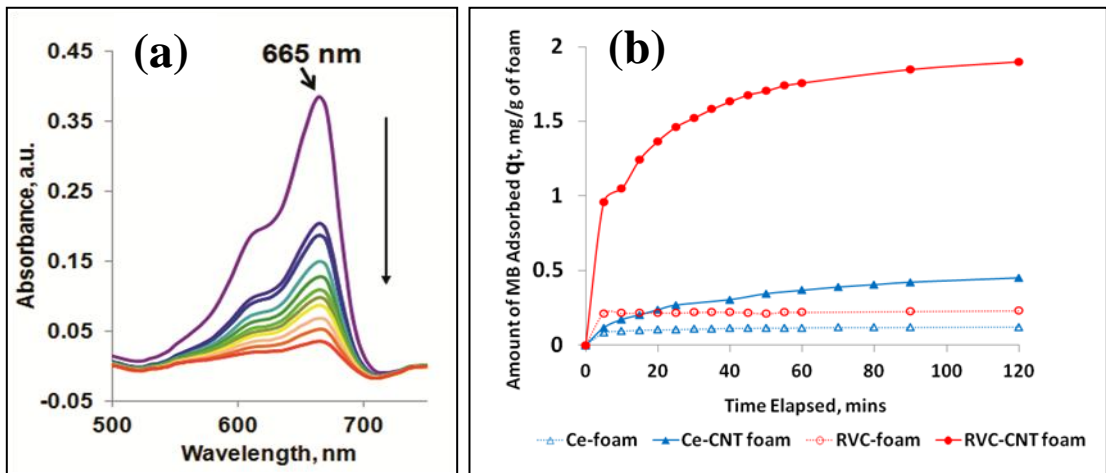


Figure 5.1 (a) UV-Vis absorbance spectrum of MB solution, $\lambda_{max} \sim 665$ nm, (b) Plot showing influence of different porous structures on adsorption of methylene blue obtained with bare and CNT coated: cellular (Ce-foam) and reticulated (RVC) foams, at initial concentration – 2 mg/L.

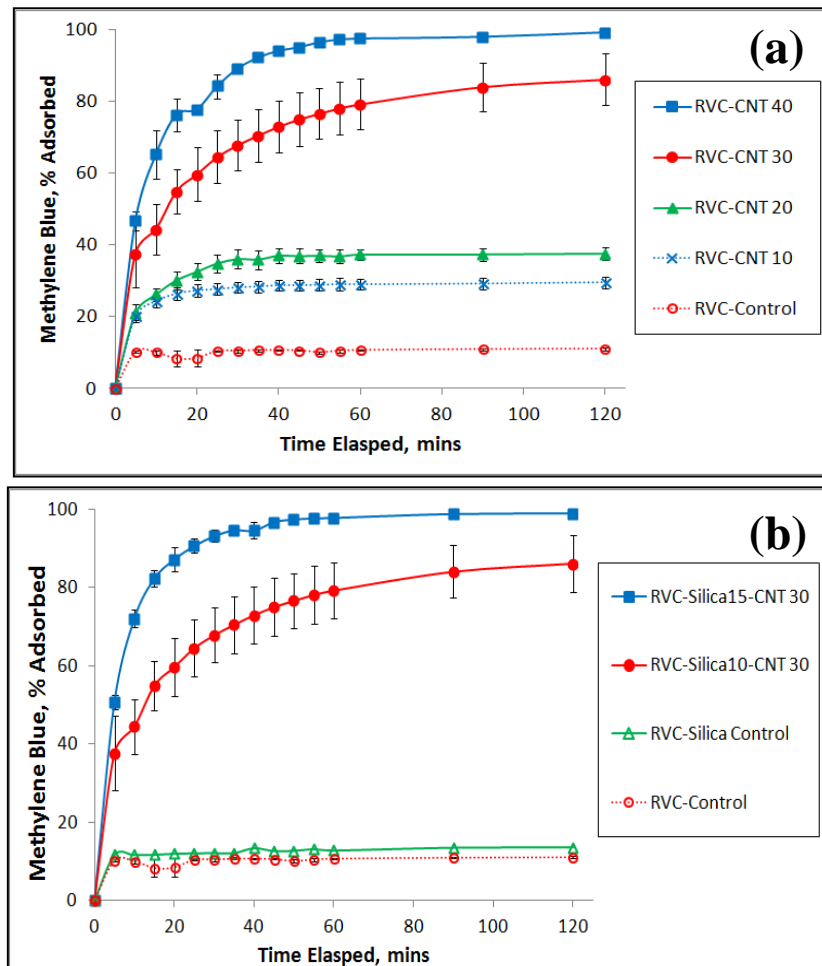


Figure 5.2 Adsorption efficiency of methylene blue (initial concentration 2 mg/L) using RVC-CNT hybrids CNT obtained by (a) varying CVD growth time - 10, 20, 30, and 40 minutes, (silica coating time fixed at 10 mins), (b) Silica coating time - 10 and 15 mins (CVD run time fixed at 30 mins)

Table 5.1 Estimated specific surface area of RVC-CNT hybrids and removal efficiency at initial concentration 2 mg/L methylene blue

Sample ID	CVD Run Time, minutes	Estimated Specific Surface Area, m ² /g	Removal Efficiency $\%R = \frac{C_0 - C_e}{C_0} * 100$
RVC Control	NA	0.11	11.39
RVC-CNT 10	10	2	27.90
RVC-CNT 20	20	6	39.17
RVC-CNT 30	30	13	85.64
RVC-CNT 40	40	17	99.45

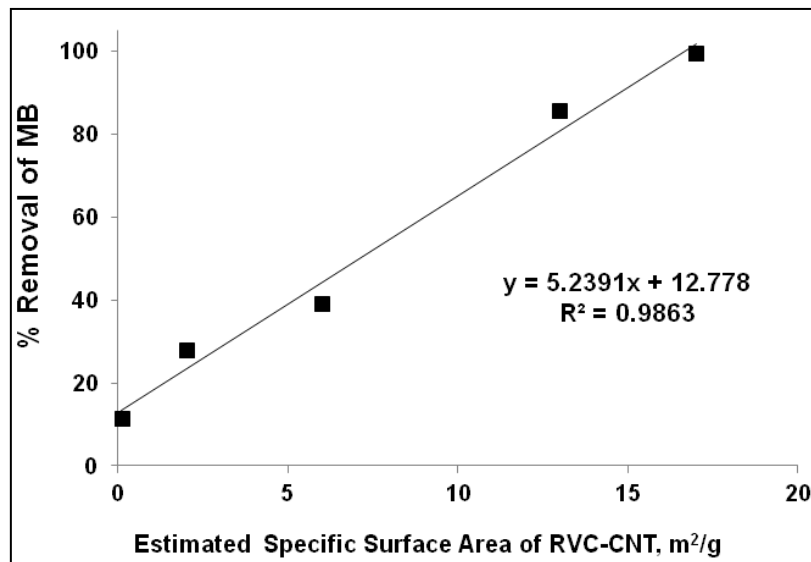


Figure 5.3 Graph showing correlation between MB removal capacity and specific surface area of RVC-CNT hybrid samples (Bare RVC foam and RVC-CNT 10, 20, 30, 40, Table 5.1). Initial concentration of MB was ~ 2 mg/L for all tests.

5.3.1.3 Correlation of MB adsorbed with specific surface area (SSA) of CNT-foam samples:

For an initial MB concentration of 2 mg/L, the fraction of MB adsorbed at equilibrium time, $t_e = 120$ minutes was considered here for comparison with available surface area and the data are tabulated in Table 5.1. Figure 5.3 shows the correlation of % MB removed with the estimated SSA of the RVC-CNT samples. The linear relationship of MB removal fraction with the available SSA shows the dye adsorption performance of the CNT hybrids is directly correlated to the amount of CNT on the foam. The slope of the graph can be used to estimate the amount of MB adsorbed per unit area of CNT. This correlation indicates that it is possible to tailor the adsorption capacity of this type of hybrid material by varying the length of CNT arrays through controllable process parameters.

5.3.2 **Kinetics Analysis**

The rate of dye adsorption by a measured quantity of material from a solution of specific concentration corresponds to its adsorption efficiency. In order to determine the suitable kinetic rate equation, the adsorption capacity of a selected RVC-CNT material (CNT-40) was determined by adsorption studies at different initial MB concentrations ranging from 1 mg/L to 16 mg/L. As discussed in section 5.2.4, the experimental data were plotted according to the pseudo-first order and pseudo-second order rate models using Equation 5.3 and Equation 5.7 respectively. Linear regression fits as shown in Figure 5.4 were used to estimate the kinetics parameters that are tabulated in Table 5.2.

It can be seen from Figure 5.4a that pseudo-first order model does not fit well with experimental data. In addition to data points not being linear, the equilibrium

adsorption capacity estimated from the intercept of the graph does not match the experimental values, as seen in Table 5.2.

In contrast, the pseudo-second order model shows a good fit (Figure 5.4b) having regression coefficients close to one and the calculated equilibrium adsorption capacity values agree well with the experimental values (Table 5.2). This suggests that the adsorption kinetics in this type of material follows the pseudo-second order rate model, *i.e.*, adsorption rate varies as square of the surface site availability. The applicability of pseudo-second order may imply that two active surface sites are involved for removal of one unit of MB.

It must be noted that, as expected, the equilibrium adsorption capacity (maximum MB adsorbed before saturation) increases with an external driving force controlled by the MB concentration in the solution. Therefore, when the initial concentration of the solution was increased from 1 mg/L to 16 mg/L, the adsorption capacity increased monotonically from 7 mg/g to 43 mg/g. Understanding the pseudo-second order rate constants, k_2 , on the other hand is not so straightforward. It was observed to decrease with initial concentration of MB till 4 mg/L and then increase again with initial concentration from 4 to 16 mg/L. It has been pointed out in the [105]–[107], that the pseudo-second order rate constant is a complex function of an initial external driving force (concentration of adsorbate in solution) and may depend on the residual surface charge and the ion exchange mechanisms. Detailed investigation about the local surface sites and their chemical potentials will be needed in future to fully explain this phenomenon.

5.3.3 Adsorption Isotherms

As discussed earlier, adsorption isotherms depicting the equilibrium state relationship between the solid-phase concentrations of MB per unit mass of the

adsorbent (q , mg/g) and the liquid-phase concentration (C , mg/L) were obtained at room temperature. The experimental data were analyzed using two widely known models - Langmuir and Freundlich isotherm models. The linear form of isotherms based on the experimental data and the equations 5.9 and 5.10 are shown in Figure 5.5. The best fit of the data is shown by the linear regression and the parameters obtained from the plots are tabulated in Table 5.3. It can be seen that the isotherm equations fit the data very well.

The Langmuir isotherm fit for the concentration range investigated was used to determine adsorption capacity. From Langmuir theory and data fit, it indicates that there is indeed a saturation capacity equivalent to a “monolayer” adsorption amount of MB molecules that can be accommodated on these surfaces. This result has also been confirmed with molecular dynamic simulation studies by Chagovets *et.al.* [110]. Their computational modeling studies on random adsorption of MB ions on nanotubes in aqueous media reveal that MB ions form a monolayer shell-like configuration around the CNT surface [110].

From the Langmuir plot, the maximum MB adsorption capacity (q_m) of the CNT in CNT 40 sample is estimated to be about 43.5 mg/g. As MB forms the monolayer adsorption on CNT surface [110], the specific surface area (SSA) of CNT or the RVC-CNT hybrids can be estimated from the maximum MB adsorption capacity ‘ q_m ’ [111]–[113]. From [113]:

$$SSA_{MB} = \frac{N_A \tau q_m}{M_{MB}} \quad \dots\dots (5.11)$$

Where ‘ N_A ’ is the Avogadro’s number ($6.023 \times 10^{23} \text{ mol}^{-1}$), ‘ q_m ’ is maximum adsorption capacity of adsorbent, ‘ τ ’ is the cross-section surface area that is occupied by MB molecule, ‘ M_{MB} ’ is the molecular weight of MB (320 g mol^{-1}) [111]–[113].

The cross-sectional surface area of MB as reported in literature is $\tau = 1.3 \text{ nm}^2$ [111]–[113]. Specific surface area of CNT using MB analysis turns out to be about $\text{SSA}_{\text{MB}} = 106 \text{ m}^2/\text{g}$. This value agrees very well with the SSA value of CNT ($\text{SSA} = 119 \text{ m}^2/\text{g}$) estimated from analytical models shown in Chapter 4 - section 4.2.3.

The maximum adsorption capacity of CNT has been compared to the maximum adsorption capacities of various other types of MB adsorbents that have been reported in the literature as tabulated in Table 5.4. It can be seen that the adsorption capacity of CNT arrays in these materials is higher than most adsorbents shown, except for a few graphene-based materials. The CNT arrays in these materials seem to have higher projected capacity compared to carbon fibers, and even compared to isolated CNT dispersed in the water. Isolated CNT dispersed in the solution would be expected to be more effective than dense packed carpets anchored to larger solids, since dispersion may offer more intimate interaction with the aqueous medium. However, this result shows otherwise implying that it is possible to fully utilize the high quality nanotubes in these hybrid materials. The only materials having higher projected adsorption capacity are the graphene-based materials [97], [99]. However, as mentioned in these papers, these aggregated graphene-containing structures disintegrate in water and would require a follow-up separation step for removal if deployed. On the other hand, the material in this study is robust and allows full utilization of the nanotube surface without the need to disperse the nanomaterials in water.

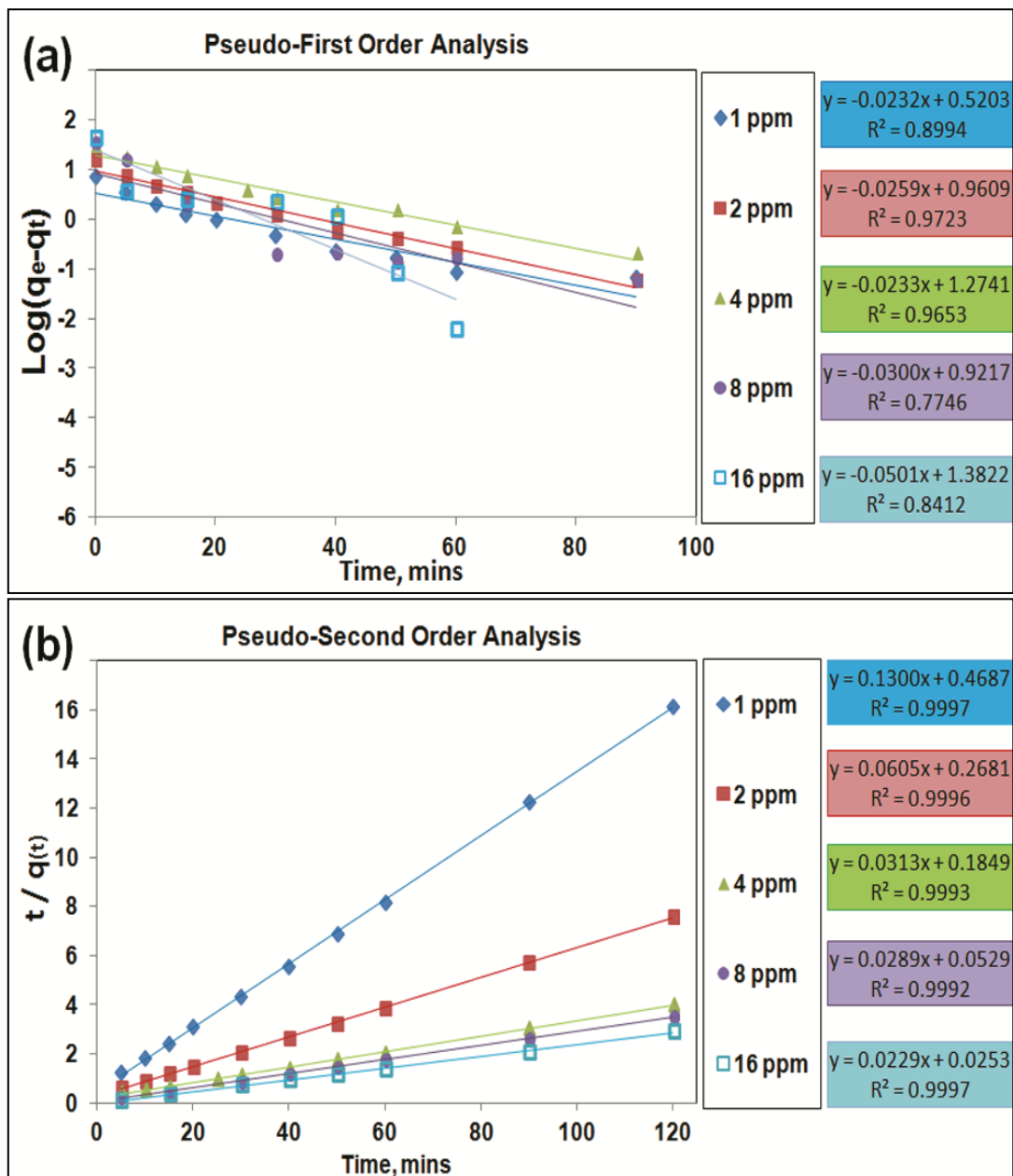


Figure 5.4 Kinetic rate plots of MB adsorbed on to RVC-CNT hybrid structure (CNT 40) showing (a) Pseudo-first order rate model and (b) Pseudo-second order rate model

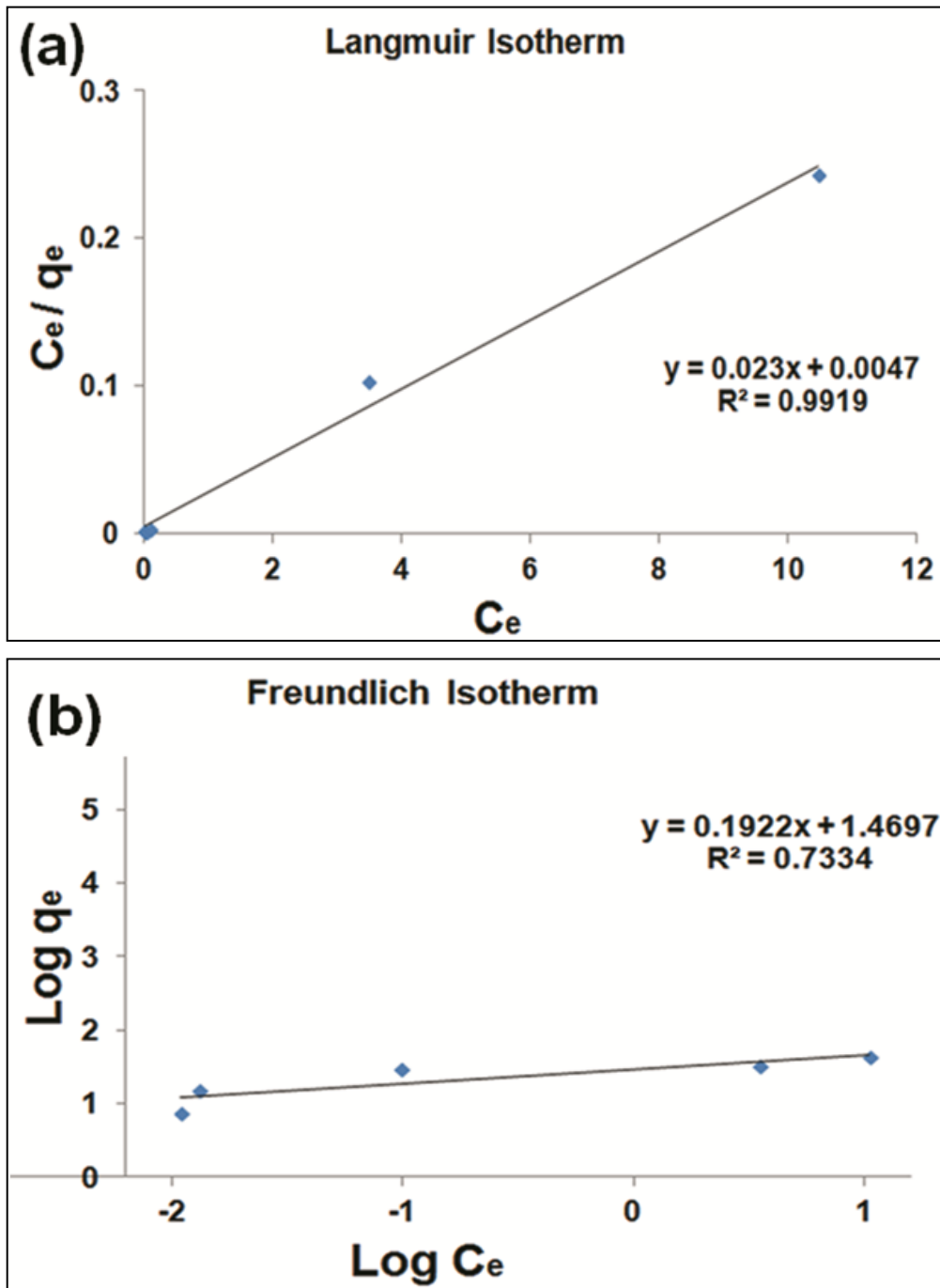


Figure 5.5 Plots showing adsorption isotherms for the adsorption of MB on to the RVC-CNT hybrid structures, CNT-40, (a) Langmuir isotherm, and (b) Freundlich isotherm

Table 5.2. Adsorption kinetic parameters obtained using Pseudo-First order and Pseudo-Second order rate kinetics for adsorption of MB on CNT-40

C_0 mg L ⁻¹	Pseudo-First Order				Pseudo-Second Order		
	q_e^{exp} mg g ⁻¹	q_e^{cal} mg g ⁻¹	k_1 min ⁻¹	R^2	q_e^{cal} mg g ⁻¹	k_2 g mg ⁻¹ min ⁻¹	R^2
1 ppm	7.43	3.31	0.053	0.8994	7.69	0.036	0.9997
2 ppm	15.82	9.14	0.060	0.9723	16.53	0.014	0.9996
4 ppm	30.15	18.80	0.054	0.9653	31.95	0.005	0.9993
8 ppm	33.94	8.35	0.069	0.7746	34.60	0.016	0.9992
16 ppm	43.13	24.11	0.116	0.8412	43.67	0.021	0.9997

Table 5.3. Isotherm parameters obtained using Langmuir and Freundlich isotherm for the adsorption of MB on CNT-40

Langmuir Isotherm			Freundlich Isotherm		
q_m (mg g ⁻¹)	b (L mg ⁻¹)	R^2	K_f	n	R^2
43.5	4.89	0.9919	29.5	5.2	0.7334

Table 5.4 Adsorption capacities of MB on various adsorbents as reported in the literature for comparison

Adsorbents	Adsorption Capacity (mg g ⁻¹)	References
CNT (on RVC Foam)	43.5	This study
Carbon Nanotubes - isolated	35	Yao et al., 2010 [70]
MWCNT – filters	29	Vecitis et al., 2011 [98]
Granular or powdered Activated carbon	21.5 - 91	Yener et al., 2008 [81]
Vegetal Fiber – activated carbon	33	Cherifi et al., 2013 [80]
Exfoliated graphene oxide	17.3	Ramesha et al., 2011 [85]
G-CNT Hybrids	81.97	Ai and Jiang, 2012 [99]
Graphene Sponge	184	Zhao et al., 2012 [36]

5.3.4 Desorption of MB and Regeneration of the Adsorbent

The possibility of regenerating the adsorbent after use was studied by attempting a simple desorption method: dipping in alcohol. Figure 5.6 shows the visual images of adsorption and desorption cycles of MB in water and 2-propanol respectively. As indicated in earlier sections, samples kept in aqueous MB solution (2 mg/L in this case) turned colorless within 120 minutes indicating adsorption of the entire MB on the CNT as demonstrated in Figure 5.6(a-b). These solids were subsequently placed in 2-propanol solution, where the adsorbed MB is gradually desorbed from the adsorbent (CNT) surface changing the appearance of 2-propanol from colorless to blue color as shown in Figure 5.6(c-e). Agitating the support in the 2-propanol solution removes the MB more swiftly and effectively. This step was repeated (1-2 times) until the 2-propanol solution stayed colorless.

5.3.5 Repeatability Test

For practical applications, it is essential to determine the reusability of a potential adsorbent such as the RVC-CNT hybrid structures of this study. In order to evaluate that, several adsorption-desorption cycles were performed on each type of RVC-CNT hybrid. The removal capacity obtained with the re-used samples was similar to that of the fresh samples and the dye degradation profiles were observed to be within the standard error bars reported for fresh samples.

The long term repeatability was seen to depend on the storage medium as seen in Figure 5.7. Figure 5.7a shows the removal percentage of MB for multiple adsorption-desorption cycles using RVC-CNT 40 that was stored in propanol. The first three cycles of MB adsorption from aqueous solution and desorption into 2-propanol were performed within one day, and the adsorption capacity was clearly unchanged. After three cycles, the samples were stored overnight submerged in 2-

propanol solution and the test resumed the following day. A detectable reduction in reusable efficiency can be observed from cycle 3 to 4 (Figure 5.7a), indicating that prolonged storage in alcohol may reduce the surface activity of the CNT. However, the tests repeated on the second day, cycles 4-6, show identical adsorption capacity, indicating that short term desorption in alcohol does-not influence adsorption activity. In order to test if prolonged storage in other media is possible without performance degradation, this test was repeated by storing the samples in air and water. Figure 5.7b shows the removal efficiency of RVC-CNT 40 sample after prolonged storage in water (between cycles 8 to 9). For overnight storage in air, the results are identical and were observed to be within the standard error bars. It can be seen that the adsorption capacity remains unchanged throughout 10 cycles and shows no decrease after storing in water or in air.

In order to investigate the desorption capacity of RVC-CNT, systematic desorption studies were carried out. Figure 5.7c shows the adsorption-desorption cycles of MB on RVC-CNT 40, showing the adsorption in water and desorption in 2-propanol. The amount of MB in 2-propanol was determined using standards of known concentration in 2-propanol. Figure 5.7c shows high desorption capacity and it appears that most of the adsorbed MB is desorbed in 2-propanol and are within the error bars.

This study points to several important characteristics of these hierarchical hybrid materials. Unlike other nanoscale adsorbents reported in the literature, these are robust solids suitable for prolonged use without dispersion of loose nano-components in water. Their adsorption capacity per unit volume can be easily increased by increasing the length of CNT carpets using known process parameters. Moreover, they are seen to retain their adsorption capacity after repeated use. These materials therefore provide significant promise for water purification applications.

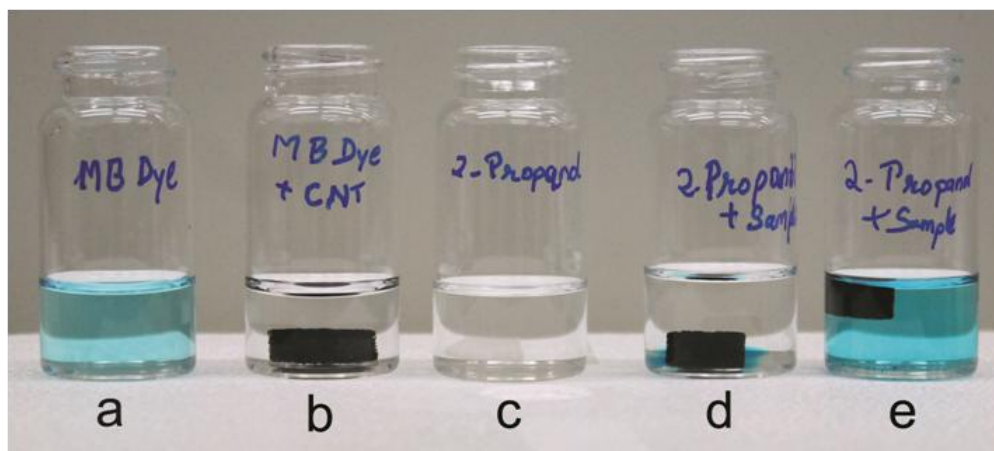


Figure 5.6. Images of the vials representing adsorption and desorption of MB using RVC-CNT foam, (a) MB in water, (b) colorless solution indicating MB adsorbed on hybrid sample, (c) 2-Propanol solution, (d) MB-adsorbed sample placed in 2-Propanol – blue ring indicates release of MB from sample, and (e) MB desorbed completely in 2-propanol solution and RVC-CNT sample is retained.

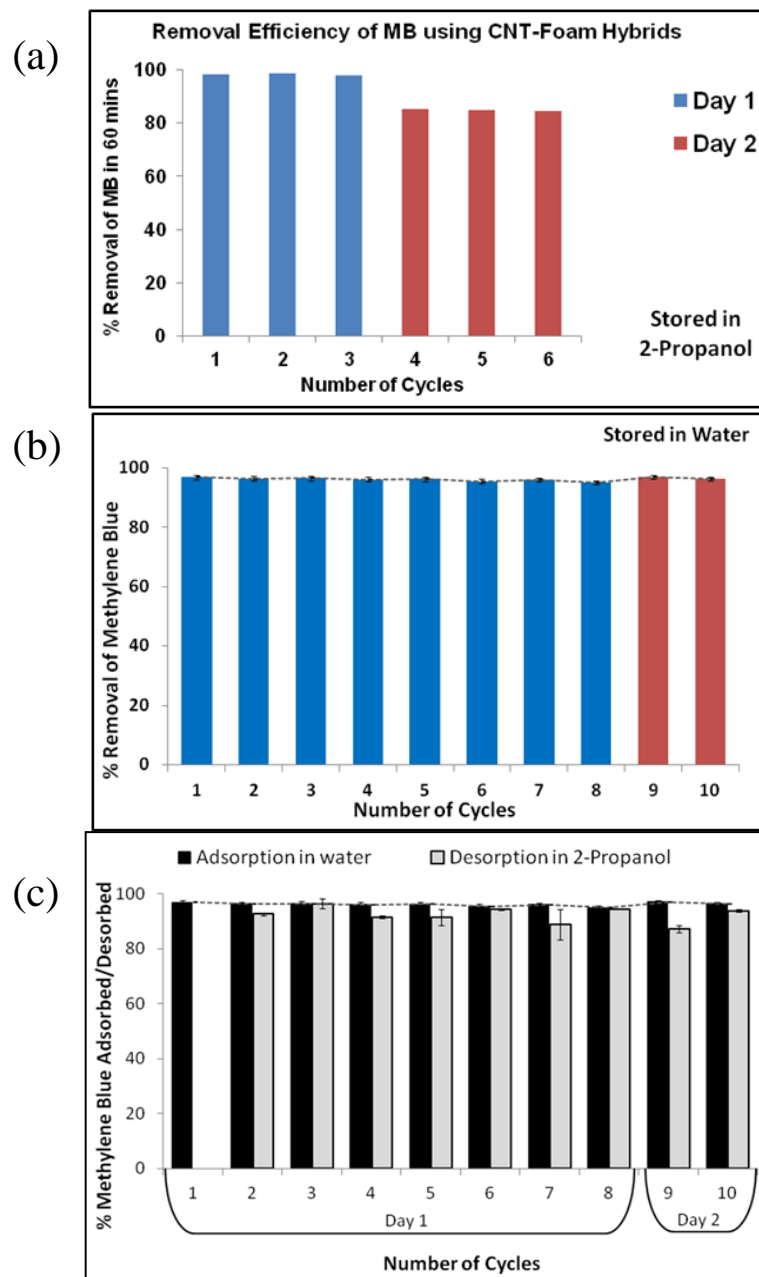


Figure 5.7 Methylene blue removal plots obtained by re-using RVC-CNT hybrid structures (a) adsorption for up to 6 cycles and samples stored in 2-propanol overnight (at cycles 3-4), (b) adsorption-desorption analysis for up to 10 cycles where the samples were stored in water and in air overnight (at cycles 8-9), and (c) adsorption-desorption cycles.

5.4 Conclusion

Hierarchical carbon structures obtained by grafting carbon nanotubes on porous structures having different porosities were used as adsorbents for removal of a model contaminant - 'methylene blue' from water. It was found that the performance of the CNT-Foams hybrids to adsorb dye is greatly influenced by the amount of CNT on the foam, which dominates the specific surface area of the material. The available surface area of the RVC foam can be controlled by changing the buffer layer thickness and CNT growth time. This surface area is directly proportional to the measured adsorption capacity of the solids. The removal rate of MB was seen to follow Pseudo-second order kinetics, and the rate model has been employed to predict the equilibrium capacity, initial adsorption rate, and second order rate constant for different dye concentrations. The saturation adsorption at a given concentration is a good fit with the Langmuir isotherm model indicating a "monolayer" adsorption limit for methylene blue molecules on the CNT surface. The maximum projected adsorption capacity for MB on CNT arrays is about 43.5 mg/g, which compares very favorably with other advanced materials reported in the literature. It is noted that the adsorption capacity can be easily increased in this design by increasing the length of the CNT carpet on the foams. Moreover, unlike other nano-material aggregates reported, these materials are robust enough to survive prolonged use over many cycles without deterioration. These attributes make the CNT-Foam hybrid solids a promising design for advanced hybrid materials for future pollutant removal applications.

6 Chapter 6: Palladium and Palladium-Oxide Nanoparticles on Hierarchical Carbon Nanostructures

6.1 Introduction

Metal and metal-oxide nanoparticles (NPs) have potential applications in various fields including bio-medicine, electronics, environment, catalysis, optics and optical sensing that can constructively be used to advance the current cutting-edge technologies [114][115][116]. Many novel applications of metal nanoparticles as sensors, absorbents, ceramics, and/or catalysts are governed by their size, structure, and surface chemical properties. Metal nanoparticles of precious metals such as Pt, Pd, Au, and Rh are well known for their activity. Among various transition and rare earth metals, Palladium (Pd) is studied extensively for its high catalytic activity, unique ability to absorb hydrogen gas while being impervious to other gases, and also as an inexpensive substitute to platinum (Pt) [117]. Supported palladium nanoparticles are commonly employed for automotive exhaust catalysis, hydrogenation reactions, dechlorination of halogenated compounds, *etc.* For many surface dependent applications, attaching nanoparticles of precious metals on high surface area supports becomes economically and ecologically desirable for effectiveness of the system [118] [119]. The hierarchical nanostructures used in this study can behave as an ideal support for anchoring metal nanoparticles.

This study builds upon the earlier studies to investigate a new class of carbon support for porous, robust, compact, and highly active Pd-based catalyst structures. This involves attachment of palladium nanoparticles on multi-scale hierarchical structures of carbon, which are formed by grafting CNT on porous structures. In earlier research, cellular carbon foams having 80% porosity were used as base

supports for constructing hierarchical support for Pd-NPs. Synthesis and characterization of supported Pd-NPs was carried out using liquid-phase infiltration and thermal reduction techniques that have been developed and published previously [16], [18]. The supported Pd-NPs were then employed as catalysts for removal of toxic chemicals such as carbon tetrachloride from water using batch reductive degradation [16][17].

In this study, new types of porous materials that have more open reticulated structures have been investigated as high surface area supports for Pd based NPs. Pd-NPs obtained using thermal reduction were in the form of zero-valent metallic palladium. Supported palladium oxide nanoparticles were then prepared by thermally oxidizing Pd-NPs. The crystal structure of Pd-NPs on CNT-foam structures was investigated and reported here. Microstructural and spectroscopic characterizations were carried out comparing the Pd and PdO nanoparticles (NPs) on various hierarchical structures.

6.2 Experimental

6.2.1 Materials

All the reagents used in this study were of analytical grade and used without further purification; that includes Tetra-amine Palladium (II) Nitrate solution (TAPN, 99.9%, 5% Pd, Alfa-Aesar Ltd.). Other materials are de-ionized water (DI water), and laboratory grade methanol. Ultra high purity hydrogen gas (H_2 , 99.999%), and laboratory purity argon gas (Ar) were used.

6.2.2 Support Preparation

The porous supports employed in this study include cellular and RVC foams as shown in Figure 2.1. Palladium-nanoparticles (Pd-NPs) were synthesized on bare foams as well as on CNT that were grafted on the above mentioned foam structures. The size of Ce-foam support used was $\text{\O} 8 \text{ mm} \times 2.5 \text{ mm}$, weighing $\sim 100 \text{ mg}$ whereas the RVC-foam support used was $\text{\O} 8 \text{ mm} \times 5 \text{ mm}$, weighing $\sim 25 \text{ mg}$, each. All the supports were rinsed with methanol and water prior to palladium deposition.

6.2.3 Synthesis of Supported Palladium Nano-Particles

In this study, supported Palladium nanoparticles on the specified foam supports were fabricated by the liquid-phase synthesis technique combined with thermal reduction process [16], [18]. The Pd-NPs synthesis process used in this study is described in detail in section 2.3.2.

6.2.4 Synthesis of Supported Palladium-Oxide Nanoparticles

Palladium oxide nanoparticles were prepared by thermally oxidizing the as-prepared supported Pd-NPs. The Pd-NPs samples were placed in the furnace with quartz tube and the oxidation treatment was carried out by heating the samples at $250 \text{ }^\circ\text{C}$ and $300 \text{ }^\circ\text{C}$ for 2 hours in air oxidation environment (inlet open to ambient air environment and outlet to exhaust).

6.2.5 Materials Characterization

Micro-structural investigation was performed using scanning electron microscopy (SEM). Spectroscopic analysis for chemical composition and structure was performed using energy dispersive X-ray spectroscopy (EDS) and X-ray photoelectron spectroscopy (XPS) techniques. Crystal structure investigation of Pd-

NPs was performed using X-ray diffraction (XRD). These techniques are briefly explained in Section 2.4.

6.3 Results and Discussion

6.3.1 Crystal Structure Characterization – XRD

Figure 6.1 shows the XRD patterns obtained from Pd-NPs on CNT Foam (Pd-CNT-Foam) sample and pristine CNT Foam sample (CNT-Foam). The XRD pattern of CNT-Foam exhibits peaks at 2Θ values of 26° , 42° , 44° , 55° , 78° , 83° , and 87° . These correspond to the graphitic structure of carbon. The strong peak at 26° corresponds to (0 0 2) plane, a characteristic peak of hexagonal structure of graphite and CNT. The XRD pattern of Pd-CNT-Foam exhibits additional peaks at 2Θ values of 40° , 46° , 69° , 82° , and 86° corresponding with the (1 1 1), (2 0 0), (2 2 0), (3 1 1), and (2 2 2) crystal planes, respectively [16]. These peaks are in good agreement with those reported in the literature for the face centered cubic (FCC) structure of palladium nanoparticles having a lattice constant, $a = 3.91 \text{ \AA}$ [120], [121], [122].

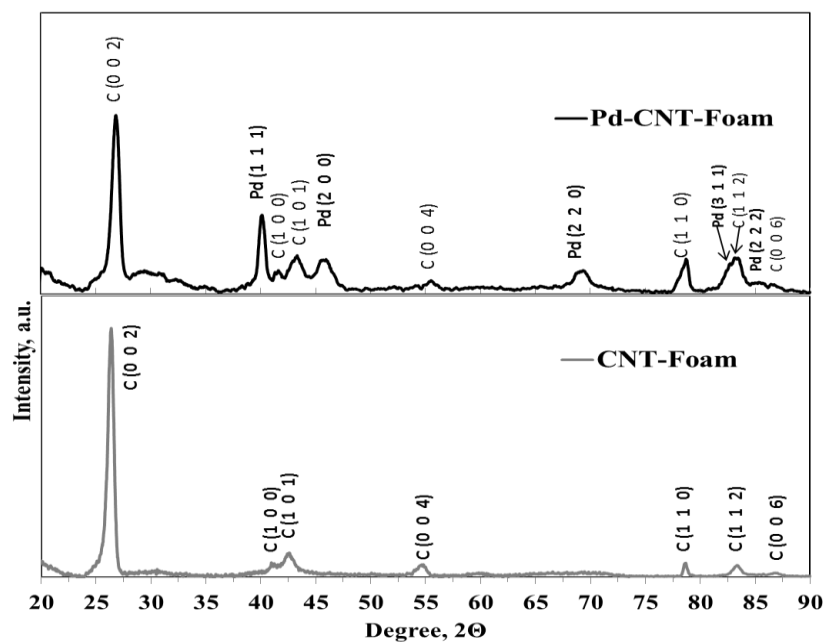


Figure 6.1 X-ray diffraction pattern for CNT grafted Ce-Foam and Pd-CNT grafted Ce-Foam, range $20^\circ < 2\theta < 90^\circ$

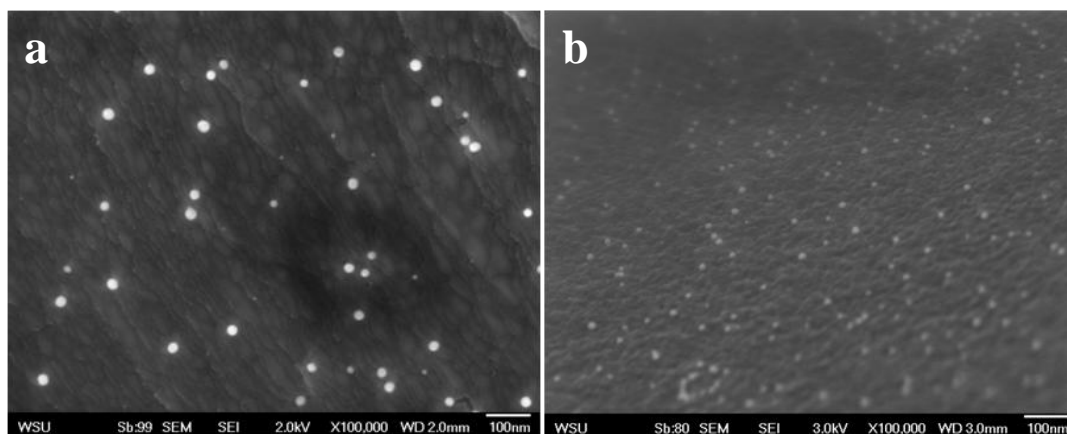


Figure 6.2 SEM micrographs showing Pd-NPs fabricated on (a) Ce-foam and (b) RVC foam

6.3.2 Microstructure Characterization – Pd on Various Porous Structures

Figure 6.2 shows the SEM images of Pd-NPs on bare Ce-foam and RVC-foam structures fabricated by one-coating cycle of Pd. Multiple coating of Pd synthesis was carried out for fabricating Pd-NPs on the CNT-grafted Ce-foams as well as RVC-foams using similar coating process.

Figure 6.3 depicts the SEM micrographs of Pd-NPs deposited on the CNT-foam supports. The high loading of Pd is desirable and the hierarchical structures developed with CNT-grafting provide additional surface for anchoring NPs. The SEM images (Figure 6.3) show that uniformly distributed Pd-NPs were fabricated on the CNT hierarchical architecture.

Figure 6.4 shows the SEM images of Pd-NPs fabricated on CNT-grafted Ce-foams by one- and two- coating cycles of Pd. SEM micrographs reveal that the two-coating of palladium significantly enhances the amount of nanoparticles loaded on the support, whereas any further increase in Pd content would result in sintering of particles in to large and continuous film like metal coating. The compositional element data was obtained using EDS that are tabulated in Table 6.1. The spectroscopy analysis using EDS system on these supports shows strong peaks for Pd and the elemental data confirms that the Pd content (wt%) obtained with two-coating cycles was twice the amount obtained with one-coating cycle on CNT grafted Ce-foams.

Figure 6.5 shows the SEM micrographs of Pd-NPs coated on CNT-RVC foams. Pd-NPs were fabricated by one-, two-, and three-coating cycles of Pd on RVC foams, so as to increase the amount of Pd-loading. The SEM images shown in Figure 6.4 and Figure 6.5 reveal that the amount of Pd loading was significantly improved

with multiple coating cycles of Pd. EDS analysis data as tabulated in Table 6.1 shows that Pd content (wt%) increases with the number of coating cycles of Pd.

6.3.3 Microstructure of Pd-O Nanoparticles

Figure 6.6 shows the SEM micrographs of Pd-NPs decorated on the CNT-foam supports before (a-b) and after (c-h) the oxidation treatment. Figure 6.6(c-d) shows the palladium nanoparticles that were oxidized at 250 °C and Figure 6.6(e-f) shows the palladium nanoparticles that were oxidized at 300 °C. These samples are referred as Pd-O₂₅₀ and Pd-O₃₀₀, respectively. The microstructure of Pd-NPs after the oxidation treatment does not show any detectable difference in size and structure of nanoparticles. Furthermore, no detectable difference in the structure of CNT was observed.

6.3.4 Chemical State of Pd and Pd-O Nanoparticles

The chemical state of palladium and palladium oxide nanoparticles attached on CNT-RVC foams is studied using the XPS. The XPS survey-scans and fine-scans were taken for as-synthesized and oxidized palladium nanoparticles samples. The general scan shows low resolution peaks that gives an outlook to the various elements in a sample. Semi-quantitative compositional analysis was also obtained from the survey-scans. A detailed investigation was done on high resolution fine-scan peaks obtained for the core level (orbital) spectra of the corresponding elements. By examining the binding energy (BE), full width at half maximum (FWHM), intensities of the component peaks and their relative sensitivity factor (RSF), the relative quantitative surface compositional analysis was obtained for the above mentioned samples.

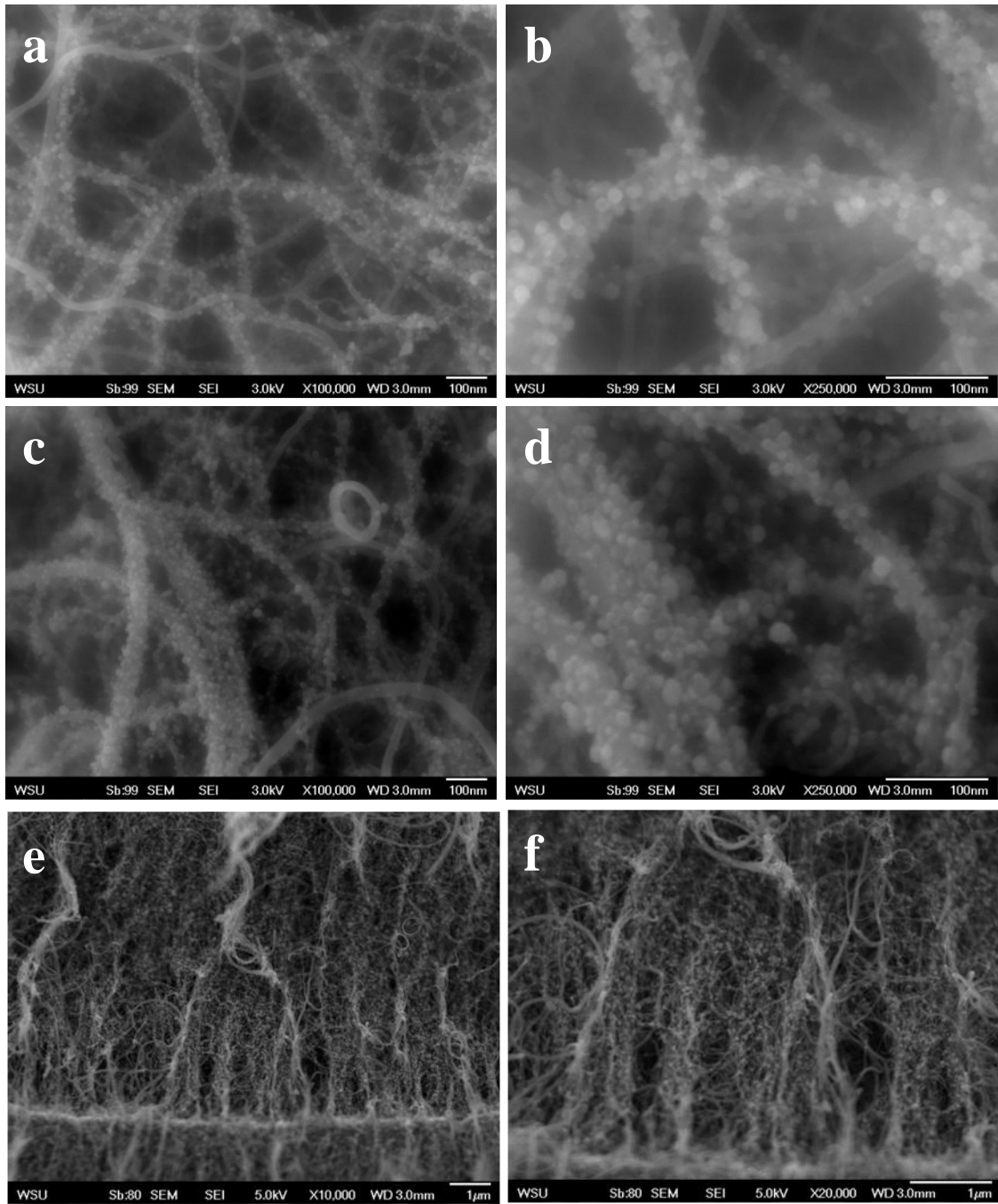


Figure 6.3 Typical SEM images of one-coating cycle of Pd-NPs fabricated on CNT-coated foams (a-d) top view of CNT arrays, (e-f) side view of the CNT arrays

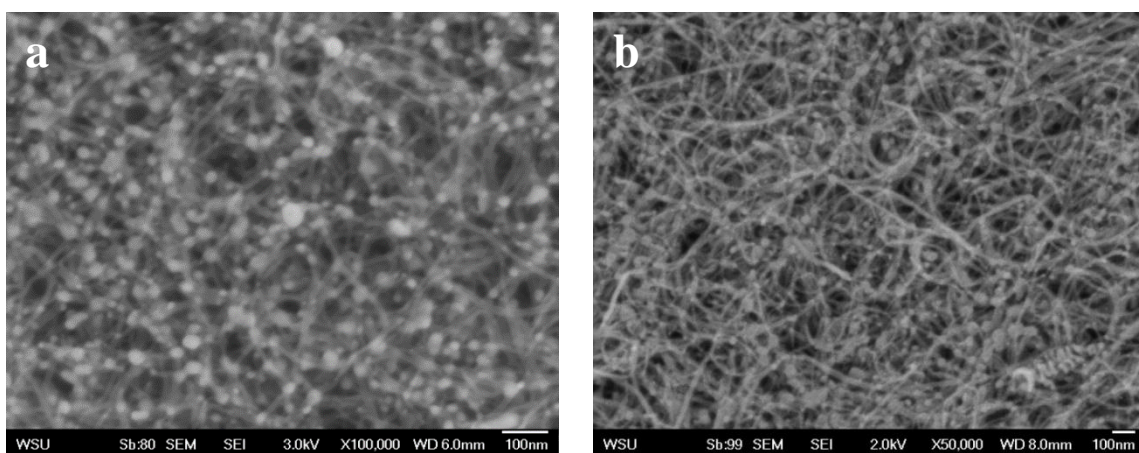


Figure 6.4 SEM micrographs showing Pd-NPs fabricated on CNT-grafted cellular foam by one-coating cycle (a), and two-coating cycle (b), processes

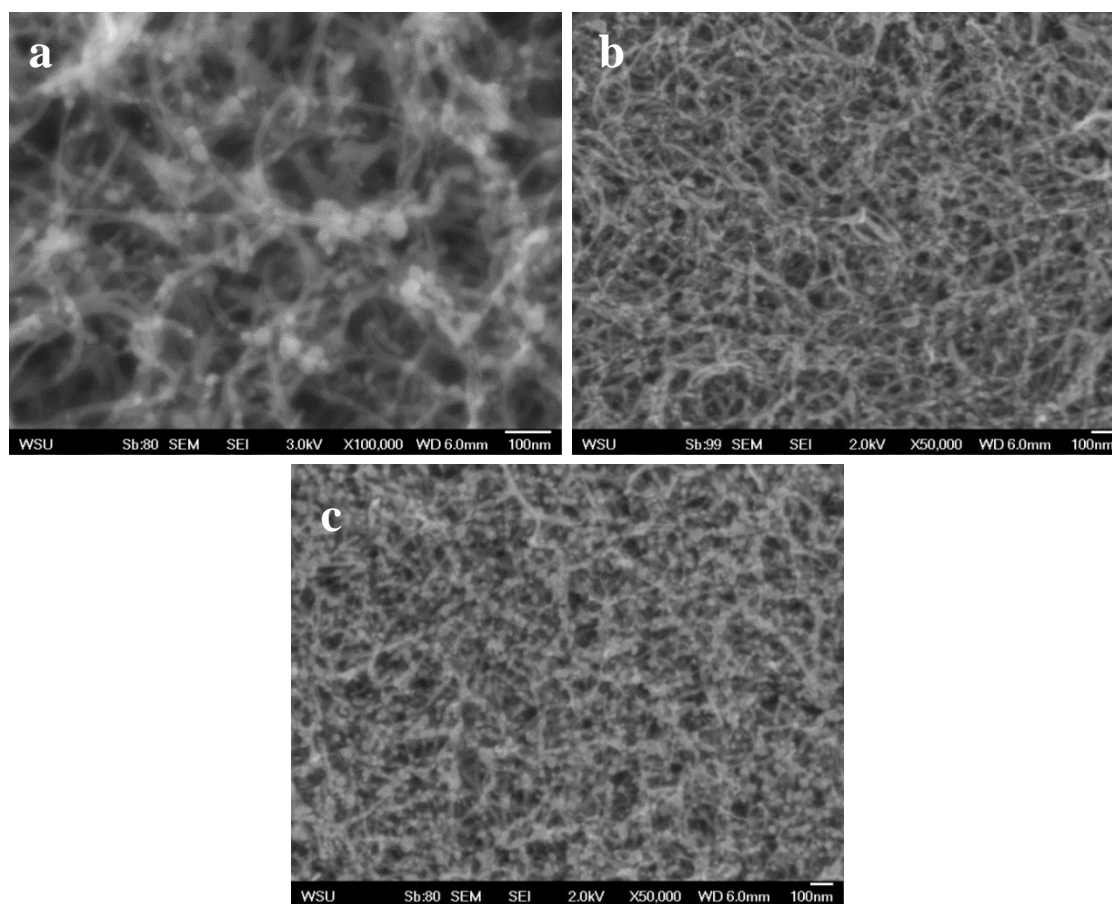


Figure 6.5 SEM micrographs showing Pd-NPs fabricated on CNT-grafted RVC-foam by one-coating cycle (a), two-coating cycle (b), and three-coating cycle (c), processes

Table 6.1 Elemental composition obtained from EDS analysis of Pd-NPs fabricated on the Cellular foam and RVC foams with one, two, or three coating cycles.

Samples	Coating cycles	CK	OK	FeL	PdL	SiK
Pd-NPs on CNT Ce-Foam	One	72.97	2.85	2.22	21.06	0.88
	Two	53.81	1.14	1.29	43.14	0.60
Pd-NPs on CNT RVC Foam	One	92.03	3.06	1.71	3.19	-
	Two	86.24	4.10	1.91	7.75	-
	Three	83.04	4.34	2.48	10.14	-

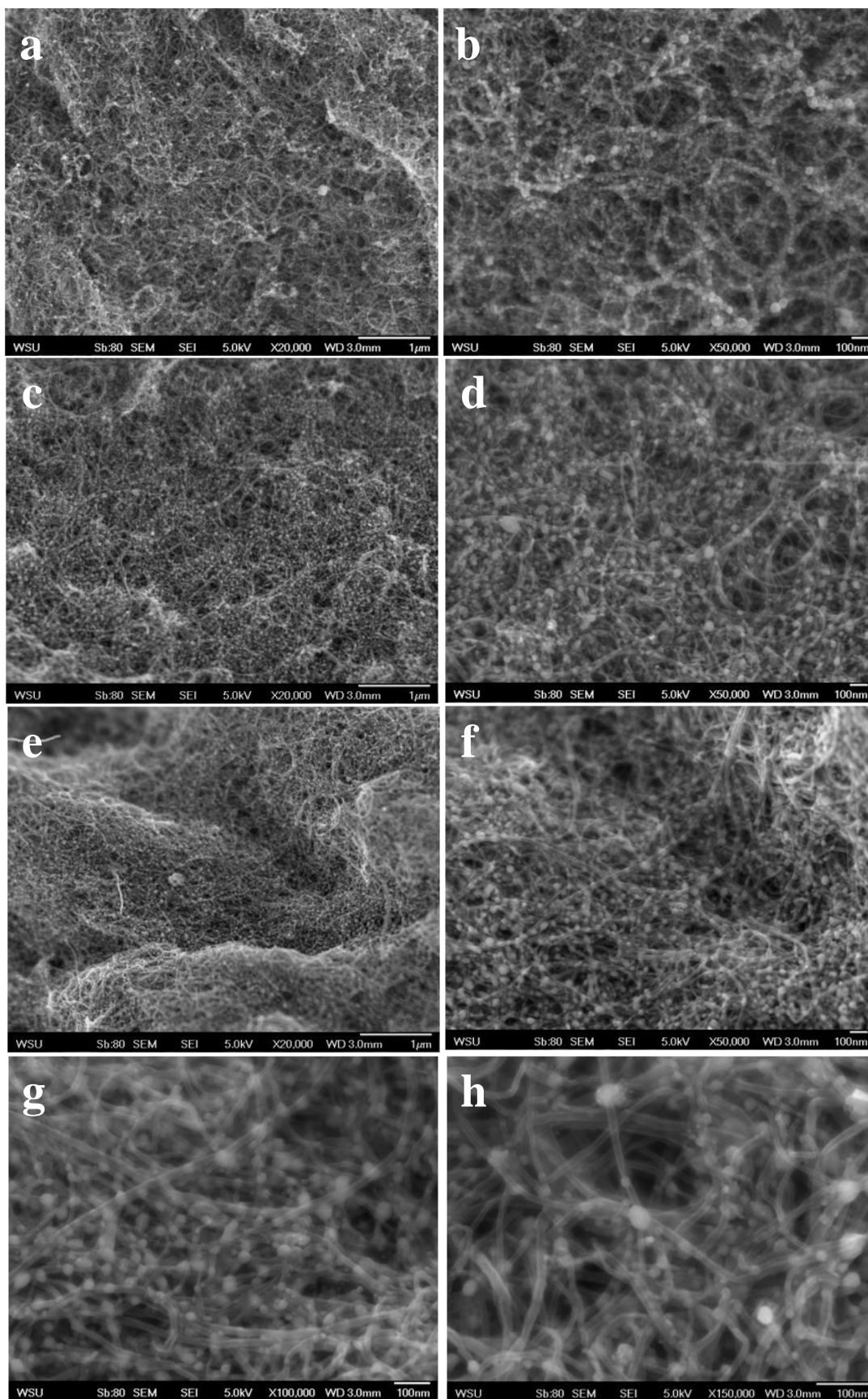


Figure 6.6 SEM micrographs of (a-b) Pd, (c-d) Pd-O₂₅₀, and (e-h) Pd-O₃₀₀ synthesized on RVC-CNT hybrid structures

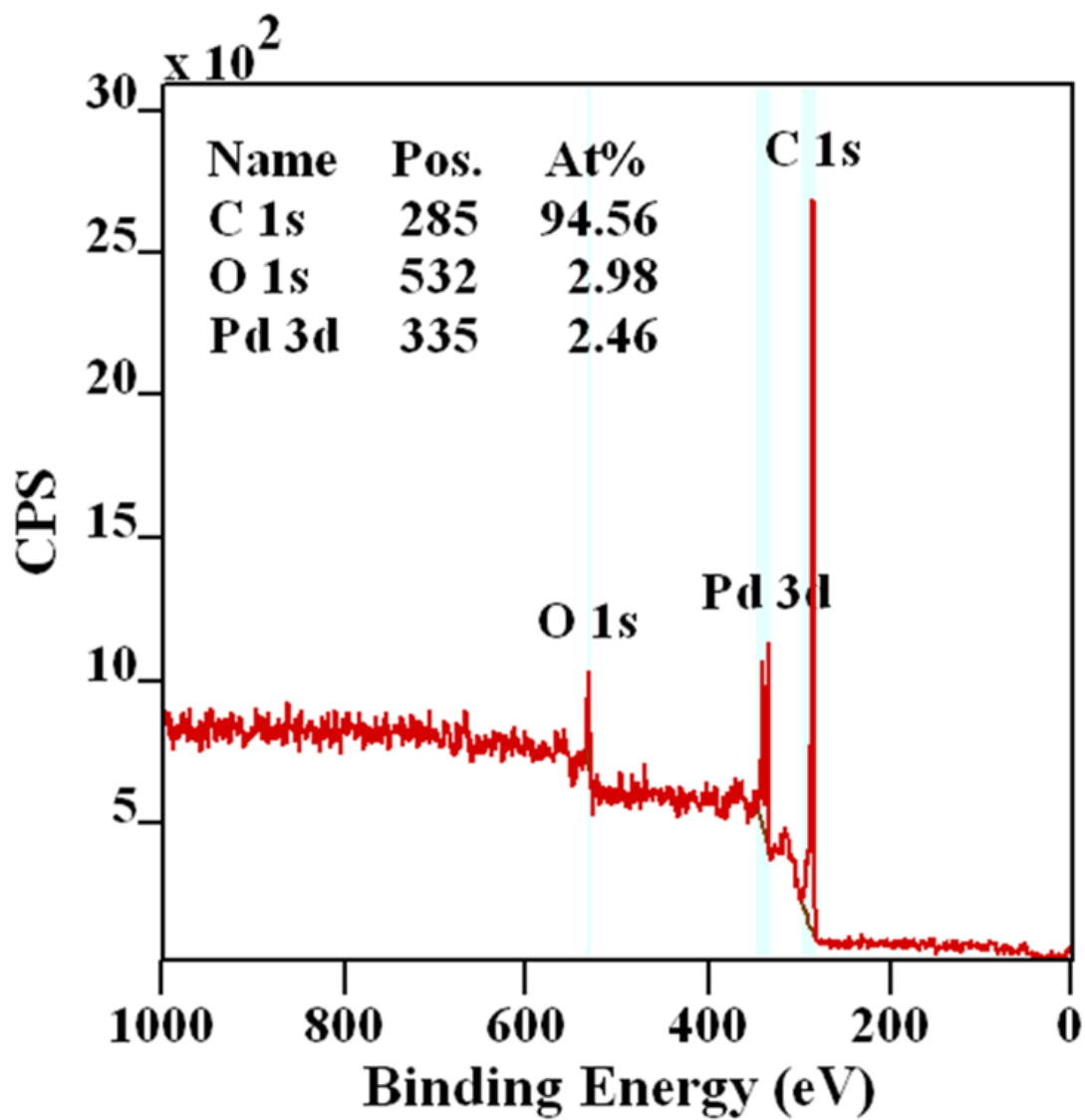


Figure 6.7 Survey scan (general scan) of as-prepared palladium nanoparticles sample

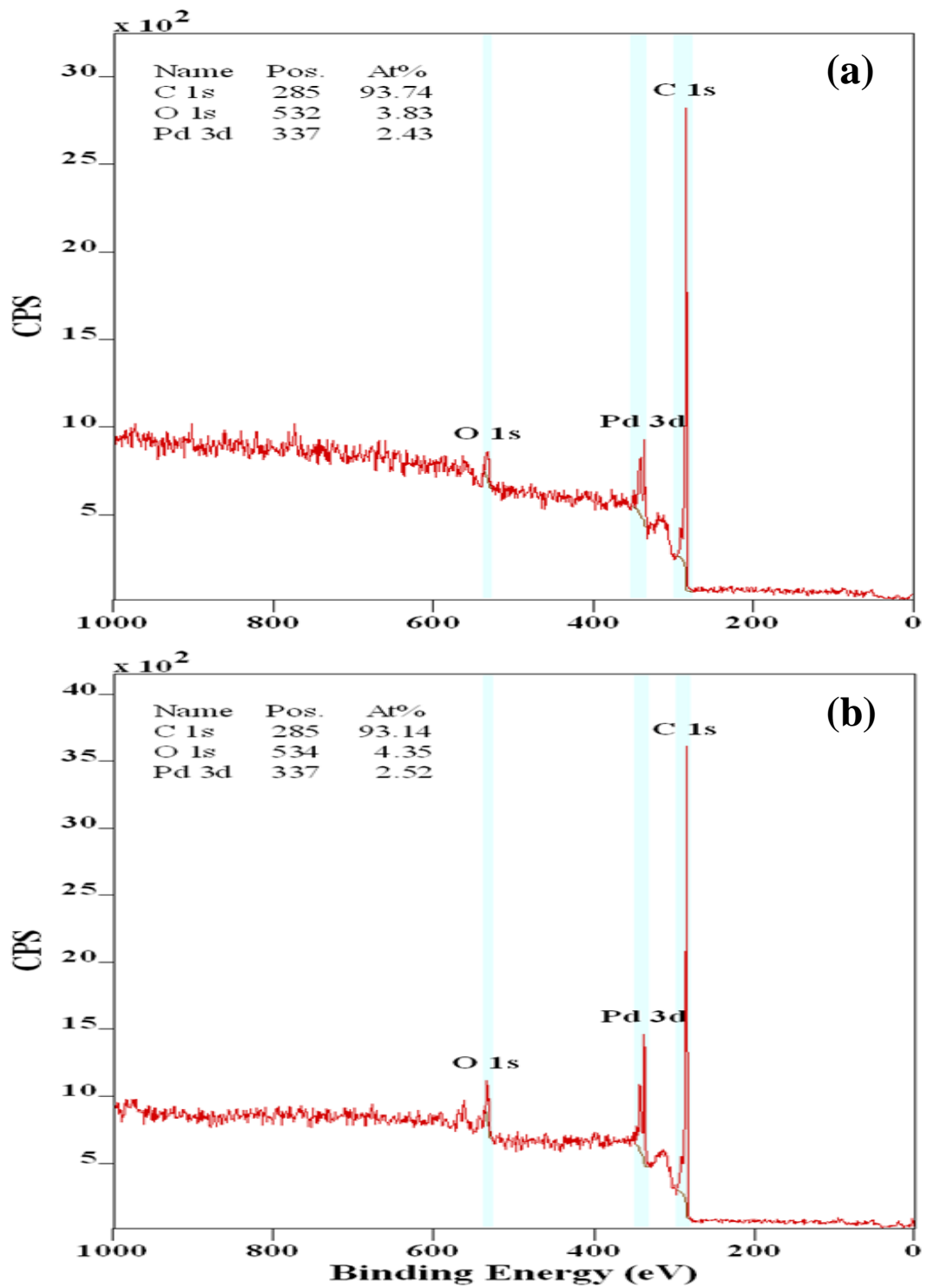


Figure 6.8 Survey scans (general scan) of oxidized palladium nanoparticles samples, (a) Pd-O₂₅₀ and (b) Pd-O₃₀₀ treated at 250 °C and 300 °C, respectively

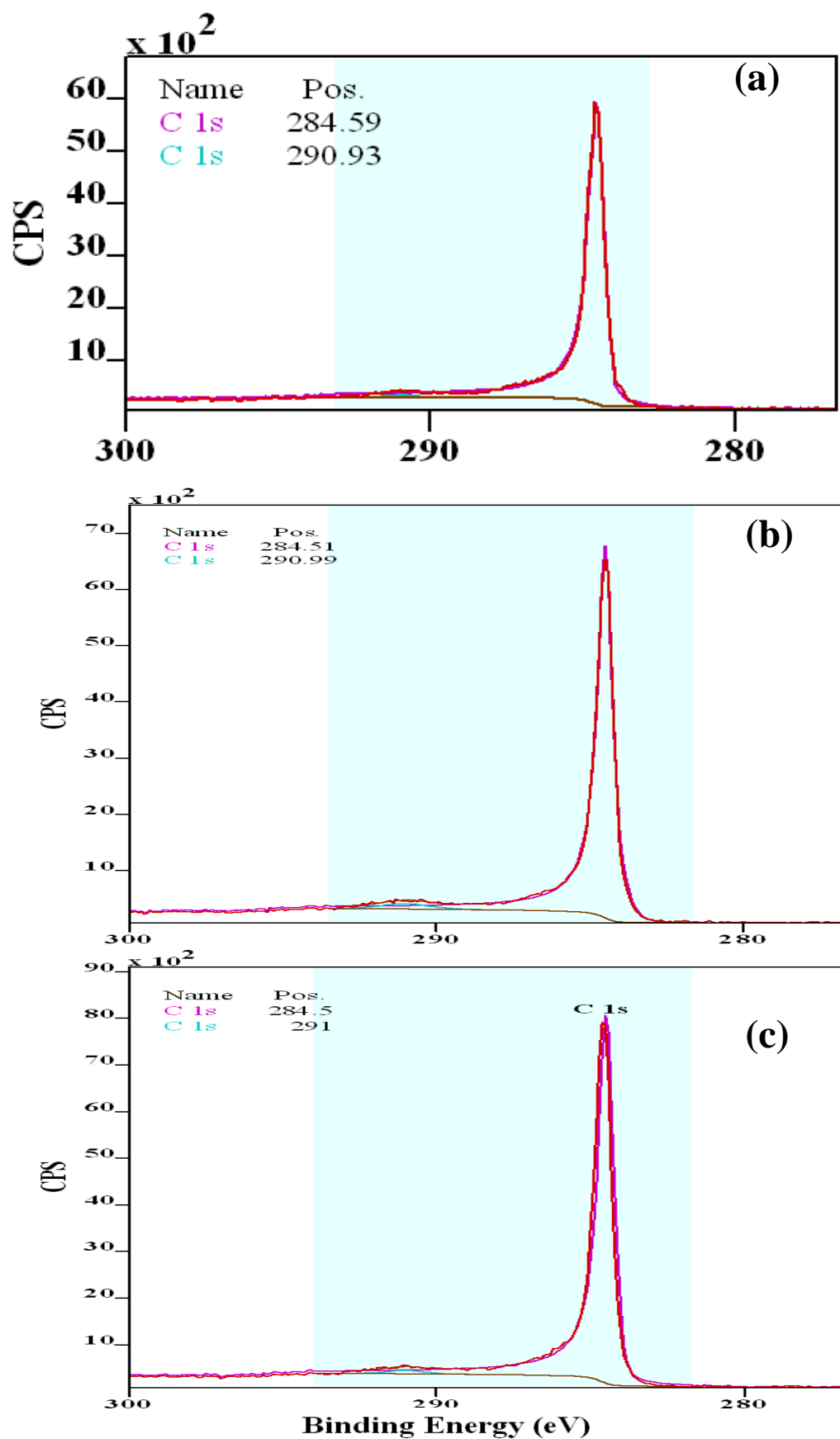


Figure 6.9 XPS C 1s peak fine-scan obtained from (a) Pd, (b) Pd-O₂₅₀ and (c) Pd-O₃₀₀ samples

Figure 6.7 and Figure 6.8 shows the XPS survey scans obtained from Pd NPs and Pd-O NPs on RVC-CNT samples. It must be pointed out that the signal/noise ratio is lower as the analysis is carried out on porous structures having irregular surfaces (at both macro and micro scales) that greatly diffuse the signals. Analysis on these samples was carried out by carefully optimizing the maximum output counts as well as by analysing multiple spots in each sample (including duplicate samples).

The peaks in the survey scan are at the characteristic positions for carbon, oxygen, and palladium peaks. The annotation in the survey scan figures shows the semi-quantitative compositional values obtained from quantifying the low resolution regions. The high resolution fine scans of these peaks were also obtained. Each fine scan was obtained by averaging over multiple sweeps to enhance the signal/noise ratio from these uneven surfaces. Figure 6.9 shows the fine scans of C $1s$ peaks for all the three samples. The prominent peak at 284.5 eV is the C-C type bonding of graphitic nature that corresponds to the CNT in the sample [16]. No iron or silica signals (precursors for CNT growth) were observed in these samples. Figure 6.10 shows the high resolution fine scan spectrum of Pd $3d$ peaks, the core level spectra of palladium, obtained from Pd-NPs samples. Figure 6.11a and Figure 6.11b shows the Pd $3d$ peaks for oxidized Pd-NPs treated at 250 °C and 300 °C, respectively. The $3d_{5/2}$ peak position for as-prepared *i.e.* reduced Pd-NPs sample is at 335.2eV, which represents the metallic palladium (Pd^0) state (Figure 6.10). For the oxidized Pd-NPs samples treated at 250 °C, the $3d_{5/2}$ peak at 335.2 eV reduces significantly and an additional peak is observed at position 336.9 eV, which represents the oxide form of palladium (Figure 6.11a) [16]. This indicates that the Pd-NPs are partially coated with an oxide layer forming PdO. The oxidized sample treated at higher temperature *i.e.* 300 °C shows a near complete oxidation of Pd (Figure 6.11b) as the $3d_{5/2}$ peak at 335.2 eV

diminishes significantly and peak at 336.9 ± 0.1 eV becomes stronger. The XPS for Pd samples treated at 300 °C for 2 hours in air environment shows that the Pd-NPs are (significantly) fully oxidized (~96%).

Figure 6.12 shows the fine scan spectrum of O $1s$ and Pd $3p$ peaks, ranging from 570 - 525 eV and it is denoted as 'O $1s$ - Pd $3p$ ' peak. It must be pointed out that the O $1s$ peak overlaps with the Pd $3p_{3/2}$ peak observed between 531 - 534 eV, whereas as the Pd $3p_{1/2}$ peak is clearly separated at ~ 560 eV. The O $1s$ peak is resolved by separating the Pd $3p_{3/2}$ components using the intensity of $3p_{1/2}$ and appropriate ' p ' orbital ratios for the Pd $3p$ peaks.

The O $1s$ – Pd $3p$ peaks of the oxidized Pd samples (Pd-O₂₅₀ and Pd-O₃₀₀) are as shown in Figure 6.12b and Figure 6.12c, respectively. It can be seen that a new oxygen (O $1s$) component appears at the lower binding energy side (~530 eV) for palladium samples after oxidization. This O $1s$ peak at 530 eV corresponds to the oxygen atoms bonded to Pd during the formation of PdO. However, there are now multiple components of Pd $3p$ also that co-exist and/or overlap within the main O $1s$ peak. For partially oxidized Pd samples, there would be two components of Pd $3p_{3/2}$ peaks (metallic and oxidized state components of Pd) as shown in Figure 6.12b. The areas of these peaks are estimated using appropriate ratios from the respective Pd $3d$ components and thus careful peak processing of Pd $3p$ and O $1s$ peak components was carried out. The preliminary atomic percentage estimates of peak components of Pd, Pd-O₂₅₀ and Pd-O₃₀₀ are shown in the Table 6.2. The low binding energy O-Pd component for Pd-O₂₅₀ and Pd-O₃₀₀, (at ~ 530 eV) increases from 0.67% to 1.32% with the increase in oxidation temperature from 250 to 300 °C. This clearly indicates more complete oxidation of Pd at 300 °C (Pd-O₃₀₀). As shown in Table 6.2, the total concentration of Pd (sum of Pd and/or Pd-O $3d$ components percent) across the three

types of samples is similar with the surface averaged Pd% of 1.34%. This data is also confirmed from EDS analysis as shown in Table 6.3, where all the three samples have similar At% of Pd (4.6%). It must be noted that because XPS and EDS have very different analysis depths and resolutions, their quantitative values are expected to be different. So, only the trends from XPS and EDS are being compared here. The EDS analysis also shows that At% of oxygen follows an increasing trend with oxidation temperature.

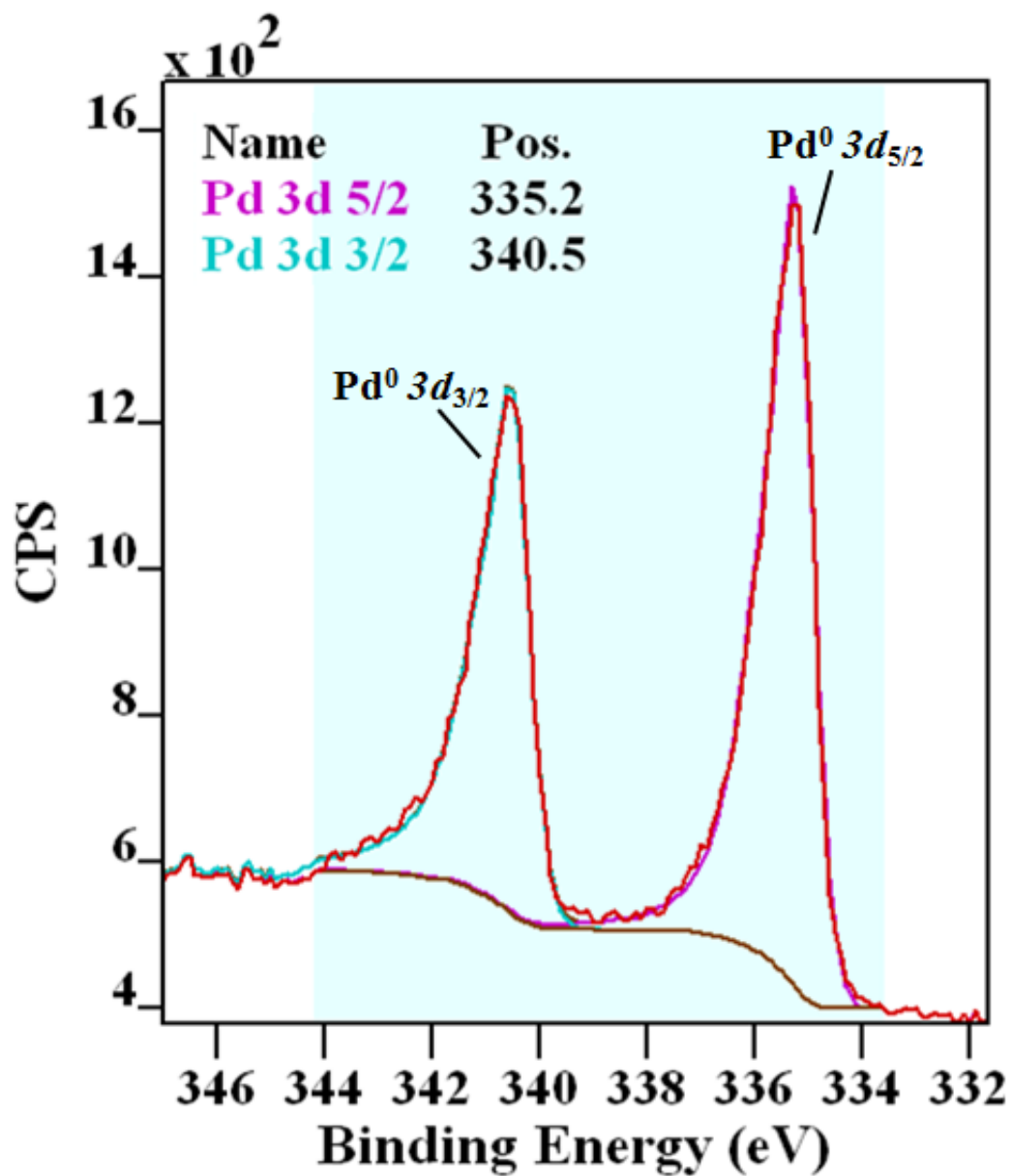


Figure 6.10 XPS fine-scan spectra of Pd 3d peak obtained from palladium nanoparticles (Pd-NPs)

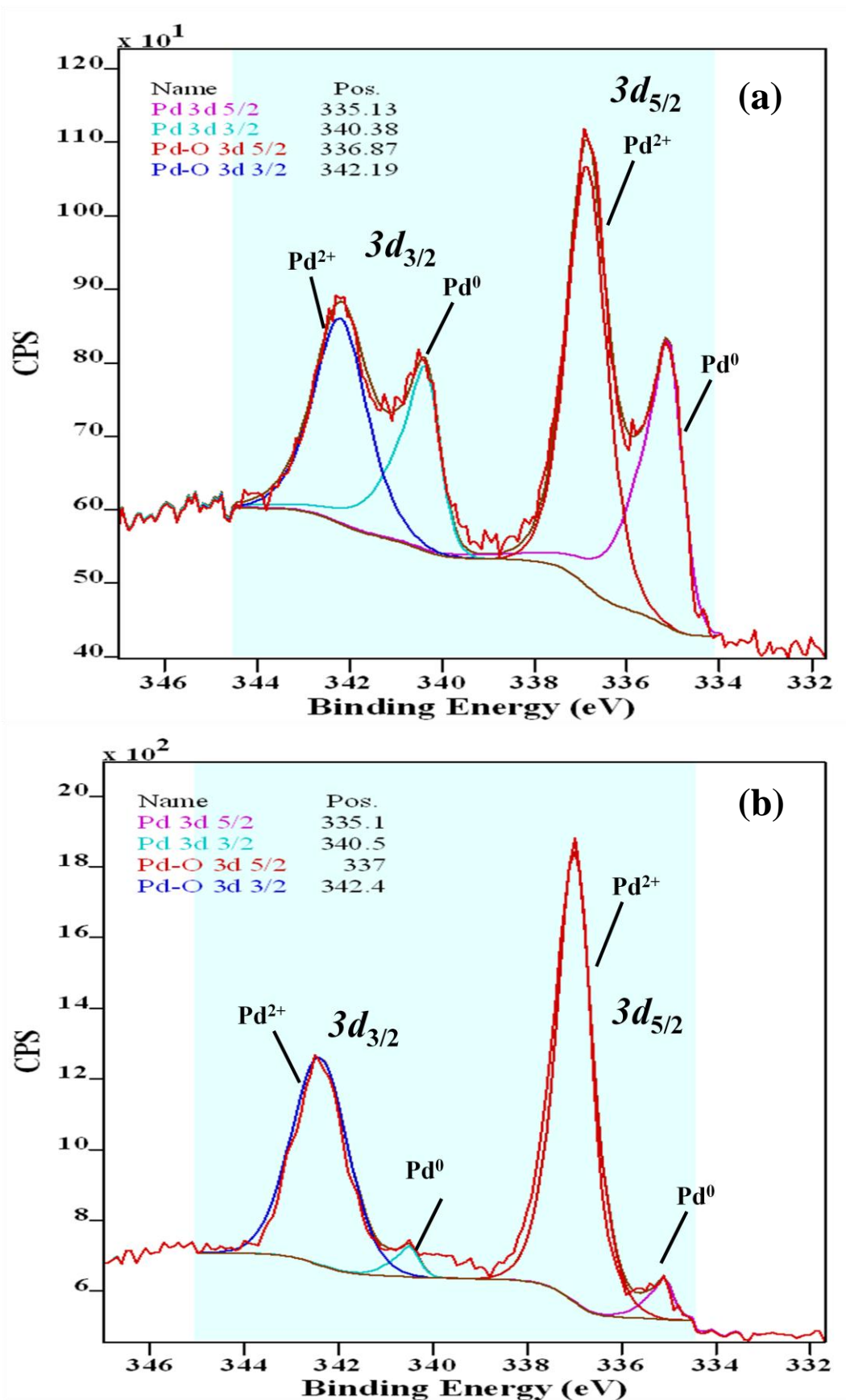


Figure 6.11 XPS Pd 3d fine-scan of samples oxidized at (a) 250 °C (Pd-O₂₅₀), and (b) 300 °C (Pd-O₃₀₀)

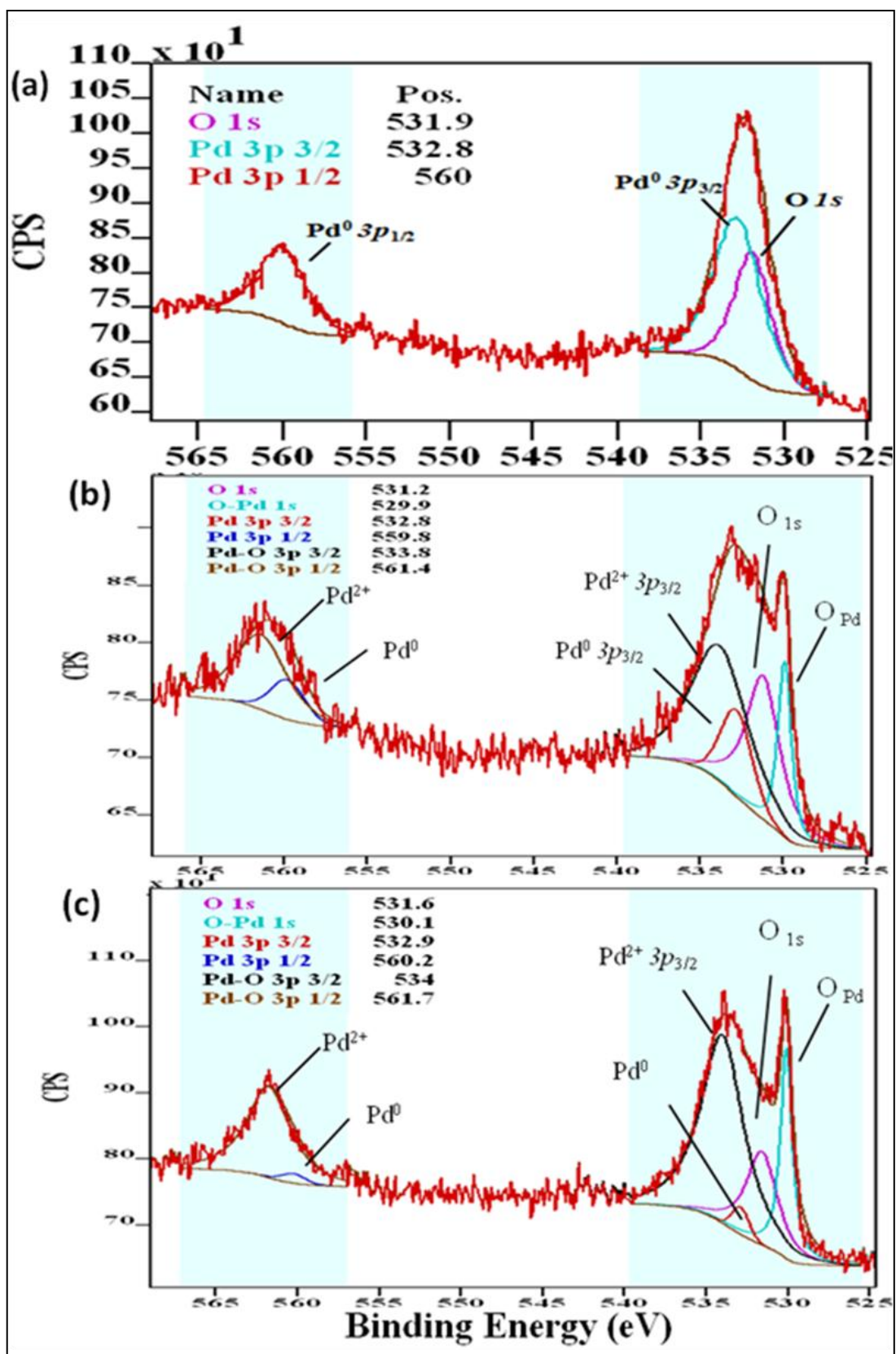


Table 6.2 Elemental chemical composition and characteristic core spectra positions of elements from Pd, Pd-O₂₅₀, and Pd-O₃₀₀ samples using XPS analysis

XPS Element Composition	Pd Sample		Pd-O ₂₅₀ Sample		Pd-O ₃₀₀ Sample	
	<i>Binding Energy, eV</i>	Atomic %	<i>Binding Energy, eV</i>	Atomic %	<i>Binding Energy, eV</i>	Atomic %
C 1s	284.5	96.45	284.9	96.61	284.4	95.94
O 1s	531.9	2.23	531.2	1.49	531.6	1.28
Pd 3d	335.2	1.32	335.1	0.40	335.15	0.07
Pd 3d – O	NA		336.8	0.84	337.0	1.39
O 1s - Pd	NA		529.9	0.67	530.1	1.32

NA- Not applicable

Table 6.3 Elemental chemical composition obtained using EDS analysis for Pd, Pd-O₂₅₀, and Pd-O₃₀₀ samples

At%	Pd	Pd-O₂₅₀	Pd-O₃₀₀
CK	91.9	91.2	91.6
OK	2.9	3.6	4.0
SiK	0.3	0.2	0.3
PdL	4.7	5.0	4.1

6.4 Conclusion

In this study, Pd-NPs and PdO-NPs were synthesized on vertically aligned carbon nanotubes attached to porous structures forming multi-scale architecture. Crystal structure investigation using X-ray diffraction of Pd-NPs indicates FCC structure. Thermal oxidation of Pd in air shows formation of oxidized palladium particles. XPS analysis shows that Pd-NPs can be partially oxidized or fully oxidized by thermal heating at 250 °C or 300 °C, respectively. The catalyst particles on hierarchical structures can provide very high surface activity for smaller and lighter components. Moreover, these nano-catalysts can be used easily for treating contaminated water treatment, as they are adhered to larger supports. This makes them reusable and eco-friendly as the NPs and the CNT are immobilized on larger porous supports.

7 Chapter 7: Bimetallic Nanoparticles: Palladium – Silver Bimetallic Nanoparticles on Hierarchical Carbon Nanostructures

7.1 Introduction

As discussed in earlier chapters (Chapter 6), metal nanoparticles have potential applications in various fields including bio-medicine, electronics, environment, catalysis, optics and optical sensing [114][115][116]. Many novel applications of metal nanoparticles as sensors, absorbents, ceramics, and/or catalysts are governed by their size, structure, and surface chemical properties. These applications are dependent on the characteristics properties of the metal nanoparticles. Assembling two or more types of metals in the same nanoparticle can improve their chemical and structural properties. Bimetallic or multi-metallic nanoparticles can advance the current cutting-edge technologies by constructively enhancing their characteristics [123]–[125].

In this study, Ag/Pd bimetallic nanoparticles on CNT-Foam structures were synthesized by subsequent synthesis of silver on the as-prepared palladium nanoparticles-CNT hybrids. This was achieved by thermal reduction of a palladium precursor (tetraamine palladium nitrate) to form Pd-NPs followed by chemical reduction of silver nitrate on as-prepared Pd-NPs using dimethyl-sulfoxide and tri sodium citrate as reducing/stabilizing agents [16], [18], [103], [104].

7.2 Experimental

7.2.1 Materials

All the reagents used in this study were of analytical grade and used without further purification. These include Tetra-amine Palladium (II) Nitrate solution (TAPN, 99.9%, 5% Pd, Alfa-Aesar Ltd.), Silver Nitrate (AgNO_3 , 99.99%, Sigma Aldrich Ltd.), Dimethyl sulfoxide (DMSO, 99.5% Sigma Aldrich Ltd.), and Tri sodium citrate ($\text{Na}_3\text{C}_6\text{H}_5\text{O}_7$, 99%, MP bio Ltd.). Other materials are de-ionized water (DI water), and laboratory grade methanol. Ultra high purity hydrogen gas (H_2 , 99.999%), and laboratory purity argon gas (Ar) were used.

7.2.2 Synthesis of Silver-Palladium Bimetallic Nanoparticles

In this study, Ag/Pd bimetallic nanoparticles on CNT-Foam structures were fabricated by synthesis of palladium followed by subsequent synthesis of silver on the as-prepared Pd-CNT-Foam structures. The CNT-Foam structures used in this study are CNT on RVC structures obtained by growing CNT for 40 minutes as described in Chapter 3 and Chapter 4.

Initially, palladium was synthesized on the CNT-RVC foams using the thermal reduction process [16], [18] as discussed in Section 2.3.2. The CNT-foam samples were infiltrated with tetraamine palladium (II) nitrate solution (62.5 mM TAPN) for 120 mins followed by thermal treatment and reduction steps using hydrogen gas as the reducing agent (described in detail in section 2.3.2) to form Pd-NPs on CNT-Foams.

Consequently, silver was synthesized using a pre-developed chemical reduction process developed in as reported by [103], [104]. The process involves infiltration of the support with AgNO_3 precursor solution followed by in-situ chemical

reduction using sodium citrate and DMSO. The details of silver deposition on Pd-NPs CNT-foam supports are described as follows.

The silver synthesis process is carried out in a dark room to avoid degradation of silver nitrate under visible light [103], [104]. Silver nitrate of a known concentration (0.72 M AgNO_3) is used as a silver precursor solution. As-prepared Pd-NPs CNT samples are wetted by rinsing with methanol and DI water, and are then immersed in an aqueous precursor solution of AgNO_3 for 12 hours. The solid supports are recovered from the silver solution and the excess non-interacting solution on the sample is washed-off by briefly dipping the support in methanol. The AgNO_3 adsorbed sample is now is treated chemically to reduce it to form silver

In-situ chemical reduction method was carried out using DMSO and Tri sodium citrate in a 25 mL pyrex glass beaker under dark room conditions. Initially, 15 mL DMSO was heated to 60 °C on a hot plate and 5 mg of tri sodium citrate was added to the DMSO (1 mM Citrate). The as-prepared Pd CNT sample was immersed in the beaker containing DMSO and 1 mM citrate solution. Continuous stirring was carried out using a stir bar and the temperature was maintained at 60 °C. The reactions were allowed to take place for 2 hours. As the reactions occur, *i.e.* the AgNO_3 is reduced to silver; the colorless DMSO-citrate solution changes its color. The samples were removed from the solution after 2 hours and rinsed with DI water followed by air drying for 24 hours.

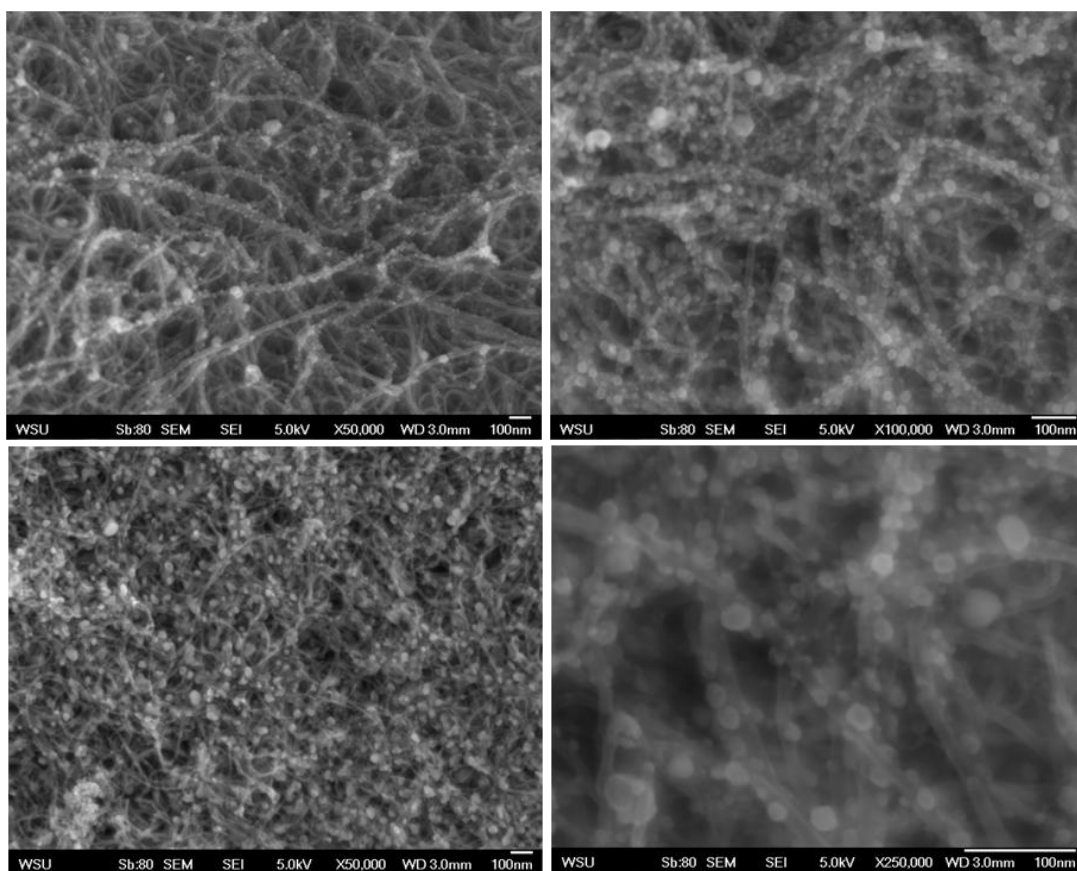


Figure 7.1 SEM micrograph of Pd-NPs attached on CNT-RVC foam samples

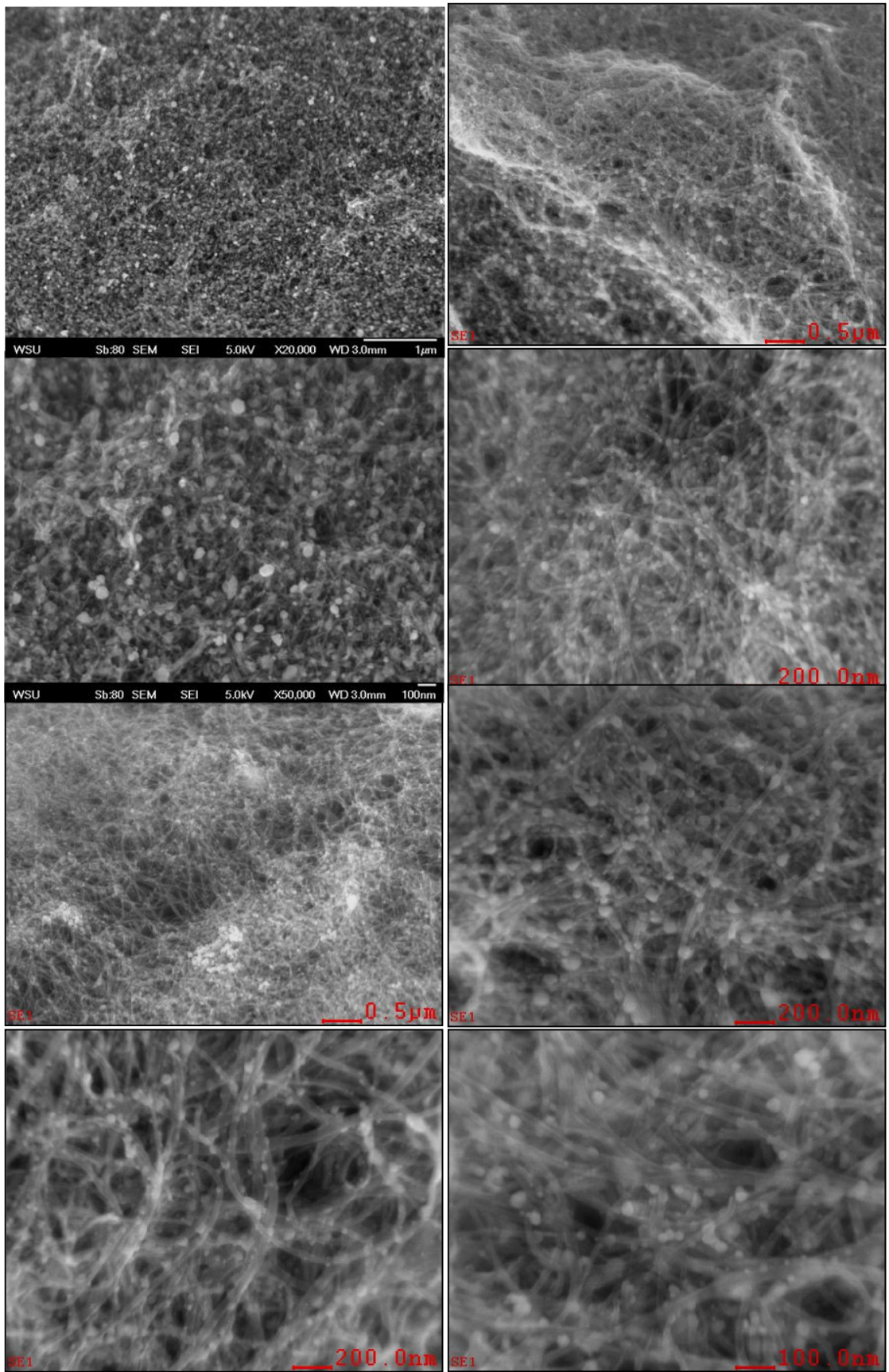


Figure 7.2 SEM micrographs of Ag coated Pd-NPs attached on CNT-RVC foam samples (Ag-Pd NPs)

7.3 Results and Discussion

Figure 7.1 shows SEM micrographs for the microstructure of Pd-NPs on CNT-foams and Figure 7.2 shows the microstructure of Ag-Pd nanoparticles on CNT foam structures. The SEM images do not show any significant difference in the silver and palladium particles.

Figure 7.3 shows the XPS survey scans obtained from Ag-Pd NPs on RVC-CNT samples. It must be pointed out that as the analysis is carried out on porous structures the noise to signal ratio is high. XPS analysis was carried out for multiple spots in a sample (including duplicate samples).

The peaks in the survey scan (Figure 7.3) are at the characteristic positions for carbon, oxygen, palladium, and silver. The annotation in the Figure 7.3 shows the semi-quantitative values for surface compositions obtained from quantifying regions of the low resolution survey scans. The high resolution fine scans of these peaks were also obtained. Figure 7.4 shows the fine scan of C 1s peaks obtained from Ag-Pd on RVC-CNT sample. The prominent peak at 284.5 eV is the C-C type bonding of graphitic nature that corresponds to the CNT in the sample. Figure 7.5 shows the high resolution fine scan spectrum for the core level of silver and palladium, the Ag 3d peaks and Pd 3d peaks respectively. The Ag 3d_{5/2} peak position is at 368.3 eV as shown in Figure 7.5a. It must be noted that it is not possible to determine the oxidation state of Ag from the 3d_{5/2} peaks, because the peaks for the Ag and Ag-O are within 0.3 eV of each other [104]. The O 1s component is discussed in next paragraph. The Pd 3d_{5/2} peak position is at 335.2 eV as shown in Figure 7.5b, which represents the metallic palladium (Pd⁰) state (Figure 6.10) [16], [18].

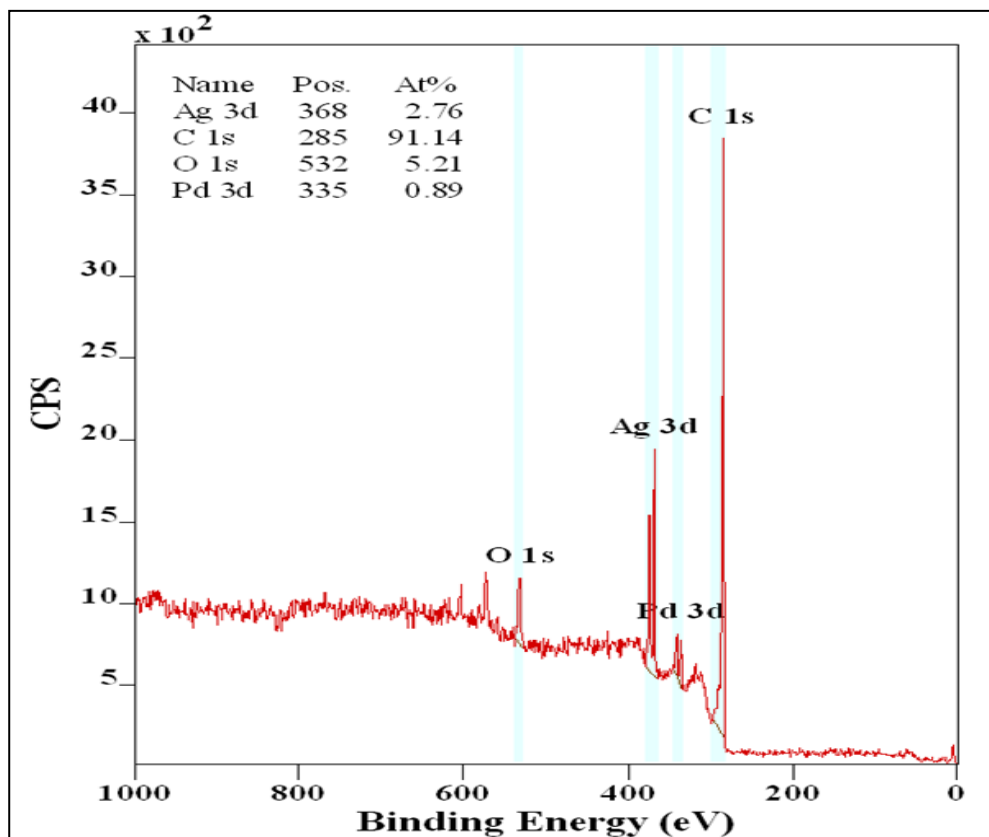


Figure 7.3 XPS survey scan (general scan) of Ag-Pd bimetallic nanoparticles on RVC-CNT foam samples

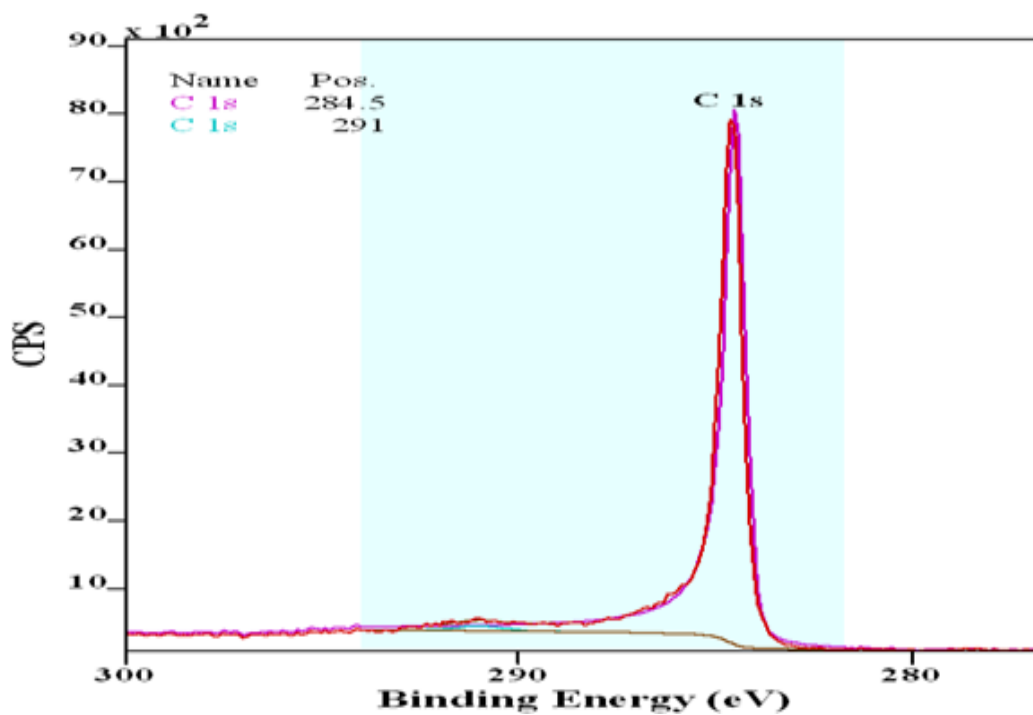


Figure 7.4 XPS C 1s fine-scan obtained from Ag-Pd bimetallic nanoparticles on RVC-CNT foam samples

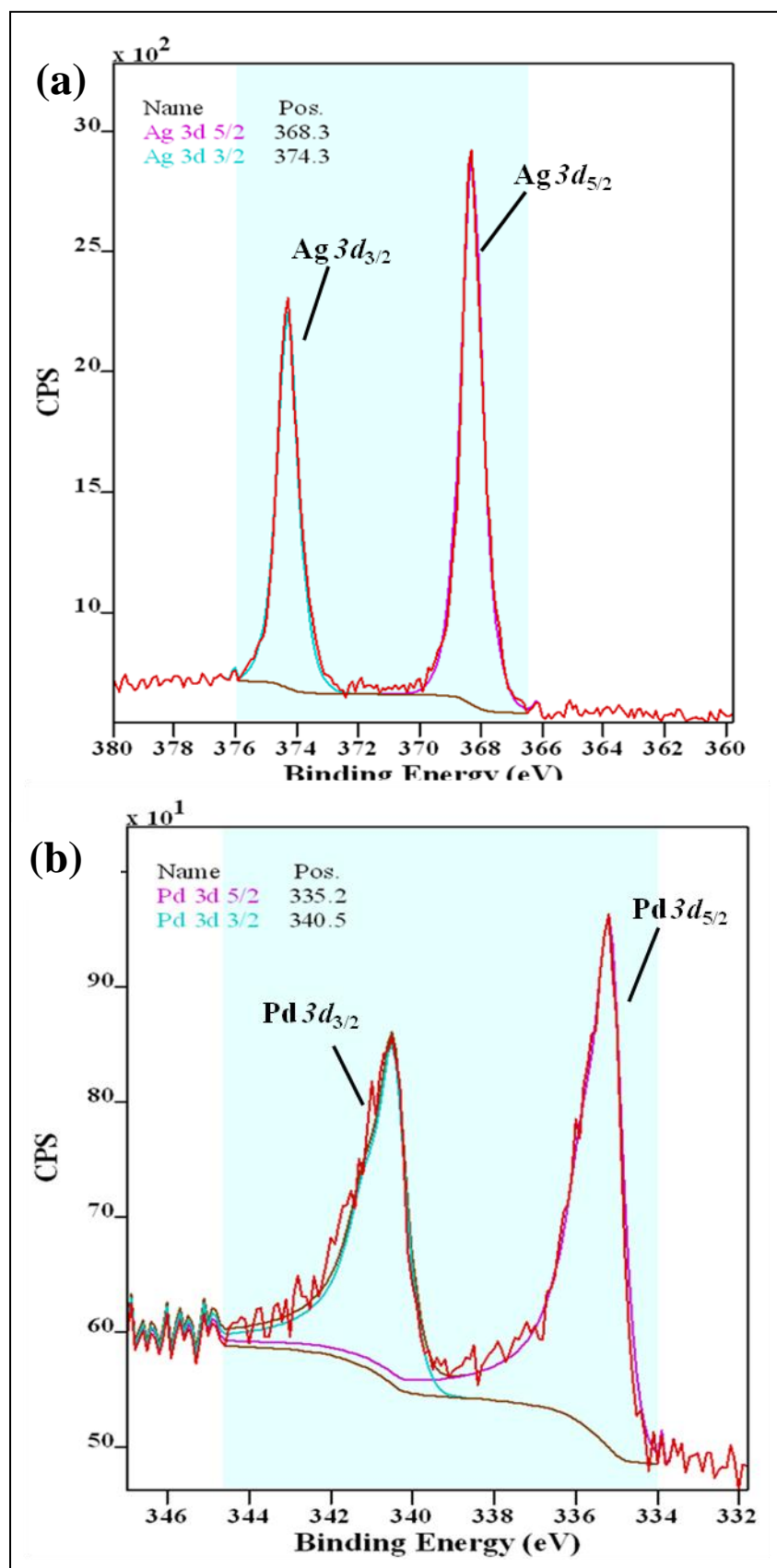


Figure 7.5 XPS fine scan spectra of (a) Ag 3d and (b) Pd 3d obtained from Ag-Pd bimetallic nanoparticles

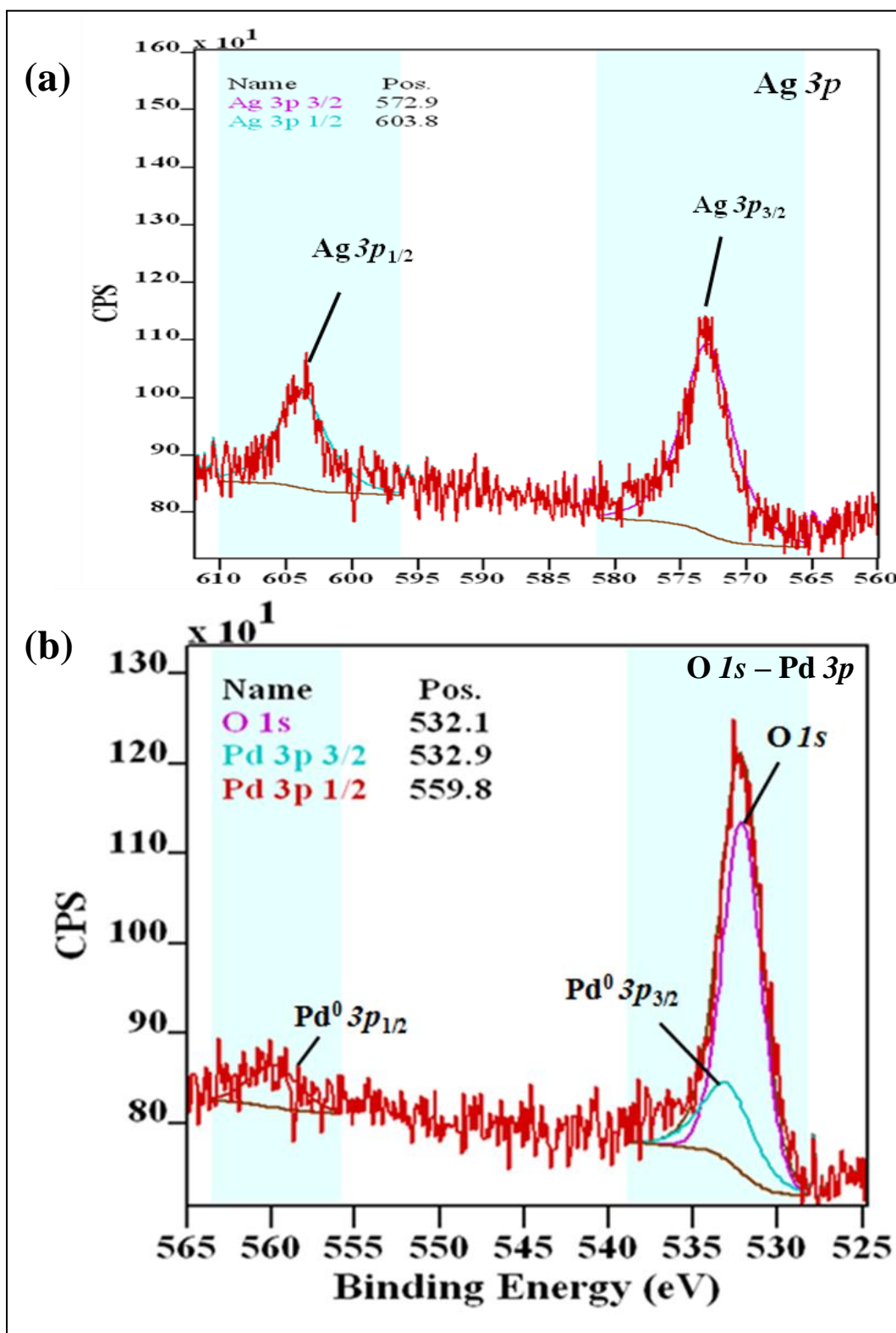


Figure 7.6 XPS fine scan spectra of (a) Ag 3p, and (b) O 1s – Pd 3p obtained from Ag-Pd bimetallic nanoparticles

Figure 7.6a shows the fine scan spectrum of Ag $3p$ peaks, where the Ag $3p_{3/2}$ is at 572.9 eV. Figure 7.6b shows the fine scan spectrum of O $1s$ and Pd $3p$ peaks, ranging from 570 - 525 eV. As discussed earlier in section 6.3.4, the Pd $3p_{3/2}$ peak for a Pd sample overlaps with the O $1s$ peak as shown in Figure 7.6b. The $3p_{3/2}$ component is processed using the intensity of $3p_{1/2}$ and 'p' orbital ratios as discussed in chapter 6 (section 6.3.4). For the Ag-Pd sample no additional O $1s$ component was observed indicating that there may not be any noticeable Ag-O signal. As reported in literature [119], [120], Ag-O bond should have an O $1s$ component at low binding energy side in the 528 – 530 eV energy range.

The atomic percentage of the elemental compositions obtained from the XPS peak area analysis of fine-scan spectrums are shown in the Table 7.1. It must be noted that the XPS peaks are extremely surface sensitive, and signals are averaged over large areas of very uneven surface morphologies, so the absolute concentrations need further analysis. The trends of how these peaks change with processing provide useful insights. The surface fractional content of Pd (calculated from the Pd $3d$ peak area) decreases from 1.3% to 0.52% after silver deposition. This may indicate covering of the Pd surfaces with Ag film, resulting in loss of XPS signal from Pd.

The EDS analysis results of Pd and Ag-Pd bimetallic samples are tabulated in Table 7.2. The At% of Pd in Ag-Pd samples is ~ 6.3% and that of silver is ~ 1.3% (4 to 5 times less). Moreover, the Pd concentration is not reduced by silver deposition, unlike seen in the signals from XPS surface analysis. This is because, whereas XPS provides data from only few nanometers in the surface, the EDS analysis provides elemental composition of the surface depth of up to few microns in the sample, larger than the size of Pd nanoparticles. Combining XPS and EDS results, it can be concluded that in Ag-Pd bimetallic samples the Pd-NPs are coated with a layer of

silver, creating core-shell type of structure. Further investigation involving HRTEM and XRD can reveal more details of these bi-metallic nano-particles.

Table 7.1 Elemental chemical composition and characteristic core spectra positions of elements from Pd and Ag-Pd bimetallic samples using XPS analysis

XPS Element Composition	Pd CNT Sample		Ag-Pd CNT Sample	
	<i>Binding Energy, eV</i>	Atomic %	<i>Binding Energy, eV</i>	Atomic %
C _{1s}	284.5	96.45	284.5	92.87
O _{1s}	531.9	2.23	532	4.21
Pd _{3d}	335.2	1.32	335.2	0.52
Ag _{3d}	NA		368.3	2.40
Ag - Pd _{3d}	NA		ND	

NA – Not applicable; ND – Not detectable

Table 7.2 Elemental chemical composition obtained using EDS analysis for Pd and Ag-Pd bimetallic on RVC-CNT foam samples

EDS Analysis	Pd Sample At%	Ag-Pd Sample At%
CK	91.9	87.0
OK	2.9	4.4
SiK	0.3	0.9
PdL	4.7	6.3
AgL	NA	1.33

NA – Not applicable

7.4 Conclusion

In this study, silver was deposited on palladium nanoparticles attached to vertically aligned carbon nanotubes and porous structures. This deposition coating was carried out to form Ag-Pd bimetallic nanoparticles forming multi-scale architecture. Microstructural and Surface chemical characterization was carried out using SEM, EDS, and XPS. The SEM microstructure analysis does not show any detectable variation in the Ag and Pd samples. The EDS analysis shows that Pd is present in high amount in the sample, where as the XPS analysis shows a low concentration of Pd that accounts for less Pd on the surface. A similar trend was observed with Ag concentration, indicating that a layer of silver is coated on Pd-NPs surfaces. High resolution TEM or XRD characterization is required to confirm the formation of bimetallic nanoparticles. The Ag-Pd nanoparticles on CNT foam structures were employed in this study for catalytic degradation of chlorinated contaminants that are discussed in later chapters. The catalytic activity of palladium and silver-palladium catalysts - Pd, PdO, and Ag-Pd nanoparticles structures were also investigated (Chapter 9).

8 Chapter 8: Catalytic Dechlorination of Trichloroethylene and Trichloroethane using Palladium Based Catalysts

8.1 Introduction

Halogenated hydrocarbons are organic contaminants that are commonly present in soil and groundwater across the globe and they are of great concern worldwide. Ground water contamination by halogenated organic compounds such as chlorinated organic compounds (COCs), which include chlorinated alkanes, alkenes, halo-aromatics, and chloro-flouro hydrocarbons (CFCs) have harmful effects on the environment and human health. The common chlorinated hydrocarbon compounds (CHCs) that contaminate the soil, water, and air environment in large quantities include Carbon tetrachloride, Trichloroethylene, and Trichloroethane. These chemicals have widespread industrial applications and therefore are easily released into the environment. Due to their toxicity and green house effects, strict restrictions have been posed on the usage and disposal of such chemicals [126], [127]. They also posses high resistance to biological degradation and are able to easily migrate into ground water and atmosphere, thereby contaminating the environment on the whole. Therefore, many treatment methods have been developed to remove COCs from the environment [66], [128].

The traditional techniques used for the removal of CHCs include combustion, adsorption, and osmosis. However, for toxic contaminants these techniques are not very effective and may require additional steps for disposing of the recovered contaminants. Researchers are exploring more ecologically and economically friendly techniques to remove these toxic chemical compounds from soil and water. A widespread approach is to selectively degrade the toxic chemical compounds into

smaller daughter products that are less toxic or non-toxic. Degradation of such chlorinated compounds can be done with the aid of catalyst material such as transition metals by the following processes: electrochemical dechlorination, reductive dechlorination, radiation dechlorination, and hydro-dechlorination. Use of a catalyst facilitates the removal by selective degradation pathways [128][129]. The common metals used for catalytic dechlorination of COC include platinum, palladium, rhodium, zinc, silver, gold, copper, etc.; among which, Pd is a well known catalyst for selective reduction of chlorinated carbon species. In this study, we evaluate the catalytic activity of palladium-based catalyst for dechlorination of Trichloroethylene and Trichloroethane in the presence of hydrogen gas. The dechlorination reaction involves breaking/reducing the carbon-chlorine bonds facilitated by a catalyst such as Pd which requires H₂ to catalyse the reactions. Here the molecular hydrogen initially dissociates on the catalyst surface and the hydrogen therefore replaces the chlorine in the compound that produces a reduced chlorinated compound.

Catalysis is a surface specific phenomenon, therefore supports having high specific surface area such as activated carbon, free-standing carbon nanotubes (CNT), and carbon nano-fibers (CNFs) have been extensively used for anchoring metal nanocatalysts [20][130]. For heterogeneous catalysis, the reactants are in the liquid-phase and the catalyst materials although in solid-phase, are anchored on such free-standing supports in suspended form [130]. If the supported nanoparticles for treating water are in suspended form, successful recovery of the nanoparticles from the treated water can be difficult and intricate. This presents certain challenges in water treatment. If the suspended nanoparticles are not recovered completely, it can be uneconomical and also pose environmental safety hazards [21], [22]. This may require further purification of the treated water thereby increasing the cost of the

system. The supports used in this study are robust porous supports that consist of high surface area carbon nanotubes strongly attached to microcellular carbon foams. The robustness, ease of handling, and structural integrity along with the high surface area of these supports surpasses currently available supports. Pd-NPs are strongly attached to the supports, thereby preventing the nanocatalyst from dispersing into the environment [16]–[18]. These types of hierarchical materials with Pd catalysts and hydrogen have already proven to be effective and successful for repeated use for degradation of carbon tetrachloride [17], [18].

The objective of this work is to demonstrate the use of a hierarchical substrate as an effective catalyst support for water treatment applications and also to evaluate the reactivity of various Pd based catalysts for dechlorination reactions. This study focuses on bench-scale investigations of catalytic reductive dechlorination of Trichloroethylene (TCE) and Trichloroethane (TCA) in the aqueous phase using carbon supported palladium catalysts. Gas chromatography was used to quantify the volatile compounds present in the gaseous samples. The effects of varying amount of palladium-based catalysts (Pd, PdO, isolated Pd) with hydrogen in the serum bottle reactor, on the kinetics of TCE and TCA degradation and the formation of daughter products are discussed. We select 5% H₂ balance N₂ as the hydrogen environment based on the previous studies [17], [18], which shows that Pd catalysts requires hydrogen to reduce chlorinated compounds and that 5% or 50% H₂ has similar effects. The Pd-NPs are one coating of Pd on CNT-RVC foam samples, the PdO sample used in this study is PdO_{300°C}, obtained by oxidizing Pd at 300 °C as described in section 6.2.4, and isolated Pd was obtained by scratching the Pd from the ceramic boat that is used in the furnace for Pd preparation.

8.2 Experimental

8.2.1 Chemicals

The chemical reagents used in this study were of analytical grade and consumed without further purification. These include Trichloroethylene (TCE, C_2HCl_3 , Fisher Scientific), 1,1,1 -Trichloroethane (TCA, $C_2H_3Cl_3$, Fisher Scientific), 1,1 - Dichloroethane (DCA, $C_2H_4Cl_2$, Fisher Scientific), and 2-propanol (99.9%, HPLC Grade, Fisher Scientific). The water used in this study was MiliQ DI water that has resistivity of 18 Megaohm-cm ($M\Omega$ -cm). Other materials are laboratory grade high purity gases that include 5% H_2 balance N_2 . Gas-tight syringes (Hamilton, Inc.) and end-to-end rotators at 60 rpm (Glas-Col®) were used. The pH of buffer solution was monitored using a pH meter (HACH®, HQ 411d pH/mV). Teflon-lined butyl rubber stopper (PTFE-lined) of size 20 mm and aluminium crimp were purchased from Wheaton Inc.

8.2.2 Stock Solution and Standards

The stock solutions of chlorinated hydrocarbons (CHCs) such as TCE (182.5 mg/L) and TCA (165 mg/L) were separately prepared in 160 mL glass serum bottle filled completely with MilliQ water. These were securely capped with Teflon-lined butyl rubber stoppers and sealed with aluminum crimp leaving no headspace. The TCE in liquid phase is known to be sensitive to light and therefore the clear serum bottles were wrapped with Aluminum foil. To make the stock solution, 20 μ L of free-phase CHCs compound was injected into the 160 mL serum bottle. The stock solution serum bottles were equilibrated prior to use by rotating on a rotary shaker for 48 to 72 hours.

CHCs standards as the gaseous analytical standards were prepared in 60 mL amber colour serum bottles by adding 36 mL MilliQ water leaving 24 mL of air headspace volume, so as to maintain the water to headspace ratio of 60:40. The serum bottles were sealed with Teflon lined stoppers and Al-crimps. Standards were prepared for concentrations ranging from 0.1 mg/L up to 10 mg/L, without H₂ purging (sealed in ambient air) and with H₂ purging (purged with 5% H₂ balance N₂ gas for 20 mins) into the serum bottles. Measured amount of stock solution was injected into the sealed serum bottles using appropriate volume micro-syringes. 100 µL volume of gas samples were extracted from the headspace of each reactor using a Hamilton© gas-tight syringe and analyzed on gas chromatography-mass spectrometry (GC-MS). The known concentration of CHCs in both liquid and gaseous phase was calculated using the ideal gas law equation and their Henry's constant at 25 °C. The Henry's constant values were obtained from USEPA [131], [132]. The stock solutions and standards for the expected daughter products (1,1-dichloroethane) were also obtained similarly. The standard calculation and analysis of the CHCs and the daughter products are shown in Table B.1 and Table B.2 of Appendix B.

8.2.3 Batch Experiments

The dechlorination of TCE and TCA was carried out in a batch reactor system of 60 mL amber colour glass serum bottles. Since, TCE is sensitive to light, amber colour serum bottles were used for these batch experiments. The catalyst foam samples (~25 mg) were attached to the sides of the serum bottle using a double sided carbon tape. MilliQ de-ionized water (36 mL) was added to the reactors, maintaining the solution to headspace ratio of 60:40. The reactors were sealed with Teflon-lined butyl rubber septa and aluminum crimp. For hydrogen purging experiments, the reactors were then purged with a gas mixture of nitrogen and hydrogen (95% N₂ - 5%

H₂, 40 kpa, 0.05 atm) for 20 minutes. Appropriate amounts of CHCs from the stock solution were injected into each batch reactor using a gas-tight syringe and the time was recorded as the reaction initiation time. The bottles were spun on an end-to-end rotary shaker (60 rpm, 45° inclination), at room temperature. The reactors were rotated so as to minimize the liquid-gas mass transfer effects and were maintained at a certain angle so that the samples attached on the walls of the reactors remain in the solution at all times. No mass transfer limitations from liquid to gaseous phase were assumed i.e. equilibrium was attained rapidly. 100 µL of the gaseous samples were removed from the headspace of the reactor at various intervals using a gas-tight glass syringe and were analyzed instantly by direct injection into the inlet port at the front injector of gas chromatograph (GC). The injection port was maintained at a temperature of 150 °C. GC was equipped with a MSD detector and DB-5MS capillary column. High purity He gas was used as a carrier with a flow rate of 1 mL/min.

Batch degradation experiments were carried out for TCE analysis and TCA analysis separately by the above mentioned method using various Pd-based catalysts with and without the H₂ purging. These experiments were repeated for validation of the data. A repeatability test was also done to determine the stability of the Pd and PdO catalysts.

8.3 Results and Discussion

8.3.1 Trichloroethylene (TCE) Experiments

The dechlorination reactions of Trichloroethylene using a palladium-based catalyst were monitored by analysing the headspace of the reactors using GC-MS. The GC is equipped with a mass selective detector (MSD), which provides the capability of detecting the compound by its ionizations and molecular weights. TCE

standards of varying concentration and samples of unknown concentration were analyzed using headspace GC-MS analysis and the compounds were detected using the library. Catalytic dechlorination reactions of TCE using Pd-based catalysts were carried out for initial concentrations of 1 mg/L and 5 mg/L (ppm) *i.e.* for total initial mass of TCE in the bottle of 0.278 μ moles and 1.389 μ moles, respectively.

Figure 8.1 shows the calibration curves obtained from the GC-MS analysis of standards and by plotting the area of TCE peaks with the known mass in the bottle (ranging from 0.028 to 1.389 μ moles). The curve shows excellent linearity with the regression coefficient close to 1, $R^2 \sim 0.99$. The calibration curve equation is used for determining the concentration of TCE in the headspace of the reactor with H_2 and without H_2 purging. Calibration curves were obtained for every experiment.

Figure 8.2 shows the degradation kinetics of TCE at an initial concentration of 1 mg/L or initial TCE mass of 0.278 μ moles obtained with following materials; (a) control (no support or catalyst), (b) RVC Foam, (c) CNT Foam, (d) Pd-Foam, (e) Pd-CNT Foam, (f) PdO-CNT Foam, (g) CNT-Foam Oxidized (h) Isolated CNTs, and (i) Isolated Pd particles. Figure 8.2a shows the reaction kinetics of TCE using different materials without hydrogen purging. It is clear from the graph that no significant degradation of TCE was observed in the reactors without the presence of hydrogen. Figure 8.2b shows the reaction dechlorination kinetics using different materials in the presence of hydrogen. It is evident from the graph that Pd based catalysts in the presence of hydrogen (Pd-foam, isolated Pd, Pd-CNT, and PdO-CNT) show improved removal rates for TCE as compared to its non-Pd counterparts (CNT-Foam, CNT-Foam oxidized, and isolated-CNT). The removal rate compares well with the formation of other compounds indicating dechlorination reactions have occurred as discussed later in this section. However, at lower initial amount of TCE (1 mg/L or

0.278 μmoles), no significant difference in dechlorination kinetics was observed for Pd-CNT and PdO-CNT (Figure 8.2b).

Figure 8.3 shows the dechlorination kinetics of TCE at an initial concentration of 5 mg/L or initial TCE mass of 1.389 μmoles in the bottle, obtained with CNT-foam, Pd-CNT foam, and PdO-CNT foam samples. As the initial concentration or amount of TCE mass increases the competition for the available catalyst sites increases, which determines the rate at which the reactions occur. In this case (at 1.389 μmoles TCE), PdO-CNT samples show increased catalytic activity in the presence of hydrogen compared to Pd-CNT. Also, the repeat experiments on these samples show similar dechlorination rates showing the effectiveness of the catalyst. The repeatability test for up to three cycles as shown in Figure 8.4, shows that the Pd and PdO on CNT can be reused effectively as catalysts for dechlorination of TCE.

8.3.1.1 Kinetic Analysis:

The reaction rate kinetics of dechlorination of TCE was fitted using Pseudo-first order rate equation as given by the linear form of the exponential mass decay equation in the following equation:

$$\ln M_t = \ln M_{t0} - k_{obs} t \quad \dots\dots (8.1)$$

Where M_{t0} is the initial mass of TCE in the batch reactor and M_t is the mass of TCE present at time t . k_{obs} is the apparent pseudo-first order rate coefficient (min^{-1}). Note that k_{obs} is the pseudo-first order rate coefficient based on the entire mass of TCE in the reactor. Since TCE degradation occurs in the aqueous phase only, the actual rate constant, k'_{obs} , is equal to k_{obs}/F_w where F_w is the fraction of total mass in the aqueous phase. Details for calculating F_w and k'_{obs} are in Burris *et.al.* [133] and are obtained using Henry's constant [131], [132] as shown in Appendix B Table B.3.

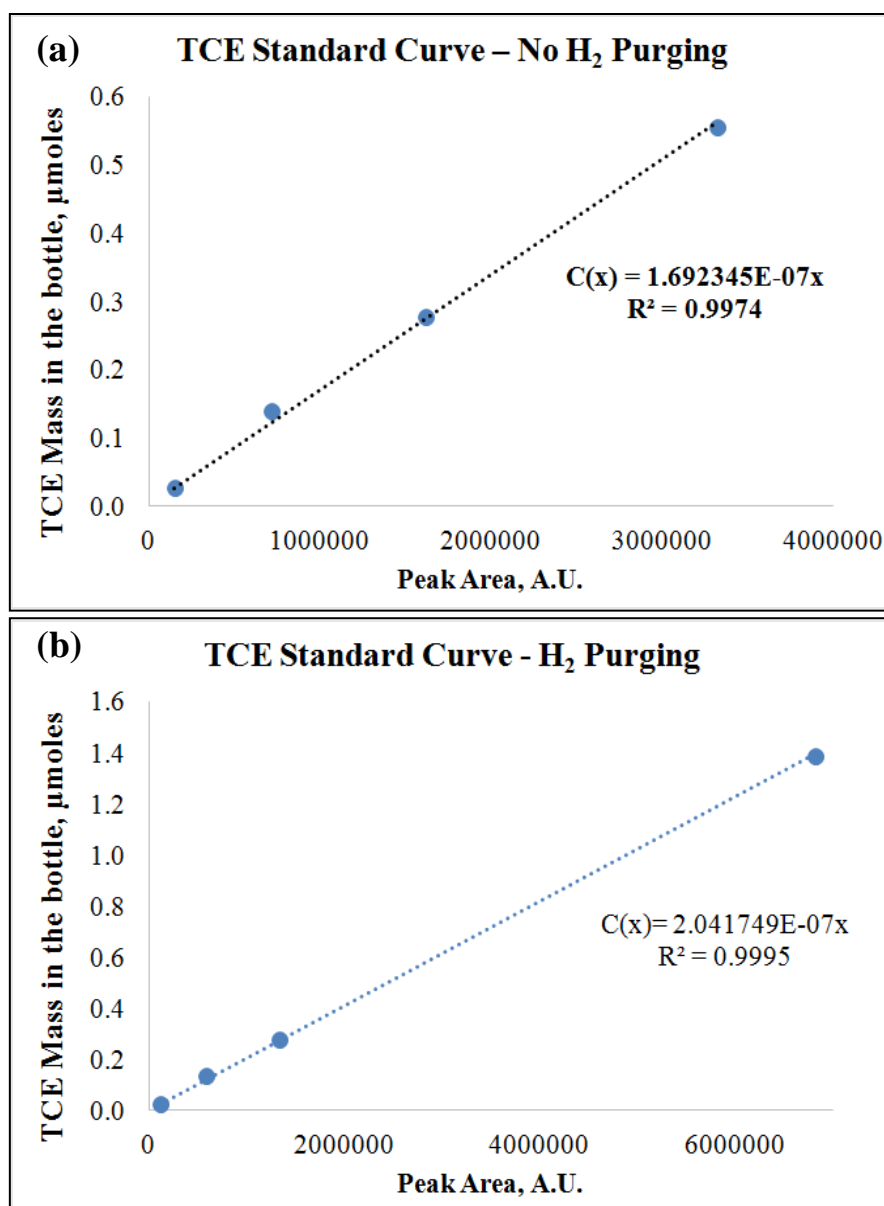


Figure 8.1 Calibration curves of TCE compound in 60 mL reactors with mass varying from 0.028 μmoles to 1.389 μmoles (a) without H₂ purging, and (b) with H₂ purging in the reactors obtained by plotting peak areas with known TCE standards

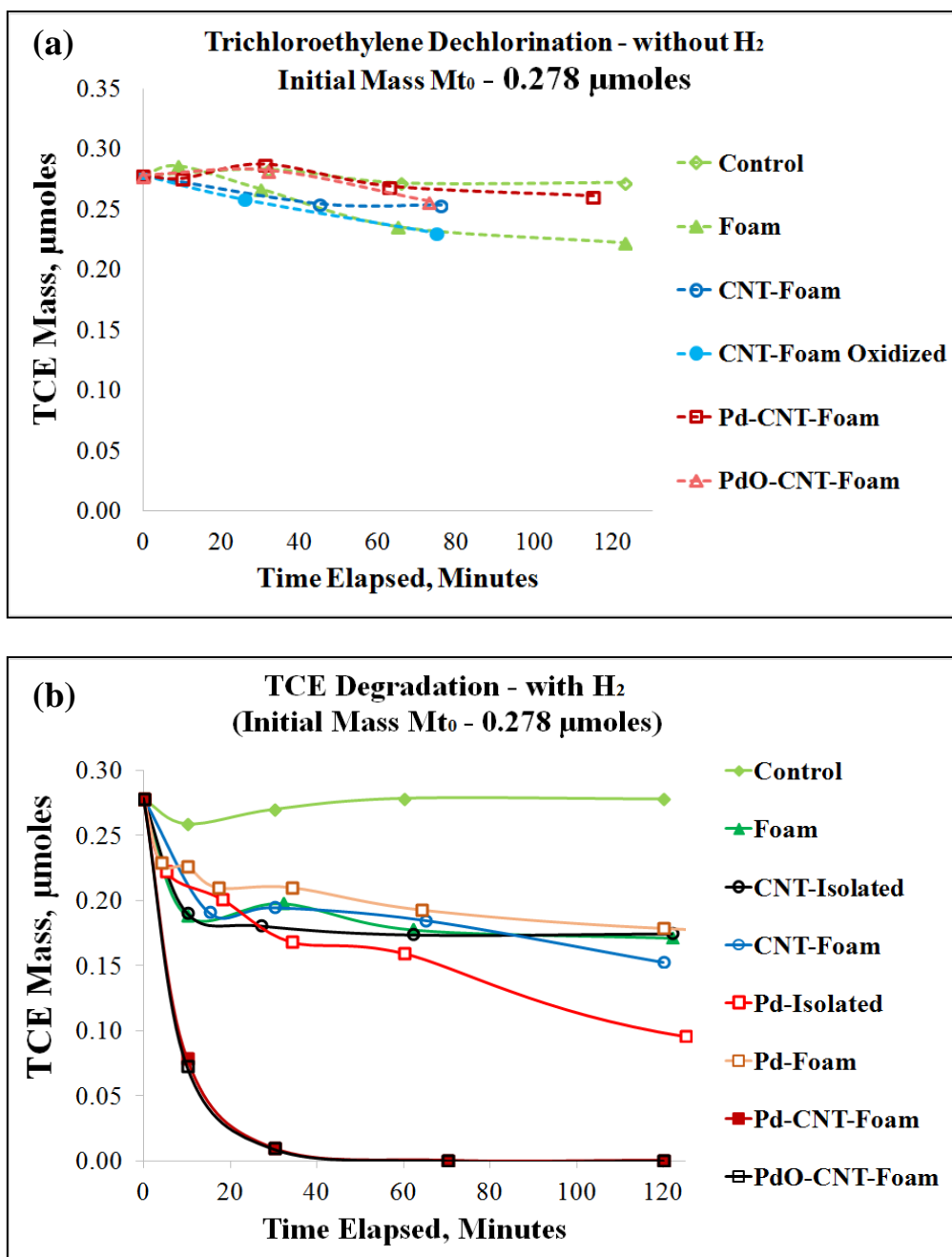


Figure 8.2 Dechlorination profile of TCE using various carbon and Pd-based catalysts (a) without Hydrogen gas purging, and (b) with Hydrogen gas purging (5% H₂ balance N₂) for 20 minutes. Total initial mass of TCE in bottle, [TCE]₀ = 0.278 µmoles

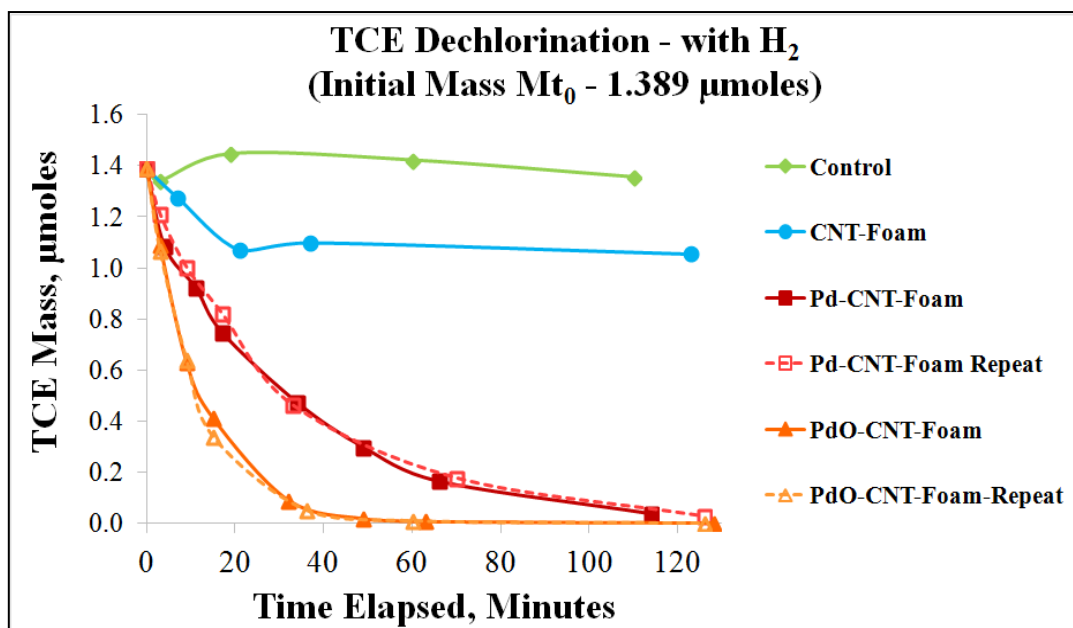


Figure 8.3 Dechlorination profile of TCE using various carbon and Pd-based catalysts with hydrogen gas purging (5% H₂ balance N₂) for 20 minutes. Total initial mass of TCE in bottle, [TCE]₀ = 1.389 μmoles

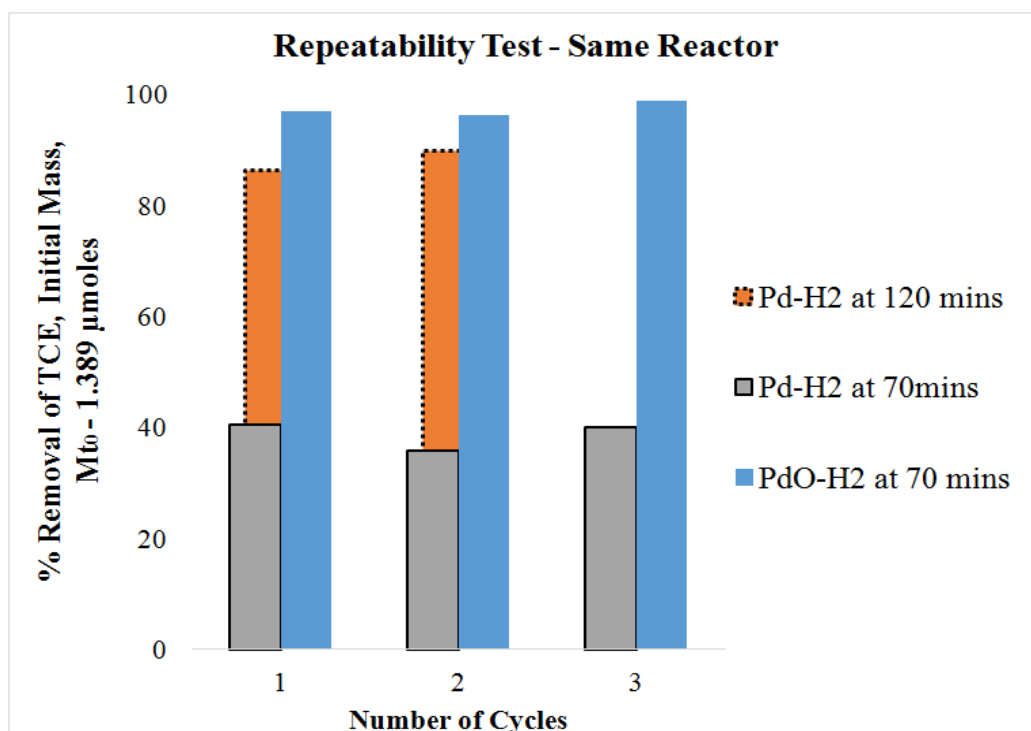


Figure 8.4 Trichloroethylene removal plots obtained by re-using Pd-CNT and PdO-CNT hybrid structures as catalysts showing repeatability of TCE removal capacity after three cycles

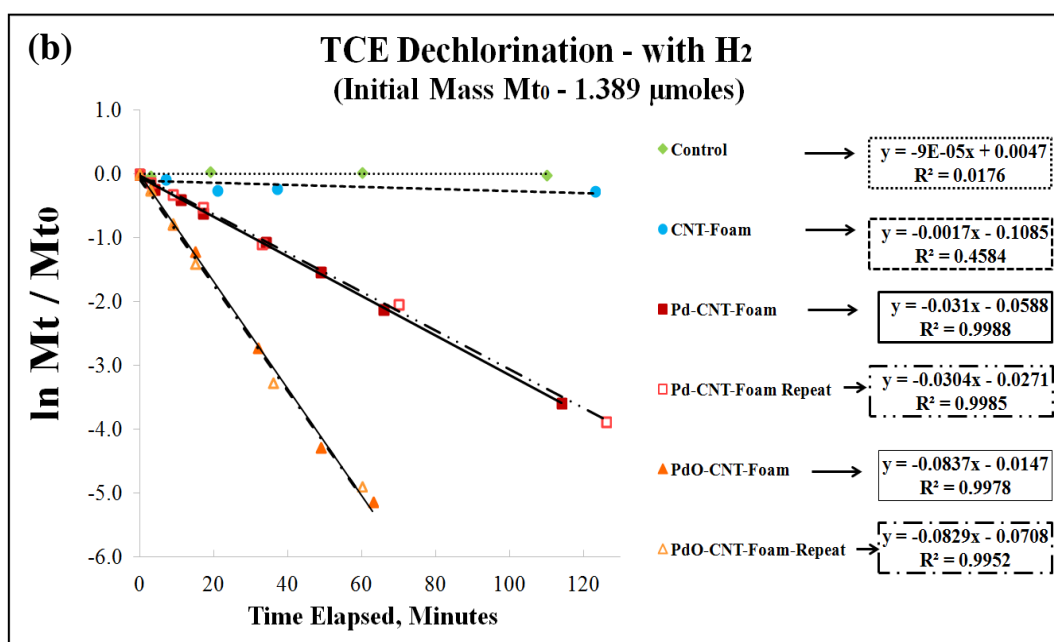
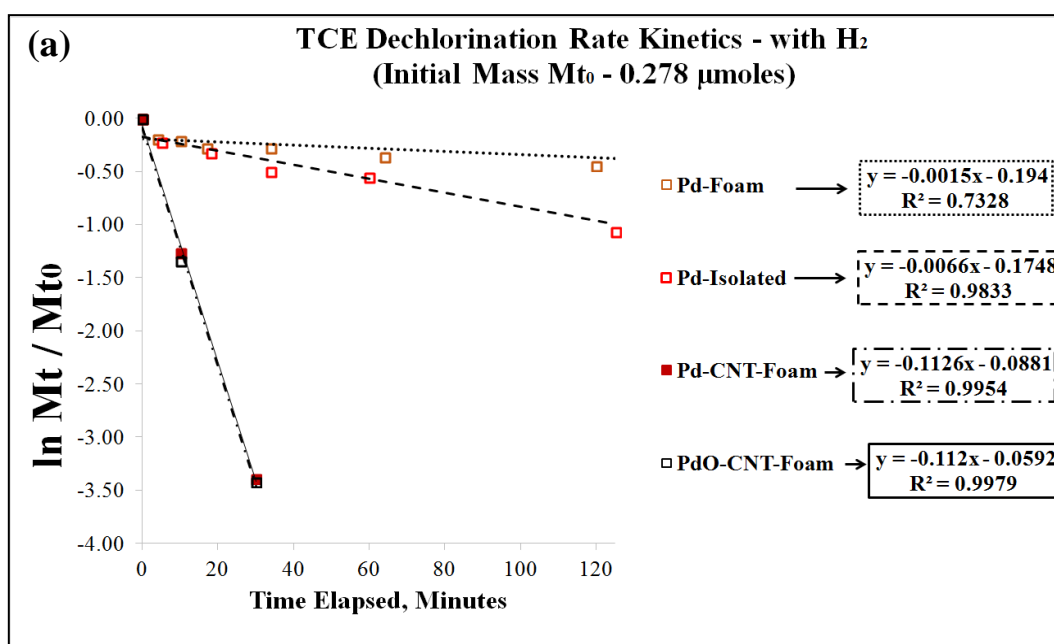


Figure 8.5 Pseudo-first order rate plots for the dechlorination of TCE by Pd-based catalysts on RVC foams with H₂ showing total initial mass (a) [TCE]₀ – 0.278 μmoles, and (b) [TCE]₀ – 1.389 μmoles

Table 8.1 Pseudo-first order rate constants for dechlorination of TCE using Pd based catalysts in the presence of H₂

Total mass of TCE, μmoles	Sample	$k_{\text{obs}}, \text{min}^{-1}$	$k'_{\text{obs}}, \text{min}^{-1}$
0.278	Pd- Foam	0.0015	0.0019
	Pd-Isolated	0.0066	0.0085
	Pd-CNT foam	0.1126	0.1442
	PdO-CNT foam	0.112	0.1434
1.389	Control	0.00009	0.0001
	CNT-foam	0.0017	0.0022
	Pd-CNT foam	0.031	0.0397
	Pd-CNT foam Repeat	0.0304	0.0389
	PdO-CNT foam	0.0837	0.1072
	PdO-CNT foam Repeat	0.0829	0.1062

k'_{obs} calculated from k_{obs} as shown in Table B.3 using a dimensionless Henry's constant for Trichloroethylene at 25 °C, $K_{\text{H}}' = 0.421$ [131], [132]

Figure 8.5 shows the reaction rate coefficients of the TCE degradation using carbon and Pd-based samples at initial mass of (a) 0.278 μmoles and (b) 1.389 μmoles TCE in the reactor bottle. The linear regression fits as shown in Figure 8.5 were obtained for the Pseudo first order plots and the rate coefficients are tabulated in Table 8.1.

8.3.1.2 Catalyst Chemical Analysis

After the dechlorination reactions the catalyst samples were retained from the reactors for surface chemical analysis. The samples (foam supports with catalyst) were rinsed with methanol and water and allowed to dry for up to 48 hours in air. The chemical state of Pd-based catalyst was studied before and after TCE dechlorination reactions. The chemical state of Pd-CNT samples for as-prepared and used sample were observed to be at 335.2 eV for Pd $3d_{5/2}$ and shows no significant difference in the chemical state before and after TCE dechlorination. Figure 8.6 shows the fine scan of Pd $3d$ peak obtained from PdO_{300°C} sample before and after dechlorination of TCE. It can be observed that the PdO sample reduced to metallic state after dechlorination as the Pd $3d_{5/2}$ peak of Pd²⁺ at 337 eV shifts towards the 335.3 eV, indicating release of surface oxide. Figure 8.7 shows the fine scan spectra of C $1s$ before and after TCE dechlorination. The C $1s$ peak broadens after dechlorination showing a satellite peak at ~286 eV, which can be attributed to the adsorbed hydrocarbon impurities on CNT.

8.3.1.3 Daughter Products Formation

Catalytic dechlorination of TCE using palladium based catalysts in the presence of hydrogen gas forms various daughter compounds as shown in Figure 8.8. The formation of daughter compounds includes n-butane, n-hexane, and acetylhydride. As shown in Figure 8.8a, the dechlorination reactions using Pd-NPs and H₂ gas transformed TCE to non-chlorinated hydrocarbons, mostly alkanes and alkenes

such as butane, hexane, and diethylethene (~85%). DCE (dichloroethylene) was detected as the reactive intermediate product and subsequently disappeared. Trace amounts of vinyl chloride (VC) were observed and no ethylene was detected. These daughter products show that all the three chlorine atoms in the TCE compound are being replaced by hydrogen in the dechlorination reaction with Pd-NPs. It significantly forms coupled hydrocarbons (C4, C6) as final products.

A similar trend was observed for the TCE dechlorination reactions using PdO-NPs as catalysts with the H₂ gas, where the TCE mostly transformed to non-chlorinated hydrocarbons. Coupled hydrocarbons were mostly formed (~80%), such as propane, butane, methyl-pentane, and diethyl-ethene (C3, C4, C6). No chlorinated compounds such as DCE or VC were observed as daughter products or reactive intermediates. However, when using PdO, significant amounts of acetic aldehyde (CH₃CHO) formation was observed (~17%). This can be attributed to the donation of the oxygen by the PdO. Formation of the daughter compound in all cases correlates well with the decrease in TCE concentration. Some of the dechlorination products reported in literature include are ethene, ethane, coupled hydrocarbons [133]–[139].

Table 8.2 summarizes the final products of TCE dechlorination using Pd and PdO catalysts with H₂. The dechlorination of TCE using Pd-based catalysts (Pd or PdO) in the presence of H₂ results in smaller compounds by breaking the carbon-chlorine bonds. This leads to formation of HCl compound, which in this case was observed to affect the final pH of the solution. For TCE dechlorination reactions (at initial pH ~6.5) the pH decreases to pH ~5 at the end of the reactions.

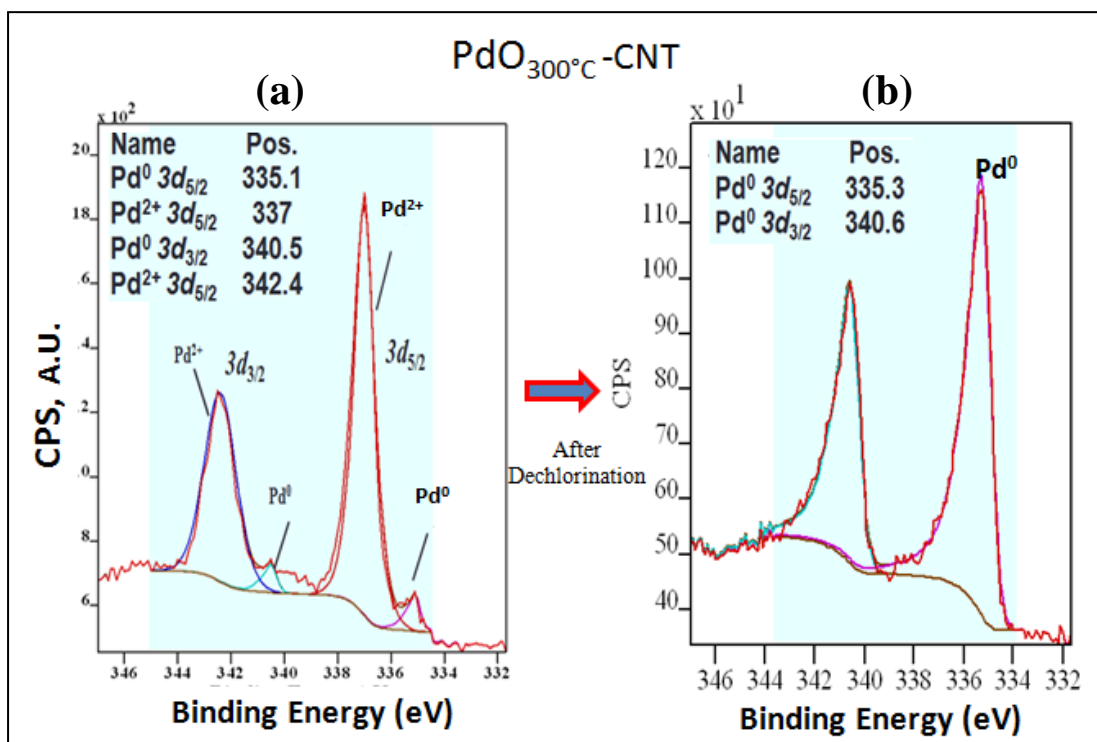


Figure 8.6 XPS Pd 3d fine-scan spectra of PdO-CNT on RVC foam (a) before and (b) after TCE dechlorination

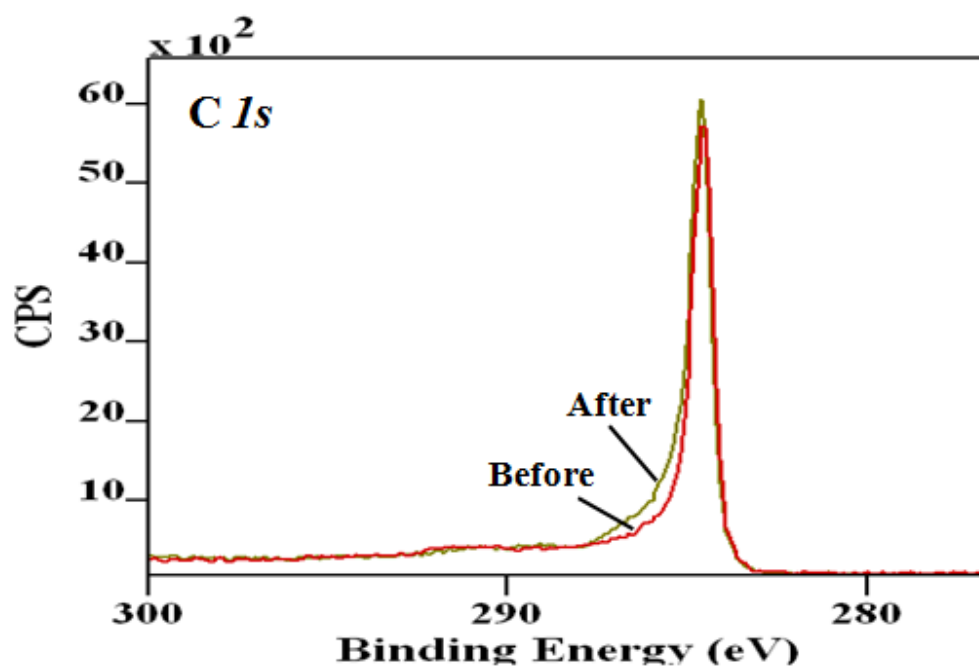


Figure 8.7 XPS C 1s fine-scan spectra of PdO-CNT-Foam before and after TCE dechlorination

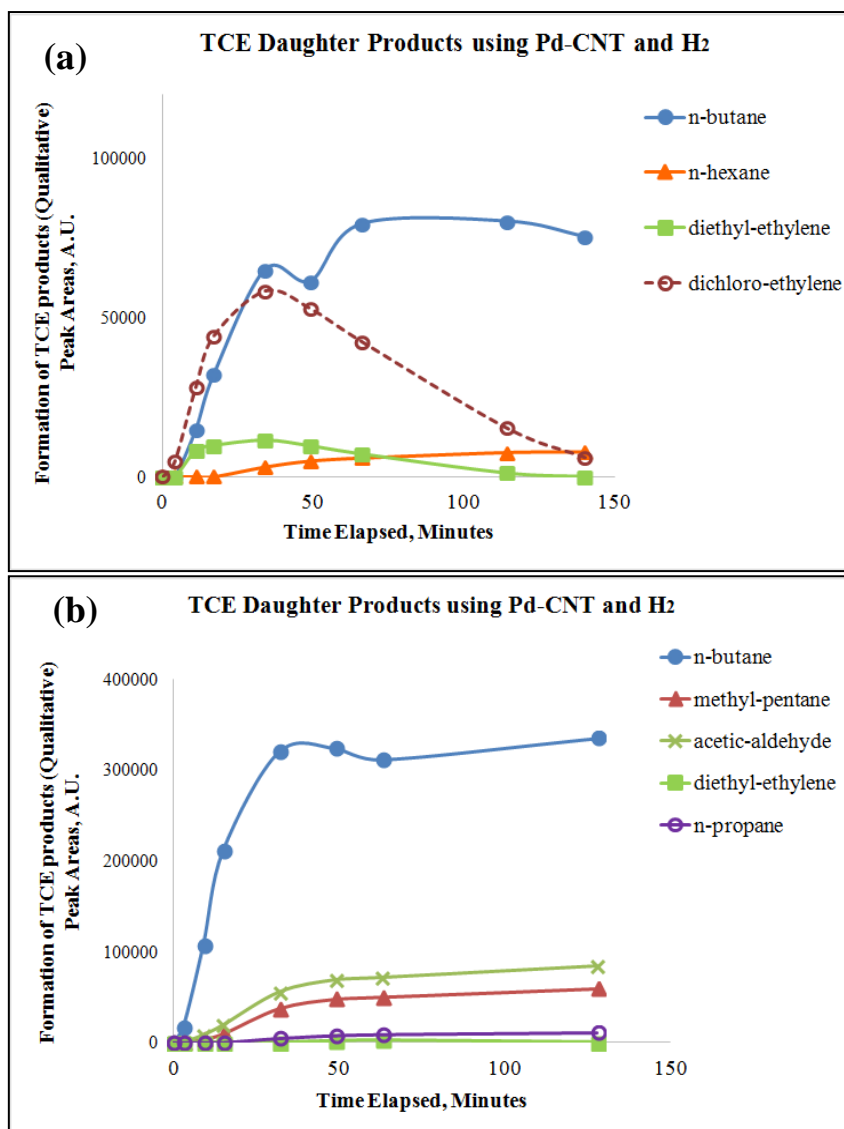


Figure 8.8. Formation of daughter products of TCE ($[TCE]_0 = 1.389 \mu\text{moles}$ or $C_0 = 5 \mu\text{g/mL}$) during dechlorination with (a) Pd-CNT Foam, and (b) PdO-CNT Foam samples in the presence of H₂.

Table 8.2 Daughter products of TCE by dechlorination with Pd and PdO as catalysts

Compound		Chemical Structure	Pd-NPs	PdO-NPs
TCE	Trichloroethylene	$\text{Cl}_2\text{C} = \text{CHCl}$	Initial compound	Initial compound
DCE	Dichloroethylene	$\text{ClHC} = \text{CHCl}$	Intermediate product	nd
VC	Vinyl Chloride	$\text{H}_2\text{C} = \text{CHCl}$	trace	nd
C3	n-propane	$\text{n-C}_3\text{H}_8$	nd	✓
C4	n-butane (diethyl)	$\text{n-C}_4\text{H}_{10}$	✓	✓
C6	n-hexane	$\text{n-C}_6\text{H}_{14}$	✓	nd
	1,1-diethylethene	$(\text{C}_2\text{H}_5)_2 - \text{C} = \text{CH}_2$	✓	✓
	3-methyl pentane	$(\text{C}_2\text{H}_5)_2 - \text{CHCH}_3$	nd	✓
- HC = O	acetic aldehyde	$\begin{array}{c} \text{O} \\ \parallel \\ \text{H}_3\text{C} - \text{C} - \text{H} \end{array}$	nd	✓

nd – not detected, trace – observed in minute quantities

8.3.2 Trichloroethane (TCA) Experiments

1,1,1 - Trichloroethane (TCA) batch experiments were carried out similar to the TCE experiments as described in section 8.2. The dechlorination reactions of 1,1,1 - Trichloroethane using palladium based catalyst were monitored by analysing the headspace of the reactors using GC-MS. TCA standards of varying concentration and samples of unknown concentration were analyzed using headspace GC-MS analysis and the degradation compounds were detected by analysing the actual compound and also using library. Catalytic dechlorination reactions of TCA using Pd-based catalysts were carried out for initial concentrations of 1 mg/L and 5 mg/L (ppm) *i.e.* for total initial mass of TCA in the bottle of 0.247 μ moles and 1.237 μ moles, respectively.

Figure 8.9 shows the calibration curves obtained from GC-MS analysis of standards and by plotting the area of TCA peaks with the known mass in the bottle (ranging from 0.025 to 1.237 μ moles). The curve shows excellent linearity with the regression coefficient close to 1, $R^2 \sim 0.99$. The calibration curve equation is used for determining the concentration of TCA in the headspace of the reactor with H_2 purging. Calibration curves were obtained for every experiment.

Figure 8.10 and Figure 8.11 shows the dechlorination kinetics of TCA at an initial concentration of 1 mg/L or total initial TCA mass of 0.247 μ moles obtained with various materials. Figure 8.10 shows the effect of hydrogen for degradation of TCA using Pd-CNT foam samples. The Pd-CNT foam sample without hydrogen shows only 30% of TCA removal. However, the Pd-CNT foam sample in the presence of hydrogen gas in the reactor shows complete removal of TCA. Figure 8.11 shows the reaction kinetics of TCA with following materials in the presence of hydrogen gas: (a) control (no support or catalyst), (b) RVC Foam, (c) CNT Foam, (d)

Pd-CNT Foam, (e) PdO-CNT Foam, and (f) isolated Pd. The control reactor (no support or catalyst) shows no significant change in the concentration of TCA. The RVC-foam and CNT-RVC foam in the presence of hydrogen shows only 30% degradation of TCA. This TCA removal is similar to that of Pd-CNT foam sample without H₂. This can be attributed to the adsorption of TCA on carbon or Pd surface. Interestingly the removal rate for both carbon samples is similar showing no additional effect due to CNT grafting on RVC. This result contradicts the results observed previously with other non-volatile compounds (methylene blue – Figure 5.1b).

As shown in Figure 8.11, the dechlorination of TCA using Pd based catalysts (Isolated Pd, Pd-CNT, PdO-CNT) in the presence of H₂ shows improved removal rates compared to that of CNT-RVC foam samples. The Pd-CNT and PdO-CNT samples show complete dechlorination of TCA within 150 mins with identical dechlorination kinetics. However, the isolated palladium shows only 50% TCA dechlorination, which can be due to agglomeration of the Pd particles as the isolated palladium particles are in suspended form in the liquid.

Additional dechlorination experiments were carried out with an initial concentration of TCA of 5 mg/L or total initial TCA mass of 1.237 μmoles with Pd-CNT and PdO-CNT RVC foam samples in the presence of H₂ gas in the reactor. The dechlorination kinetics are as shown in Figure 8.12. The TCA dechlorination profile with H₂ (Figure 8.12) shows the average of two runs, where PdO shows a higher dechlorination rate compared to that of Pd-CNT. Note the Pd-CNT profile has large error bars that overlap the PdO-CNT rate profile. In this research, it has been shown that PdO-CNT catalysts show higher dechlorination rates compared to Pd-CNT in the presence of hydrogen for dechlorination of other contaminants such as

Trichloroethylene. However, it is not clear in the TCA dechlorination study if PdO-CNT shows a higher rate for dechlorination of TCA, owing to the TCA compound being unstable in water. This requires additional experiments to confirm the data for TCA.

Figure 8.13 shows the reaction rate coefficients of the TCA degradation using carbon and Pd-based samples at initial mass of (a) 0.247 μmoles and (b) 1.237 μmoles TCA in the reactor bottle. The linear regression fits as shown in Figure 8.13 were obtained for the Pseudo first order plots and the rate coefficients are tabulated in Table 8.3. The TCA dechlorination reactions are observed to fit the Pseudo-first order equations.

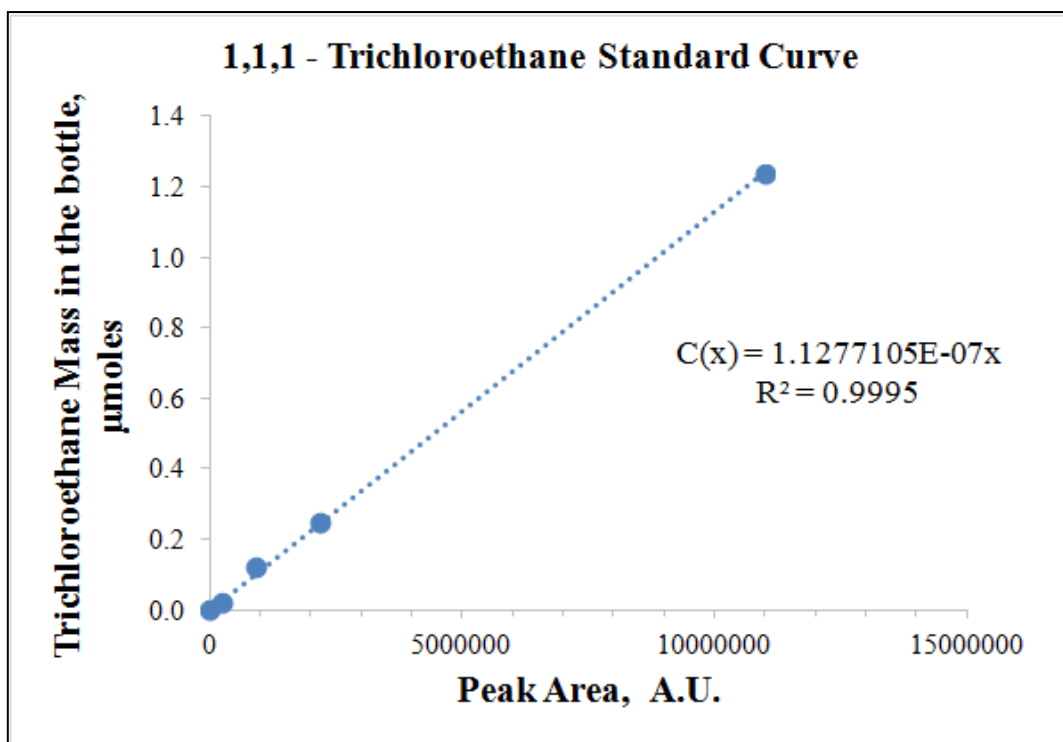


Figure 8.9 Calibration curves of TCA compound in 60 mL reactors for mass varying from 0.025 μmoles to 1.237 μmoles with H_2 purging in the reactors obtained by plotting peak areas with known TCA standard

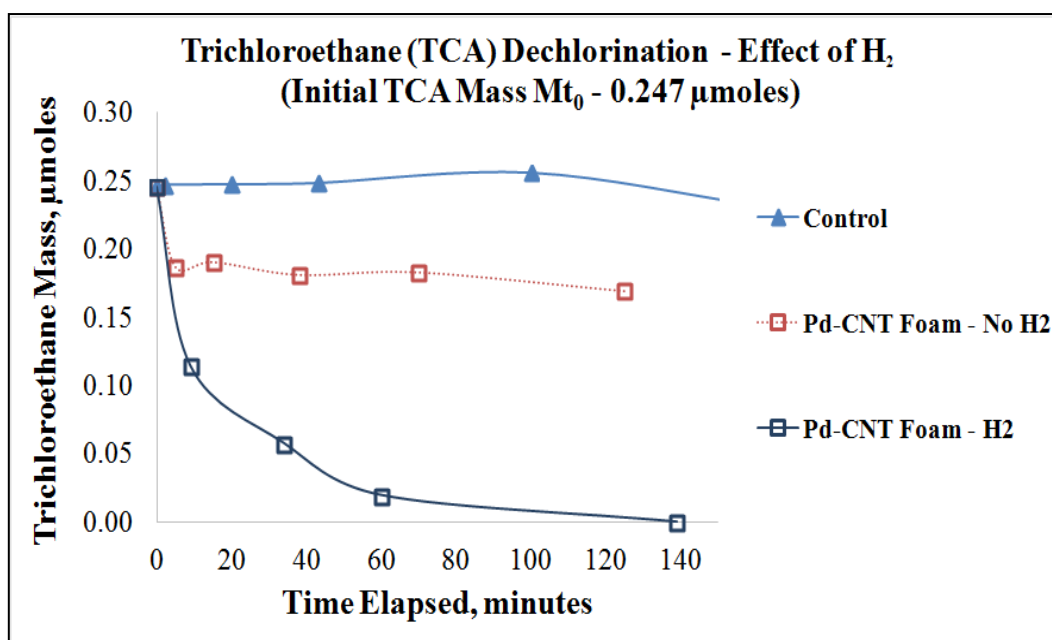


Figure 8.10. Dechlorination kinetics profile of TCA ($[\text{TCA}]_0 - 0.247 \mu\text{moles}$ or $C_0 = \sim 1 \mu\text{g/mL}$) showing the effect of H_2 gas obtained for the control and Pd-CNT foam samples without and with H_2 purging.

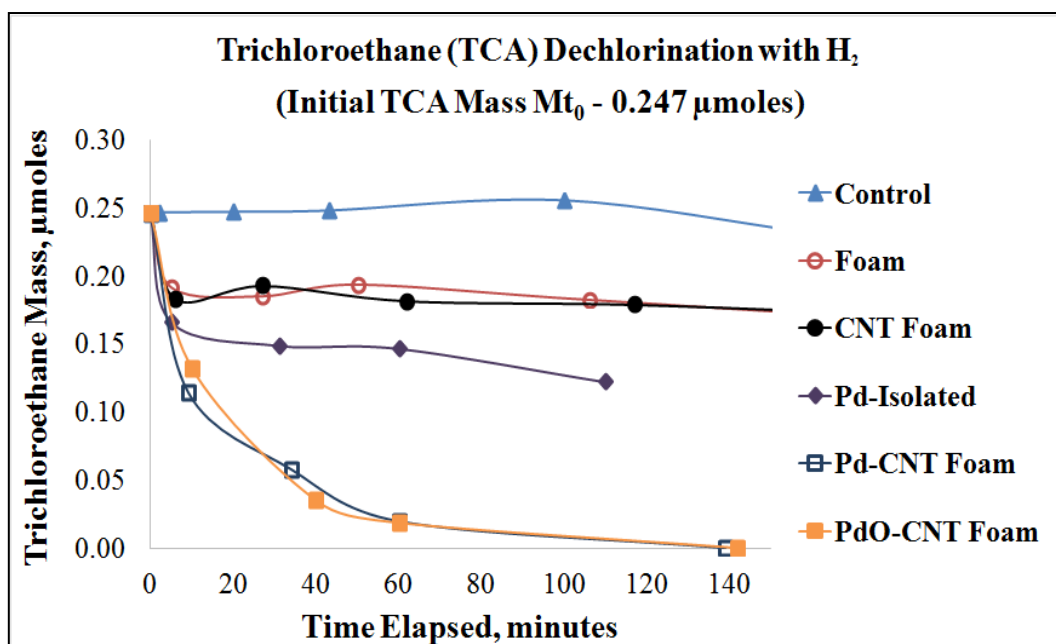


Figure 8.11 Dechlorination kinetics profile of TCA ($[TCA]_0 = 0.247 \mu\text{moles}$ or $C_0 = \sim 1 \mu\text{g/mL}$) obtained with different samples in the presence of H_2

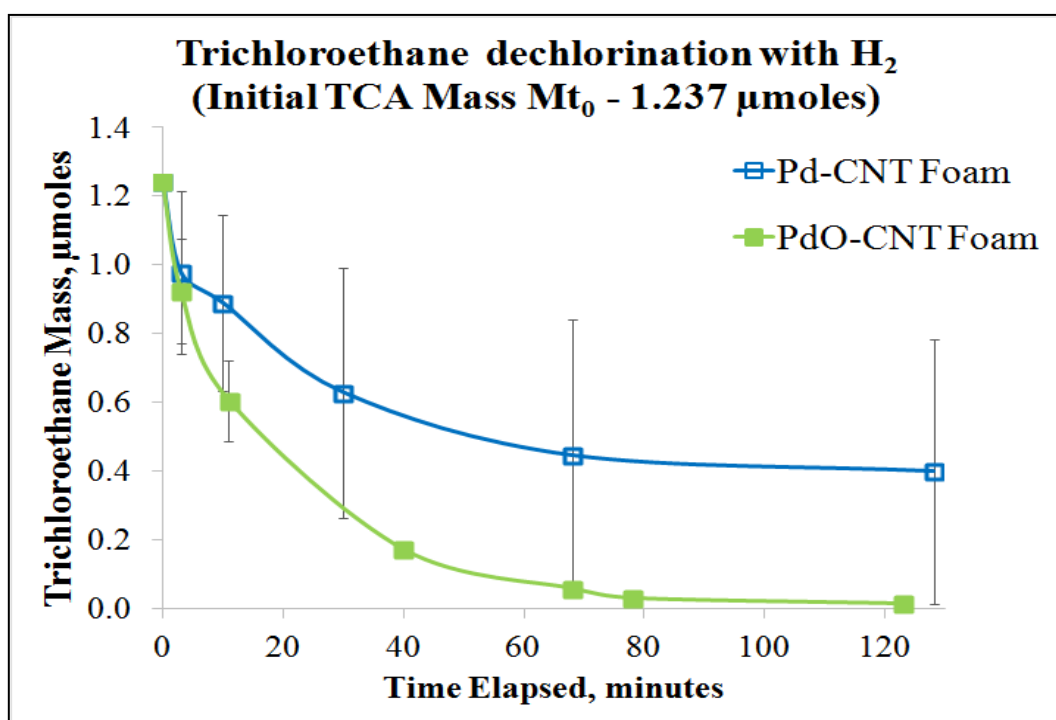


Figure 8.12 Dechlorination kinetics profile of TCA ($[TCA]_0 = 1.237 \mu\text{moles}$ or $C_0 = \sim 5 \mu\text{g/mL}$) obtained using Pd-CNT, and PdO-CNT foam samples in the presence H_2 .

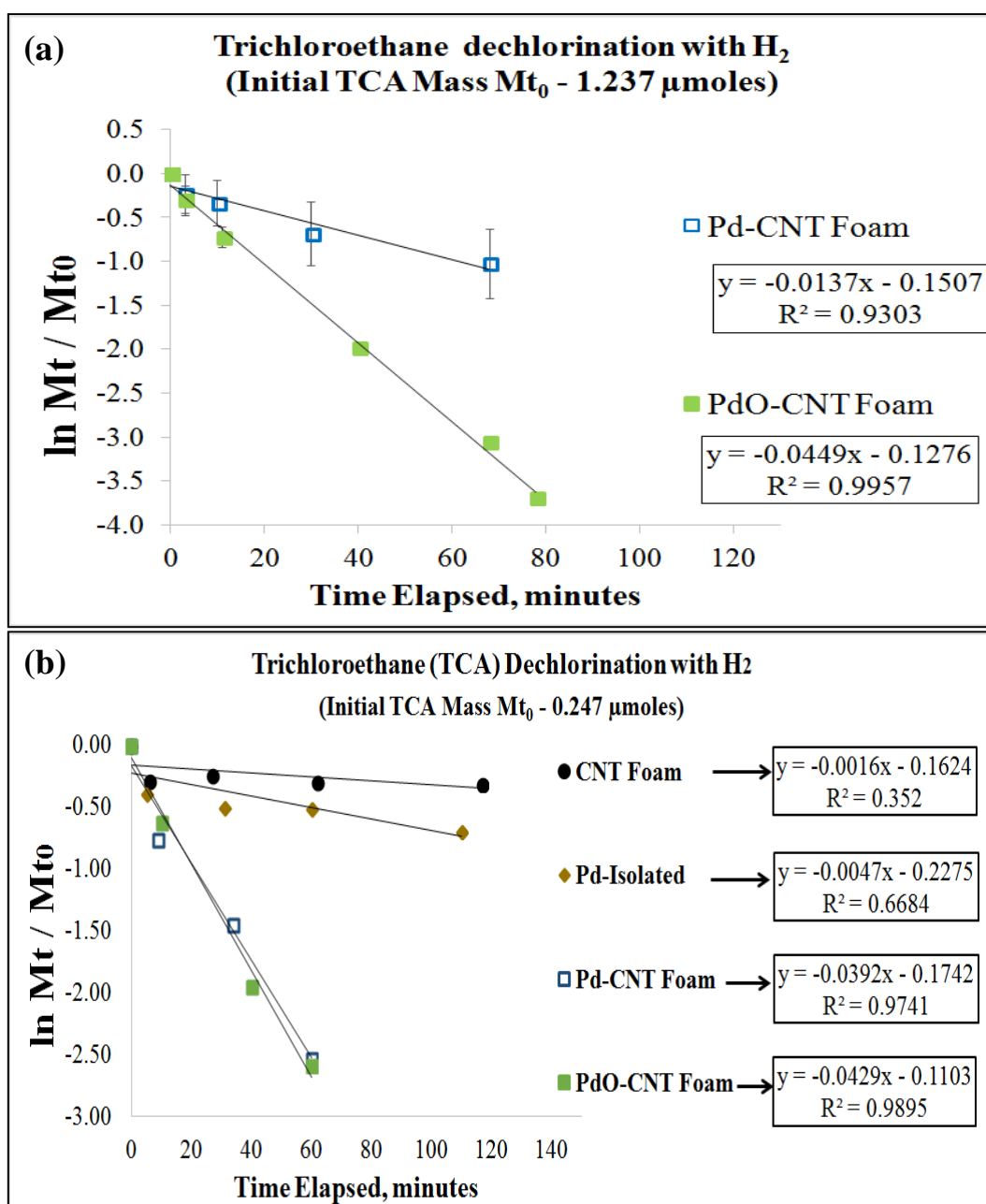


Figure 8.13 Pseudo-first order rate plots for the dechlorination of TCA by Pd-based catalysts with H₂ showing for total initial mass (a) [TCA]₀ - 0.247 μ moles, and (b) [TCA]₀ - 1.237 μ moles

Table 8.3 Pseudo-first order rate constants for dechlorination of TCA using Pd-based catalysts in the presence of H₂

Total mass of TCA, μmoles	Sample	$k_{\text{obs}}, \text{min}^{-1}$	$k'_{\text{obs}}, \text{min}^{-1}$
0.247	Control	0.0003	0.0004
	Foam	0.0009	0.0013
	CNT-foam	0.0016	0.0023
	Pd-CNT-No H ₂	0.0018	0.0026
	Pd-Isolated	0.0047	0.0069
	Pd-CNT foam	0.0392	0.0576
	PdO-CNT foam	0.0429	0.0630
1.237	Pd-CNT foam	0.0137	0.0201
	PdO-CNT foam	0.0449	0.0659

k'_{obs} calculated from k_{obs} as shown in Table B.3 using a dimensionless Henry's constant for 1,1,1-Trichloroethane at 25 °C, $K_{\text{H}}' = 0.703$ [131], [132]

8.3.2.1 TCA Daughter Products Formation:

The dechlorination reactions of 1,1,1 – Trichloroethane using palladium based catalyst in the presence of hydrogen gas breaks the carbon-chlorine bonds and forms HCl and other smaller compounds. The catalytic dechlorination of TCA at initial concentration of 1 mg/L or mass of 0.247 μ moles with Pd-CNT and PdO-CNT as catalysts was observed to produce small amounts of dichloroethane at low concentrations. No other daughter products were observed at 1 mg/L TCA concentration. It must be noted that in the presence of H₂ gas, no daughter products of TCA were observed for RVC and CNT-RVC sample. Also, no daughter products were observed for Pd-CNT catalyst without H₂ gas. This indicates that Pd requires hydrogen gas to catalyse the dechlorination reactions of TCA.

For TCA at an initial concentration of 5 mg/L or mass of 1.237 μ moles, multiple daughter products were formed using Pd-CNT and PdO-CNT as catalysts with hydrogen gas as shown in Figure 8.14. Using both Pd and PdO as catalysts with H₂, TCA was mainly transformed to 1,1- dichloroethane (DCA) as the major product [139]. As shown in Figure 8.14a, Pd transforms TCA to DCA and dichloro-butane. These chemical structures are summarized in Table 8.4.

With PdO as catalyst, along with dichloroethane, acetyl-propyl chloride (C₅H₉OCl) containing a C=O group was observed to form as a product (Figure 8.14b). Oxygen is acquired from the PdO-NPs, which are known to be reduced to Pd after the dechlorination reactions. The final products of trichloroethane dechlorination using Pd and PdO with H₂ are summarized in Table 8.4.

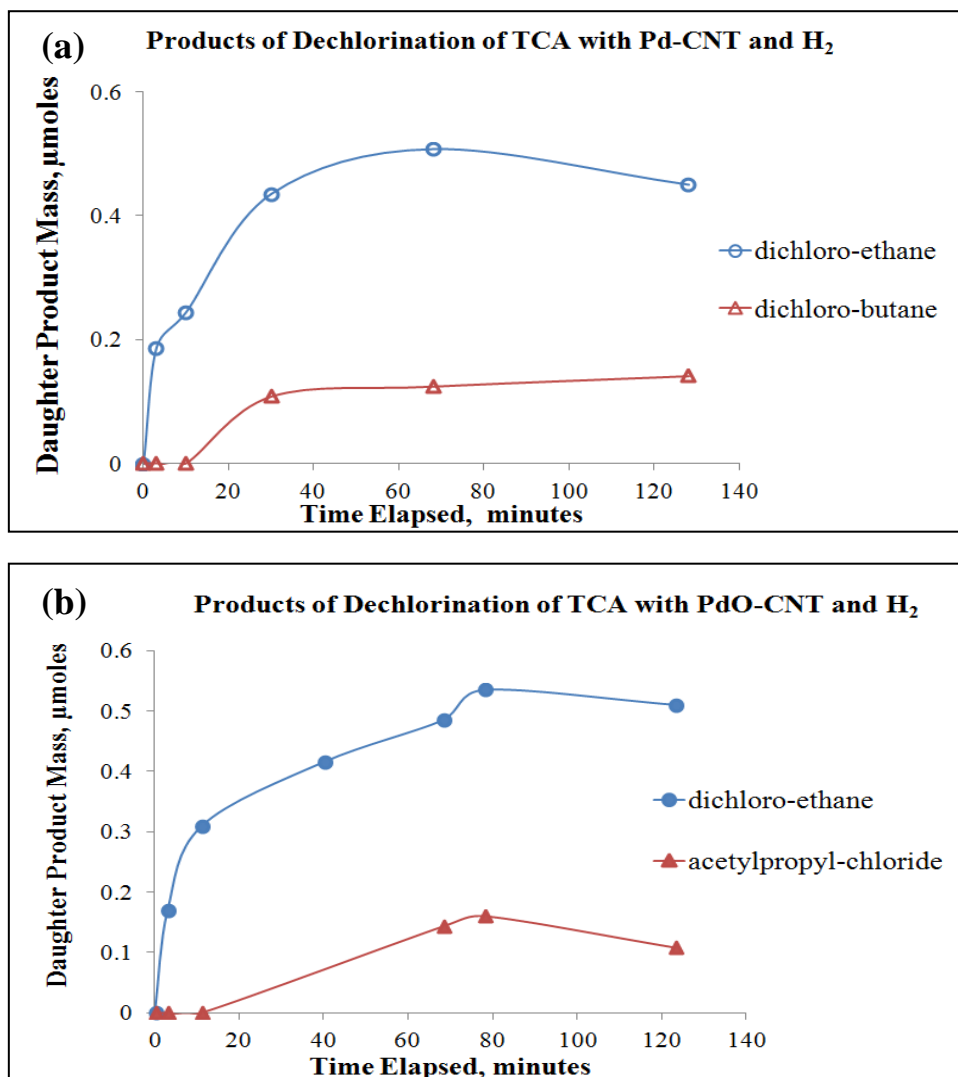
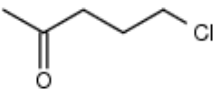


Figure 8.14 Formation of daughter products of TCA during dechlorination with (a) Pd-CNT Foam, and (b) PdO-CNT Foam samples in the presence of H₂.

Table 8.4 Daughter products of TCA by dechlorination with Pd and PdO as catalysts

Compound		Chemical Structure	Pd-NPs	PdO-NPs
TCA	1,1,1 - Trichloroethane	$\text{Cl}_3\text{C} - \text{CH}_3$	Initial compound	Initial compound
DCA	1,1 - Dichloroethane	$\text{Cl}_2\text{HC} - \text{CH}_3$	major final product	major final product
Cl-C4-Cl	1,4, - Dichlorobutane	$\text{ClH}_2\text{C}_2 - \text{C}_2\text{H}_4\text{Cl}$	product	nd
$\text{O}=\text{HC}-\text{C}_4\text{H}_8\text{Cl}$	Acetylpropylchloride		nd	product

nd – not detected, trace – observed in minute quantities

8.3.3 Dechlorination Mechanisms with the Pd/H₂ System

In this study, aqueous phase degradation of chlorinated hydrocarbons (TCE and TCA) at ambient temperatures was accomplished using Pd-based catalysts on hierarchical carbon supports in the presence of H₂ gas as a reducing agent.

The reduction of trichloroethylene (TCE) can happen through various reaction pathways. The most favorable catalyzed reaction pathway is often observed, where TCE yields daughter products such as dichloroethylene (C₂H₂Cl₂), chloro ethylene (C₂H₃Cl), and/or ethylene (C₂H₄), and other non-chlorinated carbon species which are less toxic or non-toxic [133]–[139]. In this study, in the presence of Pd and H₂, TCE is catalytically reduced to dichloroethylene (C₂H₂Cl₂), coupled hydrocarbons such as butane or hexane. The degradation mechanism presumably involves steps that include dissociative adsorption of chemical species on the surface of the Pd (through dissociation of H₂ and C₂HCl₃ into intermediate species on the active sites), chemical reaction between the intermediate species forming the reduced product (for example C₂H₂Cl₂ and HCl), and the desorption of the final products from the catalyst surface or further degradation of the adsorbed intermediate species into the smaller daughter products.

With PdO in the presence of H₂, we observe the formation of aldehyde group (-HC=O) containing oxygen. Here, the degradation mechanism involves dissociative adsorption of chemical species on the surface of the PdO, chemical reaction between the intermediate species and the surface oxygen, which may include subsequent dissociation of oxygen from the surface of Pd. This leads to formation of the acetic aldehyde as a daughter product. In this study, the PdO is reduced to Pd as observed by XPS surface analysis.

The reduction of Trichloroethane (TCA) can happen through multiple pathways [139]. However, the most favorable reaction pathway observed in this study is where TCA is reduced to its immediate daughter products such as dichloroethane and chloroethanes. Additionally using PdO as a catalyst, we observe formation of acetylpropyl chloride (-HC=O --Cl) instead of chloroethane. The dechlorination mechanism as observed for TCE is demonstrated here for TCA products where surface oxygen of Pd reacts with intermediate compounds and reduces to Pd.

8.4 Conclusion

In this study, Pd and PdO on hierarchical carbon structures were used as catalysts in the presence of hydrogen gas for dechlorination of chlorinated hydrocarbons, Trichlorethylene (TCE) and Trichloroethane (TCA) in simulated water. It was found that performance of the Pd-based catalyst is greatly influenced by the presence of hydrogen in the reactors to catalyze the dechlorination reactions. Moreover, it was observed that PdO as a catalyst has higher catalytic activity compared to that of Pd for dechlorination of TCE. With the Pd based catalysts in the presence of hydrogen, complete removal of TCE was observed by dechlorination reactions, where all the chlorines are replaced with hydrogens and n-butane is the primary product. The dechlorination reaction for TCA using Pd-based catalyst on hierarchical substrates shows complete removal in the presence of hydrogen. TCA was observed to primarily form dichloroethane. For dechlorination reactions, PdO shows improved catalytic activity and also formation of aldehyde groups (-HC=O). The surface oxygen of PdO reacts with the adsorbed intermediate products and the PdO reduces to zerovalent Pd. All of the dechlorination reactions with the aid of hydrogen releases HCl compound in the liquid and the solution becomes acidic (pH decreases from ~6.9 to ~ 5).

9 Chapter 9: Catalytic Degradation of Emerging Contaminants – Atrazine using Palladium Based Catalysts

9.1 Introduction

A wide variety of emerging contaminants, known as contaminants of emerging concern (CECs) which are of immediate concern due to their potential threat to health and the environment, have recently been identified by the United States Environmental Protection Agency (USEPA) [140]–[143]. These include a variety of detergents, pharmaceutical agents, antimicrobial agents, plasticizers, fertilizers, herbicides, and pesticides. A few such compounds are Atrazine, Bisphenol-A, Triclosan, Triclocarban, Perfluorooctanoic acid, Octylphenol, Nonylphenol, Carbamazepine, and Progesteron. These chemicals are non-point source pollutants that are commonly present in ground water as well as in treated wastewater effluents that are released into water ways. Wide varieties of CECs have been detected in treated drinking water in various places [142]. Research is being done to explore various technologies to remove these contaminants from wastewater and treated water. There are several techniques that are being investigated to remove such chemicals from water such as adsorption on carbon, ozonation, hydrolysis, biodegradation, photodegradation, advanced oxidation and catalytic degradation techniques [144]–[147].

In this study, we focus on catalytic degradation using palladium and silver based catalysts for treating such emerging contaminants in water. The choice of a model emerging contaminant for this study is atrazine. Atrazine, chemically known as 6-chloro-N-ethyl-N'-(1-methylethyl)-1,3,5- triazine-2,4-diamine or 2-Chloro-4-ethylamino-6-isopropylamino-1,3,5-triazine has a chemical formula of $C_8H_{14}ClN_5$ and

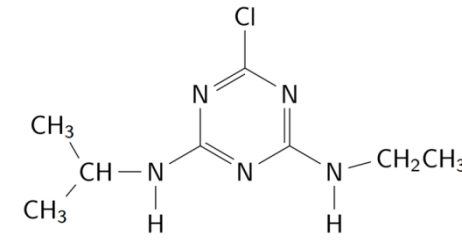
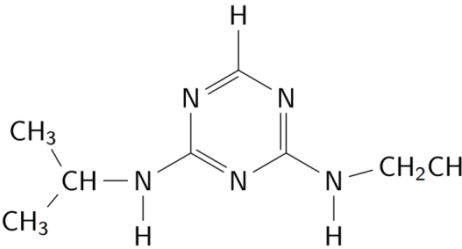
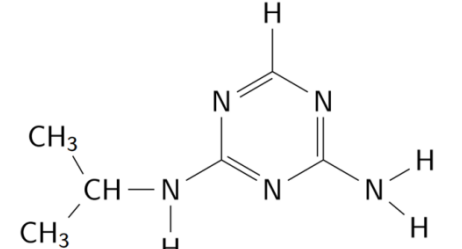
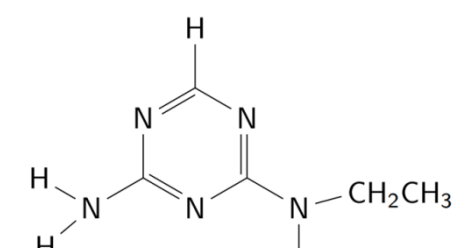
a molecular weight of 215.1. The chemical structure of atrazine is shown in Table 8.1. The solubility of atrazine in water at 20 °C is 30 mg/L. Atrazine is a triazine herbicide that inhibits photosynthetic electron transport and is commonly used for controlling the growth of weed on various crops such as wheat, sugarcane, guava, and a wide range of grasses. It is also used for corn and sorghum production. It is a widely used herbicide in the United States (~64 to 75 million pounds per year) [148], [149]. As a herbicide, atrazine is directly applied to the soil during pre-planting process and due to its high solubility in water it can easily migrate into the ground and surface waters. As a result of its extensive usage and very low natural biodegradability, it is persistent in the environment. Due to its potential ecological and health effects, its usage has been restricted in many developed countries including USA. As instituted by the USEPA, the maximum contamination level of atrazine in drinking water is 3 µg/L or ppb [149], [150].

The adsorption of atrazine on adsorbents is relatively ineffective due to its low adsorption ability. More commonly atrazine is treated using biological or oxidative/reductive degradation techniques. Common reducing agents employed for atrazine reductive degradation include zerovalent iron (ZVI) and a common catalyst used to promote reduction is palladium [78], [146]. Nadagouda et. al. have investigated the reactivity of Pd catalyst in aerobic conditions for reductive or oxidative removal of some emerging contaminants such as atrazine, triclosan, and/or octylphenol [78]. As shown by Nadagouda et.al., the reactivity of palladium for degradation of atrazine in aerobic conditions is very low.

In this study, we test the reactivity of palladium based catalysts: Pd-NPs, PdO-NPs, and Ag/Pd-NPs supported on carbon hierarchical supports in the presence of hydrogen (anaerobic conditions) for the effective degradation of such emerging

contaminants. The objective is to demonstrate the potential of the hierarchical structuring of the materials, which can provide high surface activity as well as robustness for smaller and lighter components. The degradation kinetics and mechanism for such catalytic reduction experiments were studied using LC-MS techniques. The catalytic degradation of atrazine can produce various daughter products that are discussed in this chapter. Some of the possible daughter products of atrazine formed due to hydrogenated and hydroxylated degradation are shown in Table 9.1 and Table 9.2, respectively. Attempts were made to detect daughter product formation using LC-MS analysis. Potential degradation pathways are also proposed herein. An internal standard 'd₅-Atrazine' was used to quantify the peak intensities of the compounds in the HPLC analysis. The chemical structure of d₅-atrazine is shown in Table 9.1. Structural and chemical correlation properties of the hierarchical catalyst material were investigated using SEM and XPS.

Table 9.1 Chemical structure, chemical name, molecular formula, molecular weight of atrazine and related hydrogenated atrazine products

No.	Chemical <ul style="list-style-type: none"> • Chemical Name • Molecular formula • Molecular weight; ion 	Chemical Structure
1	Atrazine <ul style="list-style-type: none"> • 2-Chloro-4-ethylamino-6-isopropylamino-1,3,5-triazine • $C_8H_{14}ClN_5$ • 215.68 g/mol; $[(\mu+1)^+ : 216.10]$ 	
2	Dechlorinated Atrazine <ul style="list-style-type: none"> • 2-ethylamino-4-isopropylamino-1,3,5-triazine • $C_8H_{15}N_5$ • 181.14 g/mol; $[(\mu+1)^+ : 182.14]$ 	
3	De-ethyl-Dechlorinated Atrazine <ul style="list-style-type: none"> • 2-amino-4-isopropylamino-1,3,5-triazine • $C_6H_{11}N_5$ • 153.11 g/mol; $[(\mu+1)^+ : 154.11]$ 	
4	De-isopropyl-Dechlorinated Atrazine <ul style="list-style-type: none"> • 2-amino-4-ethylamino-1,3,5-triazine • $C_5H_9N_5$ • 139.04 g/mol; $[(\mu+1)^+ : 140.04]$ 	

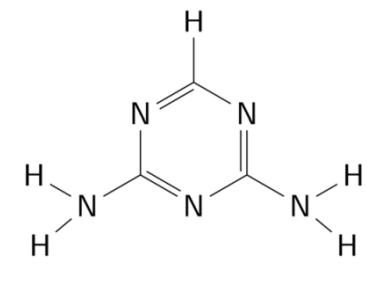
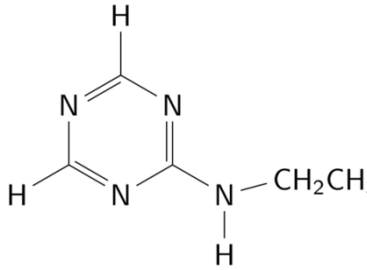
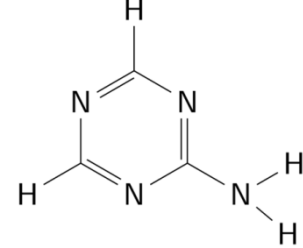
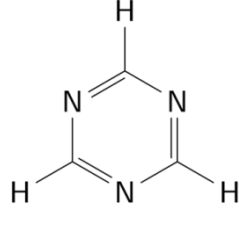
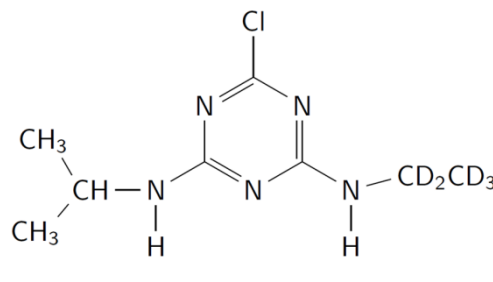
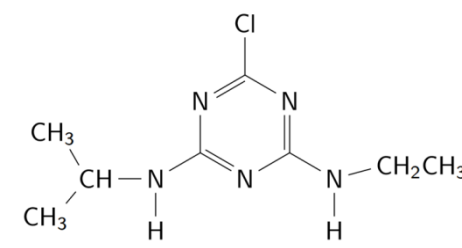
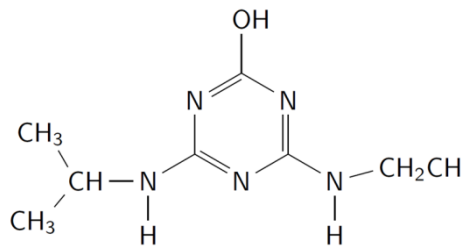
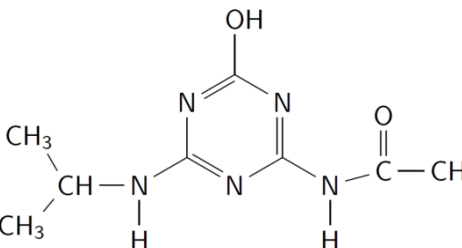
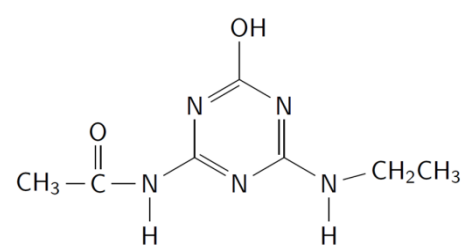
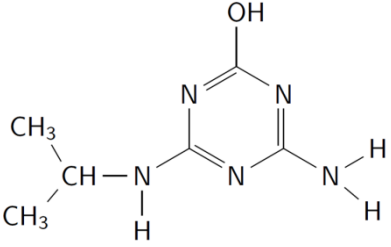
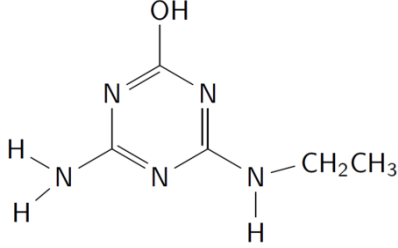
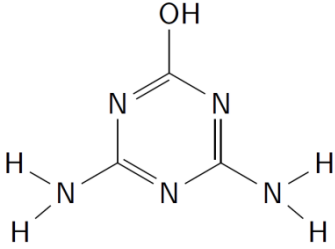
No.	Chemical <ul style="list-style-type: none"> • Chemical Name • Molecular formula • Molecular weight; ion 	Chemical Structure
5	Di-Dealkyl-Dechlorinated Atrazine 'or' Guanamine <ul style="list-style-type: none"> • 2,4-diamino-1,3,5-triazine • C₃H₅N₅ • 111.05 g/mol; [(μ+1)⁺ : 112.06] 	
6	<ul style="list-style-type: none"> • 2- ethylamino-1,3,5-triazine • C₅H₈N₄ • 124.07 g/mol; [(μ+1)⁺ : 125.08] 	
7	<ul style="list-style-type: none"> • 2- amino-1,3,5-triazine • C₃H₄N₄ • 96.04 g/mol; [(μ+1)⁺ : 97.05] 	
8	Cyanidine or s-triazine <ul style="list-style-type: none"> • 1,3,5-triazine • C₃H₃N₃ • 81.03 g/mol; [(μ+1)⁺ : 82.04] 	
9	<u>Internal Standard</u> d ₅ -Atrazine or Deuterated Atrazine <ul style="list-style-type: none"> • 2-Chloro-4-pentadeutero ethylamino-6-isopropylamino-1,3,5-triazine • C₈H₉D₅ClN₅ • 220.71 g/mol; [(μ+1)⁺ : 221.1] 	

Table 9.2 Chemical structure, chemical name, molecular formula, molecular weight of atrazine and related hydroxylated atrazine products [151]

No.	Chemical <ul style="list-style-type: none"> • Chemical Name • Molecular formula • Molecular weight; ion 	Chemical Structure
1	Atrazine <ul style="list-style-type: none"> • 2-Chloro-4-ethylamino-6-isopropylamino-1,3,5-triazine • $C_8H_{14}ClN_5$ • 215.68 g/mol; $[(\mu+1)^+ : 216.10]$ 	
2	Hydroxy-Atrazine <ul style="list-style-type: none"> • 2-hydroxy-4-ethylamino-6-isopropylamino-1,3,5-triazine • $C_8OH_{15}N_5$ • 197.13 g/mol; $[(\mu+1)^+ : 198.14]$ 	
3	<ul style="list-style-type: none"> • 2-hydroxy-4-Acetylamino-6-isopropylamino-1,3,5-triazine • $C_8O_2H_{12}N_5$ • 211.1 g/mol; $[(\mu+1)^+ : 212.1]$ 	
4	<ul style="list-style-type: none"> • 2-hydroxy-4-ethylamino-6-Acetylamino-1,3,5-triazine • $C_7O_2H_{11}N_5$ • 197.1 g/mol; $[(\mu+1)^+ : 198.1]$ 	

No.	Chemical <ul style="list-style-type: none"> • Chemical Name • Molecular formula • Molecular weight; ion 	Chemical Structure
5	De-ethyl-hydroxy-Atrazine <ul style="list-style-type: none"> • 2-hydroxy-4-amino-6-isopropylamino-1,3,5-triazine • $C_6H_{11}N_5$ • 169.11 g/mol; $[(\mu+1)^+ : 170.1]$ 	
6	De-isopropyl-hydroxy-Atrazine <ul style="list-style-type: none"> • 2-amino-4-ethylamino-1,3,5-triazine • $C_5H_9N_5$ • 155.03 g/mol; $[(\mu+1)^+ : 156.04]$ 	
7	Di-dealkyl hydroxy- Atrazine 'or' Ammeline <ul style="list-style-type: none"> • 2-hydroxy-4,6-diamino-1,3,5-triazine • $C_3OH_5N_5$ • 127.04 g/mol; $[(\mu+1)^+ : 128.05]$ 	

9.2 Experimental

9.2.1 Materials and Chemicals

The chemical reagents used in this study were of analytical grade and consumed without further purification. These include atrazine ($C_8H_{14}ClN_5$, Sigma Aldrich, Fluka Analytical Pesternal® Analytical Standard 45330), d_5 -atrazine ($C_8H_9D_5ClN_5$, Sigma Aldrich, Fluka Analytical Pesternal® Analytical Standard) and 2-propanol (99.9%, HPLC Grade, Fisher Scientific). Teflon-lined butyl rubber stopper (PTFE-lined) of size 20mm and aluminium crimp were purchased from Wheaton Inc, and PTFE syringe filters (Supelco©) were used. Other materials are de-ionized water (DI water) and laboratory grade gases that include 5% H_2 balance N_2 . The atrazine stock solution of 100 $\mu\text{g/mL}$ concentration was prepared by dissolving 5 mg of atrazine in 50 mL methanol.

9.2.2 Substrates used

Palladium based catalysts supported on hierarchical carbon structures were used in this study. Palladium (metallic state), palladium oxide, and palladium-silver bimetallic nanoparticles were synthesized on carbon nanotube grafted reticulated vitreous carbon (RVC) foam structures. The fabrication process is discussed in the earlier sections (section 6.2 and section 7.2). The supports used in this study are RVC foam, CNT-RVC foam, Pd-CNT-RVC foam, PdO-CNT-RVC foam, and Ag-Pd on CNT-RVC foam. The weight of sample (e.g. Pd-CNT-RVC weight) used in each reactor was ~ 50 mg.

9.2.3 Batch Degradation Studies

The bench-scale investigation of atrazine degradation was carried out in batch reactors consisting of 160 mL glass serum bottles. The batch experiments were carried

out using palladium based catalyst supports (Pd-CNT, PdO-CNT, and Ag-Pd CNT on RVC foams), with and without hydrogen gas in the reactors. The supported catalysts were attached to the inside wall of the serum bottle using double-sided carbon tape. Two samples, each of size $\text{Ø } 8 \text{ mm} \times 5 \text{ mm}$ and weight $\sim 25 \text{ mg}$ were introduced in each serum bottle and attached to the side walls. Samples were rinsed in 2-propanol and water. Approximately 80 mL of 5% v/v methanol in Milli-Q water was added to the reactors, maintaining the solution to headspace ratio of 50:50. The pH was monitored using a pH meter. The reactors were sealed with Teflon-lined butyl rubber stoppers and aluminum crimps. The reactors were then purged with a high purity 5% H_2 and balance N_2 gas mixture ($[\text{pH}_2] = 0.05 \text{ atm}$) for approximately 30 min. For reactors without hydrogen purging, the reactors were sealed with ambient air. Atrazine stock solution was injected into each reactor (initial atrazine conc. = $1 \mu\text{g mL}^{-1}$ or $4.63 \mu\text{M}$; initial atrazine amount = $0.463 \mu\text{moles}$ in 100 mL) using a gas-tight syringe. The reactors were then placed on an end-over-end rotary shaker at room temperature (60 rpm, 30° inclination). The bottles were placed on the rotator at an inclination such that the solid samples attached on the walls of the reactors remain immersed in liquid-phase at all times during rotation, so that the reactions occur (in liquid-phase) continuously. A control reactor without any support or catalyst material was also investigated.

Aliquot samples of 2 mL were derived from the bottles using a syringe at specified time intervals. Samples collected in the syringe at different reaction times were filtered using disposable PTFE syringe filters. Initially 1 mL aliquot sample was discarded by running it through the filter in order to saturate the filter and then the remaining liquid sample was collected through the saturated filter in a 2 mL vial for HPLC analysis.

9.2.3.1 Internal Standard – d₅-Atrazine

An internal standard was added to the aliquot samples collected in a 2 mL vial for high performance liquid chromatography (HPLC) quantification. In this study, deuterated atrazine - 'd₅-atrazine' compound was used as an internal standard for atrazine analysis. Stock solution of d₅-atrazine was prepared to obtain the concentration 10 µg/mL in 65% (v/v) methanol 2mM acetic acid. 50 µL of d₅-atrazine stock solution (10 µg/mL) was carefully measured using an automatic micro-pipette and added to each vial having 1 mL solution. The concentration of internal standard in each vial was maintained at 0.5 µg/mL.

9.2.4 **Standard Concentration Analysis**

For analytical purpose, standard concentration of atrazine was studied for concentrations ranging from 0.01µg/mL to 1 µg/mL (ppm). The standard solutions were prepared in 10 mL vials by adding the appropriate amount of atrazine stock solution in 5% (v/v) methanol in Milli-Q water. 1 mL solution from each standard was collected in small vials and a known amount of internal standard was added to this for quantitative HPLC analysis.

9.2.5 **Chemical Analysis – HPLC**

Atrazine in water was analyzed by using Waters Micromass Quattro Micro equipped with a mass spectrometer for liquid chromatography (LC-MS) and an auto-sampler. The HPLC column is a Restek Biphenyl Column - Pinnacle DB Biphenyl Column of dimensions 100 x 2.1 mm² (1.9 µm) and temperature was set to 50 °C. A mixture of water and methanol containing 2mM acetic acid (NH₄OAc) was used as the mobile phase. The ratio of methanol to reagent water containing 2mM acetic acid was maintained at 10 : 90 (v/v %) for atrazine analysis. The flow rate of the pump was

set at 0.3 ml/min and the actual sample injection volume was 20 μ l. Each run was conducted for 24 min and the method is shown in section 2.4.8. The method detection limit for atrazine was 0.5 ng/mL. Selective ion reaction monitoring (SIR) was carried out for pure atrazine and the fragment ion spectra was used for MS/MS analysis. SIR for all possible metabolites of atrazine was carried out using analyte solution to determine their formation due to the degradation of atrazine. The liquid analyte samples were analyzed in the multiple reaction mode (MRM) using the fragment ions spectra for MS/MS analysis of atrazine and the possible metabolite (daughter product) compounds.

9.3 Results and Discussion

9.3.1 Atrazine Degradation

Figure 9.1 shows a typical total ion current (TIC) chromatogram acquired from the full scan mode in LC/MS and the graph shows the mass scan data collected over time. From this plot, the atrazine compound is obtained at retention time of ~8 mins using the above mentioned HPLC method. Figure 9.1b shows the multiple reaction monitoring (MRM) analysis modes that shows the mass separation scan acquired in the MS experiment. The MRM peak acquired at 216.2 represents protonated atrazine - ionization ($\mu+1$) of atrazine and the MRM peak acquired at 221.1 represents protonated d_5 -atrazine, ionization ($\mu+1$) of d_5 -atrazine. The ratio of atrazine peak area to d_5 -atrazine peak area is utilized here to control the run-to-run variability in injection and ionization intensity of HPLC. Similarly, other mass compounds were determined using SIR mode and acquired using MRM mode.

Figure 9.2 shows the calibration curves obtained from standard solution analysis by plotting the area ratios of atrazine and d_5 -atrazine peaks with the known

concentrations. The curve shows excellent linearity with the regression coefficient of $R^2 = 0.999$. The calibration curve equation is used for determining the concentration of atrazine in the water samples. The calibration curves were obtained for every experiment.

Figure 9.3 shows the degradation kinetics of atrazine at an initial concentration of 1 $\mu\text{g/mL}$ obtained by CNT foam, Pd-CNT foam, and for the control reactor without hydrogen purging *i.e.* under aerobic conditions of ambient air and with hydrogen purging (Figure 9.3). It is clear from Figure 9.3 that the control reactor with and without hydrogen purging shows no significant effect for the degradation or removal of atrazine. The degradation kinetics obtained for the reactors containing CNT foam structures without H_2 purging shows some reduction (~30%) in atrazine concentration. The Pd-CNT catalysts without H_2 do not show any significant increase in atrazine removal compared to that with the CNT foam. The 30% reduction in concentration using CNT and Pd-CNT without H_2 can be attributed to the adsorption of atrazine on the CNT and/or Pd surface. The CNT foam reactor with hydrogen (Figure 9.3) shows a similar removal rate as its no- H_2 counterpart. However, addition of H_2 to the Pd-CNT reactor shows near-complete degradation of atrazine within 120 minutes as shown in Figure 9.3. This indicates that the degradation reaction of atrazine using Pd catalyst is carried with the aid of H_2 . A study by Nadagouda *et. al.* for degradation of atrazine using Pd and PdO catalyst in ambient air conditions (with no added hydrogen) shows no significant removal of atrazine using palladium catalyst [78].

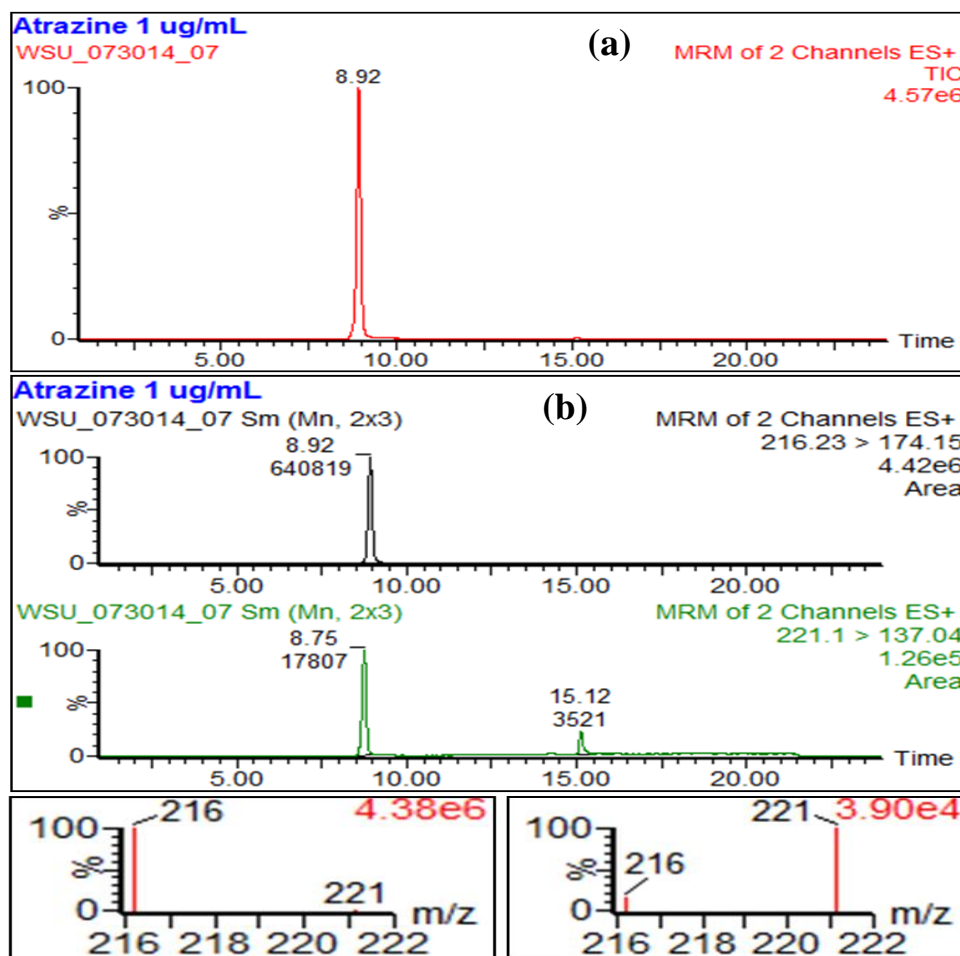


Figure 9.1 A typical (a) full scan TIC chromatograph and (b) LC-MS/MS chromatogram acquired in multiple reaction monitoring mode for Atrazine (216.2) and d₅-Atrazine (221.1) ion channels.

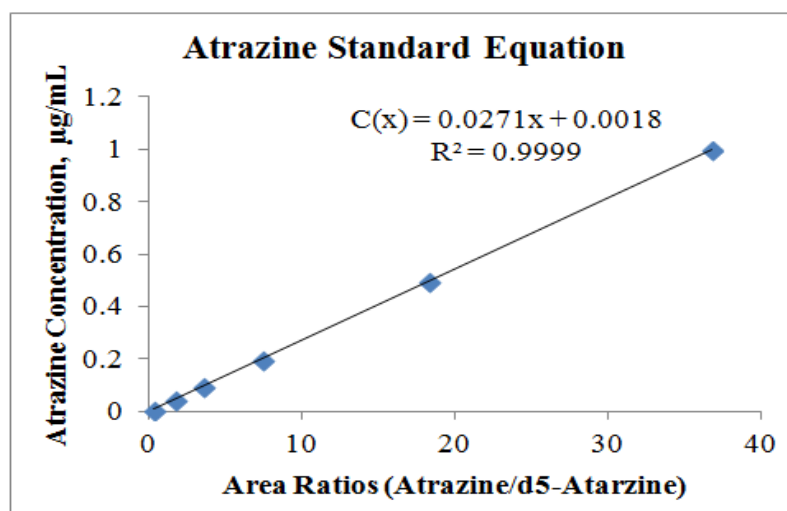


Figure 9.2 Calibration curve of atrazine concentrations varying from 0.01 µg/mL to 1 µg/mL obtained by plotting peak area ratios (Atrazine to d₅-atrazine peak area ratio) with known standard atrazine concentration.

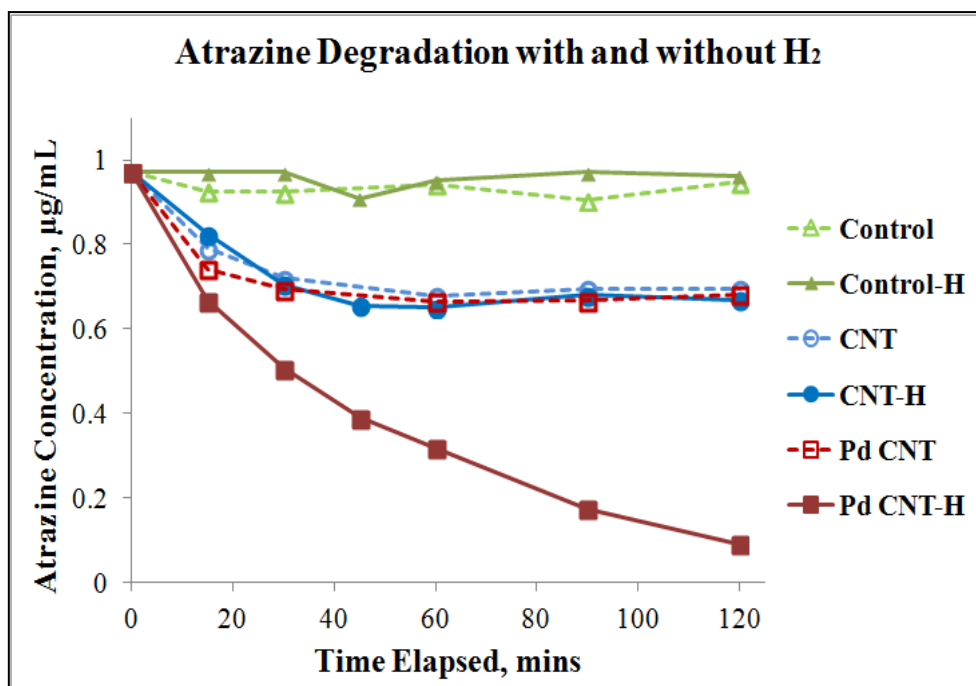


Figure 9.3 Degradation kinetics of atrazine (initial concentration of 1 µg/mL) obtained for the control, CNT foam, and Pd-CNT foam reactor samples with and without H₂ gas purging. Dotted lines are reactions without H₂ purging.

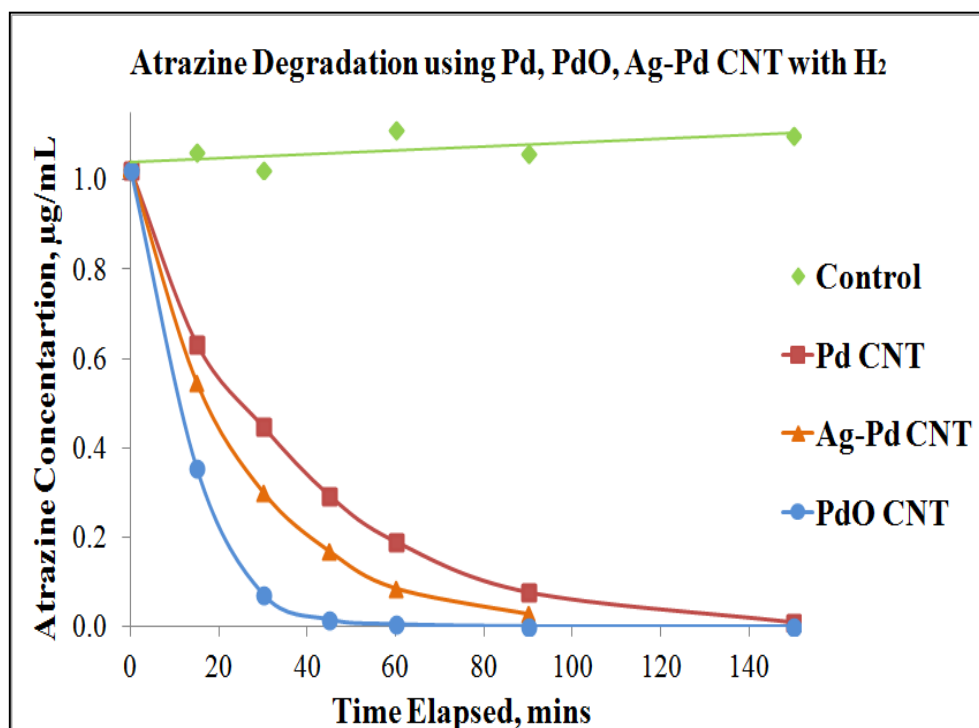


Figure 9.4 Degradation kinetics of atrazine (initial concentration of 1 µg/mL) obtained for the Pd-CNT, PdO-CNT, and bimetallic Ag-Pd CNT foam samples with H₂ gas purging (5% H₂ balance N₂) for 30 minutes.

Figure 9.4 shows the degradation kinetics of atrazine with various Pd-based catalysts and H₂ purging. The catalysts investigated here are Pd-CNT, PdO-CNT, and Ag-Pd CNT foam. It is evident from Figure 9.4 that nanoparticles of Pd-O and Ag-Pd on CNT structure are more effective in catalytic degradation of atrazine compared to Pd-CNT foam samples. Furthermore, the PdO nanoparticles have the highest removal rate that reaches nearly complete degradation within 40 minutes.

9.3.2 Catalyst Chemical Analysis

After the degradation reactions the catalyst samples were retained from the reactors for surface chemical analysis. The samples (Pd, PdO, and Ag-Pd NPs on CNT-foam supports) were rinsed with methanol and water and allowed to dry for up to 48 hours in air. The chemical state of Pd-based catalysts was studied before and after atrazine degradation reactions. The chemical state of Pd-CNT samples for as-prepared and used catalyst is shown in Figure 9.5a. The Pd $3d_{5/2}$ peak at 335.3 eV for Pd-CNT sample remains unchanged after atrazine degradation. Figure 9.5b shows the fine scan of Pd $3d$ peak obtained from PdO_{250°C} sample before and after atrazine degradation. It can be observed that the partially oxidized PdO sample reduced to fully metallic state after degradation as the Pd $3d_{5/2}$ peak of Pd²⁺ at 336.9 eV shifts towards the 335.3 ± 0.1 eV, indicating release of surface oxide. The chemical state of Ag and Pd in Ag-Pd CNT samples remains unchanged after atrazine degradation (spectra not shown here). The fine-scan spectra of C $1s$ (not shown here) after atrazine degradation shows a satellite peak at around ~ 286 eV that can be attributed to the adsorbed impurities on CNT.

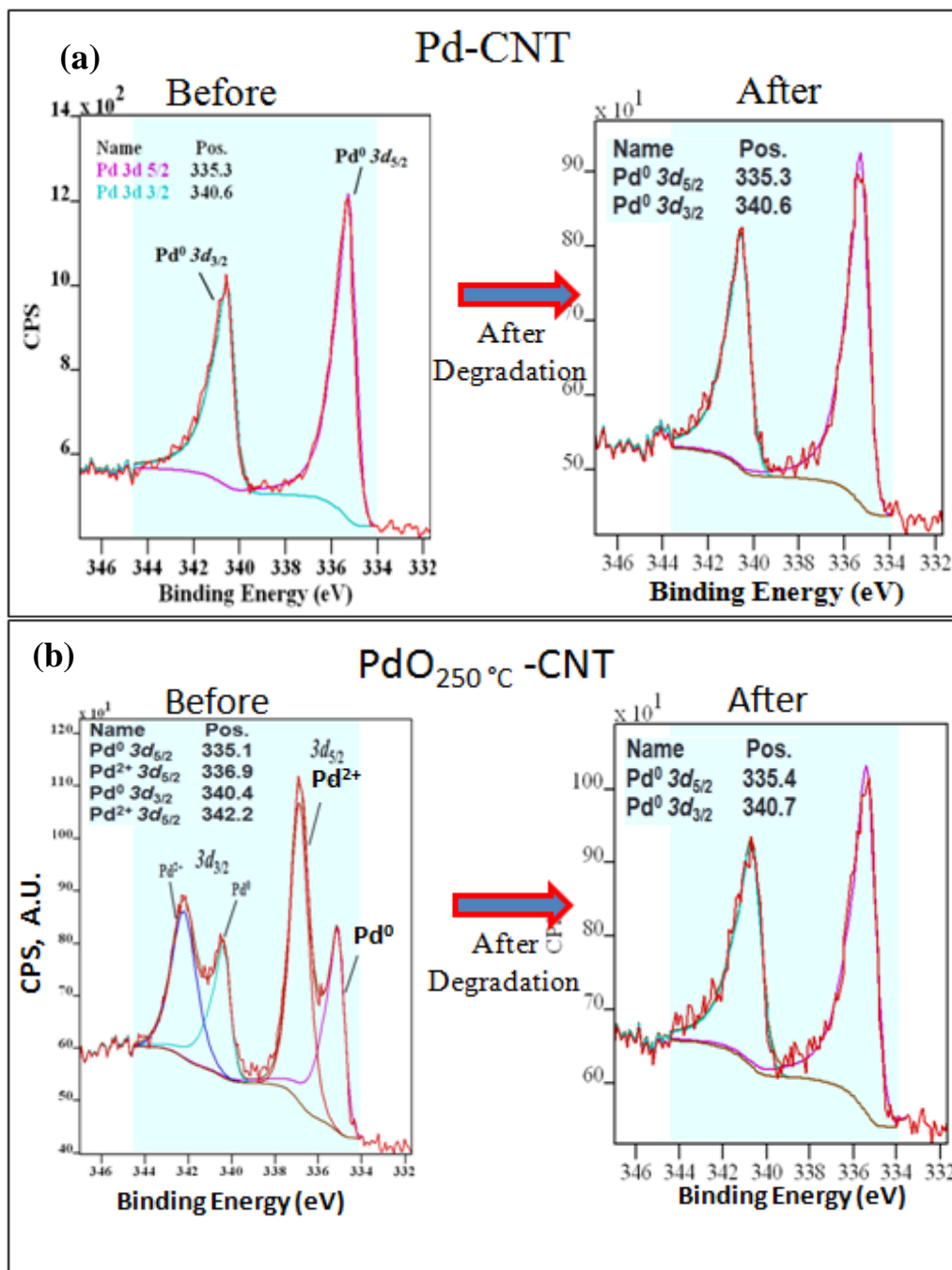


Figure 9.5 XPS Pd 3d fine-scan spectra of before and after atrazine degradation using (a) Pd-CNT and (b) PdO-CNT on RVC foam

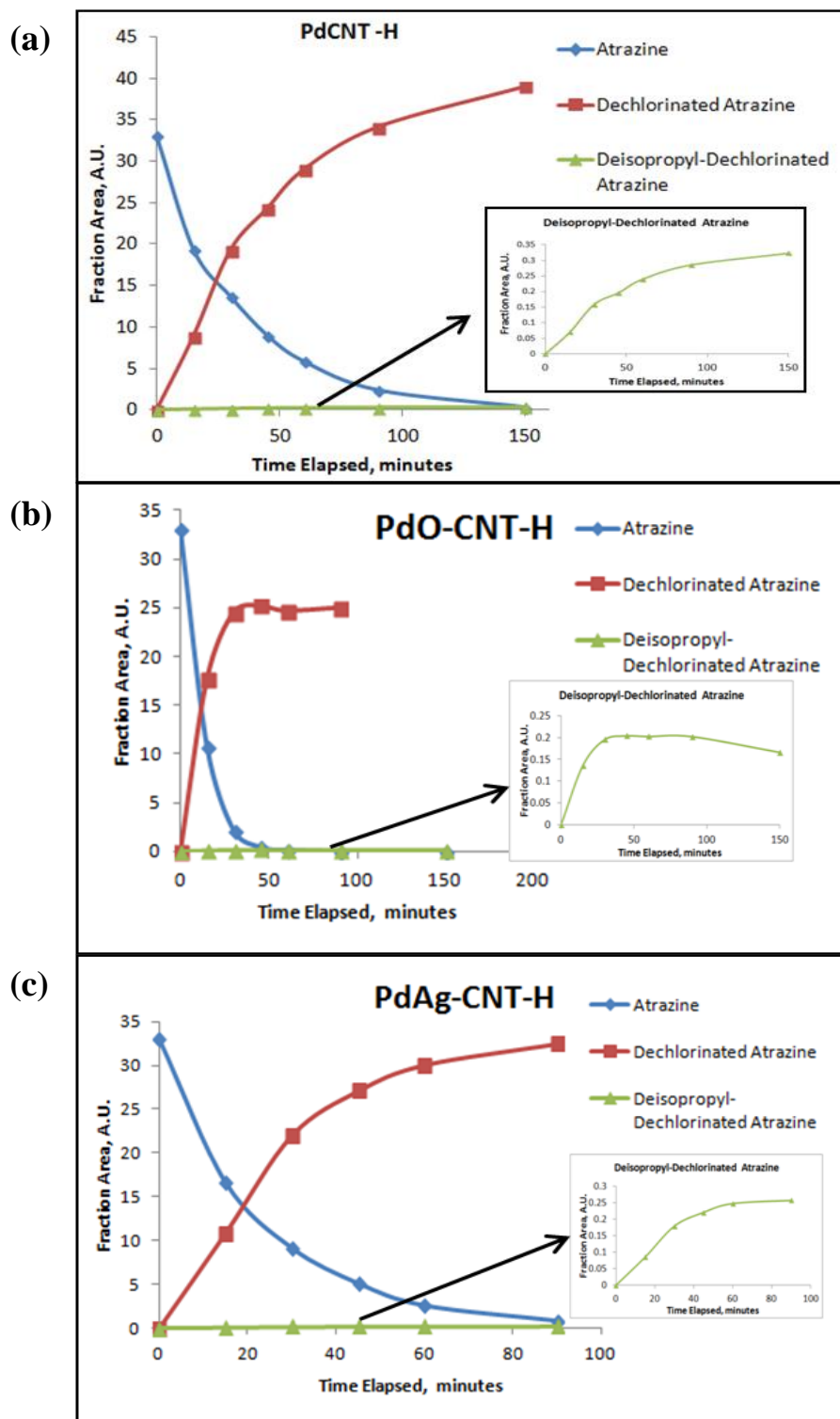


Figure 9.6. Atrazine degradation and daughter products formation curves with (a) Pd-CNT Foam, (b) PdO-CNT Foam, and (c) Ag-Pd CNT Foam samples in the presence of hydrogen gas.

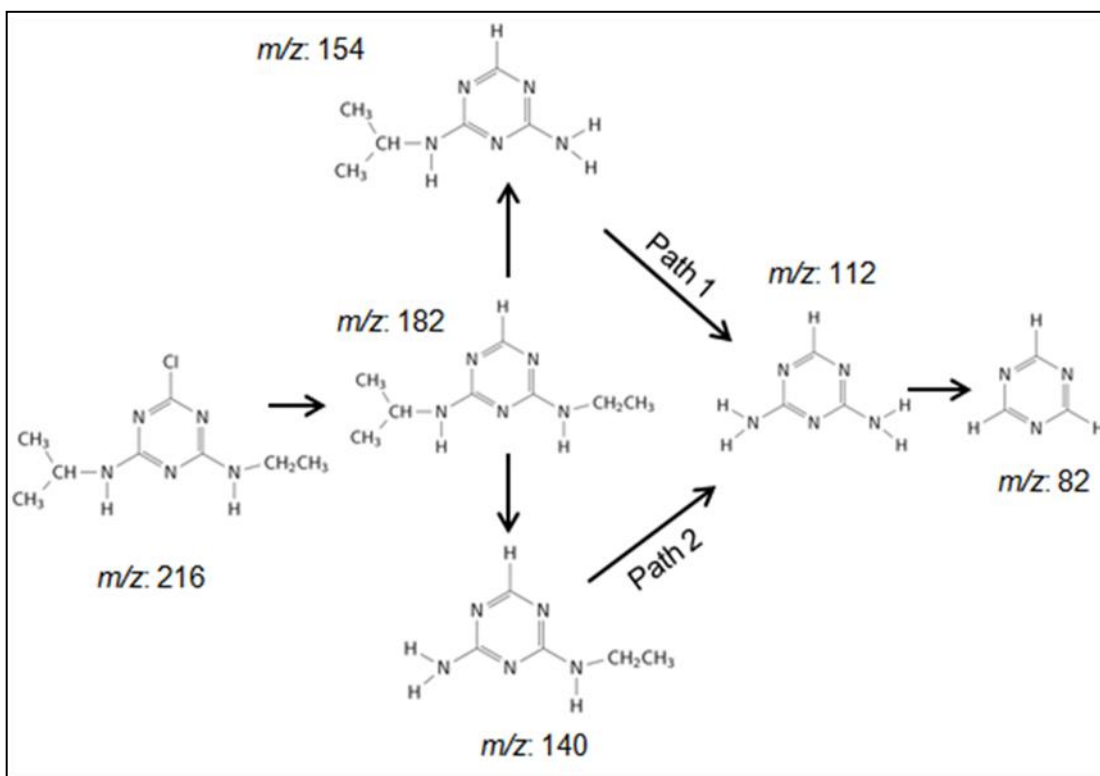


Figure 9.7 Proposed mechanism for hydrogenated products of atrazine - catalytic degradation with palladium based catalysts in the presence of hydrogen

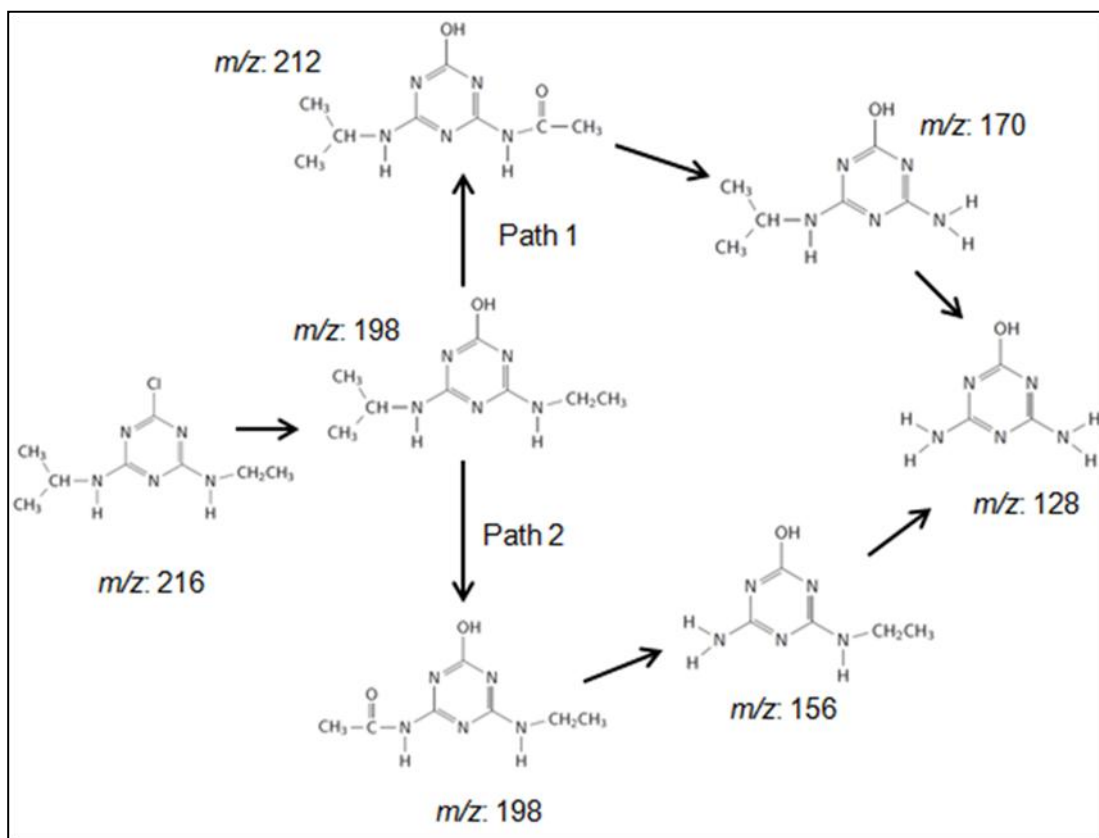


Figure 9.8 Proposed mechanism for hydroxylated products of atrazine - catalytic degradation with palladium (oxide) catalysts in the presence of hydrogen [151], [153]

9.3.3 Daughter Products Formation

Degradation of atrazine using palladium-based catalysts in the presence of hydrogen gas forms various daughter compounds. Some of the most common daughter products are shown in Figure 9.6. The daughter compounds include significant amounts of dechlorinated atrazine and deisopropyl-dechlorinated atrazine. Only trace amounts of de-ethyl-dechlorinated atrazine and de-ethyl-deisopropyl-dechlorinated atrazine were observed. As shown in Figure 9.6, the degradation of atrazine yielded dechlorinated atrazine compound as the major product of the reaction in all cases and this formation correlates well with the decrease in atrazine concentration. Formation of trace amounts of other daughter products indicate further reduction of dechlorinated atrazine.

9.3.4 Atrazine Degradation Mechanism with Pd/H₂ System

In this study, aqueous phase degradation of atrazine at ambient temperatures was accomplished using Pd-based catalysts on hierarchical carbon supports in the presence of H₂ gas as a reducing agent. A proposed mechanism for the degradation of atrazine using palladium and hydrogen is shown in Figure 9.7. This figure shows the possible daughter products of atrazine as a result of degradation. As shown in this figure, reduction of atrazine can happen through various reaction pathways. The favorable catalyzed reaction pathway often observed is where atrazine yields dechlorinated atrazine [152]. Reduction of dechlorinated atrazine to de-isopropyl-dechlorinated atrazine was observed, subsequently leading to formation of “Guanmine” in trace amounts using path 2 as shown in Figure 9.7 (Refer to Table 9.1 for labels). Some traces of de-ethyl-de-chlorinated atrazine were observed indicating reduction with path 1. In this study, using Pd-based catalysts and Ag-Pd catalysts in the presence of H₂, atrazine is catalytically reduced to dechlorinated-atrazine. The

degradation mechanism presumably involves steps that include dissociative adsorption of chemical species on the surface of the Pd (through dissociation of H₂ and atrazine into intermediate species on the active sites), chemical reaction between the intermediate species forming the reduced product including HCl, and the desorption of the final products from the catalyst surface or further degradation of the adsorbed intermediate species into the smaller daughter products.

The degradation mechanism using PdO can be different as compared to Pd-based catalyst. The proposed degradation mechanism of atrazine with PdO catalyst in the presence of H₂ is shown in Figure 9.8. With PdO catalyst in the presence of H₂ the degradation of atrazine is significantly fast, but the formation of detected daughter product (dechlorinated atrazine) is low (Figure 9.6c). There may be additional products such as hydroxylated atrazine [151]–[153], with PdO and H₂, as it was observed that the oxide layer was released from the PdO surface forming reduced Pd after degradation. The degradation of atrazine using Ag-Pd bimetallic nanoparticles in the presence of H₂ was observed to follow a similar mechanism as with Pd-NPs.

9.4 Conclusion

In this study, Pd, PdO, and Ag/Pd on hierarchical carbon structures were used as catalysts in the presence of hydrogen gas for degradation of a model emerging contaminant, atrazine, in water. It was found that the performance of the Pd-based catalyst is greatly influenced by the presence of hydrogen in the reactors to catalyze the degradation reactions. Moreover, it was observed that PdO as a catalyst has higher activity compared to Pd and Ag/Pd on hierarchical substrates. The catalytic activity for degradation of atrazine in the presence of hydrogen follows the order: PdO-CNT > Ag/Pd-CNT > Pd-CNT. Complete degradation of atrazine was observed with the Pd-based catalysts in the presence of hydrogen, where atrazine initially transformed to

form dechlorinated-atrazine and de-ethyl-deisopropyl-dechlorinated-atrazine. This architecture of catalyst particles attached to larger hierarchical carbon supports can be recovered easily. Such structures may therefore provide a nonpolluting, reusable, and cost-effective solution for the removal of pollutants from contaminated water.

10 Summary

In this study, various porous structures - cellular carbon foams and reticulated vitreous carbon foams having different porosities and pore densities were investigated for fabrication of hierarchical carbon structures. Approaches of maximizing the surface functionalities by enhancing the pore surfaces with vertically aligned carpet-like arrays of carbon nanotubes (CNT) were investigated. CNT arrays can be grown on surfaces of interconnected porous foams by pre-activating them with an oxide buffer layer followed by Chemical Vapor Deposition (CVD). Key process parameters were identified for controlling the growth rate of CNT and the permeation of CNT through the porous structure were investigated. It was seen that longer CVD run times results in increased length of CNT arrays overall, and creating a thickness gradient of the silica buffer layer (thicker buffer layer towards the back end of the porous substrate) improved the CNT permeation deeper into the pores. This type of hierarchical morphology increases surface area by several orders of magnitude, and provides opportunity of tuning the morphology for targeted applications by varying the packing density and/or the height of CNT arrays. Analytical models using surface morphologies to estimate the specific surface area of CNT arrays on porous structures were developed using input from two experimental methods: microstructural analysis and weight gain method. The SSA increase matches well with BET measurements and the reported surface adsorption data indicates that the entire surface functionality of individual nanotubes in the carpet (arrays) are retained in this multiscale architecture.

The hierarchical carbon structures obtained by grafting aligned carbon nanotubes on porous structures were used as adsorbents for removal of a model contaminant, methylene blue, from water. It was found that adsorption of dye on the

CNT-foam hybrids is greatly influenced by the amount of CNT on the foam, which dominates the specific surface area of the material. The maximum adsorption capacity for MB on CNT arrays is about 43.5 mg/g, which compares very favorably with other advanced, less durable, nanomaterials reported in the literature.

In this study, Pd-NPs, PdO-NPs and Ag-Pd bimetallic NPs were synthesized on vertically aligned carbon nanotubes attached to porous structures forming multi-scale architecture. Thermal oxidation of Pd-NPs in air forms oxidized palladium nanoparticles. XPS analysis shows that Pd-NPs can be partially oxidized or fully oxidized by thermal heating at 250 °C or 300 °C, respectively. Silver was synthesized on Pd-NPs using a chemical reduction process. The XPS and EDS qualitatively analyses for Ag-Pd samples indicate that Pd nanoparticles may possibly have a layer of Ag coating on the surface.

The palladium based hierarchical structures were employed in water purification for removal of aqueous contaminants such as atrazine, trichloroethylene, and trichloroethane. All degradation rates in the presence of hydrogen follows the order PdO-CNT > Ag/Pd-CNT > Pd-CNT. It was seen that atrazine is mostly transformed to dechlorinated-atrazine and trace de-ethyl-deisopropyl-dechlorinated atrazine. TCE and TCA also show complete dechlorination, mostly forming butane and dichloroethane, respectively, as daughter products.

This study shows that anchoring carbon nanotube carpets on these types of porous substrates may be a very practical approach to create robust solid devices that fully utilize the surface area benefits of carbon nanotubes without dispersing loose nanomaterials in the environment. This makes them reusable and eco-friendly solids that can provide very effective and portable water purification devices.

11 Future Work

The current results can be expanded to a broader range of applications involving high surface area solids. A few examples of future applications are briefly summarized here.

1. **Hydrogen Storage:** Palladium is known to absorb hydrogen by forming palladium-hydride under certain temperature and pressure conditions. This property has received significant interest in the scientific community for exploring new materials for hydrogen sensing, storage, separation, extraction, and transport applications. The hydrogen storage capacity of Pd-NPs attached on CNT grafted foam supports can be determined using the chemisorption BET method with hydrogen as the carrier gas.
2. **Electrodes:** The robustness and high surface area of catalyst palladium particles attached on CNT-porous foam hybrids can be attractive as electrode materials for fuel cell or electrochemical cell applications.
3. **Bimetallic Systems:** Synthesis and characterization of various bimetallic nanoparticles systems including Pd, Pt, Ag, or Fe on the hybrid structures can be designed. These can have applications in sensors, electrodes, and environmental purification.
4. **Detailed Catalysis Studies:** Palladium or bimetallic systems of palladium with silver, iron or platinum for additional emerging contaminants such as bisphenol-A, triclosan, pharmaceutical, perfluorooctanoic acid, nitrate compounds or a mixture of compounds to simulate real wastewater conditions can be possible future work issues. Studies involving influence of particles sizes, deactivation of catalyst, regeneration issues, and in-column flow reactor studies are required in future to expand determining the practical applications of these materials.

5. **Surface Characterization and Ion Leaching:** Future studies to understand the catalysis pathway and possible leaching of catalyst ions in water are needed.
6. **Computational Modeling:** The interactions of catalyst particles on the CNT can be studied using molecular modeling and quantum mechanics. Also, the adsorption of environmental pollutants such as dyes are attributed to various adsorption interaction mechanisms such as hydrogen bonding, electrostatic interactions, defect filling, and strong π - π interactions with CNT [110]. Possible non-covalent interaction of cationic methylene blue dye or similar organic pollutant compounds with multi-walled carbon nanotubes using molecular dynamics simulation should be investigated.
7. **High Surface Area Porous Structures:** The correlation of process parameter described in this research for permeation of CNT through porous structures can be used as baseline to grow CNT on other interconnected porous geometries.

12 Bibliography

- [1] M. E. Davis, “Ordered porous materials for emerging applications,” *Nature*, vol. 417, pp. 813–821, 2002.
- [2] H. Chae, D. Siberio-Pérez, J. Kim, Y. Go, M. Eddaoudi, A. J. Matzger, M. O’Keeffe, and O. M. Yaghi, “A route to high surface area, porosity and inclusion of large molecules in crystals,” *Nature*, vol. 427, no. February, pp. 523–527, 2004.
- [3] J. Rouquerol, D. Avnir, C. W. Fairbridge, D. H. Everett, J. H. Haynes, N. Pernicone, J. D. F. Ramsay, K. S. W. Sing, and K. K. Unger, “Recommendations for the characterization of porous solids,” *Int. Union Pure Appl. Chem.*, vol. 66, no. 8, pp. 1739–1758, 1994.
- [4] B. D. Zdravkov, J. J. Čermák, M. Šefara, and J. Janků, “Pore classification in the characterization of porous materials: A perspective,” *Cent. Eur. J. Chem.*, vol. 5, no. 2, pp. 385–395, Mar. 2007.
- [5] M. A. Meyers, P.-Y. Chen, A. Y.-M. Lin, and Y. Seki, “Biological materials: Structure and mechanical properties,” *Prog. Mater. Sci.*, vol. 53, pp. 1–206, Jan. 2008.
- [6] P.-Y. Chen, A. Y. M. Lin, Y.-S. Lin, Y. Seki, A. G. Stokes, J. Peyras, E. A. Olevsky, M. A. Meyers, and J. McKittrick, “Structure and mechanical properties of selected biological materials,” *J. Mech. Behav. Biomed. Mater.*, vol. 1, no. 3, pp. 208–26, Jul. 2008.
- [7] J. Aizenberg and P. Fratzl, “Biological and Biomimetic Materials,” *Adv. Mater.*, vol. 21, no. 4, pp. 387–388, Jan. 2009.
- [8] Z.-Y. Yuan and B.-L. Su, “Insights into hierarchically meso–macroporous structured materials,” *J. Mater. Chem.*, vol. 16, no. 7, pp. 663–677, 2006.
- [9] G. G. Wildgoose, C. E. Banks, and R. G. Compton, “Metal nanoparticles and related materials supported on carbon nanotubes: methods and applications,” *Small*, vol. 2, no. 2, pp. 182–93, Feb. 2006.

- [10] H. Hou and D. H. Reneker, "Carbon Nanotubes on Carbon Nanofibers: A Novel Structure Based on Electrospun Polymer Nanofibers," *Adv. Mater.*, vol. 16, no. 1, pp. 69–73, Jan. 2004.
- [11] C. Lai, Q. Guo, X. Wu, D. H. Reneker, and H. Hou, "Growth of carbon nanostructures on carbonized electrospun nanofibers with palladium nanoparticles," *Nanotechnology*, vol. 19, p. 195303, 2008.
- [12] B. Q. Wei, R. Vajtai, Y. Jung, J. Ward, R. Zhang, G. Ramanath, and P. M. Ajayan, "Organized assembly of carbon nanotubes," *Nature*, vol. 416, pp. 495–496, 2002.
- [13] E. Zawadzak, M. Bil, J. Ryszkowska, S. N. Nazhat, J. Cho, O. Bretcanu, J. a Roether, and A. R. Boccaccini, "Polyurethane foams electrophoretically coated with carbon nanotubes for tissue engineering scaffolds.," *Biomed. Mater.*, vol. 4, no. 1, p. 015008, Feb. 2009.
- [14] W. Wang, S. Guo, M. Penchev, I. Ruiz, K. N. Bozhilov, D. Yan, M. Ozkan, and C. S. Ozkan, "Three dimensional few layer graphene and carbon nanotube foam architectures for high fidelity supercapacitors," *Nano Energy*, vol. 2, no. 2, pp. 294–303, Mar. 2013.
- [15] S. M. Mukhopadhyay, A. Karumuri, and I. T. Barney, "Hierarchical nanostructures by nanotube grafting on porous cellular surfaces," *J. Phys. D. Appl. Phys.*, vol. 42, no. 19, p. 195503, Oct. 2009.
- [16] H. Vijwani and S. M. Mukhopadhyay, "Palladium nanoparticles on hierarchical carbon surfaces : A new architecture for robust nano-catalysts," *Appl. Surf. Sci.*, vol. 263, pp. 712–721, 2012.
- [17] H. Vijwani, A. Agrawal, and S. M. Mukhopadhyay, "Dechlorination of Environmental Contaminants Using a Hybrid Nanocatalyst: Palladium Nanoparticles Supported on Hierarchical Carbon Nanostructures," *J. Nanotechnol.*, vol. 2012, pp. 1–9, 2012.
- [18] H. Vijwani, "Highly Active Porous Catalysts Fabricated By Attachment of Palladium Nanoparticles on Hierarchical Carbon Structures," 2011.

- [19] A. Demirbas, "Agricultural based activated carbons for the removal of dyes from aqueous solutions: a review," *J. Hazard. Mater.*, vol. 167, no. 1–3, pp. 1–9, Aug. 2009.
- [20] C.-L. Lee, Y.-C. Huang, L.-C. Kuo, and Y.-W. Lin, "Preparation of carbon nanotube-supported palladium nanoparticles by self-regulated reduction of surfactant," *Carbon N. Y.*, vol. 45, pp. 203–228, Jan. 2007.
- [21] N. Savage and M. S. Diallo, "Nanomaterials and Water Purification: Opportunities and Challenges," *J. Nanoparticle Res.*, vol. 7, pp. 331–342, Oct. 2005.
- [22] C. M. Sayes, J. D. Fortner, W. Guo, D. Lyon, A. M. Boyd, K. D. Ausman, Y. J. Tao, B. Sitharaman, L. J. Wilson, J. B. Hughes, J. L. West, and V. L. Colvin, "The Differential Cytotoxicity of Water-soluble Fullerenes," *Nano Lett.*, vol. 4, no. 10, pp. 1881–1887, 2004.
- [23] J. M. Friedrich, C. Ponce-de-León, G. W. Reade, and F. C. Walsh, "Reticulated vitreous carbon as an electrode material," *J. Electroanal. Chem.*, vol. 561, pp. 203–217, Jan. 2004.
- [24] R. V. Pulikollu and S. M. Mukhopadhyay, "Nanoscale coatings for control of interfacial bonds and nanotube growth," *Appl. Surf. Sci.*, vol. 253, pp. 7342–7352, Jun. 2007.
- [25] P. Marcus and C. Hinnen, "XPS study of the early stages of deposition of Ni, Cu and Pt on HOPG," *Surf. Sci.*, vol. 392, pp. 134–142, Dec. 1997.
- [26] W. Lu, M. Zu, J.-H. Byun, B.-S. Kim, and T.-W. Chou, "State of the art of carbon nanotube fibers: opportunities and challenges," *Adv. Mater.*, vol. 24, no. 14, pp. 1805–33, Apr. 2012.
- [27] A. Stein, Z. Wang, and M. a. Fierke, "Functionalization of Porous Carbon Materials with Designed Pore Architecture," *Adv. Mater.*, vol. 21, no. 3, pp. 265–293, Jan. 2009.
- [28] L. Borchardt, M. Oschatz, and S. Kaskel, "Tailoring porosity in carbon materials for supercapacitor applications," *Mater. Horizons*, vol. 1, no. 2, pp. 157–168, 2014.

- [29] C. J. Shearer, A. Cherevan, and D. Eder, "Application and future challenges of functional nanocarbon hybrids," *Adv. Mater.*, vol. 26, no. 15, pp. 2295–318, Apr. 2014.
- [30] K. Nakagawa, "Foam Materials Made from Carbon Nanotubes," in *Carbon Nanotubes - From Research to Applications*, S. Bianco, Ed. 2011.
- [31] X. Gui, J. Wei, K. Wang, A. Cao, H. Zhu, Y. Jia, Q. Shu, and D. Wu, "Carbon nanotube sponges," *Adv. Mater.*, vol. 22, no. 5, pp. 617–21, Feb. 2010.
- [32] Y. Lan, Y. Wang, and Z. F. Ren, "Physics and applications of aligned carbon nanotubes," *Adv. Phys.*, vol. 60, no. 4, pp. 553–678, 2011.
- [33] P. M. Ajayan and O. Z. Zhou, "Applications of Carbon Nanotubes," in *Carbon Nanotubes: Synthesis, Structure, Properties, and Applications*, vol. 425, M. S. Dresselhaus, G. Dresselhaus, and Ph. Avouris, Eds. Springer-Verlag Berlin Heidelberg, 2001, pp. 391–425.
- [34] R. Andrews and M. . Weisenberger, "Carbon nanotube polymer composites," *Curr. Opin. Solid State Mater. Sci.*, vol. 8, no. 1, pp. 31–37, Jan. 2004.
- [35] Z. Spitalsky, D. Tasis, K. Papagelis, and C. Galiotis, "Carbon nanotube–polymer composites: Chemistry, processing, mechanical and electrical properties," *Prog. Polym. Sci.*, vol. 35, no. 3, pp. 357–401, Mar. 2010.
- [36] J. Zhao, W. Ren, and H.-M. Cheng, "Graphene sponge for efficient and repeatable adsorption and desorption of water contaminations," *J. Mater. Chem.*, vol. 22, no. 38, p. 20197, 2012.
- [37] P. W. A. M. Wenmakers, J. van der Schaaf, B. F. M. Kuster, and J. C. Schouten, "'Hairy Foam': carbon nanofibers grown on solid carbon foam. A fully accessible, high surface area, graphitic catalyst support," *J. Mater. Chem.*, vol. 18, no. 21, pp. 2426–2436, 2008.
- [38] B. Q. Wei, R. Vajtai, Y. Jung, J. Ward, R. Zhang, G. Ramanath, and P. M. Ajayan, "Assembly of Highly Organized Carbon Nanotube Architectures by Chemical Vapor Deposition," *Chem. Mater.*, vol. 15, pp. 1598–1606, 2003.
- [39] C. Gommès, S. Blacher, C. Bossuot, P. Marchot, J. B. Nagy, and J.-P. Pirard, "Influence of the operating conditions on the production rate of multi-walled

- carbon nanotubes in a CVD reactor,” *Carbon N. Y.*, vol. 42, no. 8–9, pp. 1473–1482, Jan. 2004.
- [40] C. Singh, M. Shaffer, I. Kinloch, and A. Windle, “Production of aligned carbon nanotubes by the CVD injection method,” *Phys. B Condens. Matter*, vol. 323, no. 1–4, pp. 339–340, Oct. 2002.
- [41] G. Zhang, D. Mann, L. Zhang, A. Javey, Y. Li, E. Yenilmez, Q. Wang, J. P. Mcvittie, Y. Nishi, J. Gibbons, and H. Dai, “Ultra-high-yield growth of vertical single-walled carbon nanotubes: Hidden roles of hydrogen and oxygen,” *PNAS*, vol. 102, no. 45, pp. 16141–16145, 2005.
- [42] C. Singh, M. S. P. Shaffer, and A. H. Windle, “Production of controlled architectures of aligned carbon nanotubes by an injection chemical vapour deposition method,” *Carbon N. Y.*, vol. 41, pp. 359–368, 2003.
- [43] W. Cho, M. Schulz, and V. Shanov, “Growth and characterization of vertically aligned centimeter long CNT arrays,” *Carbon N. Y.*, vol. 72, pp. 264–273, Jun. 2014.
- [44] C. Singh, M. S. . Shaffer, K. K. . Koziol, I. a Kinloch, and A. H. Windle, “Towards the production of large-scale aligned carbon nanotubes,” *Chem. Phys. Lett.*, vol. 372, no. 5–6, pp. 860–865, May 2003.
- [45] C. Zhang, F. Yan, C. S. Allen, B. C. Bayer, S. Hofmann, B. J. Hickey, D. Cott, G. Zhong, and J. Robertson, “Growth of vertically-aligned carbon nanotube forests on conductive cobalt disilicide support,” *J. Appl. Phys.*, vol. 108, no. 2, p. 024311, 2010.
- [46] C. R. Oliver, E. S. Polsen, E. R. Meshot, S. Tawfick, S. J. Park, M. Bedewy, and A. J. Hart, “Statistical Analysis of Variation in Laboratory Growth of Carbon Nanotube Forests and Recommendations for Improved Consistency,” *ACS Nano*, vol. 7, no. 4, pp. 3565–3580, 2013.
- [47] G. D. Nessim, A. J. Hart, J. S. Kim, D. Acquaviva, J. Oh, C. D. Morgan, M. Seita, J. S. Leib, and C. V Thompson, “Tuning of Vertically-Aligned Carbon Nanotube Diameter and Areal Density through Catalyst Pre-Treatment,” 2008.

- [48] Y. C. Choi, Y. M. Shin, Y. H. Lee, B. S. Lee, G.-S. Park, W. B. Choi, N. S. Lee, and J. M. Kim, "Controlling the diameter, growth rate, and density of vertically aligned carbon nanotubes synthesized by microwave plasma-enhanced chemical vapor deposition," *Appl. Phys. Lett.*, vol. 76, no. 17, p. 2367, 2000.
- [49] J. Bin In, C. P. Grigoropoulos, A. A. Chernov, and A. Noy, "Growth Kinetics of Vertically Aligned Carbon Nanotube Arrays in Clean Oxygen-free Conditions," no. 12, pp. 9602–9610, 2011.
- [50] W. Cho, M. Schulz, and V. Shanov, "Growth termination mechanism of vertically aligned centimeter long carbon nanotube arrays," *Carbon N. Y.*, vol. 69, pp. 609–620, Apr. 2014.
- [51] O. a. Louchev, T. Laude, Y. Sato, and H. Kanda, "Diffusion-controlled kinetics of carbon nanotube forest growth by chemical vapor deposition," *J. Chem. Phys.*, vol. 118, no. 16, p. 7622, 2003.
- [52] I. T. Barney, "Fabrication and Testing of Hierarchical Carbon Nanostructures for Multifunctional Applications," Wright State University, 2012.
- [53] S. Fan, M. G. Chapline, N. R. Franklin, T. W. Tomblor, A. M. Cassell, and H. Dai, "Self-Oriented Regular Arrays of Carbon Nanotubes and Their Field Emission Properties," *Science (80-.)*, vol. 283, no. January, pp. 512–514, 1999.
- [54] M. Terrones, N. Grobert, J. Olivares, J. P. Zhang, H. Terrones, K. Kordatos, W. K. Hsu, J. P. Hare, P. D. Townsend, K. Prassides, A. K. Cheetham, H. W. Kroto, and D. R. M. Walton, "Controlled production of aligned-nanotube bundles," *Nature*, vol. 388, no. July, pp. 961–963, 1997.
- [55] G. D. Nessim, A. Al-Obeidi, H. Grisar, E. S. Polsen, C. Ryan Oliver, T. Zimrin, a. John Hart, D. Aurbach, and C. V. Thompson, "Synthesis of tall carpets of vertically aligned carbon nanotubes by in situ generation of water vapor through preheating of added oxygen," *Carbon N. Y.*, vol. 50, no. 11, pp. 4002–4009, Sep. 2012.

- [56] J. R. Raney, A. Misra, and C. Daraio, "Tailoring the microstructure and mechanical properties of arrays of aligned multiwall carbon nanotubes by utilizing different hydrogen concentrations during synthesis," *Carbon N. Y.*, vol. 49, no. 11, pp. 3631–3638, Sep. 2011.
- [57] S. Esconjauregui, M. Fouquet, B. C. Bayer, C. Ducati, R. Smajda, S. Hofmann, and J. Robertson, "Growth of Ultrahigh Density Vertically Aligned Carbon Nanotube Forests for Interconnects," *ACS Nano*, vol. 4, no. 12, pp. 7431–7436, 2010.
- [58] H. Vijwani, M. N. Nadagouda, V. Namboodiri, and S. M. Mukhopadhyay, "Hierarchical hybrid carbon nano-structures as robust and reusable adsorbents: Kinetic studies with model dye compound," *Chem. Eng. J.*, vol. 268, pp. 197–207, May 2015.
- [59] P. M. Ajayan, "Nanotubes from Carbon.," *Chem. Rev.*, vol. 99, no. 7, pp. 1787–1799, Jul. 1999.
- [60] C. Laurent, E. Flahaut, and a. Peigney, "The weight and density of carbon nanotubes versus the number of walls and diameter," *Carbon N. Y.*, vol. 48, no. 10, pp. 2994–2996, Aug. 2010.
- [61] A. Peigney, C. Laurent, E. Flahaut, R. R. Bacsa, and A. Rousset, "Specific surface area of carbon nanotubes and bundles of carbon nanotubes," *Carbon N. Y.*, vol. 39, pp. 507–514, 2001.
- [62] H. Bouwer, "Integrated water management: emerging issues and challenges," *Agric. Water Manag.*, vol. 45, no. 3, pp. 217–228, Aug. 2000.
- [63] S. D. Richardson, M. J. Plewa, E. D. Wagner, R. Schoeny, and D. M. DeMarini, "Occurrence, genotoxicity, and carcinogenicity of regulated and emerging disinfection by-products in drinking water: a review and roadmap for research," *Mutat. Res.*, vol. 636, no. 1–3, pp. 178–242, 2007.
- [64] R. Benigni and C. Bossa, "Mechanisms of chemical carcinogenicity and mutagenicity: a review with implications for predictive toxicology.," *Chem. Rev.*, vol. 111, no. 4, pp. 2507–36, Apr. 2011.

- [65] G. O. Bizzigotti, H. Castelly, A. M. Hafez, W. H. B. Smith, and M. T. Whitmire, "Parameters for evaluation of the fate, transport, and environmental impacts of chemical agents in marine environments," *Chem. Rev.*, vol. 109, no. 1, pp. 236–56, Jan. 2009.
- [66] R. E. Doherty, "A History of the Production and Use of Carbon Tetrachloride, Tetrachloroethylene, Trichloroethylene and 1,1,1-Trichloroethane in the United States: Part 2--Trichloroethylene and 1,1,1-Trichloroethane," *Environ. Forensics*, vol. 1, no. 2, pp. 83–93, Jan. 2000.
- [67] H. M. Pinheiro, E. Touraud, and O. Thomas, "Aromatic amines from azo dye reduction: status review with emphasis on direct UV spectrophotometric detection in textile industry wastewaters," *Dye. Pigment.*, vol. 61, no. 2, pp. 121–139, May 2004.
- [68] S. Srivastava, R. Sinha, and D. Roy, "Toxicological effects of malachite green," *Aquat. Toxicol.*, vol. 66, pp. 319–329, Feb. 2004.
- [69] A. Y. Zahrim and N. Hilal, "Treatment of highly concentrated dye solution by coagulation/flocculation–sand filtration and nanofiltration," *Water Resour. Ind.*, vol. 3, pp. 23–34, Sep. 2013.
- [70] Y. Yao, F. Xu, M. Chen, Z. Xu, and Z. Zhu, "Adsorption behavior of methylene blue on carbon nanotubes," *Bioresour. Technol.*, vol. 101, no. 9, pp. 3040–6, May 2010.
- [71] S. Wang, C. W. Ng, W. Wang, Q. Li, and Z. Hao, "Synergistic and competitive adsorption of organic dyes on multiwalled carbon nanotubes," *Chem. Eng. J.*, vol. 197, pp. 34–40, Jul. 2012.
- [72] G. Crini, "Non-conventional low-cost adsorbents for dye removal: A review," *Bioresour. Technol.*, vol. 97, no. 9, pp. 1061–85, Jun. 2006.
- [73] N. Bao, Y. Li, Z. Wei, G. Yin, and J. Niu, "Adsorption of Dyes on Hierarchical Mesoporous TiO₂ Fibers and Its Enhanced Photocatalytic Properties," *J. Phys. Chem. C*, vol. 115, pp. 5708–5719, 2011.

- [74] M. N. Chong, B. Jin, C. W. K. Chow, and C. Saint, "Recent developments in photocatalytic water treatment technology: a review," *Water Res.*, vol. 44, no. 10, pp. 2997–3027, May 2010.
- [75] D. Dogan and H. Turkdemir, "Electrochemical Treatment of Actual Textile Indigo Dye Effluent," *Polish J. Environ. Stud.*, vol. 21, no. 5, pp. 1185–1190, 2012.
- [76] M. Constantin, I. Asmarandei, V. Harabagiu, L. Ghimici, P. Ascenzi, and G. Fundueanu, "Removal of anionic dyes from aqueous solutions by an ion-exchanger based on pullulan microspheres," *Carbohydr. Polym.*, vol. 91, no. 1, pp. 74–84, Jan. 2013.
- [77] J. H. Ramirez, F. J. Maldonado-Hódar, A. F. Pérez-Cadenas, C. Moreno-Castilla, C. a. Costa, and L. M. Madeira, "Azo-dye Orange II degradation by heterogeneous Fenton-like reaction using carbon-Fe catalysts," *Appl. Catal. B Environ.*, vol. 75, no. 3–4, pp. 312–323, Sep. 2007.
- [78] M. N. Nadagouda, I. Desai, C. Cruz, and D. J. Yang, "Novel Pd based catalyst for the removal of organic and emerging contaminants," *RSC Adv.*, vol. 2, pp. 7540–7548, 2012.
- [79] Y. Yu, J. C. Yu, C.-Y. Chan, Y.-K. Che, J.-C. Zhao, L. Ding, W.-K. Ge, and P.-K. Wong, "Enhancement of adsorption and photocatalytic activity of TiO₂ by using carbon nanotubes for the treatment of azo dye," *Appl. Catal. B Environ.*, vol. 61, pp. 1–11, Oct. 2005.
- [80] H. Cherifi, B. Fatiha, and H. Salah, "Kinetic studies on the adsorption of methylene blue onto vegetal fiber activated carbons," *Appl. Surf. Sci.*, vol. 282, pp. 52–59, Oct. 2013.
- [81] J. Yener, T. Kopac, G. Dogu, and T. Dogu, "Dynamic analysis of sorption of Methylene Blue dye on granular and powdered activated carbon," *Chem. Eng. J.*, vol. 144, no. 3, pp. 400–406, Nov. 2008.
- [82] X. Qu, P. J. J. Alvarez, and Q. Li, "Applications of nanotechnology in water and wastewater treatment.," *Water Res.*, vol. 47, no. 12, pp. 3931–46, Aug. 2013.

- [83] M. S. Mauter and M. Elimelech, "Critical Review Environmental Applications of Carbon-Based Nanomaterials," *Environ. Sci. Technol.*, vol. 42, no. 16, pp. 5843–5859, 2008.
- [84] X. Ren, C. Chen, M. Nagatsu, and X. Wang, "Carbon nanotubes as adsorbents in environmental pollution management: A review," *Chem. Eng. J.*, vol. 170, no. 2–3, pp. 395–410, Jun. 2011.
- [85] G. K. Ramesha, A. Vijaya Kumara, H. B. Muralidhara, and S. Sampath, "Graphene and graphene oxide as effective adsorbents toward anionic and cationic dyes," *J. Colloid Interface Sci.*, vol. 361, no. 1, pp. 270–7, Sep. 2011.
- [86] C. W. Tan, K. H. Tan, Y. T. Ong, A. R. Mohamed, S. H. Zein, and S. H. Tan, "Energy and environmental applications of carbon nanotubes," *Environ. Chem. Lett.*, vol. 10, no. 3, pp. 265–273, Feb. 2012.
- [87] J. Ma, F. Yu, L. Zhou, L. Jin, M. Yang, J. Luan, Y. Tang, H. Fan, Z. Yuan, and J. Chen, "Enhanced adsorptive removal of methyl orange and methylene blue from aqueous solution by alkali-activated multiwalled carbon nanotubes," *ACS Appl. Mater. Interfaces*, vol. 4, no. 11, pp. 5749–60, Nov. 2012.
- [88] X. Zhu, L. Zhu, Y. Chen, and S. Tian, "Acute toxicities of six manufactured nanomaterial suspensions to *Daphnia magna*," *J. Nanoparticle Res.*, vol. 11, pp. 67–75, Jun. 2009.
- [89] C. J. Smith, B. J. Shaw, and R. D. Handy, "Toxicity of single walled carbon nanotubes to rainbow trout, (*Oncorhynchus mykiss*): respiratory toxicity, organ pathologies, and other physiological effects," *Aquat. Toxicol.*, vol. 82, no. 2, pp. 94–109, May 2007.
- [90] W. Fan, W. Gao, C. Zhang, W. W. Tjiu, J. Pan, and T. Liu, "Hybridization of graphene sheets and carbon-coated Fe₃O₄ nanoparticles as a synergistic adsorbent of organic dyes," *J. Mater. Chem.*, vol. 22, no. 48, p. 25108, 2012.
- [91] J.-L. Gong, B. Wang, G.-M. Zeng, C.-P. Yang, C.-G. Niu, Q.-Y. Niu, W.-J. Zhou, and Y. Liang, "Removal of cationic dyes from aqueous solution using magnetic multi-wall carbon nanotube nanocomposite as adsorbent," *J. Hazard. Mater.*, vol. 164, no. 2–3, pp. 1517–22, May 2009.

- [92] L. Tang, Y. Cai, G. Yang, Y. Liu, G. Zeng, Y. Zhou, S. Li, J. Wang, S. Zhang, Y. Fang, and Y. He, “Cobalt nanoparticles-embedded magnetic ordered mesoporous carbon for highly effective adsorption of rhodamine B,” *Appl. Surf. Sci.*, vol. 314, pp. 746–753, Sep. 2014.
- [93] S. C. N. Tang and I. M. C. Lo, “Magnetic nanoparticles: essential factors for sustainable environmental applications.,” *Water Res.*, vol. 47, no. 8, pp. 2613–32, May 2013.
- [94] G. Tao, L. Zhang, Z. Hua, Y. Chen, L. Guo, J. Zhang, Z. Shu, J. Gao, H. Chen, W. Wu, Z. Liu, and J. Shi, “Highly efficient adsorbents based on hierarchically macro/mesoporous carbon monoliths with strong hydrophobicity,” *Carbon N. Y.*, vol. 66, pp. 547–559, Jan. 2014.
- [95] B. Fugetsu, S. Satoh, T. Shiba, T. Mizutani, Y.-B. Lin, N. Terui, Y. Nodasaka, K. Sasa, K. Shimizu, T. Akasaka, M. Shindoh, K. Shibata, A. Yokoyama, M. Mori, K. Tanaka, Y. Sato, K. Tohji, S. Tanaka, N. Nishi, and F. Watari, “Caged multiwalled carbon nanotubes as the adsorbents for affinity-based elimination of ionic dyes.,” *Environ. Sci. Technol.*, vol. 38, no. 24, pp. 6890–6, Dec. 2004.
- [96] H. Cong, X. Ren, P. Wang, and S. Yu, “Macroscopic Multifunctional Graphene-Based Hydrogels and Aerogels by a Metal Ion Induced Self-assembly Process,” *ACS Nano*, vol. 6, no. 3, pp. 2693–2703, 2012.
- [97] F. Liu, S. Chung, G. Oh, and T. S. Seo, “Three-dimensional graphene oxide nanostructure for fast and efficient water-soluble dye removal.,” *ACS Appl. Mater. Interfaces*, vol. 4, no. 2, pp. 922–7, Feb. 2012.
- [98] C. D. Vecitis, G. Gao, and H. Liu, “Electrochemical Carbon Nanotube Filter for Adsorption, Desorption, and Oxidation of Aqueous Dyes and Anions,” *J. Phys. Chem. C*, vol. 115, no. 9, pp. 3621–3629, Mar. 2011.
- [99] L. Ai and J. Jiang, “Removal of methylene blue from aqueous solution with self-assembled cylindrical graphene–carbon nanotube hybrid,” *Chem. Eng. J.*, vol. 192, pp. 156–163, Jun. 2012.

- [100] Z. Shahryari, A. S. Goharrizi, and M. Azadi, "Experimental study of methylene blue adsorption from aqueous solutions onto carbon nano tubes," *Int. J. Water Resour. Environ. Eng.*, vol. 2, no. 2, pp. 16–28, 2010.
- [101] A. K. Karumuri, D. P. Oswal, H. a. Hostetler, and S. M. Mukhopadhyay, "Silver nanoparticles attached to porous carbon substrates: Robust materials for chemical-free water disinfection," *Mater. Lett.*, vol. 109, pp. 83–87, 2013.
- [102] I. T. Barney, D. S. R. Lennaerts, S. R. Higgins, and S. M. Mukhopadhyay, "Specific surface area of hierarchical graphitic substrates suitable for multi-functional applications," *Mater. Lett.*, vol. 88, pp. 160–163, Dec. 2012.
- [103] A. A. Maleszewski, "The Functionalization and Characterization of Adherent Carbon Nanotubes with Silver Nanoparticles for Biological Applications," Wright State University, 2011.
- [104] A. K. Karumuri, A. A. Maleszewski, D. P. Oswal, H. a. Hostetler, and S. M. Mukhopadhyay, "Fabrication and characterization of antibacterial nanoparticles supported on hierarchical hybrid substrates," *J. Nanoparticle Res.*, vol. 16, no. 4, p. 2346, Mar. 2014.
- [105] Y. S. Ho and G. McKay, "Pseudo-second order model for sorption processes," *Process Biochem.*, vol. 34, no. 5, pp. 451–465, Jul. 1999.
- [106] Y.-S. Ho, "Review of second-order models for adsorption systems.," *J. Hazard. Mater.*, vol. 136, no. 3, pp. 681–9, Aug. 2006.
- [107] Y. . Ho and G. McKay, "A kinetic study of dye sorption by biosorbent waste product pith," *Resour. Conserv. Recycl.*, vol. 25, no. 3–4, pp. 171–193, Mar. 1999.
- [108] I. Langmuir, "The adsorption of gases on plane surfaces of glass, mica and platinum," *J. Am. Chem. Soc.*, vol. 40, no. 9, pp. 1361–1403, 1918.
- [109] H. M. F. Freundlich, "Over the adsorption in solution," *J. Phys. Chem.*, vol. 57, pp. 385–471, 1906.
- [110] V. V. Chagovets, M. V. Kosevich, S. G. Stepanian, O. a. Boryak, V. S. Shelkovsky, V. V. Orlov, V. S. Leontiev, V. a. Pokrovskiy, L. Adamowicz, and V. a. Karachevtsev, "Noncovalent Interaction of Methylene Blue with Carbon

- Nanotubes: Theoretical and Mass Spectrometry Characterization,” *J. Phys. Chem. C*, vol. 116, no. 38, pp. 20579–20590, Sep. 2012.
- [111] P. T. Hang and G. W. Brindley, “Methylene blue absorption by clay minerals. Determination of surface areas and cation exchange capacities (clay-organic studies XVIII),” *Clays Clay Miner.*, vol. 18, no. 4, pp. 203–212, 1970.
- [112] G. Kahr and F. T. Madsen, “Determination of the cation exchange capacity and the surface area of bentonite, illite and kaolinite by methylene blue adsorption,” *Appl. Clay Sci.*, vol. 9, no. 5, pp. 327–336, 1995.
- [113] H. Wang, H. Ma, W. Zheng, D. An, and C. Na, “Multifunctional and recollectable carbon nanotube ponytails for water purification,” *ACS Appl. Mater. Interfaces*, vol. 6, no. 12, pp. 9426–9434, 2014.
- [114] S. H. Ko, I. Park, H. Pan, C. P. Grigoropoulos, A. P. Pisano, C. K. Luscombe, and J. M. J. Fréchet, “Direct nanoimprinting of metal nanoparticles for nanoscale electronics fabrication,” *Nano Lett.*, vol. 7, no. 7, pp. 1869–77, Jul. 2007.
- [115] W. Zhang, “Nanoscale iron particles for environmental remediation: An overview,” *J. Nanoparticle Res.*, vol. 5, pp. 323–332, 2003.
- [116] C. Wang, M. Waje, X. Wang, J. M. Tang, R. C. Haddon, and Y. Yan, “Proton Exchange Membrane Fuel Cells with Carbon Nanotube Based Electrodes,” *Nano Lett.*, vol. 4, no. 2, pp. 345–348, Feb. 2004.
- [117] C. Batchelor-McAuley, C. E. Banks, A. O. Simm, T. G. J. Jones, and R. G. Compton, “Nano-electrochemical detection of hydrogen or protons using palladium nanoparticles: distinguishing surface and bulk hydrogen,” *J. Chem. Phys. Phys. Chem.*, vol. 7, no. 5, pp. 1081–5, May 2006.
- [118] F. Rahimi and A. Iraj, “Characterization of Pd nanoparticle dispersed over porous silicon as a hydrogen sensor,” vol. 40, pp. 7201–7209, 2007.
- [119] Z. Shi and J. A. Szpunar, “SYNTHESIS OF AN ULTRA-THIN PALLADIUM MEMBRANE FOR HYDROGEN EXTRACTION,” *Rev. Adv. Mater. Sci.*, vol. 15, pp. 1–9, 2007.

- [120] A. K. Mishra and S. Ramaprabhu, "Palladium nanoparticles decorated graphite nanoplatelets for room temperature carbon dioxide adsorption," *Chem. Eng. J.*, vol. 187, pp. 10–15, Apr. 2012.
- [121] T. Teranishi and M. Miyake, "Size Control of Palladium Nanoparticles and Their Crystal Structures," *Chem. Mater.*, vol. 4756, no. 23, pp. 594–600, 1998.
- [122] Y.-H. Qin, Yue-Jiang, H.-H. Yang, X.-S. Zhang, X.-G. Zhou, L. Niu, and W.-K. Yuan, "Synthesis of highly dispersed and active palladium/carbon nanofiber catalyst for formic acid electrooxidation," *J. Power Sources*, vol. 196, pp. 4609–4612, May 2011.
- [123] C. C. Yang, C. C. Wan, and Y. Y. Wang, "Synthesis of Ag/Pd nanoparticles via reactive micelles as templates and its application to electroless copper deposition," *J. Colloid Interface Sci.*, vol. 279, no. 2, pp. 433–439, 2004.
- [124] V. K. Rao and T. P. Radhakrishnan, "Hollow bimetallic nanoparticles generated in situ inside a polymer thin film: fabrication and catalytic application of silver–palladium–poly(vinyl alcohol)," *J. Mater. Chem. A*, vol. 1, no. 43, p. 13612, 2013.
- [125] H. Wang, C. Wang, H. Yan, H. Yi, and J. Lu, "Precisely-controlled synthesis of Au@Pd core–shell bimetallic catalyst via atomic layer deposition for selective oxidation of benzyl alcohol," *J. Catal.*, vol. 324, pp. 59–68, 2015.
- [126] USEPA 1979. and EPA-440/4-79-029b (1979), "Water-related environmental fate of 129 priority pollutants, Volume II. Office of water planning and standards and Office of water and waste management," 1979.
- [127] *Handbook for the Montreal Protocol on substances that deplete the ozone layer - 7th Edition, United Nations Environment Programme.* 2006.
- [128] X. Wang, C. Chen, H. Liu, and J. Ma, "Characterization and Evaluation of Catalytic Dechlorination Activity of Pd/Fe Bimetallic Nanoparticles," *Ind. Eng. Chem. Res.*, vol. 47, no. 22, pp. 8645–8651, Nov. 2008.
- [129] J. Feng and T.-T. Lim, "Pathways and kinetics of carbon tetrachloride and chloroform reductions by nano-scale Fe and Fe/Ni particles: comparison with

- commercial micro-scale Fe and Zn.,” *Chemosphere*, vol. 59, no. 9, pp. 1267–77, Jun. 2005.
- [130] G. G. Wildgoose, C. E. Banks, and R. G. Compton, “Metal nanoparticles and related materials supported on carbon nanotubes: methods and applications.,” *Small*, vol. 2, no. 2, pp. 182–93, Feb. 2006.
- [131] USEPA, “Estimated Henry’s Law Constants, EPA On-line Tools for Site Assessment Calculation, Ecosystems Research (Athens, GA). <http://www.epa.gov/athens/learn2model/part-two/onsite/esthenry.html>.”
- [132] USEPA, “Part 5: Chemical-Specific Parameters, Table 36. Chemical-Specific Properties Used in SSL Calculations, Dimensionless Henry’s law constant. http://www.epa.gov/superfund/health/conmedia/soil/pdfs/part_5.pdf.”
- [133] D. R. Burris, C. a. Delcomyn, M. H. Smith, and a. Lynn Roberts, “Reductive dechlorination of tetrachloroethylene and trichloroethylene catalyzed by vitamin B12 in homogeneous and heterogeneous systems,” *Environ. Sci. Technol.*, vol. 30, no. 10, pp. 3047–3052, 1996.
- [134] G. V. Lowry and M. Reinhard, “Hydrodehalogenation of 1- to 3-Carbon Halogenated Organic Compounds in Water Using a Palladium Catalyst and Hydrogen Gas,” *Environ. Sci. Technol.*, vol. 33, pp. 1905–1910, 1999.
- [135] Y. Liu, S. a Majetich, R. D. Tilton, D. S. Sholl, and G. V Lowry, “TCE dechlorination rates, pathways, and efficiency of nanoscale iron particles with different properties.,” *Environ. Sci. Technol.*, vol. 39, no. 5, pp. 1338–45, Mar. 2005.
- [136] G. V. Lowry and M. Reinhard, “Pd-Catalyzed TCE Dechlorination in Groundwater: Solute Effects, Biological Control, and Oxidative Catalyst Regeneration,” *Environ. Sci. Technol.*, vol. 34, no. 15, pp. 3217–3223, Aug. 2000.
- [137] D. R. Burris and C. a Delcomyn, “Reductive Dechlorination of Trichloroethene Mediated by Humic - Metal Complexes,” pp. 1145–1147, 1999.

- [138] B. Schrick, J. L. Blough, a. D. Jones, and T. E. Mallouk, “Hydrodechlorination of trichloroethylene to hydrocarbons using bimetallic nickel-iron nanoparticles,” *Chem. Mater.*, vol. 14, no. 12, pp. 5140–5147, 2002.
- [139] M. Tobiszewski and J. Namieśnik, “Abiotic degradation of chlorinated ethanes and ethenes in water,” *Environ. Sci. Pollut. Res.*, vol. 19, no. 6, pp. 1994–2006, 2012.
- [140] D. C. Wilson and T. L. Jones-Lepp, “Emerging Contaminant Sources and Fate in Recharged Treated Wastewater, Lake Havasu City, Arizona,” *Environ. Eng. Geosci.*, vol. 19, pp. 231–251, 2013.
- [141] USEPA. 2009, “Occurrence of Contaminants of Emerging Concern in Wastewater From Nine Publicly Owned Treatment Works, EPA-821-R-09-009, U.S. Environmental Protection Agency Office of Water (4303T),” 2009.
- [142] L. Schaider, J. Ackerman, R. Rudel, S. Dunagan, and J. Brody, “Emerging Contaminants in Cape Cod Private Drinking Water Wells,” 2011.
- [143] USEPA. 2010 and EPA-820-R-10-002, “Treating Contaminants of Emerging Concern - A Literature Review Database. U.S. Environmental Protection Agency Office of Water (4303T),” 2010.
- [144] J. Li, Y. Zhan, J. Lin, A. Jiang, and W. Xi, “Removal of bisphenol A from aqueous solution using cetylpyridinium bromide (CPB)-modified natural zeolites as adsorbents,” *Environ. Earth Sci.*, vol. 72, no. 10, pp. 3969–3980, May 2014.
- [145] S. K. Behera, S.-Y. Oh, and H.-S. Park, “Sorption of triclosan onto activated carbon, kaolinite and montmorillonite: effects of pH, ionic strength, and humic acid,” *J. Hazard. Mater.*, vol. 179, no. 1–3, pp. 684–91, Jul. 2010.
- [146] S. H. Joo and D. Zhao, “Destruction of lindane and atrazine using stabilized iron nanoparticles under aerobic and anaerobic conditions: effects of catalyst and stabilizer,” *Chemosphere*, vol. 70, no. 3, pp. 418–25, Jan. 2008.
- [147] K. Chiang, T. M. Lim, L. Tsen, and C. C. Lee, “Photocatalytic degradation and mineralization of bisphenol A by TiO₂ and platinized TiO₂,” *Appl. Catal. A Gen.*, vol. 261, no. 2, pp. 225–237, Apr. 2004.

- [148] USEPA. 2001h., “Revised Preliminary Human Health Risk Assessment: Atrazine. U.S. Environmental Protection Agency, Office of Pesticide Programs, Washington, D.C.,” 2001.
- [149] R. N. Brent, J. Schofield, K. Miller, and USEPA. 2001 EPA 905R-01-010., “Results of the Lake Michigan Mass Balance Study: Atrazine Data Report December 2001,” 2001.
- [150] USEPA. 1995b., “National Primary Drinking Water Regulations, Contaminant Specific Fact Sheets, Synthetic Organic Chemicals, Technical Version. EPA 811/F-95/003-T.,” 1995.
- [151] R. N. Lerch and W. W. Donald, “Analysis of Hydroxylated Atrazine Degradation Products in Water Using Solid-Phase Extraction and High-Performance Liquid Chromatography,” *J. Agric. Food Chem.*, vol. 42, no. 4, pp. 922–927, 1994.
- [152] T. Dombek, E. Dolan, J. Schultz, and D. Klarup, “Rapid reductive dechlorination of atrazine by zero-valent iron under acidic conditions,” *Environ. Pollut.*, vol. 111, pp. 21–27, 2001.
- [153] R. N. Lerch, P. E. Blanchard, and E. M. Thurman, “Contribution of Hydroxylated Atrazine Degradation Products to the Total Atrazine Load in Midwestern Streams,” *Environ. Sci. Technol.*, vol. 32, pp. 40–48, 1998.

Appendix A: Methylene Blue Removal - using supported Pd-NPs

Batch test for removal of MB dye from simulated water as discussed in Chapter 5 were also carried out using Pd-NPs fabricated on hierarchical carbon structures and studied using UV-Vis Spectroscopy. Figure A1 shows the removal of MB with and without Pd-NPs catalysts on foam as well as CNT grafted foams. CNT-Foam structures again prove to be better for removal of MB as compared to bare porous foams. However, additional Pd catalysts on Foam or CNT-Foam (Pd-Foam and Pd-CNT-Foam) did not show any significant increase (Figure A1) in the removal kinetics of MB indicating that the mechanism of MB removal using metallic palladium may not be catalytically significant. The excess surface created by Pd-NPs on CNT structures may account for adsorbing sites for MB. Future studies involving characterization of the structures as well as HPLC analysis may provide insight to the current findings.

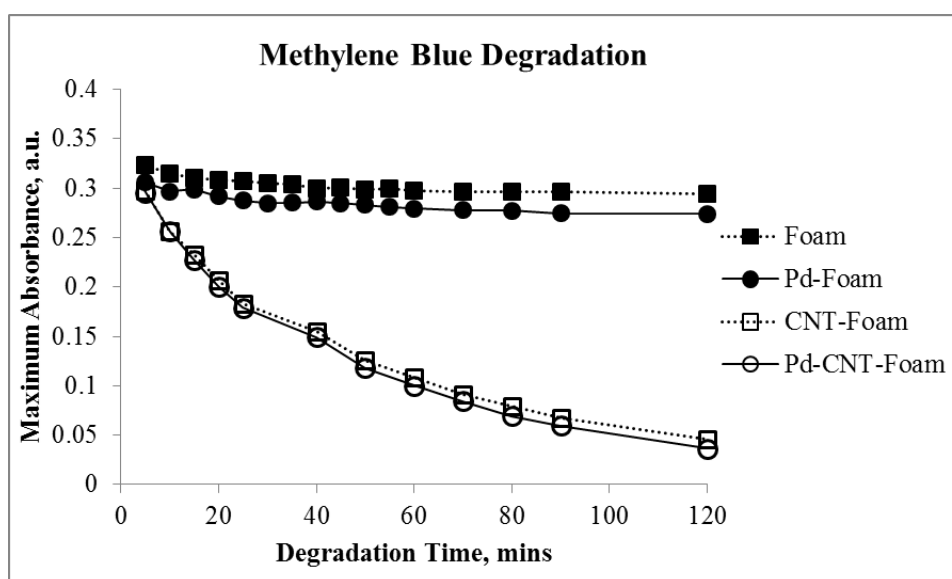


Figure A1 Methylene blue removal plot obtained with (a) Ce-Foam, (b) Pd/Ce-Foam, (c) CNT Ce-Foam, and (d) Pd/CNT Ce-Foam hybrid structures.

Appendix B : Chlorinated Hydrocarbons Quantification

Chlorinated hydrocarbon compounds (CHCs) studied and analyzed are

1. Trichloroethylene – TCE
2. Trichloroethane – TCA
3. Dichloroethane – DCA

CHCs Quantification:

1. Stock solutions of CHCs were prepared in a 160 mL serum bottle filled with water and 20 μ L of the pure compound was added to the stock. Concentration of the stock (mg/L) was determined as shown in Table B1.
2. Standard solutions of the CHCs were prepared in MilliQ water for various concentrations or total initial mass of CHCs in the 60 mL reactor bottles containing 40% headspace. The total mass added to reactors is calculated using equations as shown in Table B2.
3. Calibration curves were obtained by plotting the GC peak areas of corresponding compounds (x- abscissa) with the total known standard mass (at y-coordinate)
4. Using ideal gas law equations and dimensionless Henry's constant at 25 °C [131], [132], the fraction in water or partitioning coefficient was determined as shown in Table B2 (*S.No.* 5 and 6). The partitioning coefficient, F_w , was used to determine the aqueous mass in μ moles after partitioning as shown in *S.No* 8 to 10 of Table B2
5. The rate constants were obtained from the Psuedo-first order model as determined by Burris *et.al.* [133] and the actual (aqueous) rate constant, k'_{obs} was determined using the partitioning coefficient as shown in Table B3.

Table B.1 Chlorinated hydrocarbons compounds (CHCs) - stock solution calculations

CHCs STOCK Solution Preparations – Ex: Trichloroethylene			
<i>S.No</i>	<i>Description</i>	<i>Formula</i>	<i>Amount</i>
1	Density of Trichloroethylene	ρ_{TCE}	1.46 g/mL
2	Volume of water in bottle	V	160 mL
3	Vol. Pure TCE injected into stock bottle	V_{pure}	20 μ L
4	Mass. TCE in stock bottle	$M_{TCE} = \rho_{TCE} \times V_{pure}$	29.2 mg
5	Concentration of stock solution	$C_S = M_{TCE} / V$	182.5 mg/L (ppm)

Table B.2 Chlorinated hydrocarbon compounds (CHCs) standard calculations

CHCs Standard Solution Preparations – Ex: Trichloroethylene			
<i>S.No</i>	<i>Description</i>	<i>Formula</i>	<i>Amount</i>
1	Total Volume of Reactor Bottle	V_T	60 mL
2	Volume of water, 60%	V_w	36 mL
3	Volume of air, 40%	V_a	24 mL
4	Molecular Weight TCE	MW_{TCE}	131.4 g/mol
5	Dimensionless Henry's Constant for TCE at 25°C, [131], [132]	K_H'	0.421
6	F_w (fraction in water), partitioning coefficient	$F_w = \frac{1}{\left(1 + K_H' \frac{V_a}{V_w}\right)}$	0.7808
7	Volume of stock to be injected (0.02, 0.1, 0.2, 0.4, 1 or 2 mL)	V_S	200 μ L
8	Total TCE mass in the bottle (μ moles)	$M_T (moles) = \frac{V_S * C_S}{MW_{TCE}}$	0.278 μ moles
9	Total TCE mass in the bottle (μ g)	$M_T (gms) = M_T (moles) * MW_{TCE}$	36.5 μ g
10	Aqueous mass after partitioning (μ moles)	$M'_w = M_T * F_w$	0.2169 μ moles
11	Aqueous TCE conc. before partitioning (mg/L)	$C_w = \frac{M_T}{V_w}$	1.014 mg/L (ppm)
12	Aqueous TCE after partitioning (mg/L)	$C'_w = C_w * F_w$	0.7917 mg/L (ppm)

Table B.3 Pseudo-first order equation and rate constant calculations for chlorinated hydrocarbons (CHCs) in reactors

Pseudo-First Order Model Calculations – Ex: Trichloroethylene Dechlorination Rates			
<i>S.No</i>	<i>Description</i>	<i>Formula</i>	<i>Amount</i>
1	Volume of stock to be injected	V_S	200 μL
2	Total TCE mass in the bottle (μmoles)	$M_T (\text{moles}) = \frac{V_S * C_S}{MW_{TCE}}$	0.278 μmoles
3	Initial TCE mass in the reactor, (μmoles)	M_{t0}	0.278 μmoles
4	Mass of TCE in the reactor at time t, (determined using calibration curve and peak areas) (μmoles)	M_t	μmoles
5	Pseudo-First order Equation	$\ln M_t = \ln M_{t0} - k_{obs} t$	Linear equation
6	Apparent Pseudo-first order rate constant (obtained from plot in Figure 8.6 and Table 8.1) Ex: Pd-CNT foam	k_{obs}	0.1126 min^{-1}
7	F_w (mass fraction TCE in water), partitioning coefficient	$F_w = \frac{1}{\left(1 + K'_H \frac{V_a}{V_w}\right)}$	0.7808
8	Actual Pseudo-first order rate constant (aqueous)	$k'_{obs} = \frac{k_{obs}}{F_w}$	0.1442 min^{-1}

Appendix C: Abbreviations and Chemical Compounds

Ag	Silver
Ag-Pd	Silver-Palladium
Ag-Pd NPs	Silver-Palladium nanoparticles
Ar	Argon
BE	Binding energy
BET	Brunauer-Emmett-Teller
Ce-Foam	Cellular Foam
CECs	Contaminants of emerging concern
CFCs	Chlorofluorocarbons
CHCs	Chlorinated hydrocarbons
CNFs	Carbon nanofibers
CNT	Carbon nanotubes
COCs	Chlorinated organic compounds
CS	Cross-section
CVD	Chemical vapor deposition
DCA	Dichloroethane
DCE-	Dichloroethylene
DI	De-ionized
DMSO	Dimethyl sulfoxide
EDS	Energy dispersive X-ray spectroscopy
FCC	Face centered cubic
FE-SEM	Field emission scanning electron microscopy

Fe/Xy	Ferrocene/Xylene
FWHM	Full width half maximum
GC-MS	Gas Chromatography – Mass Spectrometry
H ₂	Hydrogen
HCl	Hydrochloric acid
HMDSO	Hexmethyl-di-siloxane
HPLC	High Performance Liquid Chromatography
KE	Kinetic energy
LC-MS	Liquid Chromatography – Mass Spectrometry
MRM	Multiple reaction mode
MSD	Mass selective detector
MW	Microwave
MWCNT	Multi wall carbon nanotubes
NPs	Nanoparticles
O	Oxygen
Pd	Palladium
Pd-NPs	Palladium nanoparticles
PdO	Palladium Oxide
PdO-NPs	Palladium Oxide nanoparticles
ppm	Parts per million
ppi	Pores per inch
Pt	Platinum
PTFE	Polytetrafluoroethylene, Teflon
RSF	Relative sensitivity factor

RVC	Reticulated vitreous carbon
RVC-CNT	Carbon nanotubes grown on Reticulated vitreous carbon
SEM	Scanning electron microscopy
SiO ₂ or SiO _x	Silica
SIR	Selective ion reaction monitoring
SSA	Specific surface area
STEM	Scanning transmission electron microscopy
SWCNT	Single wall carbon nanotubes
TAPN	Tetraamine palladium (II) nitrate, [Pd(NH ₃) ₄](NO ₃) ₂
TCA	Trichloroethane
TCE	Trichloroethylene
TIC	Total ion chromatogram
UHV	Ultra high vacuum
UV-Vis	UV-Vis Spectrophotometry
VACNT	Vertically aligned carbon nanotubes
XPS	X-ray photoelectron spectroscopy
XRD	X-ray diffraction
Z	Atomic number
ZVI	Zero valent iron
3-D	Three Dimensional